Doctoral theses at NTNU, 2020:213

Dennis Monteban

Measurements and modelling of Arctic coastal environments

NTNU
Norwegian University of
Science and Technology

Dennis Monteban

Doctoral Thesis

Doctoral theses at NTNU, 2020:213

NTNU
Norwegian University of
Science and Technology
Faculty of Engineering
Department of Civil and Environmental Engineering

NTNU

ISBN 978-82-326-4774-3 (printed version)
ISBN 978-82-326-4775-0 (electronic version)
ISSN 1503-8181

NTNU
Norwegian University of
Science and Technology

Dennis Monteban

Measurements and modelling of Arctic coastal environments

Thesis for the Joint Degree of Philosophiae Doctor (PhD)

Lyngby, March 2020

Technical University of Denmark
DTU space - National Space Institute
Division of Innovation and Research-based Consultancy

&

Norwegian University of Science and Technology
Faculty of Engineering
Department of Civil and Environmental Engineering

DTU

NTNU
Norwegian University of
Science and Technology

DTU
Technical University of Denmark
DTU space - National Space Institute
Division of Innovation and Research-based Consultancy

NTNU
Norwegian University of Science and Technology
Faculty of Engineering
Department of Civil and Environmental Engineering

Thesis for the Joint Degree of Philosophiae Doctor

Preface

This PhD work entitled "*Measurements and modelling of Arctic coastal environments*" is submitted to the Technical University of Denmark (DTU) and the Norwegian University of Science and Technology (NTNU) for the partial fulfilment of the requirements of the joint Degree of Philosophiae Doctor. This thesis is the outcome of a three-year PhD programme.

The candidate was supervised by:

- Senior Scientist Jens Olaf Pepke Pedersen at DTU Space, Technical University of Denmark
- Associate Professor Raed Lubbad at the Department of Civil and Environmental Engineering, Norwegian University of Science and Technology

The candidate was co-supervised by:

- Associate Professor Thomas Ingeman-Nielsen at the Department of Civil Engineering, Technical University of Denmark

Abstract

The most pronounced effects of climate change are observed in the polar regions, especially in the Arctic, which is currently warming more rapidly than the rest of the world. The Arctic is losing sea ice, and the oceans are changing. The consequences of this polar transition affect the whole planet. The 13th goal of the United Nations Sustainable Development Goals is to take urgent action to combat climate change and its impacts. This Climate Action goal includes targets such as strengthening the resilience against climate-related hazards and improve climate change impact reduction, adaptation, mitigation and early warning systems. The main objective of this PhD was to improve our understanding of the physical environment of the Arctic using in-situ measured data, remote sensing techniques and numerical modelling. Such an understanding is crucial to fully comprehend the ongoing changes and predict the effects due to climate change, and, therefore, indirectly contributes to the targets of the 13th United Nation Sustainability Goal.

In this PhD thesis, three Arctic phenomena/topics were studied, including:

1) Wave propagation through ice-covered oceans
2) The physical oceanographic environment of the Arctic fjord Kangerlussuaq
3) Iceberg drift modelling in the Barents Sea

First, ocean waves travelling through icy waters were studied using satellite remote sensing data. *Synthetic aperture radar* (SAR) data were found to be the most valuable source of satellite information to study wave-ice interactions. This type of data was used to study the change of wave parameters (peak wavelength and dominant wave direction) as waves enter the ice-covered waters of the Barents Sea, where accompanying in-situ data were available from the *Barents Sea Metocean and Ice Network* (BaSMIN) programme. A change in dominant wave direction was found towards the normal, relative to the ice edge, which is partly due to refraction and due to a SAR imaging artefact. The peak wavelength slightly increases as waves travel within the sea ice, which is due to the spatial dispersion of waves and is possibly enhanced by wave-ice interactions. Furthermore, the wave dispersion relation within sea ice was estimated from Sentinel-1 SAR Interferometric Wide swath data by using an innovative new implementation of a known method. In-situ data of sea currents from the BaSMIN campaign allowed the quantification of these data's influence on the wave dispersion relation, which is a significant improvement over previous studies. The dispersion relation was derived for long waves (peak wavelengths between 100 m – 350 m) within thin ice (ice thickness less than 40 cm). The derived relation does not deviate from the theoretical open-water dispersion relation, which agrees with previous findings. Presently, however, the resolution of the SAR data is too coarse to study the wave dispersion relation of short waves within sea ice.

Secondly, the seasonal variations of the physical oceanographic conditions and the wave climate in the Arctic fjord Kangerlussuaq were studied. Two high-fidelity numerical models were set up and calibrated against in-situ data. Having such models allows us to fill in the spatial and temporal gaps left by in-situ data. The fjord consists of a deep, inner part with very slow currents and a shallow, outer part that is characterised by very strong tidal currents. These strong currents are most likely the cause of the absence of sea ice during winter in the outer part. During summertime, the inner part of the fjord is strongly stratified, and three water masses are present: water from the West Greenland Current, a brackish surface layer and a homogeneous deep-lying water mass. The brackish surface layer is heavily affected by the meltwater from the inland ice, and this layer has a net outflow towards the open ocean. The deep-lying water mass is hardly subject to renewal during summer and appears dynamically decoupled from the open ocean. Furthermore, the 50-year return period significant wave height and peak wave period were estimated, which have a value of 1.8 m and 5 s, respectively.

Finally, iceberg occurrence in the Barents Sea was studied using a numerical iceberg drift and deterioration model taken from the literature. Estimating annual iceberg encounter frequencies is vital for designing offshore structures and planning ice management operations. It was found that considerable uncertainties exist in two parameters of the model input at the iceberg sources, namely 1) the annual number of icebergs released from the sources that drift freely into the Barents Sea, and 2) the initial size characteristics of the released icebergs. Satellite remote sensing data collected by the Sentinel-2 constellation were utilised to derive iceberg size characteristics at the major iceberg sources. More than 22,000 icebergs were manually identified and provided statistics of the initial iceberg lengths and iceberg widths. Furthermore, a methodology is proposed using the Copernicus iceberg number density dataset, which primarily consists of Sentinel-1 data, to estimate the annual number of icebergs released. This results in approximately 2600 icebergs released per year. The model is forced with the newly obtained data to produce maps of the annual iceberg encounter frequencies and the annual expected number of icebergs in the Barents Sea.

Dansk Resumé

De mest markante effekter af klimaændringer observeres i de polare områder, hvor Arktis i øjeblikket opvarmes hurtigere end resten af verden. Arktis mister havis, og oceanerne ændrer sig, og konsekvenserne af denne forandring påvirker hele planeten. Det 13. af FN's Verdensmål for en bæredygtig udvikling er en hurtig indsats for at bekæmpe klimaforandringer og dens konsekvenser. Dette klimahandlingsmål inkluderer delmål såsom styrkelse af modstandskraften over for klimarelaterede risici og forbedring af kapaciteten til at modvirke, tilpasse og begrænse skaderne samt tidlig varsling af klimaændringer

Hovedformålet med dette ph.d.-projekt er at forbedre vores forståelse af det fysiske miljø i Arktis ved hjælp af in-situ-målte data, remote sensing-teknikker og numeriske modelsimuleringer. En sådan forståelse er afgørende for fuldt ud at forstå de igangværende ændringer og forudsige virkningerne som følge af klimaændringer, og projektet bidrager derfor indirekte til det 13. bæredygtighedsmål.

I denne ph.d.-afhandling blev tre arktiske fænomener / emner undersøgt, herunder:

1) Bølgeforplantning gennem isdækkede oceaner
2) Det fysiske oceanografiske miljø i den arktiske fjord Kangerlussuaq
3) Modellering af isbjerges drift i Barentshavet

For det første blev oceanbølger, der udbreder sig gennem iskolde farvande, undersøgt ved hjælp af remote sensing-data fra satellitter. Det blev fundet, at *syntetisk aperturradar-data* (SAR) var den mest værdifulde kilde til satellitinformation til undersøgelse af bølge/is-interaktioner. Denne type data blev brugt til at undersøge ændringen af bølgeparametre (bølgetops-længden og den dominerende bølgeretning), når bølger kommer ind i de isdækkede farvande i Barentshavet, hvor tilhørende in-situ-data er tilgængelige fra *Barents Sea Metocean and Ice Network* (BaSMIN) program. Der blev fundet en ændring i den dominerende bølgeretning i forhold til normalretningen af iskanten, hvilket delvis skyldes brydning og delvist er en artefakt ved SAR-billeder. Bølgetops-længden øges således lidt, når bølger bevæger sig ind under havisen. Dette skyldes hovedsageligt den rumlige spredning af bølger og øges muligvis af vekselvirkningen mellem bølge og is. Bølgedispersionsrelationen for havis blev anslået ud fra Sentinel-1 SAR Interferometric Wide Swath-data ved at benytte en ny og innovativ implementering af en kendt metode. In-situ-data for havstrømme fra BaSMIN-kampagnen muliggjorde desuden en kvantificering af disse datas indflydelse på bølgedispersionsforholdet, hvilket er en betydelig forbedring i forhold til tidligere undersøgelser. Spredningsforholdet er afledt for lange bølger (bølgetopslængder mellem 100 m og 350 m) i tynd is (istykkelse mindre end 40 cm) og afviger ikke fra det teoretiske spredningsforhold på åbent vand. I øjeblikket er opløsningen af SAR-data imidlertid for grov til at undersøge bølgedispersionsforholdet i havis.

For det andet blev de sæsonbestemte variationer af de fysiske oceanografiske forhold og af bølger i den arktiske fjord Kangerlussuaq undersøgt. I dette arbejde blev to numeriske modeller med høj troværdighed konfigureret og kalibreret mod in-situ data. At have sådanne modeller til rådighed giver mulighed for at udfylde de rumlige og tidsmæssige huller mellem in-situ-data. Fjorden består af en dyb, indre del med meget langsomme strømme og en lav, ydre del, der er kendetegnet ved meget stærke tidevandsstrømme. Disse stærke strømme er sandsynligvis årsagen til fraværet af is om vinteren i den ydre del. Om sommeren er den indre del af fjorden stærkt lagdelt, og tre vandmasser er til stede: vand fra Den Vestgrønlandske Havstrøm, et brakt overfladelag og en homogen dybere liggende vandmasse. Brakvandslaget er stærkt påvirket af smeltevandet fra Indlandsisen, og om sommeren har dette lag en nettoudstrømning mod det åbne hav. Den dybliggende vandmasse er næppe genstand for fornyelse om sommeren og ser ud til at være dynamisk

afkoblet fra det åbne hav. Endvidere blev den 50-årige returperiode for signifikant bølgehøjde og bølgeperiode, anslået til at have en værdi på henholdsvis 1,8 m og 5 s.

Endelig blev forekomsten af isbjerge i Barentshavet undersøgt ved hjælp af en numerisk model for drift og smeltning af isbjerge, hentet fra litteraturen. Det er vigtigt at anslå den årlige frekvens for forekomsten af isbjerge for at designe offshore-strukturer og planlægge isstyringsoperationer. Det blev konstateret, at der eksisterer betydelige usikkerheder i to af de parametre, der føder isbjerge ind i modellen, nemlig 1) det årlige antal isbjerge, der tilføres til Barentshavet, og 2) de oprindelige karakteristika for de isbjerge, der tilføres. Data fra satellitsensorer, indsamlet af Sentinel-2-konstellationen blev anvendt til at udlede karakteristiske data for størrelsen af isbjerge fra de vigtigste kilder til isbjerge. Mere end 22.000 isbjerge blev manuelt identificeret og anvendt til statistik over længde og bredde af de tilførte isbjerge. Derudover foreslås en metodologi, der anvender Copernicus-data for antal og tæthed af isbjerge (som primært bruger Sentinel-1 data), til at anslå det årlige antal tilførte isbjerge. Ved at bruge de nyligt opnåede data som input modellen, er der fremstillet kort over de årlige isbjergfrekvenser og det årlige forventede antal isbjerge.

Acknowledgements

First of all, I would like to express my deepest gratitude to Jens Olaf Pepke Pedersen and Raed Lubbad, my two principal supervisors from DTU and NTNU, respectively. Without their continuous trust and guidance, this thesis would not have been possible. Jens Olaf, thank you for the instructive supervision, encouraging discussions and enabling me to travel anywhere for research-related activities. Additionally, your help in getting me adjusted to everyday life in Denmark, and support in many practicalities such as housing is highly appreciated. Raed, beside the numerous discussions, insightful feedback and excellent supervision you provided, I want to thank you particularly for your support and encouragement during my semester at NTNU. Looking back, this was probably the most challenging period of my PhD as the research topic and direction were unclear. You kept me motivated during this time, which now, two years later, resulted in multiple publications and this thesis.

Furthermore, I would like to thank various people for their contribution to this thesis and the resulting publications; Harald Johnsen for his help in processing the SAR TOPS data, his assistance in writing my first journal paper and enabling two short research stays at CIRFA in Tromsø; Morten Rugbjerg for his assistance in setting up the MIKE models and enabling me to visit the DHI office; Morten Holtegaard Nielsen for the various discussion we had on the Kangerlussuaq fjord, and the input and constructive comments on the resulting journal paper; Thomas Ingeman-Nielsen for his advice and assistance in the beginning of the PhD work; Sveinung Løset for his suggestions, feedback and assistance regarding the journal paper on iceberg drift in the Barents Sea.

I thank Equinor for permission to use the in-situ data from the BaSMIN measurement campaign, and DHI for making the MIKE software available for this research.

At DTU, I would like to thank all the colleagues at the IFR and the Geomagnetism divisions for the enjoyable work atmosphere. At NTNU, I would like to thank all the colleagues in the “PhD basement” for the many pleasant lunch discussions. In particular, I want to thank both Hongtao Li, the “other half” of this joint PhD programme, and Ilija Samardzija. Ilija, the many discussions we had on the purpose of the PhD and its challenges, the (maybe too many) coffee breaks and the feedback we could provide each other made it worthwhile to come to the office every day during my time at NTNU.

I am particularly grateful for the proofreading of this thesis by my friends John Darnall, Dominique Hooimeijer and Gerald Songy. Besides that, I deeply appreciate you guys always being there when needed and the many memories shared together.

I am deeply grateful for my family back in Holland. Their unconditional and countless support gave me the strength to keep going and contributed indirectly, but significantly, to the thesis. Some (Tom ten Voorde) even contributed directly to this thesis, by helping me with manually counting icebergs, which has been much appreciated. Finally, and most importantly, my sincerest thanks to my significant other, Ebba Celius, for all your love, patience and support during this PhD work. I bet that was not easy with the many challenges, and the ups and downs I have been through!

Dennis Monteban

March 2020

Abbreviations

1D	One-Dimensional
2D	Two-Dimensional
3D	Three-Dimensional
AO	Arctic Oscillation
BaSMIN	Barents Sea Metocean and Ice Network
CMEMS	Copernicus Marine Environment Monitoring Service
CTD	Conductivity-Temperature-Density
DMI	Danish Meteorological Institute
FJL	Franz Josef Land
GEV	Generalised Extreme Value
GIS	Greenland Ice Sheet
HD	Hydrodynamic
IDAP	Ice Data Acquisition Programme
IPCC	Intergovernmental Panel on Climate Change
IW	Interferometric Wide
MIZ	Marginal Ice Zone
MTF	Modulation Transfer Function
S1	Sentinel-1
S2	Sentinel-2
SAR	Synthetic Aperture Radar
SMOS	Soil Moisture and Ocean Salinity
SW	Spectral Waves
TOPSAR	Terrain Observation with Progressive Scans SAR
WMO	World Meteorological Organisation

Contents

1 Introduction

The Arctic is the northernmost region of the Earth that is centred around the North Pole. It is commonly defined as the region above the Arctic Circle, which is approximately located at 66° 33′ N latitude. Except for the Antarctic, the Arctic is different from all other geographical locations on Earth as it has distinct characteristics such as remoteness, low temperatures, presence of sea and glacial ice, darkness, low population density, limited accessibility, diverse ecosystems, and is rich in both non-renewable (e.g., oil, minerals) and renewable (e.g., fisheries) resources. The importance of the polar regions has become increasingly recognised in recent years because they are predicted to experience the most pronounced effects of climate change (IPCC, 2013).

The latest special report by the *Intergovernmental Panel on Climate Change* (IPCC) on the ocean and cryosphere in a changing climate (Meredith et al., 2019) concluded, amongst other things, the following: *"The polar regions are losing ice, and their oceans are changing rapidly. The consequences of this polar transition extend the whole planet and are affecting people in multiple ways"* and *"The polar regions will be profoundly different in future compared to today, and the degree and nature of that difference will depend strongly on the rate and magnitude of global climatic change".* A detailed understanding of the Arctic's physical environment is necessary to fully comprehend the observed changes, to estimate future changes of Arctic properties, and consequently, predict the effects of climate change on the whole planet.

Furthermore, the Arctic is rich in natural resources and is of strategic importance due to the Northern Sea Route, which connects the Atlantic Ocean and the Pacific Ocean and crosses multiple Arctic Seas. The lighter ice conditions during summer have enhanced the accessibility, which has increased Arctic-based ship transportation (Pizzolato et al., 2016, 2014) and caused a growing interest in resource exploitation (Henderson and Loe, 2014). It is, again, essential to understand and be able to predict the physical environment to ensure safe marine transport and offshore operations in the ice-affected waters of the Arctic.

Measurements are an excellent way to obtain information about the Arctic environment. They can be conducted in-situ, i.e., collected on-site, or through remote sensing techniques from aircraft or polar-orbiting satellites. Generally, in-situ measurements provide the most accurate and highest resolution data. However, collecting data on-site in the Arctic is extremely difficult, demanding, and expensive due to the harsh environment. Therefore, in-situ observations are sparse and typically only feasible for a short amount of time. Satellite remote sensing observations overcome these challenges and have a much more extensive and continuous coverage of the Arctic, but the acquired resolution is generally lower in comparison to in-situ measurements. For that reason, remote sensing observations are typically validated with in-situ measurements. Despite the vast and continuous coverage of satellites, this technology still leaves temporal and spatial gaps in the data. One way to fill in these gaps is through numerical modelling. Carefully calibrated and validated models provide additional information and allow us to look beyond observations. Moreover, models allow for the investigation of potential effects due to changing boundary conditions, for instance, due to climate change.

The different types of measurements and numerical models complement each other and are vital to comprehend the dynamic and complex environment of the Arctic. Therefore, the work carried out during this PhD made use of state-of-the-art numerical models and measurements obtained from satellites and collected in-situ.

1.1 Objectives

The main objective of this PhD was to acquire a better understanding of the Arctic's physical environment through various measured data and numerical model simulations. To this end, the PhD focussed and contributed to three Arctic phenomena/topics including:

- Wave propagation through ice-covered oceans
- The physical oceanographic environment of the Arctic fjord Kangerlussuaq
- Iceberg drift in the Barents Sea

Comprehending the physical environment of the Arctic and being able to predict future changes due to climate change is crucial to strengthen the resilience against climate-related hazards, and improve climate change mitigation, adaptation, early warning systems and impact reduction. These are all targets of the 13th United Nations Sustainable Development Goal: Climate Action.

1.2 Thesis outline

Chapter 2 presents an introduction to the physical environment of the Arctic. It provides a short description of the Arctic basin and its major currents, and an overview of different ice classifications. Furthermore, a selection of available datasets is presented to illustrate the available types of data and to signify the importance of having measurements to gain a proper understanding of the physical processes at play. The chapter is concluded with a description of the impacts of climate change on the Arctic.

Chapter 3 describes satellite remote sensing techniques and their ability to improve our understanding of wave-ice interactions. The primary focus is on how the sea ice affects the waves, and the main remote sensing technique considered is *Synthetic Aperture Radar* (SAR). The study site is the Barents Sea, where in-situ measurements are available from the *Barents Sea Metocean and Ice Network* (BaSMIN) programme. A selection of these measurements is used throughout this chapter as validation data. Finally, SAR data are used to investigate the change of the peak wavelength and dominant wave direction as waves propagate through ice-covered waters and to study the wave-dispersion relation within ice affected waters.

Chapter 4 presents the study of the Arctic fjord Kangerlussuaq. The objective of this work was to generate a realistic numerical model of the fjord using commercially available software to study the seasonal variability of the physical oceanographic environment, the fjord's response to changing meltwater runoff scenarios, and the wave conditions. This chapter includes a description of the regional settings, the basic equations and theory of the utilised numerical models and the model setup. The output of the numerical models is used to describe the current regime, the origin of the water masses, the effects of perturbations in the meltwater runoff forcing and the 50-year return period wave parameters.

Chapter 5 focusses on iceberg drift in the Barents Sea. A numerical model taken from the literature is applied to produce maps of the annual encounter frequency and the expected annual number of icebergs in the Barents Sea. It is found that one of the most considerable uncertainties in forcing the model is the iceberg seeding at the sources, including 1) the annual number of icebergs released from the sources that drift freely into the Barents Sea, and 2) the initial size characteristics of the released icebergs. Satellite remote sensing data from the *Sentinel-1* (S1) and *Sentinel-2* (S2) constellations are utilised to compute this information at the iceberg sources, and these newly obtained data are used to force the model.

Finally, Chapter 6 summarises the main results and provides recommendations for future work.

1.3 List of scientific publications

The scientific work carried out during this PhD resulted in the seven publications listed below. This thesis is an extended summary of these papers. While this thesis can be read as a standalone document, consulting the following publications is highly recommended for additional details and a more thorough understanding.

1) **Paper I**
   Li, H., Lubbad, R., Monteban, D., 2018. Review of wave-ice interaction studies, in: 24th IAHR International Symposium on Ice. Vladivostok, Russia, pp. 533–543.

2) **Paper II**
   Monteban, D., Lubbad, R., Johnsen, H., 2019b. Sentinel-1 SAR observations of peak wavelength and wave direction in the marginal ice zone of the Barents Sea, in: Proceedings of the 25th International Conference on Port and Ocean Engineering under Arctic Conditions. Delft, Netherlands.

3) **Paper III**
   Monteban, D., Lubbad, R., Pedersen, J.O.P., 2019c. Use of satellite remote sensing to study wave-ice interactions in the marginal ice zone - A review, in: Proceedings of the 25th International Conference on Port and Ocean Engineering under Arctic Conditions. Delft, Netherlands.

4) **Paper IV**
   Monteban, D., Johnsen, H., Lubbad, R., 2019a. Spatiotemporal Observations of Wave Dispersion Within Sea Ice Using Sentinel-1 SAR TOPS Mode. J. Geophys. Res. Ocean. 124, 8522–8537. https://doi.org/10.1029/2019JC015311.

5) **Paper V**
   Monteban, D., Pedersen, J.O.P., Nielsen, M.H., Ingeman-Nielsen, T., 2018. Modelling of hydrodynamic and wave conditions for a new harbour in Søndre Strømfjord (Kangerlussuaq), in: AIC 2018 Transportation Infrastructure Engineering in Cold Regions. Sisimiut, Greenland, pp. 28–29.

6) **Paper VI**
   Monteban, D., Pedersen, J.O.P., Nielsen, M.H., 2020b. Physical oceanographic conditions and a sensitivity study on meltwater runoff in a West Greenland fjord: Kangerlussuaq. Oceanologia. Manuscript submitted for publication.

7) **Paper VII**
   Monteban, D., Lubbad, R., Samardzija, I., Løset, S., 2020a. Enhanced iceberg drift modelling in the Barents Sea with estimates of the release rates and size characteristics at the major glacial sources using Sentinel-1 and Sentinel-2. Cold Reg. Sci. Technol. 175, 103084. https://doi.org/10.1016/j.coldregions.2020.103084

2 The Arctic environment

The general objective of this thesis was to improve the understanding of the physical environment of the Arctic through measurements and numerical modelling. In this chapter, a general introduction of the Arctic physical environment is given, with a description of the Arctic basin and its main currents provided in Section 2.1. In Section 2.2, the different definitions and classifications of ice are provided based on the sea ice nomenclature of the *World Meteorological Organisation* (WMO) (World Metrological Organization, 1970). In-situ and remote sensing measurements exist in the Arctic for many different parameters such as the sea ice extent, the sea ice thickness, the sea ice age, the sea ice drift, the snow thickness, salinity and temperature of the water, and iceberg occurrence. In Section 2.3, a description of selected measured parameters relevant for this thesis is given, which includes the sea ice extent, the sea ice thickness, the sea ice age and the presence of iceberg. Finally, the impacts of climate change on the Arctic are described in Section 2.4.

2.1 The Arctic basin and its major ocean currents

The Arctic Ocean is shown in Figure 1. It consists of a deep ocean basin, some submarine ridges, marginal plateaus and continental shelves. Sea ice exists in the Arctic Ocean and its surrounding seas including the Barents Sea, the Kara Sea, the Laptev Sea, the East Siberian Sea, the Chukchi Sea, the Beaufort Sea, the Baffin Bay and the Greenland Sea. The Arctic Ocean is the smallest of the five oceans, and together with the surrounding seas, it occupies an area of approximately 14 million km^2 (Herman, 1989).

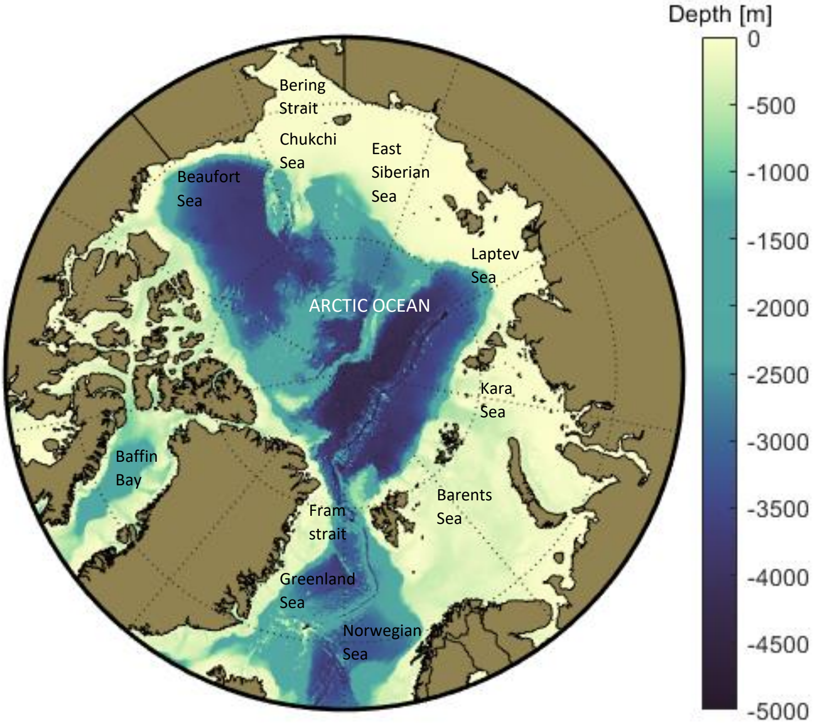

Figure 1. Bathymetry of the Arctic Ocean. The data are taken from the International Bathymetry Chart of the Arctic Ocean (Jakobsson et al., 2012).

The major surface currents in the Arctic are shown in Figure 2. There are two different inflows into the Arctic Ocean. The first is the Pacific gateway, where Pacific water flows through the Bering Strait (see Figure 1 for the locations). The inflowing water varies considerably within the season, from approximately -1.9 °C and 33 psu in winter to 2 °C and less than 31.9 psu in summertime (Woodgate et al., 2005). The other inflow into the Arctic ocean is from the Atlantic gateway that passes through the Fram Strait and the Barents Sea. The inflow from the Atlantic is warmer (> 0 °C), saltier (> 34 psu) and approximately ten times larger than the pacific inflow (Beszczynska-Möller et al., 2011).

The main circulation pattern in the Arctic Ocean is driven by the anticyclone Beaufort Gyre, which stores the most substantial amount of freshwater in the Arctic Ocean (Proshutinsky et al., 2009b) and has a significant impact on the Arctic climate (Proshutinsky et al., 2009a). Another predominant current is the Transpolar Drift Stream that transports surface water and sea ice from Siberia towards the Fram Strait.

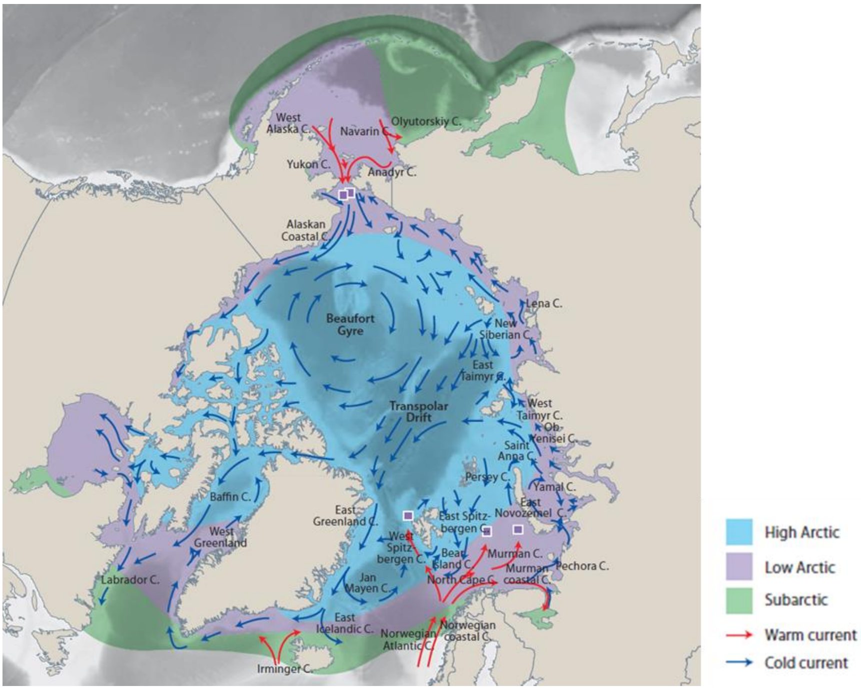

Figure 2. The major surface currents in the Arctic Ocean and the surrounding seas (AMAP (2018).

The Beaufort Gyre and the Transpolar Drift Stream are driven by the winds in the region (Dewey et al., 2018; Vihma et al., 2012). The wind, and therefore also the sea ice drift and the surface circulation, are associated with the *Arctic Oscillation* (AO). The AO is the variation of wind patterns and atmospheric pressure in the Arctic and mid-latitudes and is a key aspect of climate variability (Thompson and Wallace, 1998). Furthermore, the AO influences the sea ice significantly (e.g., Wang and Ikeda, 2000). For instance, when the AO is in its positive phase, there is a low pressure over the Arctic pulling in warm and wet air from lower latitudes. It weakens the Beaufort Gyre and strengthens the Transpolar Drift Stream. The sea ice is then transported out of the Arctic through the Fram Strait, which results in a decrease in sea ice extent and general sea ice thinning (Rigor et al., 2002). A negative AO represents higher than the normal air pressure in the Arctic. The cold and dry air is kept in the Arctic, and the frigid air is pushed southward. The winds are anticyclonic that cause the sea ice to drift clockwise, which enhances the Beaufort Gyre. Under these conditions the multi-year sea ice (see Section 2.2.2 for the definition) is generally kept in the middle of the Arctic and sea ice flowing out of the Arctic through the Fram Strait is reduced. Therefore, the negative AO phase usually favours thicker sea ice, although this is not always the case (Stroeve et al., 2011).

2.2 Ice classifications

Different ice classifications are based on different criteria. Definitions of ice are provided in the sea ice nomenclature of the WMO (World Metrological Organization, 1970) where they distinguish between different classifications according to the origin of ice, the ice age, the ice size and forms and its position to land. A short description of these classifications from the WMO is provided in this section. Additionally, different classifications of glacial ice are provided.

2.2.1 Classification of ice according to origin

Floating ice found at sea, which includes all forms and shapes of ice that are found floating in the water, is divided into three classes according to origin:

- River ice
- Ice of land origin
- Sea ice

River ice is formed on a river regardless of where it is observed. River ice is completely fresh and often has a brown colour due to a mixture of humus materials. It is found in the Arctic Ocean at the beginning of the summertime around the large Siberian rivers, but it nearly disappears over a polar summer, making its role in the ice regime of the Arctic negligible (Zubov, 1963). The ice of land origin is formed on land or in ice shelves. This category includes glacial ice (see Section 2.2.5) and grounded ice. Finally, sea ice originates from the freezing of seawater and salinity is its main characteristic.

2.2.2 Classification of ice according to age

The most common way to categorise sea ice is thickness-based. It can also be considered age-based because the thickness of the ice is closely related to age. The categories and corresponding range of ice thicknesses are:

- New ice
- Nilas (up to 10 cm in thickness)
- Young ice (between 10-30 cm in thickness)
- First-year ice (thickness 30 cm – 2 m)
- Old ice, including:
    - Second-year ice (typical thickness up to 2.5 m or more)
    - Multi-year ice (typical thickness up to 3 m or more)

New ice is the general term for recently formed ice and includes frazil ice, grease ice, slush and shuga. These ice types are composed of weakly frozen together ice crystals. Nilas are a thin elastic crust of ice. Young ice may be subdivided into grey ice and grey-white ice and is the transition between nilas and first-year ice. First-year ice is the ice of not more than one winter's growth. Ones the ice has survived one summer's melt it is referred to as second-year ice. If the ice has survived two or more summer's melt, it is called multi-year ice.

2.2.3 Classification of ice according to proximity to land

According to its position to land, or according to its mobility, ice can be classified as:

- Fast or landfast ice
- Drift of pack ice, which can be further divided into:
    - The shear zone
    - The *Marginal Ice Zone* (MIZ)

Fast ice or landfast ice is fixed to the shore, an ice wall or between shoals or grounded icebergs. It is horizontally fixed but may move vertically with the tides. The drift ice is defined as any form of ice that is free to move with winds and currents and can be further divided into a shear zone and a MIZ. The shear zone is the boundary between the fast ice and the drift ice and is formed when the drift ice moves against the coastal boundary. It is characterised by a high degree of deformation. The MIZ is defined as the part of the ice cover that is close enough to the open ocean to be significantly affected by its physical presence (Wadhams, 1986). Therefore, the MIZ is the most dynamic and complex zone.

2.2.4 Classification of ice according to size and forms

Uniform sheets of ice are seldom found, and ice can take on many different forms depending on external conditions and other physical considerations (see, e.g., Leppäranta, 2011; Shokr and Sinha, 2015). Some commonly found ice forms are:

- Pancake ice
- Brash ice
- Ice floes

Pancake ice is primarily composed of circular pieces with raised rims and is between 30 cm – 3 m in diameter and around 10 cm in thickness. It can be formed under severe wave conditions and the resulting breaking of nilas or grey ice. Moreover, it can also be formed under slight swell from grease ice, slush or shuga. Brash ice is the wreckage of other forms of ice and is the accumulation of floating ice fragments that are no more than 2 m in diameter. Finally, ice floes are contiguous, relatively flat pieces of ice that are larger than 20 m across. Pieces smaller than 20 m across are called ice cakes.

2.2.5 Classification of glacial ice

Icebergs are massive pieces of ice that have broken from a glacier. A sketch of the formation of icebergs from a glacier is given in Figure 3. The glacial ice develops from snowfall that compresses under its weight until it becomes solid ice. The iceberg producing glaciers are dynamic and flow towards the sea. The amount of iceberg calving from a glacier is controlled by whether the terminus is grounded or afloat, the rate of glacier flow, the mass balance of the glacier and crevassing within the glacier (Løset et al., 2006). Icebergs have classifications based on size and shape. Based on the size, icebergs are divided into:

- Growlers (freeboard less than 1 m and length less than 10 m)
- Bergy Bits (freeboard between 1-5 m and length between 10-30 m)
- Icebergs (freeboard more than 5 m and length more than 30 m)
- Ice islands (freeboard more than 5 m and an area ranging from thousands of square metres to 500 km^2)

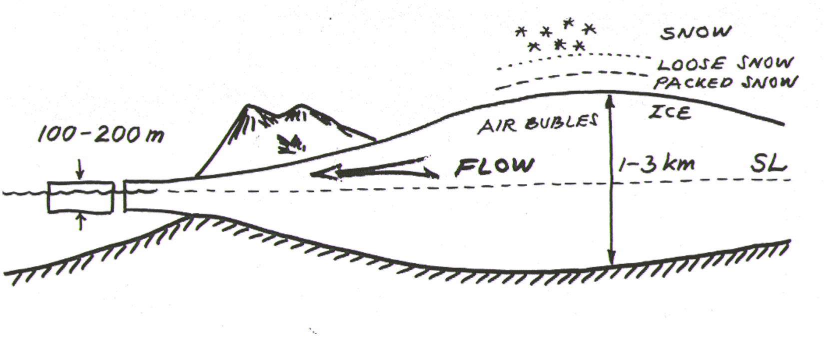

Figure 3. The formation process of an iceberg from a glacier (Løset et al., 2006).

Furthermore, the iceberg classification based on shape is:

- Tabular
- Rounded/domed
- Irregular (pinnacle, wedged and drydocked)

2.3 A selection of measured parameters in the Arctic

Measurements of sea ice in the Arctic are vital to understand the physical processes at play and to investigate the impacts of climate change on the Arctic. Ever since 1978, when the satellites Seasat (Swanson and Riley, 1980) and Nimbus-7 (Cavalieri et al., 1984) were launched, satellites have provided continuous data on the sea ice cover of the Arctic. Before 1978, trends of the sea ice were obtained by using a combination of data such as shipping records, ice charts and some sparse aircraft and satellite observations. Both the instrumentation and the processing algorithms have matured significantly since 1978. The result is that many observations are available to study the Arctic's environment.

2.3.1 Sea ice extent

The sea ice extent in the Arctic is nearly impossible to measure accurately from in-situ data because the sea ice edge is ever-changing, and a vast area is covered by the sea ice. Therefore, polar-orbiting satellites carrying microwave sensors have typically been used to obtain the sea ice concentration and extent. An example of the sea ice extent from the Sea Ice Index product (Fetterer et al., 2017) is given in Figure 4. The sea ice extent is shown for March and September, which are in general the months of the maximum and minimum ice extent, respectively. This data product is based on passive microwave sensors that measure the surface brightness temperature from which the sea ice concentration is computed. It is common to define the sea ice edge as the 15% sea ice concentration contour line. Furthermore, the uncertainties of the retrieved sea ice concentrations are much more significant in the summertime compared to wintertime (Sandven et al., 2006). The reason for this is that melt ponds are extremely difficult to distinguish from the open water and because the uncertainties increase for an increasing portion of thin ice (Cavalieri et al., 1995).

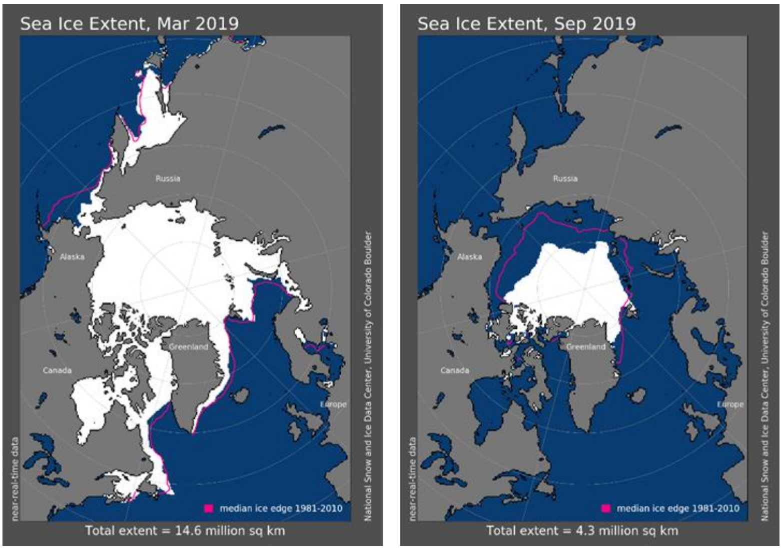

Figure 4. The sea ice extent in March 2019 and September 2019. The magenta line indicates the median sea ice edge between 1981-2010. Image courtesy of the National Snow and Ice Data Centre, Boulder, CO.

2.3.2 Sea ice thickness

The Arctic sea ice covers a vast spatial area, is constantly on the move by winds and currents and the bottom of the sea ice is highly variable. This makes the sea ice thickness challenging to measure over long periods. Various methods and techniques are available to measure the sea ice thickness, including in-situ measurements, electromagnetic sensors, upward-looking sonars, and aircraft and satellite observations.

The most accurate way to determine the sea ice thickness is through in-situ measurements by drilling holes in the sea ice cover. However, these measurements are predominantly used to validate other datasets (e.g., Haas, 2004; Haas et al., 1997). Electromagnetic sensors can estimate the sea ice thickness based on the difference in conductivity between sea ice and seawater (Tateyama et al., 2006). Such sensors were, for instance, mounted on helicopters (Haas et al., 2008) or dragged over the ice attached to sledges (Prinsenberg and Holladay, 2009). Another way of determining the sea ice thickness is by upward-looking sonars that measure the ice draft. These devices were deployed at mooring sites at fixed depths (Melling et al., 1995) or attached to submarines (Rothrock and Wensnahan, 2007).

The ICESat satellite, launched in 2003, provided a new way to obtain the sea ice thickness of the Arctic sea ice cover from altimetry (e.g., Kwok et al., 2009). The CryoSat-2 satellite, launched in 2010, is used to extend the record of ICESat to this day (Laxon et al., 2013). These satellites carrying radar altimeters determine the sea ice freeboard, which is the height of the ice and snow above the water level and consequently estimate the sea ice thickness based on hydrostatic equilibrium. The primary source of uncertainty in estimating the sea ice thicknesses is the snow depth and the snow density (Tilling et al., 2018). Furthermore, considerable uncertainties are observed over thin ice (< 1 m) and in the MIZ (Ricker et al., 2014; Wingham et al., 2006). The sea ice thickness is also retrieved from the *Soil Moisture and Ocean Salinity* (SMOS) satellite, which estimates the sea ice thickness from the brightness temperature at L-band microwave frequencies (Kaleschke et al., 2012). This method to retrieve the sea ice thickness is accurate for thin ice (< 1.5 m), but sensitivity gets lost for thicker ice (Kaleschke et al., 2010).

The SMOS and satellite altimetry such as the CryoSat-2 provide complementary information because of the favourable sea ice thickness range and associated uncertainties as explained above. Therefore, data maps combining the SMOS and CryoSat-2 data were created that considerably reduce the uncertainties (Kaleschke et al., 2015; Ricker et al., 2017). Figure 5 presents an example of the data retrieved from SMOS and CryoSat-2 alone and the resulting data fusion map.

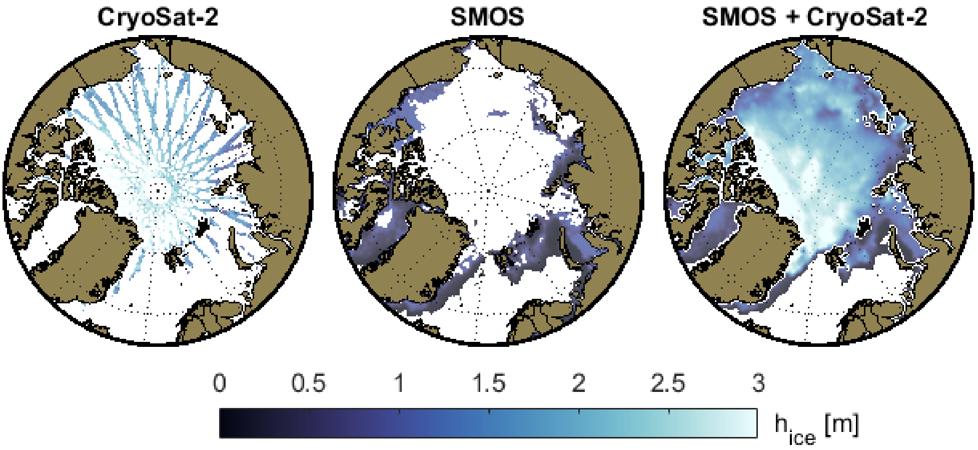

Figure 5. Sea ice thickness measurements on 28 March 2011 from CryoSat-2 (Ricker et al., 2014), SMOS (Huntemann et al., 2014) and the combination of CryoSat-2 and SMOS data (Ricker et al., 2017). All data were downloaded from meereisportal.de (Huntemann et al., 2014).

2.3.3 Sea ice type and sea ice age

In Section 2.2, many different classifications of ice were described with the type and age of ice treated in Section 2.2.2. On small spatiotemporal scales, information on the type of sea ice can be retrieved by visual observations from cameras or photography. Furthermore, passive and active microwave satellite data can be utilised to derive the type of sea ice for the entire Arctic. Active microwave sensors such as real aperture radar and SAR make use of the difference in backscatter response from different sea ice types. Considerable effort has been put over the past decades into understanding the backscatter sensitivity of various ice types and different sensor configurations, and developing identification approaches and algorithms (e.g., Johansson et al., 2018; Kwok et al., 1992; Park et al., 2019; Skriver and Dierking, 2004). Combining data from different microwave sensors resulted in maps showing the type of sea ice, as done by the Ocean and Sea Ice Satellite Application Facility. An example of such a data file is given in Figure 6, which shows the locations of first-year and multi-year sea ice.

Another dataset that distinguishes between the age of the sea ice is the EASE-Grid Sea Ice Age data product (Tschudi et al., 2019). A combination of different satellite observations and tracking drifting buoys are used to track ice parcels over the years to determine the age of the sea ice (Maslanik et al., 2011; Tschudi et al., 2010). This method has provided a continuous dataset since 1984 and was used to show the decline of old ice in the Arctic (see Section 2.4).

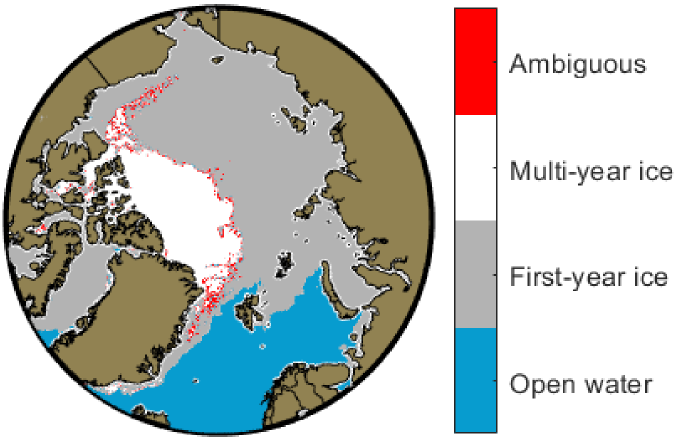

Figure 6. Map of the type of ice on 28 January 2019. The data are taken from the dataset Sea ice type product of the EUMETSAT Ocean and Sea Ice Satellite Application Facility (OSI SAF, www.osisaf.org).

2.3.4 Icebergs

Information on icebergs in the Arctic Ocean and surrounding seas has been collected by observations from ships and aircraft, research expeditions and satellites. Visual observations and expeditions have provided much information regarding icebergs (Abramov and Tunik, 1996; Abramov, 1992; Løset and Carstens, 1996). Presently, much of the research is focussed on the detection of icebergs from SAR (e.g., Akbari et al., 2018; Power et al., 2001; Wesche and Dierking, 2012). An operational service is now run by the *Danish Meteorological Institute* (DMI) for the detection of icebergs in the vicinity of Greenland. This data product is available from the EU *Copernicus Marine Environment Monitoring Service* (CMEMS) and is called the Arctic Ocean – SAR sea iceberg concentration product (CMEMS, 2019). An example of a data file for one day of the area around Svalbard is provided in Figure 7. The iceberg number density is given for 10 km × 10 km grid cells, and data are available daily. The data product is based on a constant false alarm rate concept (Gill, 2001). With this concept, pixels with an unusual high backscatter compared to the distribution of nearby background-pixels are identified. Next, a post-processing algorithm is applied to identify the correct iceberg pixels (Buus-Hinkler et al., 2019). The primary source of uncertainty in this data product is the false identification of icebergs, which is mainly due to noise in the SAR data. However, validating these kinds of observations is very challenging and nearly impossible due to the lack of ground truth data (Eastwood et al., 2019).

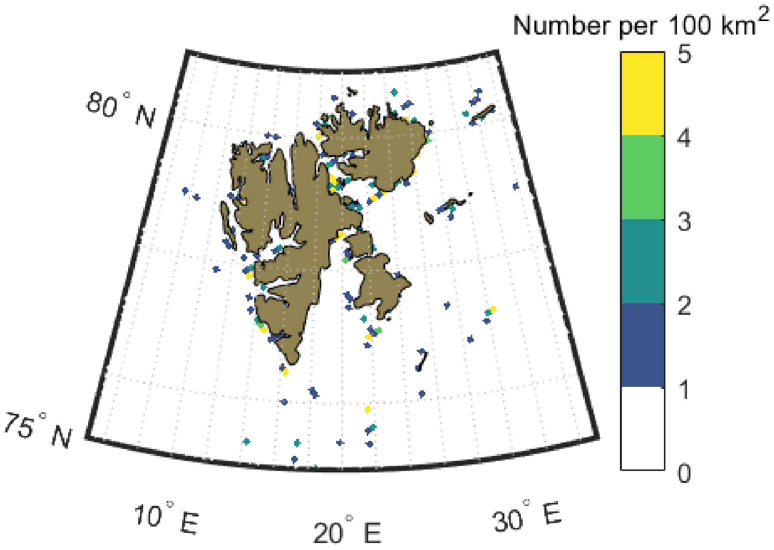

Figure 7. The iceberg number density within grid cells of 10 km × 10 km on 10 August 2018 in the vicinity of Svalbard. The data are taken from the Arctic Ocean – SAR sea iceberg concentration data product (CMEMS, 2019).

2.4 Impacts of climate change on the Arctic

As mentioned in the introduction, the most pronounced effects of global climate change are predicted to occur in the polar regions (IPCC, 2013). The Arctic is warming much more rapidly compared to the rest of the world, with an increased surface air temperature that is more than double the global average (Richter-Menge et al., 2017). This phenomenon of greater climate change effects at high latitudes in response to climate forcing (e.g., the concentration of greenhouse gasses) is called polar amplification. Various feedback mechanisms causing polar amplification were proposed (see, e.g., Goosse et al., 2018; Stuecker et al., 2018), but they are still up for debate (Meredith et al., 2019). One feedback mechanism highlighted by multiple studies is the surface-albedo feedback (Screen and Simmonds, 2010; Winton, 2006), where the loss in sea ice and snow cover lowers the albedo, leading to an increase in absorption of radiation by the surface, enhancing sea ice and snow melt. Other feedback mechanisms are for instance the increase in water vapour content (warming of the atmosphere increases the amount of water vapour, amplifying the greenhouse effects) and changes in cloudiness (warming of the atmosphere changes the number of clouds, which modifies the radiative balance).

The Transpolar Drift Stream and the Beaufort Gyre (see Section 2.1) transport sea ice out of the Fram Strait and keep sea ice in the Arctic Ocean, respectively. The sea ice drift speed in the Arctic has increased over the past few decades, both within the Fram Strait (Krumpen et al., 2019) and within the Arctic basin (Rampal et al., 2009). This is attributed to the rapid sea ice melt (Armitage et al., 2020) and changes in wind forcing (Olason and Notz, 2014). The increasing sea ice drift speed is also linked to the decrease in multi-year sea ice and a thinner sea ice cover (Kwok et al., 2013).

Probably one of the most prominent indicators of climate change is the loss of the Arctic Sea ice cover. Ever since 1979, when satellites provide continuous data on the sea ice cover, the sea ice extent has been declining for every month of the year (Stroeve and Notz, 2018). The largest trend is observed in September, with an approximate 12.8% decrease per decade, compared to a 2.7% decrease per decade in March (Onarheim et al., 2018). Furthermore, there is no precedent of the 21st century minimum Arctic Sea ice extent going back to at least 1850 (Walsh et al., 2017). The study of Walsch et al. 2017 reconstructed a dataset of the sea ice concentration dating back to the year 1850. It is a combination of satellite data, ice charts, ship and aircraft observations, diaries and whaling logbooks. In Figure 8, the minimum sea ice extent in September for three years of this dataset are presented. The three years 1854, 1935 and 2012 are the years where the minimum ice coverage was observed within the periods 1850-1900, 1901-1950 and 1951-2014, respectively (Walsh et al., 2017). The loss in summer sea ice extent is partly due to the increase in the concentration of atmospheric greenhouse gasses and partly due to internal climate variability, where the ice-albedo feedback is one of the predominant drivers (e.g., Stroeve et al., 2014). Moreover, a recent study by Polvani et al. (2020) found that approximately half of the Arctic sea ice loss for the period 1955-2005 is due to the greenhouse effect of ozone-depleting substances.

Figure 8. Minimum sea ice extent in September for 1854, 1935 and 2012. These years have the minimum sea ice coverage for the three subperiods 1850-1900, 1901-1950 and 1951-2014, respectively. The sea ice extent is defined as ice concentrations of 15%, and the data are taken from Walsh et al. (2019).

Besides the declining sea ice extent in the Arctic, the sea ice is also thinning. The age of the sea ice is closely related to the sea ice thickness, with older ice being generally thicker. The old sea ice has declined significantly over the past few decades, which is illustrated in Figure 9. The sea ice age from the EASE-Grid Sea Ice Age data product (Tschudi et al., 2019), introduced in Section 2.3.3, is shown for four different years for week 12. Since 1979, the proportion of sea ice older than four years declined from 30% to 2% (Stroeve and Notz, 2018) and correspondingly, the percentage of first-year ice increased from 40% to 60-70%. Evidence of the thinning sea ice cover was also found through in-situ measurements (Haas et al., 2017) and satellite altimetry observations (Kwok, 2018; Laxon et al., 2013). By combining these type of measurements, a reduction in sea ice thickness of 65% was found for the period 1975-2012 (Lindsay and Schweiger, 2015). Moreover, such a substantial decrease in sea ice thickness is unprecedented since at least 1900 (Schweiger et al., 2019).

Consistent with the observed decrease in sea ice extent and sea ice thickness is the observed extension of the melt season throughout the Arctic since 1979. Over the past 40 years, the melt seasons started 12 days earlier due to earlier melt onset and ended 28 days later because of later freeze-up (Stroeve and Notz, 2018).

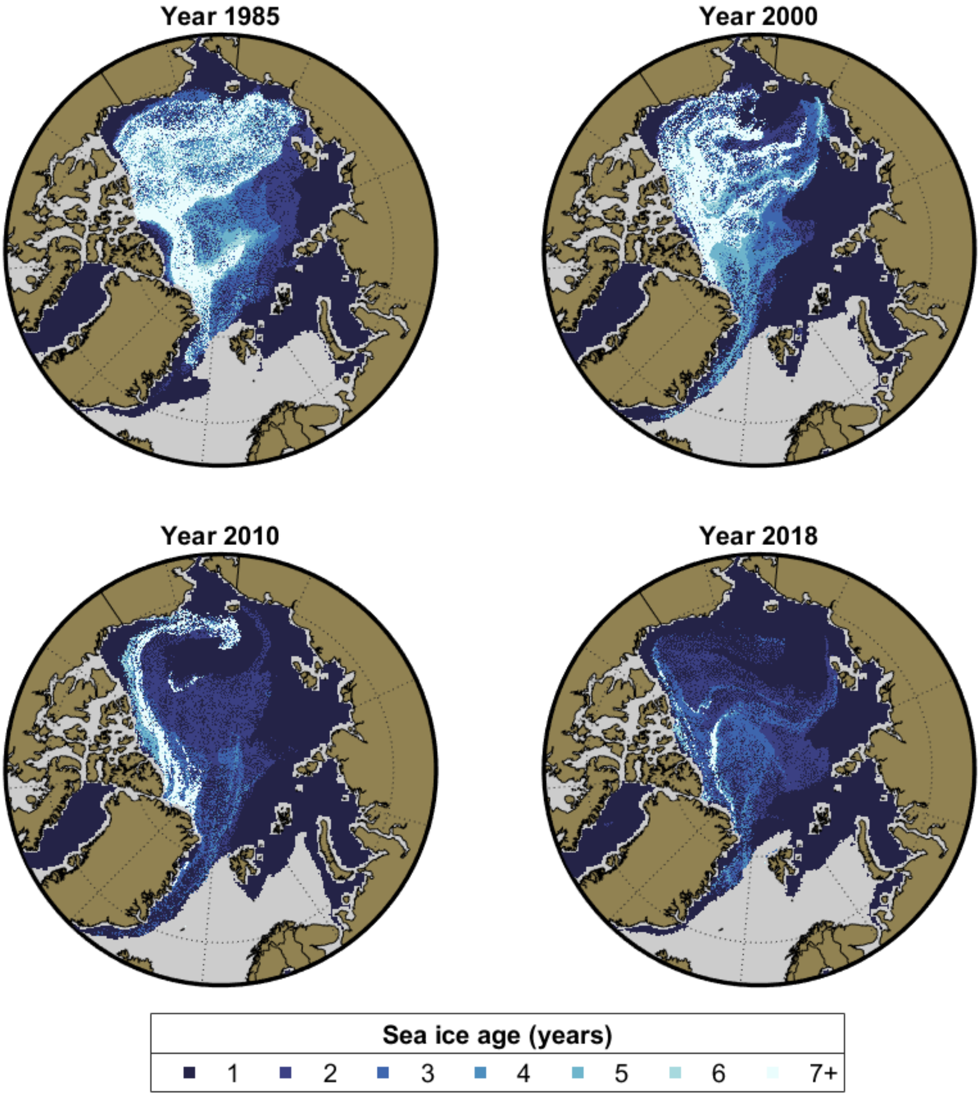

Figure 9. Arctic sea ice age for week 12. The data are taken from the EASE-Grid Sea Ice Age data product (Tschudi et al., 2019).

In this section, just a few observations showing the impacts of climate change on the Arctic region are provided. However, many other changes are occurring in the Arctic, and for an extensive overview, the reader is referred to the IPCC reports (e.g., IPCC, 2013; Meredith et al., 2019). The datasets presented in this section were shown to signify the importance and potential of measurements (especially from remote sensing) to understand the physical environment of the Arctic and the impacts of climate change. In the next chapters, the focus will be on much smaller scale Arctic phenomena/topics to which this PhD work contributed, including wave propagation through ice-covered oceans, the physical oceanographic environment of the Arctic fjord Kangerlussuaq and iceberg drift in the Barents Sea.

3 Satellite remote sensing observations of wave propagation within sea ice

Numerical wave models such as the spectral wave models WAVEWATCH III (Tolman, 1991), SWAN (Booij et al., 1999) and MIKE 21 Spectral Waves (DHI, 2017a) are commonly used to forecast and hindcast the wave climate, which is vital for safe offshore operations and safe marine transport. These numerical wave models have had a long developmental history (Komen et al., 1994), but focussed primarily on mid-latitudes. Applying these wave models in the polar regions requires sea ice to be taken into account. Several theoretical wave-ice interaction models exist in the literature, but a significant obstacle is the lack of validation data (Broström and Christensen, 2008).

In the polar regions, different techniques of satellite remote sensing are used, such as altimetry, optical imagery and SAR. Altimetry can provide, amongst other things, the significant wave height in ice-free regions. It has also been used to estimate the sea ice thickness (see Section 2.3.2) and to detect open water regions in sea-ice areas (Müller et al., 2017). Optical imagery can provide high quality and high-resolution images of the ice cover. However, a major limitation of this technique is that it requires solar illumination and cloud-free conditions, which is a severe restriction in the polar regions. SAR is arguable the most valuable method to obtain quantitative information of wave propagation in the polar regions as it does not have these limitations.

This chapter focusses on satellite remote sensing techniques and data to improve our understanding of wave-ice interactions. Primarily, the effect of sea ice on the waves is considered, and SAR is the main remote sensing technique studied. The chapter is based on four scientific publications that are included in the appendices. Section 3.1 briefly introduces the topic of wave-ice interactions and provides an overview of the known theoretical models to date. It is based on the paper by Li et al. (2018), given in Appendix A. Next, in Section 3.2, an overview of the BaSMIN measurement programme is given. Some of the collected in-situ data were used as input and/or validation in the processing techniques for the scientific publications. The basic theory of SAR regarding the imaging of ocean waves is presented in Section 3.3, together with some applications. This section is a condensed version of the papers by Monteban et al. (2019b) and Monteban et al. (2019c) provided in Appendix B and Appendix C, respectively. Finally, Section 3.4 presents a new and innovative method to derive the wave dispersion relation within sea ice from the S1 satellites. This section summarises the work by Monteban et al. (2019a), given in Appendix D.

3.1 Wave-ice interactions

It is well-known that long ocean surface waves can travel phenomenal distances into the sea ice (Ardhuin et al., 2015; Carsey et al., 1989). Waves that are propagating through an ice field show amplitude attenuation that is due to a combination of two processes: dissipation and scattering. Scattering distributes the energy and is, therefore, a conservative process. Dissipation removes energy from the waves and can be due to turbulence (Shen and Squire, 1998), collisions between ice floes (McKenna and Crocker, 1992), over-washing (Bennetts et al., 2015), fracture of sea ice (Zhang et al., 2015) and inelastic bending of sea ice (Langhorne et al., 1998). The sea ice also impacts the waves by reflection, shoaling, refraction and it alters the dispersion relation (Squire, 2007; Squire et al., 1995). Although the primary focus in this research is placed on how the sea ice affects the waves, it is important to note that the waves also strongly influence the ice cover, making wave-ice interactions a two-way, strongly coupled issue.

As described in Section 2.2.3, the MIZ is the area where the ice cover is significantly affected by the physical presence of the open ocean and is, therefore, the most complex and dynamic ice zone. In this zone, the waves can break up the ice (Collins et al., 2015; Kohout et al., 2016), transport it, induce collisions between ice floes (Herman et al., 2019; McKenna and Crocker, 1992) and compact the ice edge (Stopa et al., 2018b).

For the MIZ there are three classic wave propagation models, including the mass loading model (Weitz and Keller, 1950), the thin elastic plate model (Wadhams, 1986) and the viscous layer model (Keller, 1998). Each model is based on different assumptions, and they are useful under specific ice conditions. The mass loading model was the first model developed for wave propagation under an ice cover, and it assumes that the ice floes are considered as mass points. It can be used for pancake ice regions when the interaction between the ice floes is negligible. The dispersion relation reads:

$$k = \frac{\omega^2}{g - c\rho_{ice}h\omega^2/\rho} \tag{1}$$

with k is the wavenumber; ω is the angular frequency of the waves; c is the ice concentration; h is the ice thickness and ρ and ρ_{ice} are the density of water and ice, respectively. It can be seen that when the ice thickness converges to zero, the open water relation, assuming deep water, is obtained ($k = \omega^2/g$). The thin elastic plate model is best used for continuous ice sheets as it assumes the ice cover to be a thin and uniform elastic layer. The dispersion relation of this model is:

$$k = \frac{\omega^2}{g - M\omega^2 + Lk^4/\rho} \tag{2}$$

where M is an inertial coefficient and L is the flexural rigidity. They are defined as:

$$M = c\rho_{ice}h/\rho \tag{3}$$

$$L = \frac{Yh^3}{12(1-\upsilon^2)} \tag{4}$$

with Y the effective elastic modulus and υ the Poisson ratio. If the flexural rigidity goes to zero, the mass loading model, Eq. (1), is obtained. Finally, the viscous layer model assumes that a viscous fluid can represent the ice cover. It is most suitable for grease ice regions because viscous damping is the dominant effect. The dispersion relation for this model is long and tedious to write and therefore omitted here. It can be found in Keller (1998).

Ice covers are constantly changing in time and space, and therefore, it is desired to have a model that can deal with different types of ice. This led to the viscoelastic model developed by Wang and Shen (2010), which is a generalisation of the three above mentioned models. This model, however, has some drawbacks that were identified by Mosig et al. (2015), which are: the dispersion relation is difficult to solve numerically, and it has many solutions of relevance, making the identification of the dominant mode challenging. Furthermore, the viscoelastic model uses the effective viscosity and effective shear modulus of the ice cover that cannot be measured directly. An inverse calibration problem needs to be solved to determine these input parameters, which was performed in the study by Cheng et al. (2017).

Only a brief overview is given in this section regarding the topic of wave-ice interactions and the existing theoretical models. More in-depth reviews can be found in the literature (Broström and Christensen, 2008; Shen, 2017; Squire, 2020, 2018, 2007; Squire et al., 1995; Zhao et al., 2015).

3.2 Study site and BaSMIN measurement programme

The three publications that are given in Appendix (B-D) used the Barents Sea as a study site. The reason for this is the availability of in-situ data, which were collected during the BaSMIN measurement campaign. This measurement programme is a joint industry project that is led by Equinor and was executed by Fugro GEOS Ltd. The data were kindly made available for this PhD research project.

This 3-year metocean and sea ice measurement programme spanned from October 2015 until October 2018. Five wavescan moorings and five ice profiling moorings were deployed, and their locations can be seen in Figure 10. The wavescan moorings measured:

- Wave parameters (2D wave spectrum and the derived significant wave height, wavelength and wave period)
- Meteorological parameters (wind speed and direction, relative humidity, pressure and temperature)
- Seawater salinity
- Seawater temperature
- Seawater current velocities

The ice profiling moorings measured:

- Ice draft
- Ice drift speed
- Seawater temperature
- Seawater current velocities

During the measurement campaign, a maximum significant wave height of 13.9 m was recorded. The dominant wave direction the waves come from is from a south-westerly direction. Typically, the largest waves come from this direction because this sector has the longest wave-generating fetch length. The average current speed at the wavescan moorings is 0.15 m/s; however, the maximum current speed observed was 0.98 m/s. Strong winds can occur in the Barents Sea, with a maximum recorded wind speed of 18.8 m/s.

The ice drift is mainly driven by the wind that causes yearly variation in the ice exchange between the Arctic Ocean and the Kara Sea. Therefore, the type of ice found in the Barents Sea can be composed of a mixture of ice with different ages and origins. The measured ice drafts at the IC moorings have a mean value varying between 0.22 m and 0.3 m. A maximum ice draft of 1.75 m was observed, but ice drafts larger than 1 m are uncommon and account for less than 1% of all the measurements. In general, the nature of the sea ice is typically thin.

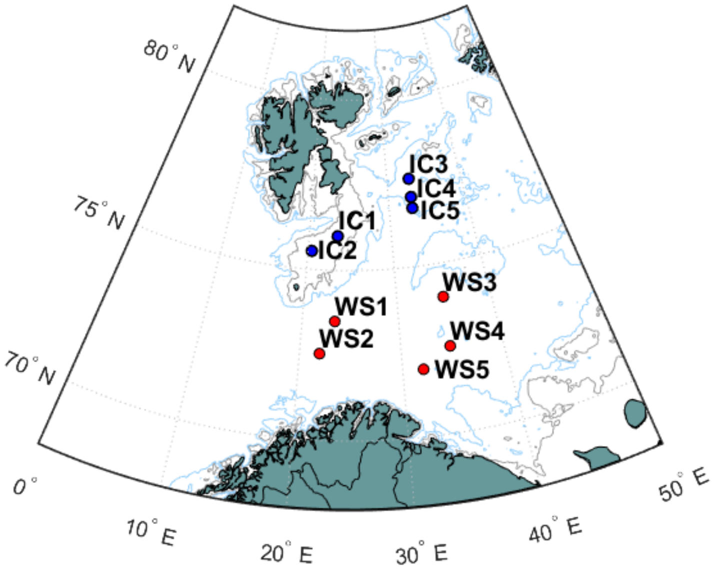

Figure 10. Overview of the BaSMIN measurement locations. The wavescan moorings are indicated by the abbreviation 'WS' and plotted as red dots. The blue dots indicate the ice profiling moorings and are abbreviated by 'IC'. The grey and light blue contour lines are the isobaths at 100 m and 200 m, respectively. The contour lines are based on bathymetry data taken from the International Bathymetry Chart of the Arctic Ocean (Jakobsson et al., 2012).

3.3 Synthetic Aperture Rader

Ever since the first SAR satellite Seasat, launched in 1978 (Born et al., 1979), data quality has improved significantly, and processing techniques have developed rapidly. Presently, different wave parameters can be retrieved from these data, both in the open water and within the sea ice, which will be discussed herein. Along with the imaging of ocean waves, SAR has many other beneficial applications in the polar regions, that include for instance the determination of the ice edge (Liu et al., 1997, 2016), the floe size distribution (Hwang et al., 2017), the ice drift velocities (Kramer et al., 2018) and the ice type (Dierking, 2010; Onstott and Shuchman, 2004).

3.3.1 SAR imaging of ocean waves within sea ice - theory

SAR is an active microwave remote sensing technique. It operates at wavelengths (typically 3-75 cm) that are generally unaffected by the cloud cover and do not require solar illumination. In the open ocean, the theory of wave imaging by SAR is rather well developed and for an extensive introduction to the subject, the reader is referred to the PhD theses by Bruck (2015) and Husson (2012), or the SAR marine user's manual (Jackson and Apel, 2004).

The basic step of ocean wave analysis of SAR data is Fourier analysis. An example is shown in Figure 11, where a simulated image of an ideal ocean surface wave is presented (Figure 11a). The image spectrum (Figure 11b) is obtained by the 2D fast Fourier transform from the following Eq. (5);

$$P(k_x, k_y) = FFT(S_s(x, y))^2 \tag{5}$$

where $S_s(x, y)$ is the sub-scene with pixel values and $P(k_x, k_y)$ the image spectrum in the spatial domain, with k_x and k_y the wavenumber in x and y direction, respectively. The spatial domain has wavenumber spacing *dkx* and *dky* that are defined as:

$$dkx = \frac{2\pi}{nx\ dx} \tag{6}$$

$$dky = \frac{2\pi}{ny\ dy} \tag{7}$$

where *nx* and *ny* being the number of pixels in x and y direction, and *dx* and *dy* being the pixel spacing of the sub-scene in x and y direction, respectively. From the measurement of the peak location *(kx_p, ky_p)*, the wave propagation direction (θ) and the peak wavelength (L) are obtained according to:

$$\theta = \tan^{-1}(kx\_p, ky\_p) \tag{8}$$

$$L = \frac{2\pi}{\sqrt{kx\_p^2 + ky\_p^2}} \tag{9}$$

However, two peaks appear in the image spectrum presented in Figure 11b. This is referred to as the 180° wave ambiguity as it is impossible to resolve the wave direction from Figure 11a alone. In other words, it is not clear whether the waves travel from bottom left (x, y = 0, 0) to top right (x, y = 10000, 10000) or vice versa. The blue arrow in Figure 11a indicates this. A technique developed by Engen and Johnsen (1995) made it possible to resolve the 180° wave ambiguity and obtain the wave direction. Their method produces independent looks from a SAR image using the single look area (see Figure 15 for the definition of this area), allowing the computation of the cross-spectrum. The cross-spectrum phase, which is associated with the propagation of the wave system during a particular time interval, usually allows for the determination of the wave direction. This technique for obtaining the image spectrum was used in the papers by Monteban et al. (2019a) and Monteban et al. (2019b) given in Appendix D and Appendix B, respectively.

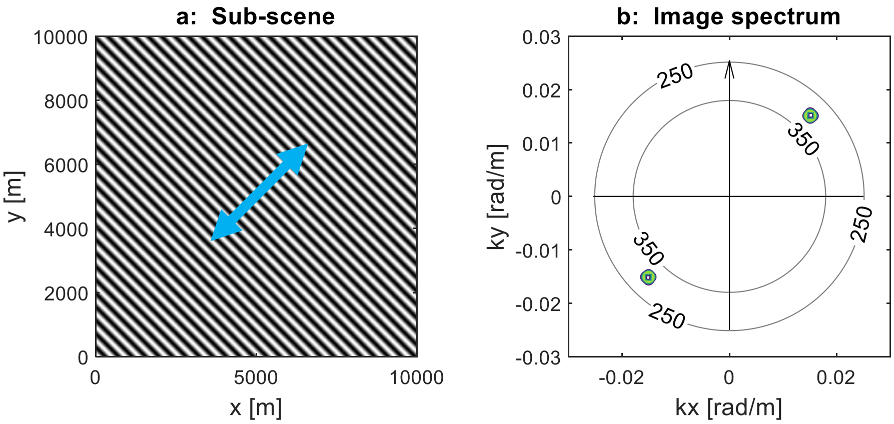

Figure 11. (a) Simulated sinusoidal wave of 300 m wavelength and wave direction of 45° relative to the x-direction. (b) Corresponding image spectrum. The circles indicate the wavelength in metres.

In the absence of ice, the mechanisms that make it possible to observe waves in SAR images are (Alpers et al., 1981; Hasselmann et al., 1985):

- Velocity bunching
- Hydrodynamic modulation
- Tilt modulation

SAR determines its azimuth (along-track) position by the instantaneous Doppler shift of the returned signal. However, the motion of ocean waves introduces an extra doppler shift. This causes an azimuthal displacement of the scatterer in the SAR image, which is referred to as velocity bunching. The tilt modulation refers to the modulation of the backscatter due to the surface slope (caused by long waves). Hydrodynamic modulation is due to the interaction between short and long waves. The orbital velocities of the long waves create zones of convergence and divergence of the short waves, thereby modulating the backscatter along the wave profile.

The wave spectrum is connected to the image spectrum through the *modulation transfer function* (MTF), see Figure 12. The MTF is a combination of the aforementioned modulation processes. The radar scattering mechanisms within the sea ice are far less understood compared to in the open ocean. Short waves are mainly absent within sea ice so that the hydrodynamic modulation can be neglected. Ardhuin et al. (2015) also neglected the tilt modulation in their study, thereby expecting that the observed wave patterns come from the velocity bunching effect.

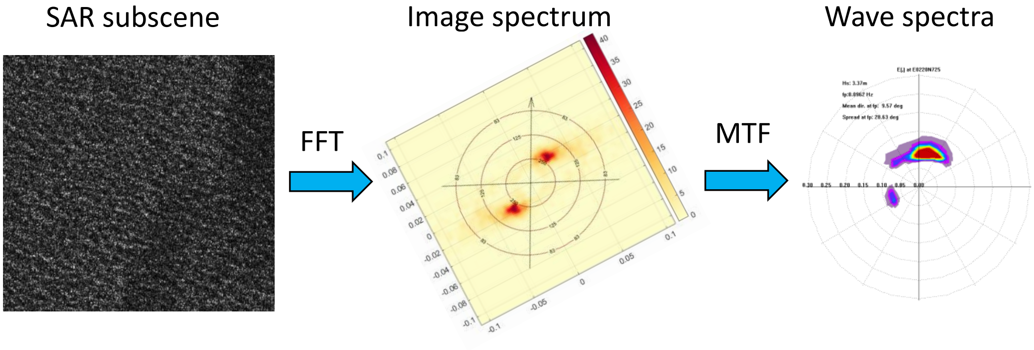

Figure 12. Schematic showing the steps to go from a SAR subscene to a 2D wave spectrum in the open ocean. The SAR subscene is taken over the open ocean in the Barents Sea. The image spectrum is obtained through fast Fourier transform (FFT), and by applying the MTF, the full 2D wave spectrum is obtained.

As mentioned above, velocity bunching is due to the extra doppler shift caused by the orbital velocities of ocean waves. The velocity bunching of long waves causes an apparent shift in scatter density that makes the waves visible in the SAR image. The random motions of the short waves cause an apparent blurring of the SAR image (Raney et al., 1989) and lead to the well-known azimuth cutoff wavelength (e.g., Kerbaol et al., 1998). In other words, the shortest visible wavelength in azimuth direction is the azimuth cutoff wavelength. It is important to note that this cutoff is only for the azimuth component of the travelling waves. The waves that travel in range direction (across-track) are not influenced by velocity bunching and can theoretically be measured up to the pixel resolution of the SAR image.

The azimuth cutoff within the sea ice is much smaller compared to the open ocean. The reason for this is that the short waves, which are the dominant contribution to the azimuth cutoff, are mainly absent. This difference in azimuth cutoff wavelength is illustrated in Figure 13. In this figure, a SAR image taken over the Barents Sea includes two different wave systems. One wave system has a peak wavelength of approximately 250 m and travels close to range direction. The other wave system has a peak wavelength of 125 m and travels in the azimuth direction. This latter wave system that travels nearly in the azimuth direction is only visible within the sea ice, and it is absent from the image spectrum in the open ocean. This is because the azimuth cutoff wavelength in the open ocean is larger than the peak wavelength of the wave system.

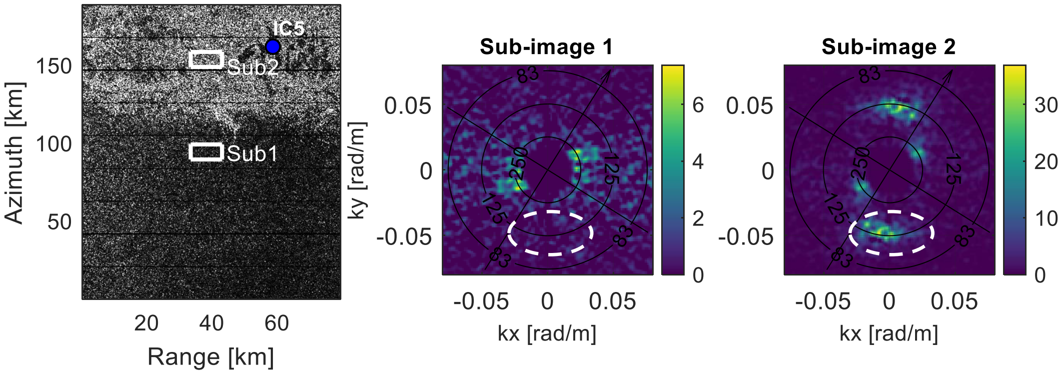

Figure 13. Comparison of the azimuth cutoff effect in the open ocean versus within the sea ice (after Monteban et al., 2019b). The left image shows a normalised intensity map acquired over the Barents Sea by S1 on 22 April 2017. The lighter areas indicate the sea ice, and the location of IC5 can be seen in Figure 10. Sub-images 1 and 2 show the real part of the cross-spectrum of the sub-images indicated by the white squares shown in the intensity map. The black circles in sub-images 1 and 2 show the wavelength in metres, and the arrow points north. kx and ky are the wavenumber in range and azimuth direction, respectively.

3.3.2 SAR observations of wave propagation in the MIZ

The first observations of waves within the sea ice by airborne SAR were made in the late 1980s and early 1990s (Carsey et al., 1989; Liu et al., 1991a; Lyzenga et al., 1985; Raney et al., 1989). The new generations of operational SAR satellites, such as the S1 and TerraSAR-X that have high-spatial resolutions and multi-polarizations, opened new possibilities to study the interactions between ocean waves and sea ice in the MIZ. Deriving the wave attenuation has proved challenging because of the complicated non-linear MTF. However, under some favourable conditions (i.e., low significant wave height, long waves), the MTF can be considered linear. In this case, the attenuation coefficient can be directly obtained from the image spectrum as was done in the studies by Liu et al. (1992) and Shen et al. (2018). A new and inventive algorithm was developed by Ardhuin et al. (2017), making use of the unique velocity bunching mechanism to estimate the wave parameters. This algorithm was used by Stopa et al. (2018a) in the most comprehensive study on wave attenuation from SAR to date. The attenuation showed piecewise exponential decays that coincide with a sharp transition in the ice cover, supporting the idea of having multiple wave decay processes.

In Monteban et al. (2019b), S1 SAR imagery collected over the Barents Sea was used to study the change in peak wavelength and dominant wave direction. One wave event with relatively long waves (peak wavelength of 160 m) was studied, where the waves travelled from the open water into the sea ice. The estimates in the open ocean were verified with in-situ observations from the BaSMIN measurement campaign and showed satisfactory results. The ice observed during this event was thin, with a mean daily ice draft of 0.28 m averaged over ice mooring stations IC3, IC4 and IC5 (Figure 10). The main findings of this study are presented in Figure 14.

The peak wavelength shows a slight increase as waves propagate through the sea ice. This increase can be attributed to the spatial dispersion of waves and is possibly enhanced by wave-ice interactions. This result was also found by Gebhardt et al. (2016), who studied the variations of peak wavelengths in the MIZ off the coast of Eastern Greenland with the TerraSAR-X satellite. Moreover, the spread in observations displayed in Figure 14b is much smaller within the sea ice compared to in the open ocean. This is because the high-frequency ocean waves are mainly filtered out by the sea ice cover. Short ocean waves blur the SAR image (Alpers and Rufenach, 1979) and, therefore, the waves appear more clearly in SAR images taken over the sea ice.

The dominant wave direction (Figure 14c) shows a shift of approximately 30° at the ice edge. This shift is partly due to refraction and is potentially an imaging artefact (Schulz-Stellenfleth and Lehner, 2002). As shown in Figure 13, waves that were not visible in the open ocean may appear within the sea ice due to the azimuth cutoff wavelength being much smaller. This may cause an apparent shift in the dominant wave direction. However, because the studied waves travelled predominantly in range direction, the azimuth cutoff wavelength is minimal, and it is suspected that the shift in dominant wave direction to be mainly due to refraction.

In addition to deriving the wave attenuation, wavelength and wave direction, SAR imaging has also been used to obtain the wave dispersion relation within the sea ice. This is the topic of the next section.

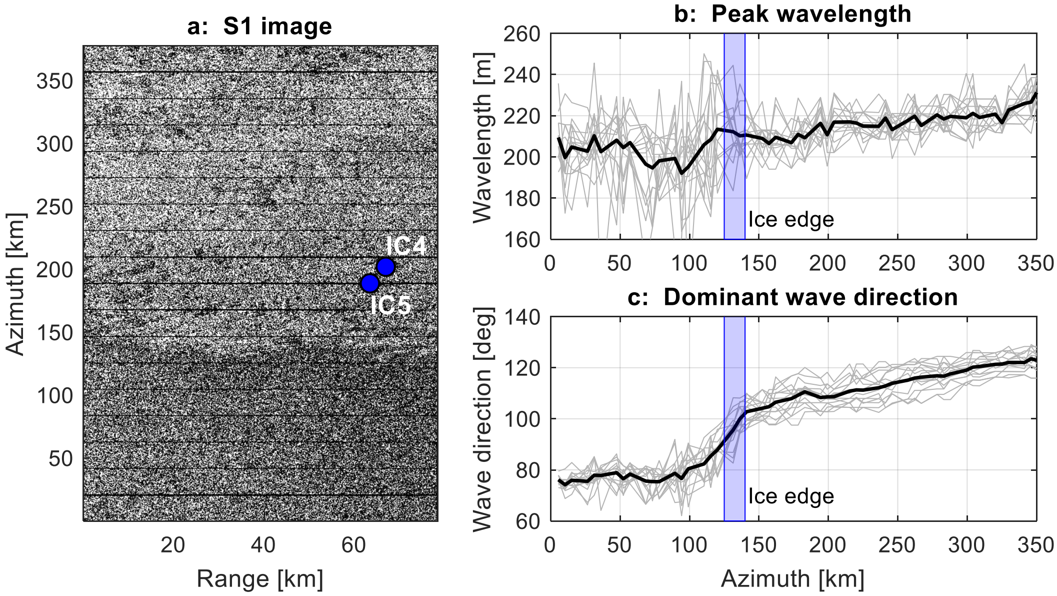

Figure 14. (a) Normalised S1 intensity image acquired on 4 April 2017. In (b) the peak wavelength is presented and in (c) the dominant wave direction is shown. The wave direction is defined as the angle relative to north, where the waves are coming from. These parameters are derived from 10 km × 10 km sub-images. Each light grey line shows the derived parameters over the azimuth direction, for a fixed range coordinate. The thick black line shows the average of the observations given in grey, i.e., it is the change in azimuth direction averaged over the range direction. The indicated ice edge in (b) and (c) is estimated from the S1 image in (a), where the dark area indicates the open ocean and the brighter area the sea ice cover. This figure is adapted from Monteban et al. (2019b).

3.4 Innovative method to obtain observations of the wave dispersion within sea ice from Sentinel-1 SAR

The wave dispersion relationship describes the relationship between the length and the frequency of ocean waves. In the open water, this relation is well known and is valid for most oceanographic conditions. Small deviations may arise when, for instance, waves get sufficiently steep and non-linear effects play a role (Stokes, 1847), or for very short waves when surface tension becomes important. On the other hand, not much is known about the wave dispersion relation within the sea ice. Several theoretical wave-ice interaction models exist in the literature that proposes different formulations of the dispersion relationship of waves travelling in icy waters. Although most of the dispersion relations are easy to write, their solutions can be complex.

Measurements of the wave dispersion are rare. Besides the challenges associated with collecting data in the polar regions, the difficulty with measuring the wave dispersion is that it requires collocated observations of the wavelength and wave period, i.e., spatiotemporal information. An overview of in-situ data collected using tiltmeters, strainmeters and seismometers is given by Collins et al. (2017). There have also been several studies performed in the laboratory. However, generalising these results is ambiguous and questionable due to the small scales in which the experiments are performed. Airborne and satellite SAR imagery were used in multiple studies to retrieve the wave dispersion by investigating the change in the two-directional wave spectrum as waves enter the sea ice (Liu et al., 1991b; Shuchman et al., 1994; Wadhams et al., 2018, 2004, 2002; Wadhams and Holt, 1991). However, retrieving the two-directional wavenumber spectrum is nontrivial as it requires the MTF.

In Monteban et al. (2019a) (Appendix D), a method to retrieve the wave dispersion relation from the S1 satellite was developed without using the MTF. Multiple wave events were studied that cover a broad range of different peak wavelengths. The study site was the Barents Sea, where in-situ data were available from the BaSMIN measurement campaign (see Section 3.2). A major drawback of many previous studies that utilised SAR to retrieve the wave dispersion was the lack of current data (Collins et al., 2017). Therefore, including the effects of sea currents in the analysis is a major improvement and allowed the quantification of the effects of the currents on the wave dispersion relation.

3.4.1 Novelty of the method

The method to derive the wave dispersion relation from the S1 constellation is based on the method proposed by Johnsen and Collard (2009). These satellites use the *Terrain Observation with Progressive Scans SAR* (TOPSAR) technique (Zan and Guarnieri, 2006) in its *Interferometric Wide* (IW) swath and Extra Wide swath mode. Compared to the traditional SAR scanning technique, where the antenna beam is only steered in range direction, the TOPSAR technique steers the antenna beam both in range and azimuth direction. The scanning geometry of TOPSAR is presented in Figure 15, and two different ground areas are indicated. The single-look area is the ground area that is only scanned once by the antenna beam, while the burst overlap area is scanned (at least) twice.

Traditionally, the processing technique to estimate the cross-spectra from Johnsen and Collard (2009) is performed using data from the single-look area but for an acquisition mode that has a higher spatial resolution (stripmap or wave mode). Usually, this solves the 180° wave ambiguity. Applying this technique on the single-look area of the S1 IW swath mode (lower spatial resolution compared to stripmap and wave mode) results in a noisy and poor-quality imaginary spectrum. This problem is overcome by applying the technique on the burst overlap area of the S1 IW swath instead. The advantage of this is that the time separation between individual looks (images) used to compute the cross-spectrum is significantly larger and, therefore, a larger phase change is present. In Figure 16, an imaginary part of a cross-spectrum computed within the sea ice and in the open ocean using the single-look area and the burst overlap area is presented. It is evident that the spectra from the burst overlap area have much better quality and are less noisy. Being able to derive a good quality imaginary spectrum enabled the derivation of the wave dispersion relation and can potentially be used for a better estimation of the wave direction in the open water.

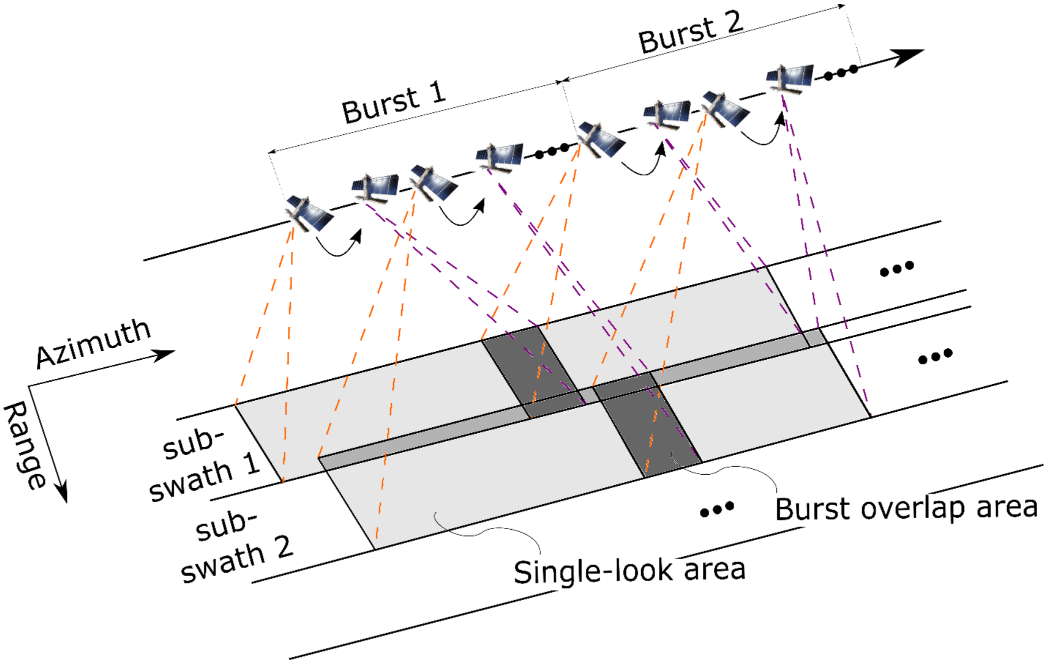

Figure 15. Acquisition geometry of the S1 TOPSAR technique (Monteban et al., 2019a). The antenna is steered forward in the azimuth direction, from the orange dotted line to the purple dotted line, for each burst and each subswath. Part of the ground area is scanned twice between bursts and subswaths, which is the burst overlap area.

Figure 17 summarises the main steps of the method. The two shown sub-scenes are of the same ground area but are scanned during a different burst, and hence, they have a time separation of 1.8-2.1 s. The cross-spectrum is computed from these two sub-scenes, which has a real part and an imaginary part. Finally, the 2D cross-spectra are converted to 1D spectra, and the wave dispersion is computed (step II in Figure 17). From the example in Figure 17, it can be seen that the computed wave dispersion from S1 agrees with the theoretical open-water dispersion relation in the range where the wave energy is located (approximately between $k = 0.025$ and $k = 0.04$).

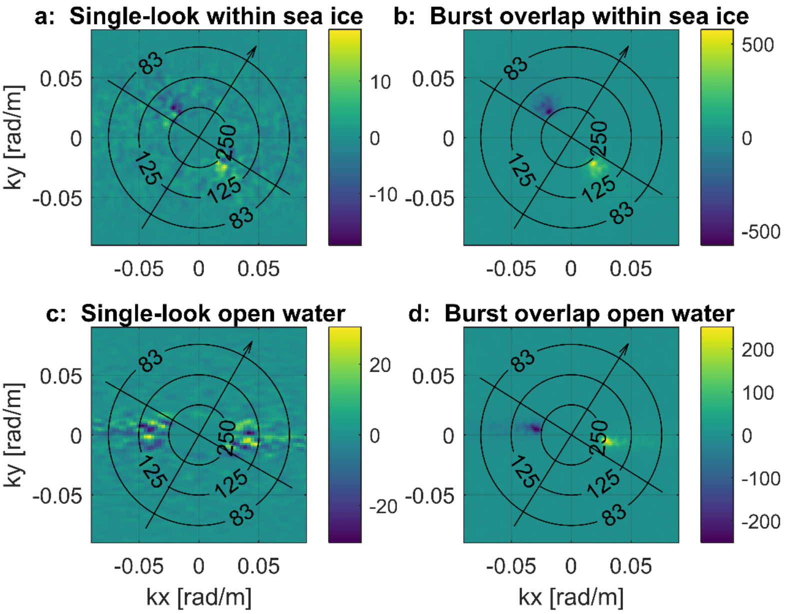

Figure 16. Derived imaginary spectrum within the sea ice (a and b) and in the open water (c and d) using the single-look area (a and c) and the burst overlap area (b and d) (altered from Monteban et al. (2019a). The circles show the wavelength in metres, and the arrow indicates north. kx and ky are the wavenumber in range and azimuth direction, respectively.

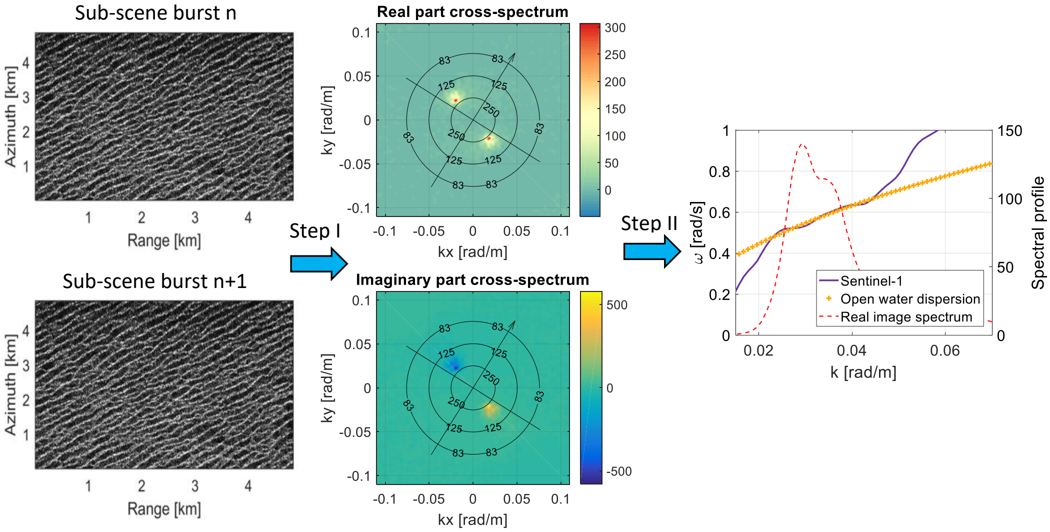

Figure 17. Schematic of the method to compute the wave dispersion from S1. For all the details of step I and step II, the reader is referred to Monteban et al. (2019a), given in Appendix D.

3.4.2 Applicability of the method

An advantage of the method is that it does not require the complicated MTF. This function is not needed because a linear ocean-to-SAR transform is assumed. Linear imaging regimes do not occur very often in the open ocean because it requires relatively long waves and a low significant wave height (thus a low azimuth cutoff). However, within the sea ice, short waves are mainly absent as the ice cover acts as a low-pass filter (Collins et al., 2015). These short waves of wind-driven seas are the dominant contribution to the azimuth cutoff (e.g., Kerbaol et al., 1998) and, therefore, it is argued that linear conditions are present within the sea ice. The computed wave dispersion for two wave events is presented in Figure 18 to demonstrate the applicability of the method. These two events are characterised by (Monteban et al. (2019a):

- Event 04-04-2017 has a peak wavelength of 160 m and an azimuth cutoff wavelength of 306 m in the open water.
- Event 16-02-2017 has a peak wavelength of 350 m and an azimuth cutoff wavelength of 260 m in the open water.

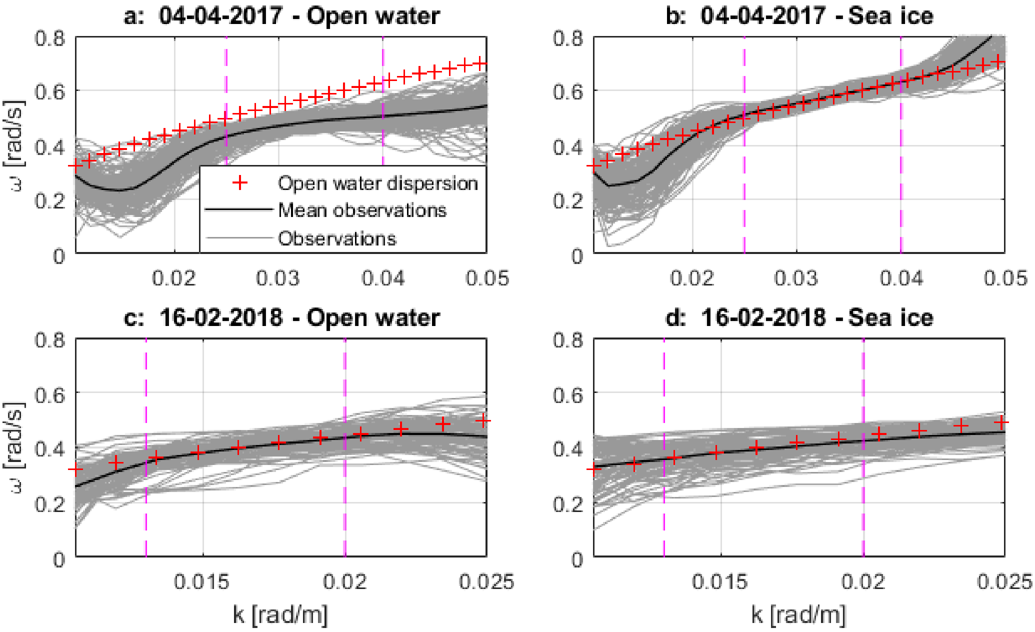

Figure 18. The estimated wave dispersion relation (angular frequency, ω, as a function of the wavenumber, k) from S1 in the open water (a and c) and within the sea ice (b and d) for two wave events. Each grey line is the result of the processing of one sub-image, and the thick black line is the mean of these observations. The magenta vertical dashed lines indicate the wavenumber range where most of the wave energy is located. This range is found by normalising the 1D real part of the cross spectrum and finding values that are larger than 0.5. The figure is taken from Monteban et al. (2019a).

The derived wave dispersion relation from S1 should be identical to the theoretical open-water dispersion relation for these two wave events as the wave dispersion relation of long waves within the sea ice is nearly similar to the theoretical open-water dispersion relation (Cheng et al., 2017; Collins et al., 2018). The computed wave dispersion from S1 shown in Figure 18 is in good agreement with the theoretical open-water dispersion relation for both wave events within the sea ice (Figure 18b and Figure 18d) and also for the 16-

02-2018 wave event in the open water (Figure 18c). For these three cases, linear conditions are present as the peak wavelength is larger than the azimuth cutoff wavelength. However, for the 04-04-2017 case in the open water, the computed angular frequencies show an underestimation. The reason for this underestimation is that the peak wavelength (160 m) is much smaller than the azimuth cutoff wavelength (306 m) and, therefore, non-linear conditions are present, and the assumption of the linear ocean-to-SAR transform is violated.

3.4.3 Derived wave dispersion within the sea ice

The results of three wave events with long waves are presented in Figure 19. The shown events have peak wavelengths of 99 m, 118 m and 194 m. For all these events, the measured ice was thin, with a mean ice draft of approximately 0.3 m. The observed ice can be classified as first-year thin and young ice, and the ice cover close to the ice edge is inhomogeneous, with open water patches and ice floes present. Each grey line in Figure 19 is the processing result of one sub-image, similar to the example shown in Figure 17. The mean of the observations is almost identical to the open water dispersion relation, which agrees well with previous findings. Furthermore, the good comparison within the sea ice provides confidence in the validity of the assumption of linear ocean-to-SAR conditions in ice-covered waters.

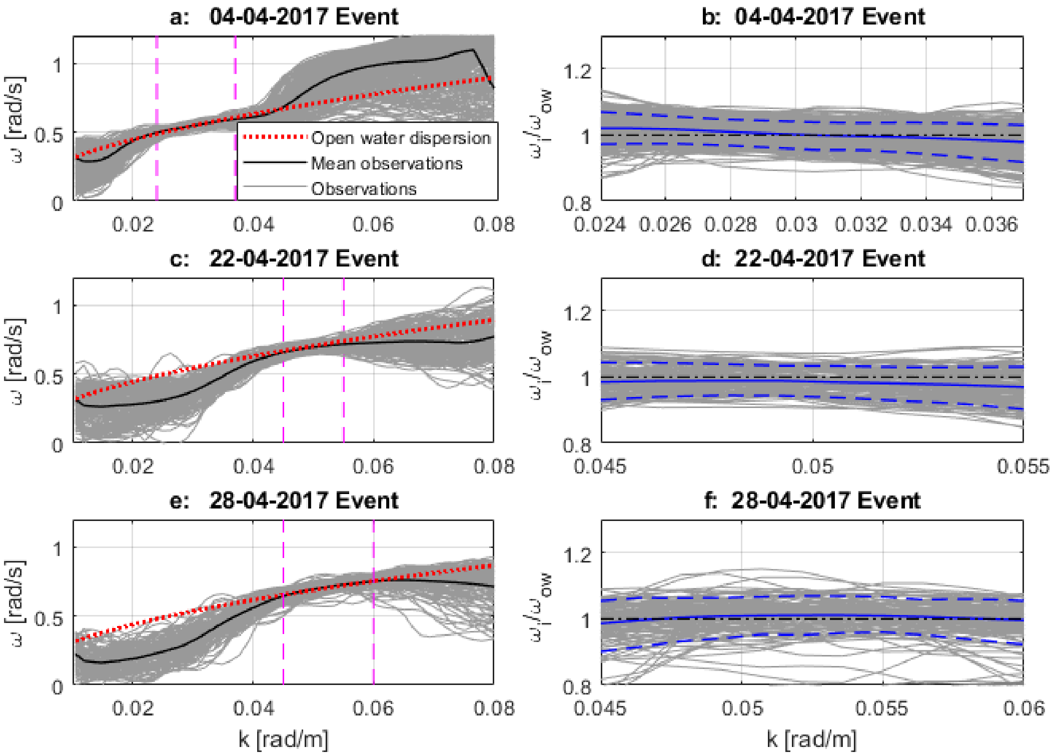

Figure 19. The computed wave dispersion from S1 within sea ice for three wave events characterised by long waves. The peak wavelengths measured at Wave Buoy WS3 (Figure 10) for the events 04-04-2017, 22-04-2017 and 28-04-2017 are 194 m, 99 m and 118 m, respectively. The magenta vertical lines indicate the range in wavenumber where most of the wave energy is located. Subfigures (b, d and f) show the ratio of the estimated angular frequency from S1 (ω_i) and the open water angular frequency (ω_{ow}). The thick blue line indicates the average of the observations, and the dashed blue lines enclose 90% of the observations. This figure is altered from Monteban et al. (2019a).

The results for three events with the shortest observed wavelengths are presented in Figure 20. Again, the observed sea ice is classified as first-year thin and young ice, with a mean draft of roughly 0.3 m. For these cases with short waves, there are fewer observations compared to the ones with long waves as there are significantly fewer sub-images where the waves are visible within the sea ice. In addition to the derived wave dispersion relation from S1, the simplest theoretical dispersion relation model, i.e., the mass loading model, is plotted as a function of the ice thickness. In theory, having accurate observations of the wavelength and wave period allows to back-calculate the ice thickness. In this study, however, this was not accomplished due to a combination of small ice thicknesses together with the limited observable range of wavelengths from S1. Under these conditions, the mass loading model predicts only a minor deviation from the theoretical open-water dispersion relation. Moreover, a relatively large spread in observations (grey dashed lines) can be seen and hence, the S1 cannot sense such a minor deviation from the theoretical open-water dispersion relation.

To be able to back-calculate the ice thickness, higher higher-resolution SAR data are needed. Having higher resolution data has two advantages, namely: 1) shorter waves can be studied, which have according to the mass loading model, a larger deviation from the theoretical open-water dispersion relation and 2) it would be possible to average more over the same spatial area, leading to an even better-quality cross-spectrum, thereby increasing the accuracy.

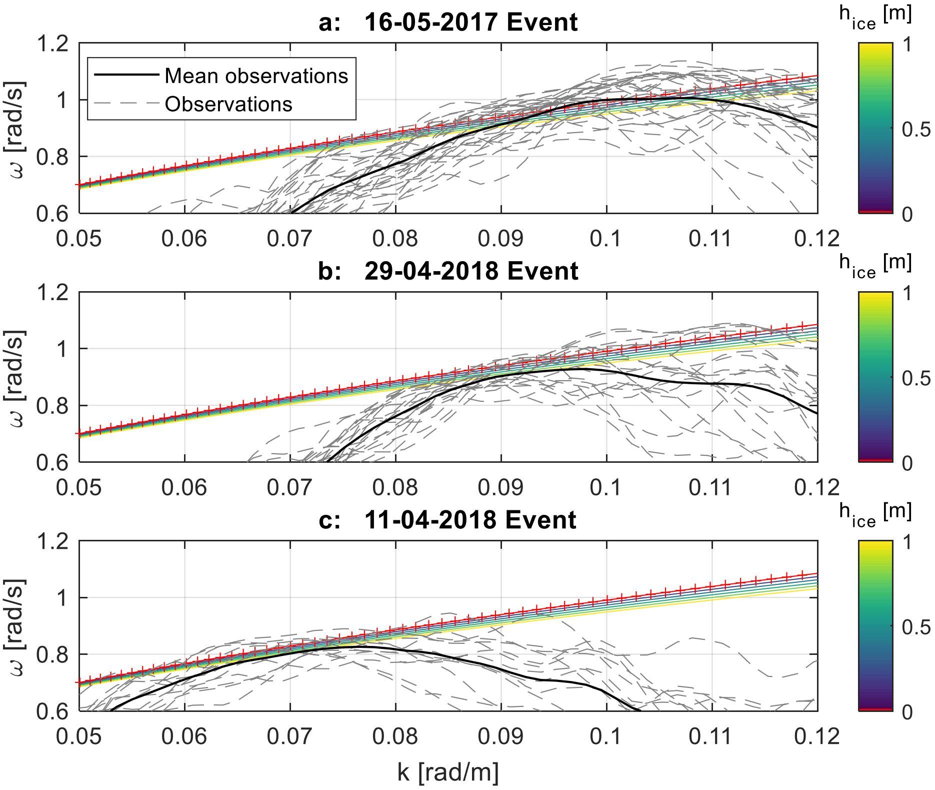

Figure 20. The derived wave dispersion relation from S1 for three wave events characterised by short waves. The peak wavelengths measured at Wave Buoy WS3 (Figure 10) for the events 16-05-2017, 29-04-2018 and 11-04-2018 are 72 m, 56 m and 75 m, respectively. In addition, the mass loading model, Eq. (1), is plotted as a function of the sea ice thickness (h_{ice}). This is given as a colour-code spectrum. The figure is taken from Monteban et al. (2019a).

4 Numerical modelling of the Arctic fjord Kangerlussuaq

The previous chapter focussed on satellite remote sensing observations to analyse wave conditions in icy waters. This chapter combines in-situ measurements with numerical modelling to achieve a better understanding of Arctic fjord's dynamics, which is important because fjords are a vital link between inland ice and the ocean (Straneo and Cenedese, 2015). Freshwater discharged from the *Greenland Ice Sheet* (GIS) that transits through fjords can be significantly modified before it reaches the open ocean. Therefore, understanding fjord dynamics will lead to proper parameterisations of fjord processes, which is necessary for obtaining adequate forcing for ocean circulation and climate models.

The objective of this work was to describe the physical oceanographic and wave conditions in the Greenlandic fjord Kangerlussuaq by using primarily numerical modelling. This fjord system is one of the most studied areas in the Arctic (Yde et al., 2018). For instance, Storms et al. (2012) studied the past ice sheet variability and sedimentary fill to better understand past relative sea-level changes and deglacial history. Nielsen et al. (2010) performed field surveys to obtain information about the water-mass characteristics and the associated foraminiferal fauna. Many researchers studied the meltwater rivers flowing into the fjord, e.g., 1) van As et al. (2018) reconstructed the GIS meltwater discharge through the Watson River (see Figure 21 for its location) from 1949 to 2017, 2) Mikkelsen and Hasholt (2013) and Hasholt et al. (2013) studied the sediment transport into the fjord and 3) Mikkelsen et al. (2013) studied jökelhaup events (ice-dammed lake outbursts). Furthermore, multiple studies focussed on biological aspects such as the light climate and optical properties, nutrients, suspended matter, sea ice primary production and growth of Arctic ice algae (Lund-Hansen et al., 2018, 2014, 2010). For all these aforementioned studies, it is of great importance to have a proper description of the physical oceanographic conditions in the fjord as this enables a better understanding of fjord-related research.

This chapter is based on the two scientific publications by Monteban et al. (2018) and Monteban et al. (2020b) provided in Appendix E and Appendix F, respectively. The chapter is structured as follows: in Section 4.1, the study area is introduced. The available in-situ data for this project are described in Section 4.2. Two different numerical models were set up for the fjord to simulate the water flow and the waves. The main equations of these models, together with their set up and the calibration procedure are provided in Section 4.3. Finally, the results of the numerical models are described in Section 4.4, which include a description of the current circulation, the water masses, the sensitivity towards different meltwater forcing and the 50-year return period wave parameters.

4.1 Regional setting

The fjord Kangerlussuaq is located at the west coast of Greenland, see Figure 21. It has a typical U-shape basin that is approximately 180 km long and stretches from southwest to northeast direction. The bathymetry of the fjord is presented in Figure 22. Based on the bathymetry, two distinct parts can be distinguished. The inner part of the fjord is defined from the Sarfartoq River to the Watson River, is up to 300 m deep and is broad (4-6 km). The outer part of the fjord is defined from the Sarfartoq River to the open ocean, is about 1 km wide and is much shallower (30-60 m). Furthermore, a magnification of the bottom of the fjord at the Northeast head is shown in Figure 22. Interestingly, multiple meandering channels are found at a depth of approximately 200 m, resembling a river delta. These channels were already reported by Storms et al. (2012), who suggested that the origin of these channels may be caused by a decrease in progradation rate or by turbidity currents.

The West Greenland Current governs the oceanographic settings at the beginning (seaside) of the fjord. This current is a mixture of the Irminger Current (Myers et al., 2007) and the East Greenland Current (Sutherland and Pickart, 2008). The Irminger Current is a branch of the warm and salty North Atlantic Current, while the East Greenland Current originates in the Arctic Ocean and is therefore relatively cold and fresh. These currents meet at Kap Farvel (the most southern point of Greenland) from where they continue north along the west coast of Greenland as the West Greenland Current.

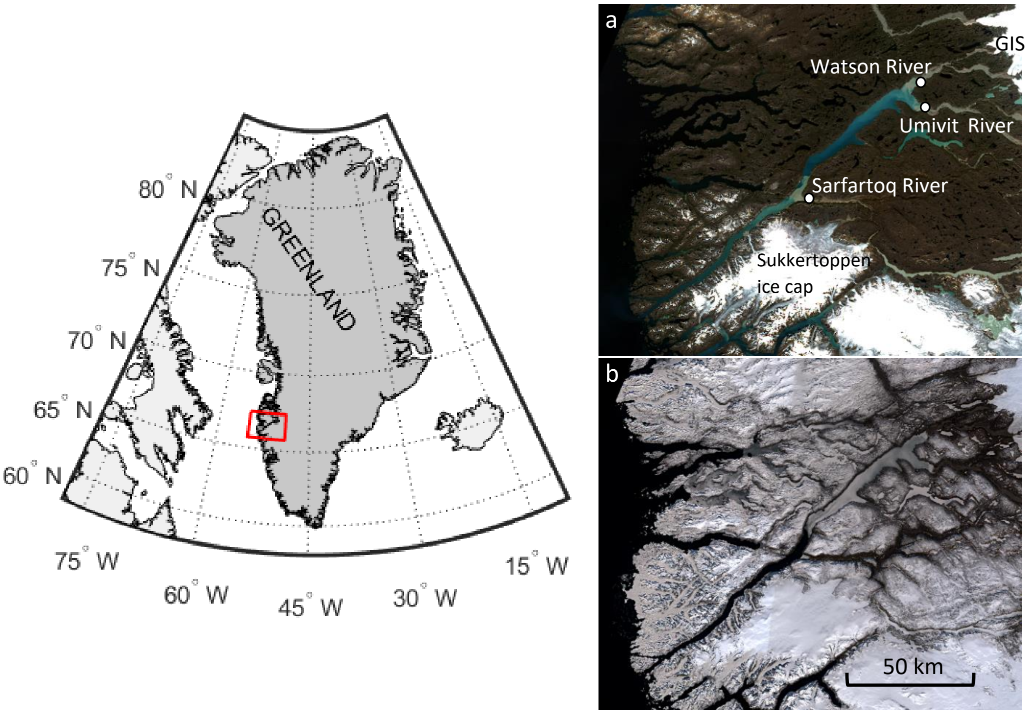

Figure 21. Map showing the location of the fjord Kangerlussuaq together with two S2 images of the fjord. Sub-image (a) is acquired on 23 July 2019 and (b) is acquired on 19 April 2019. The locations where the three main meltwater rivers enter the fjord are indicated in (a), together with the position of the GIS and the Sukkertoppen ice cap.

The fjord receives freshwater runoff primarily from three rivers: the Watson River (66° 57′ 54″ N, 50° 51′ 50″ W), the Umivit River (66° 50′ 2″ N, 50° 48′ 37″ W) and the Sarfartoq River (66° 29′ 30″ N, 52° 1 ′30″ W). The meltwater rivers transport a large amount of sediment into the fjord (Mikkelsen and Hasholt, 2013). Due to this import of sediment, the harbour that is located close to the delta of the Watson River experiences major sedimentation problems (Figure 23). This prevents large ships from entering the harbour, and an approach channel needs to be maintained, which results in high maintenance costs for the municipality. Therefore, there have been ongoing investigations to build a new harbour further into the fjord, away from the Watson River delta. Quantifying the physical oceanographic and wave conditions in the fjord provides valuable design conditions for a potential new harbour.

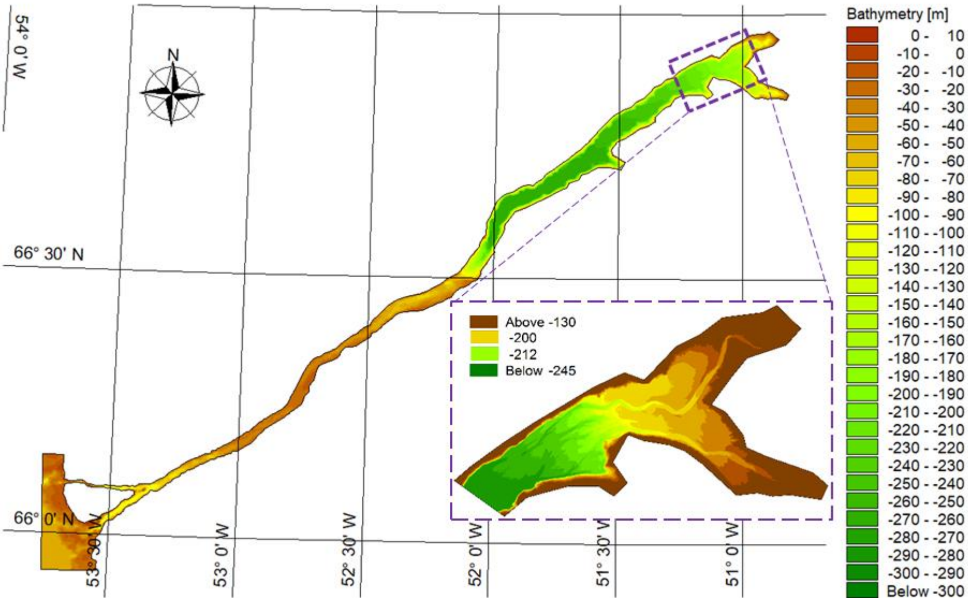

Figure 22. The bathymetry of the fjord Kangerlussuaq. Also, a magnification of the bathymetry at the end of the fjord is provided. Note that the values of the colour scale are different here.

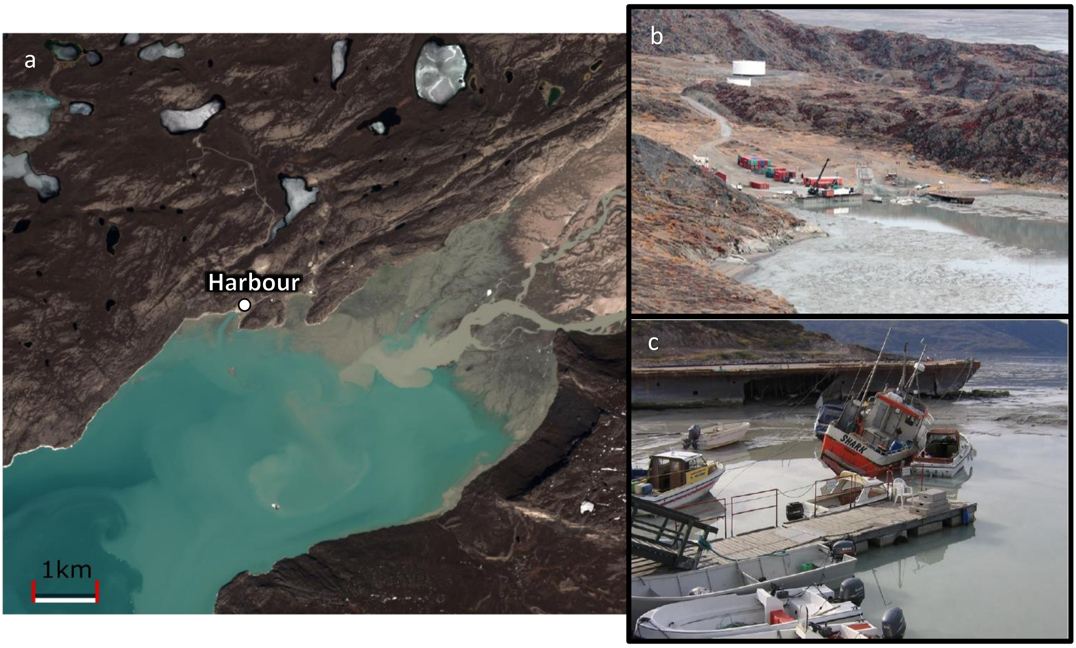

Figure 23. (a) S2 image acquired on 31 May 2017 showing the location of the harbour in the fjord Kangerlussuaq, close to the delta of the Watson River. Subfigures (b) and (c) show the sedimentation problems in the harbour and are taken from Hansen and Paulsen (2014) and Ingeman-Nielsen and Nielsen (2014), respectively.

4.2 Available measurements

Measurements in the fjord are available of the following parameters: the water level, *conductivity-temperature-densit*y (CTD) profiles, meteorological parameters, meltwater river discharge and 1D wave spectra. These parameters are briefly described here, and they are used as either input or calibration data for the numerical models.

4.2.1 Water level

The water level was measured in the fjord during the summer of 2011 (June-September) at multiple locations throughout the fjord (at points a, b and c in Figure 28). Solinst Levelogger Gold recording devices (Solinst Canada Ltd, Georgetown, Ontario, Canada) were deployed that measured the pressure difference as the tidal waves pass. The time series at the beginning (seaside) of the fjord (point a) is given in Figure 24. It takes the tidal wave approximately 3.5 hours to travel from point a to point c (see Figure 28), and a mean spring tidal range of 3.5 m was found at the end of the fjord (point c). Moreover, the tidal character is classified as semidiurnal (D Monteban et al., 2020).

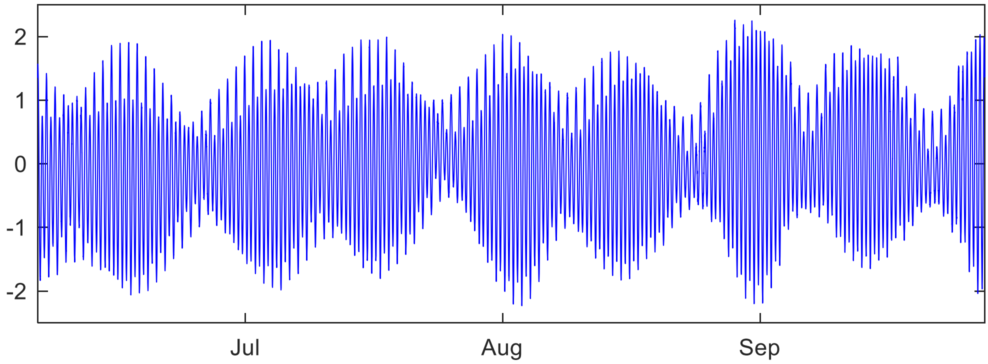

Figure 24. Time series of the measured water level at point a (see Figure 28 for the location) in 2011.

4.2.2 CTD profiles

CTD profiles were collected during summer (3-4 August 2005) and winter (26-27 February 2006) measurement campaigns (Nielsen et al., 2010) using 19plus SEACAT Profilers (Sea-bird Electronics, Bellevue, WA, USA). During the winter survey, measurements were taken at six locations in the inner, sea ice-covered part of the fjord, whereas during the summer survey sixteen locations throughout the entire fjord were visited (see Nielsen et al. (2010) for the locations). The temperature-salinity diagram for both the summer and winter survey are presented in Figure 25. Large vertical gradients are observed in the summertime, as opposed to much smaller vertical gradients in wintertime. From the August 2005 survey, a large number of points are observed in the range of 24 psu to 25 psu (practical salinity unit) (UNESCO, 1987) and -1 °C to -0.5 °C. These points correspond to the deep, inner part of the fjord and indicate a very homogeneous layer.

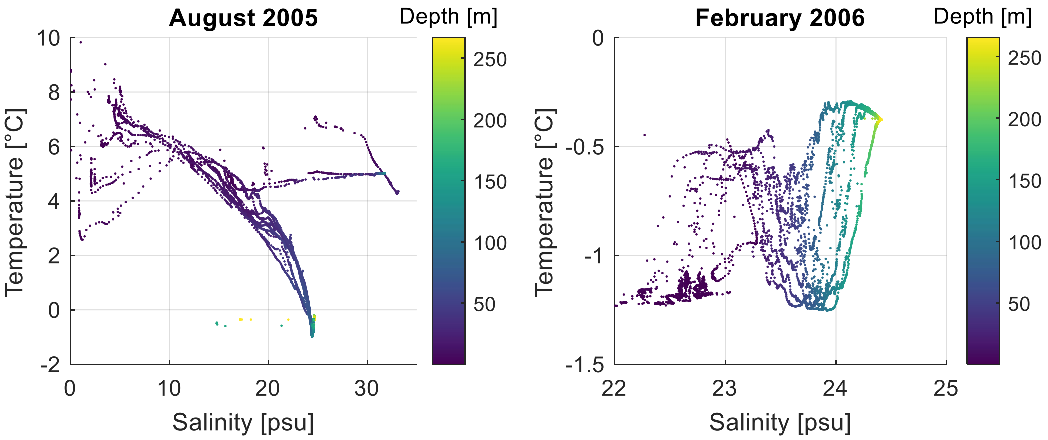

Figure 25. Salinity-temperature diagrams of the in-situ data collected during summertime and wintertime. The figure is altered from Nielsen et al. (2010).

4.2.3 Meteorological data

Meteorological observations are available from the DMI (Cappelen, 2016) weather station, which is located at the Kangerlussuaq airport (67° 1′ N, 50° 42′ W). The wind rose for more than 40 years of data is given in Figure 26, which shows that the dominant wind direction is winds coming from the northeast. Additionally, atmospheric parameters such as the relative humidity, cloud cover, precipitation and air temperature are measured. The climate of Kangerlussuaq is defined as Low Arctic (Hasholt et al., 2013). Further, the area of Kangerlussuaq is orographic shielded by the Sukkertoppen ice cap (see Figure 21), which makes the area exceptionally dry with annual average precipitation over the period 1976-2016 of 156 mm (van As et al., 2018). Air temperatures have on average positive values between approximately May and September, and frigid temperatures down to -40 °C are reached during winter.

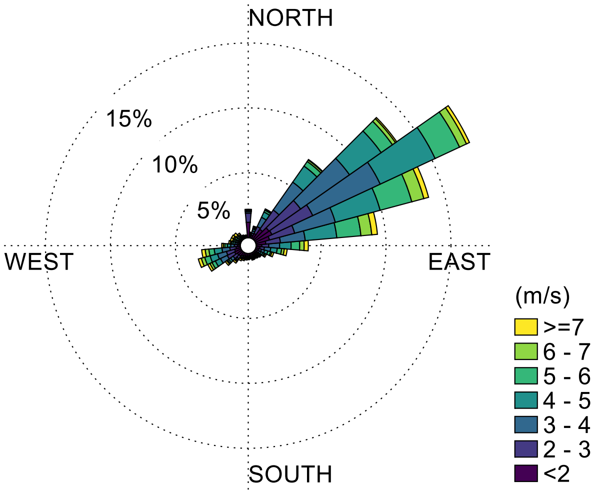

Figure 26. The wind rose of the data collected at the airport of Kangerlussuaq for the period 1973-2017 (Cappelen, 2016). The direction indicates where the wind comes from, and the measurements are made at an elevation of 50 m.

Sea ice formation usually starts in November, and the fjord is sea ice free again from roughly the beginning of June. The sea ice covers only the inner part of the fjord, up to the Sarfartoq River (see, e.g., Figure 21b). The outer part of the fjord is always sea ice free, which is most likely because the tidal currents are too strong here for sea ice to form (see Section 4.4.1).

4.2.4 Meltwater discharge

As mentioned in Section 4.1, three main meltwater rivers are flowing into the fjord. The discharge of the Watson River has been monitored since 2006 (van As et al. (2018). Hasholt et al. (2013) found an annual averaged total discharge of 1070 km^3 and a peak flow of 1620 m^3 s^{-1} between 2007 and 2010. Moreover, the discharge is almost zero from approximately October until May. No information on the discharge is available for the Sarfartoq and Umivit Rivers. Therefore, the discharge of these two rivers was estimated by scaling the discharge of the Watson River with the river catchment areas. These areas were taken from Hudson et al. (2014) and are 3639 km^2 for the Watson River, 6320 km^2 for the Umivit River and 5385 km^2 for the Sarfartoq River. The annual total discharge of the Watson River is 3.7 km^3 (Hasholt et al., 2013), and the resulting estimated annual total discharge of the Umivit and Sarfartoq Rivers is 6.4 km^3 and 5.5 km^3, respectively.

4.2.5 Surface waves

Waves were measured at the inner part of the fjord (point c in Figure 28) during September 2013. A second generation non-directional Waverider buoy (Datawell BV, Haarlem, Netherlands) with a frequency of 2.56 Hz was used, and the resulting time series is presented in Figure 27a. The WAFO toolbox (WAFO-group, 2000) implemented in MATLAB (The MathWorks, Inc., Natick, MA, USA) was used to compute the wave spectra using 3-hour time intervals and consequently, the wave parameters (significant wave height and peak wave period) were calculated. The histogram of the observed significant wave heights is given in Figure 27b. Wave heights are in general low, with a maximum observed significant wave height of 0.8 m.

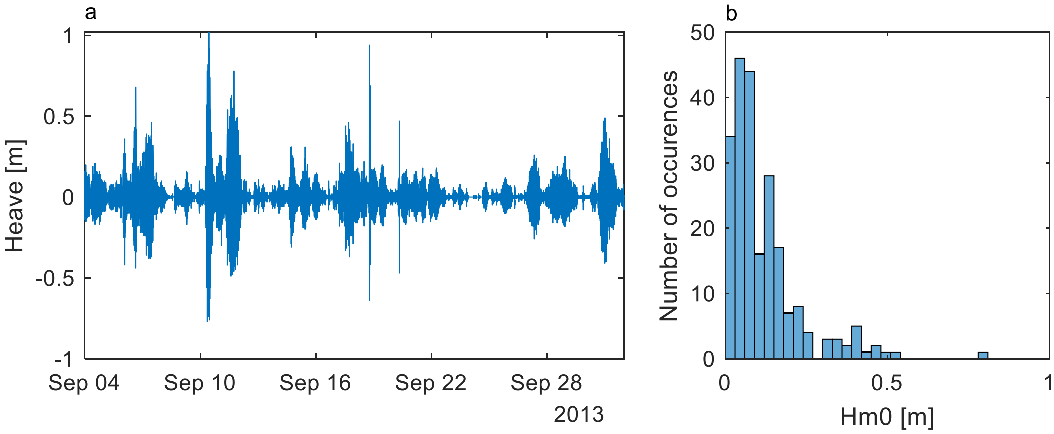

Figure 27. (a) Time series of the measured heave at point c (Figure 28). (b) Histogram of the significant wave heights (Hm0) computed using 3-hour intervals of the time series shown in subfigure (a).

4.3 Numerical models

The fjord system was modelled using the commercially available MIKE software. Two different modules of the software were used: the MIKE 21 *Spectral Waves* (SW) module (DHI, 2017a) and the MIKE 3 Flow Model - *Hydrodynamic* (HD) module (DHI, 2017b). It is possible to couple both models so that the effect of the currents on the waves are considered. However, such a coupling was not used in this study because the currents in the inner part of the fjord are small (see Section 4.4.1). Hence, the effect of the currents on the waves is negligible. In the following Section 4.3.1, only the main equations and assumptions of the models are provided. For the full set of equations and their numerical implementation, the reader is referred to the MIKE manuals.

4.3.1 Short description of the models

The MIKE 3 HD module is based on the incompressible Reynolds-Averaged Navier-Stokes equations. These equations are subject to two assumptions, namely 1) hydrostatic pressure and 2) the Boussinesq approximation. The 3D shallow water equations are solved, with continuity, momentum, temperature, salinity, density and are closed by a turbulence model.

In Cartesian coordinates, the continuity and the two horizontal momentum equations used in the MIKE 3 HD module are defined as:

$$\frac{\partial u}{\partial x}+\frac{\partial v}{\partial y}+\frac{\partial w}{\partial z}=S \tag{10}$$

$$\begin{aligned}\frac{\partial u}{\partial t}+\frac{\partial u^2}{\partial x}+\frac{\partial vu}{\partial y}+\frac{\partial wu}{\partial z}\\ =fv-g\frac{\partial \eta}{\partial x}-\frac{1}{\rho_0}\frac{\partial \rho_a}{\partial x}-\frac{g}{\rho_0}\int_z^{\eta}\frac{\partial \rho}{\partial x}dz-\frac{1}{\rho_0 h}\left(\frac{\partial S_{xx}}{\partial x}+\frac{\partial S_{xy}}{\partial y}\right)+F_u+\frac{\partial}{\partial z}\left(v_t\frac{\partial u}{\partial z}\right)+u_s S\end{aligned} \tag{11}$$

$$\begin{aligned}\frac{\partial v}{\partial t}+\frac{\partial v^2}{\partial y}+\frac{\partial uv}{\partial x}+\frac{\partial wv}{\partial z}\\ =fu-g\frac{\partial \eta}{\partial y}-\frac{1}{\rho_0}\frac{\partial \rho_a}{\partial y}-\frac{g}{\rho_0}\int_z^{\eta}\frac{\partial \rho}{\partial y}dz-\frac{1}{\rho_0 h}\left(\frac{\partial S_{yx}}{\partial x}+\frac{\partial S_{yy}}{\partial y}\right)+F_v+\frac{\partial}{\partial z}\left(v_t\frac{\partial v}{\partial z}\right)+v_s S\end{aligned} \tag{12}$$

where *u*, *v*, and *w* are the velocities in *x*, *y* and *z* Cartesian coordinates direction, respectively; *t* is the time; η is the surface elevation; *d* is the still water depth and *h* is the total water depth defined as $h=\eta+d$; *f* is the Coriolis parameter; *g* is the gravitational acceleration; S_{xx}, S_{xy}, S_{yx} and S_{yy} are the radiation stress components; ρ is the water density; ρ_0 is the reference density of water; v_t is the eddy viscosity; *S* is the magnitude of the discharge due to point sources; u_s and v_s are the velocities by which the water is discharged into the model from the source and F_u and F_v are the horizontal stress terms.

The transport equations of the salinity, *s*, and the temperature, *T*, are defined by:

$$\frac{\partial T}{\partial t}+\frac{\partial uT}{\partial x}+\frac{\partial vT}{\partial y}+\frac{\partial wT}{\partial z}= F_T+\frac{\partial}{\partial z}\left(D_v\frac{\partial T}{\partial z}\right)+H+T_s S \tag{13}$$

$$\frac{\partial s}{\partial t}+\frac{\partial us}{\partial x}+\frac{\partial vs}{\partial y}+\frac{\partial ws}{\partial z}= F_s+\frac{\partial}{\partial z}\left(D_v\frac{\partial s}{\partial z}\right)+s_s S \tag{14}$$

with F_T and F_s the horizontal diffusion terms; D_v is the vertical eddy diffusion coefficient; H is the source term due to the exchange of heat with the atmosphere, and T_s and s_s are the magnitude of the temperature and the salinity of the source, respectively.

MIKE 21 SW is a spectral wind-wave model that can simulate the growth, decay and transformation of ocean waves. The governing equation of the MIKE 21 SW model is the conservation equation for wave action (related to the energy density, see, e.g., Holthuijsen (2007), which in horizontal Cartesian coordinates can be written as:

$$\begin{aligned} &\frac{\partial N(\sigma,\theta;x,y,t)}{\partial t} + \frac{\partial c_{g,x} N(\sigma,\theta;x,y,t)}{\partial x} + \frac{\partial c_{g,y} N(\sigma,\theta;x,y,t)}{\partial y} \\ &+ \frac{\partial c_{\theta} N(\sigma,\theta;x,y,t)}{\partial \theta} + \frac{\partial c_{\sigma} N(\sigma,\theta;x,y,t)}{\partial \sigma} = \frac{S(\sigma,\theta;x,y,t)}{\sigma} \end{aligned} \tag{15}$$

where N is the action density; t is time; *x* and *y* are the Cartesian coordinates; θ is the wave direction; σ is the relative angular frequency; $c_{g,x}$, $c_{g,y}$, c_θ and c_σ are the propagation velocities of a wave group in *x, y,* θ and σ space, respectively and *S* is the source term. The wave action density is related to the wave energy (E) as $N = E/\sigma$. Moreover, the wave action is conserved in the presence of currents, which is the reason for using it instead of the wave energy. Finally, five different source terms (*S*) can be included: 1) wind input, 2) non-linear wave-wave interactions (quadruplet and triad wave-wave interactions), 3) white capping, 4) bottom friction and 5) wave breaking.

4.3.2 Setup MIKE 3 HD Flow model

The model domain and the horizontal computational mesh of the MIKE 3 HD model are presented in Figure 28, together with the bathymetry of the fjord. The horizontal grid is a combination of quadrangular and triangular grid cells. The smallest grid cells have a length of 160 m, and the largest grid cells are directed along the long-axis and are 1000 m long. The reason for primarily using quadrangular grid cells in the fjord is twofold. First, the quadrangular grid cells can be much longer in one direction compared to the other (elongated). This results in fewer grid cells compared to using only triangular cells and therefore, a reduction in computational time. Second, the flow in the fjord is mainly in along fjord direction (see Section 4.4.1). In such a case with a predominant flow direction, quadrangular grid cells simulate the flow more accurately as they favour water flow along the element, compared to the enhanced water flow divergence by triangular grid cells (DHI, 2016). Furthermore, 40 vertical layers are used to discretise the vertical direction. These vertical layers vary in resolution, from 15 m at the bottom to 1 m at the surface. The vertical mesh is a combination of 5 terrain-following sigma layers and 35 z-layers that are defined at fixed depths.

The seaside boundary (see Figure 28) is a combination of the water level, salinity and temperature. The water level is obtained from the DTU10 global ocean tide model (Cheng and Andersen, 2010) and the salinity and temperature are taken from the EU CMEMS global ocean physics reanalysis product (CMEMS, 2018). Meteorological data including the wind speed and direction, relative humidity, cloudiness and dry bulb air temperature are included and were measured at the DMI weather station (see Section 4.2.3). The three meltwater rivers are included and are represented as point sources placed in the surface layer. The sea ice cover is defined as external data, which is estimated from Envisat satellite data.

The simulation period is from 1 March 2005 to 1 March 2006. The initial conditions of the current velocities and water level were set to zero, and the initial conditions of the salinity and temperature were taken from the field survey in wintertime (Section 4.2.2). The latter initial conditions were from the winter of 2006, while the simulation starts in the winter of 2005. Using these initial conditions were believed to be valid because the conditions in the fjord during the wintertime are very homogeneous and therefore, similar from year to year (Nielsen et al., 2010). Finally, all the input parameters and module choices are summarised in Table 1.

Table 1. Module options and input parameters used in the MIIKE 3 HD model (Monteban et al., 2020b).

Input Parameter	**Value or model option**
Horizontal mesh	Resolution (min, max) = (160, 1000) m
Vertical mesh	Combined sigma/z-level; 5 sigma layers to a depth of 10 m and 35 z-layers. Resolution (min, max) = (1, 15) m
Time period	01.03.2005 – 01.03.2006
Maximum time step	300 s
Solution technique	Higher order scheme
Eddy viscosity	Horizontal eddy viscosity: Smagorinsky formulation Vertical eddy viscosity: k-ε model
Bed resistance	Constant roughness height: 0.05 m
Dispersion	Horizontal dispersion coefficient: 1 Vertical dispersion coefficient: 0.1
Coriolis forcing	Constant in domain
Atmospheric forcing	Observations available from the DMI weather station located at the airport of Kangerlussuaq and includes - Wind speed and direction - Air temperature - Cloud cover - Humidity
Ice coverage	Sea ice coverage derived from Envisat satellite imagery Sea ice roughness: 0.01 m
Initial conditions	Water level 0 m Velocities 0 m s^{-1} Salinity February 2006 measurements Temperature February 2006 measurements
Boundary conditions	Rivers Average discharge of 2007-2010 observations Sea Water levels from DTU global tide model Sea Salinity and temperature from the Global Ocean Physics Reanalysis product (Copernicus)

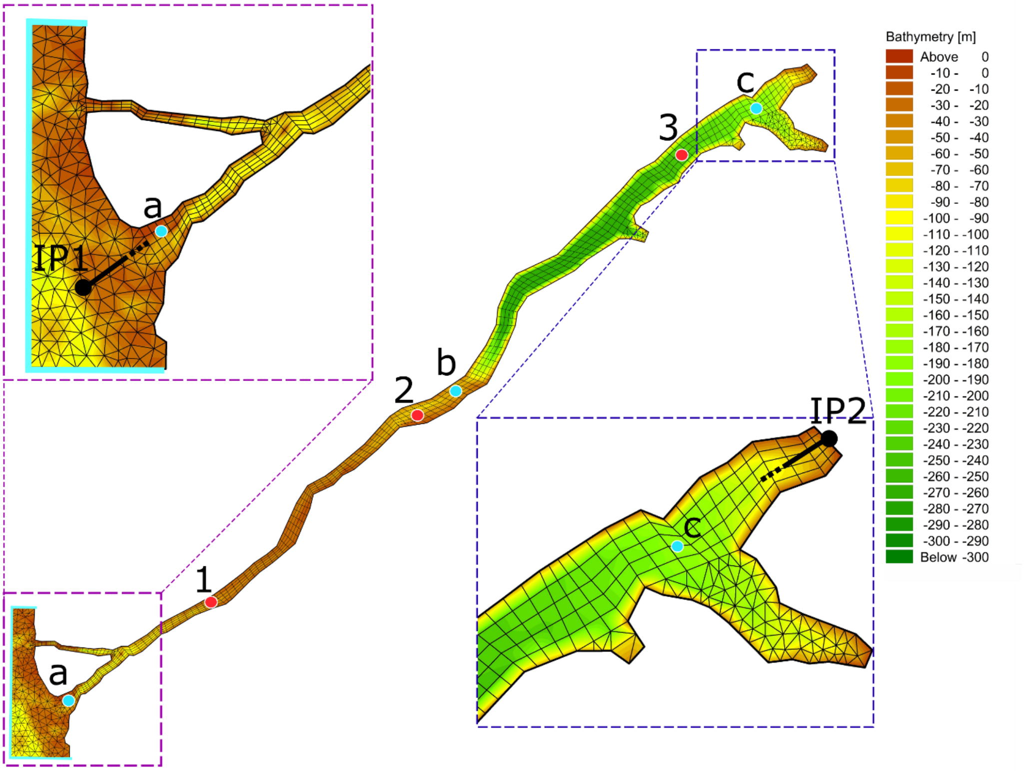

Figure 28. The horizontal computational mesh of the MIKE 3 HD model and bathymetry of the fjord. Points a, b and c indicate the locations of the calibration of the water level and points 1, 2 and 3 were used for the calibration of the vertical profiles of the salinity and the temperature. The points IP1 and IP2 indicate where the cross sections presented in multiple figures in this chapter begin and end, respectively. The solid blue line at the mouth of the fjord indicates the seaside boundary. This figure is taken from Monteban et al. (2020b).

The model was calibrated against water level measurements during August and against vertical profiles of the salinity, temperature and density on 3 August. The lack of sufficient in-situ data made it impossible to perform a validation procedure. The main calibration parameter of the water level was the horizontal mesh. A sufficiently fine resolution was required to get the right water levels in the fjord. The calibration of the water level showed a good comparison with the measurements at various locations throughout the fjord (Figure 29). At the inner part of the fjord (point c), a root mean square error of 0.12 m is obtained. Besides the amplitude of the tidal wave, the tidal phase is also well reproduced by the model. The latter indicates that the bathymetry is well represented because the water depth primarily determines the velocity of the tidal wave.

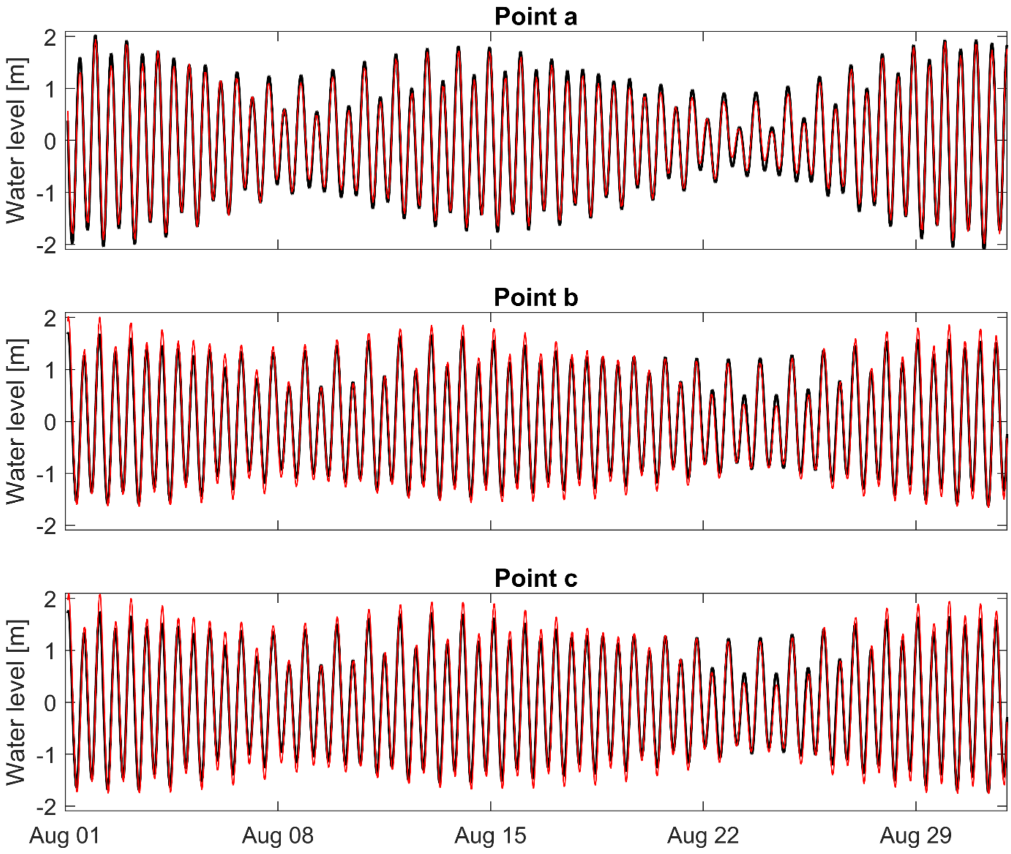

Figure 29. Results of the calibration of the water level at points a, b and c, indicated in Figure 28. The black line is the measured water level, while the red line is the computed water level from the MIKE 3 HD model. This figure is taken from Monteban et al. (2020b).

The main calibration parameters of the baroclinic part were the type and resolution of the vertical mesh and the vertical dispersion coefficient. Most of the used vertical layers were z-layers instead of sigma layers. This implementation was chosen because using more terrain-following sigma layers resulted in unrealistic mixing at the steep vertical slope present in the bathymetry close to the Sarfartoq River (see Figure 6 in Appendix F from Monteban et al. (2020b).

The final results of the calibration of the baroclinic part are shown in Figure 30. Overall, the simulation is in good agreement with the measurements. At point 2 and point 3, a good agreement is obtained. At point 1, however, some deviations are present between the simulation and the measurements. The reason for this deviation is most likely because of some discrepancies in the applied boundary conditions at the seaside open boundary (Monteban et al., 2020b). Nevertheless, the overall agreement of the simulation with the measurements provides confidence that the model captures the main physics during summertime well.

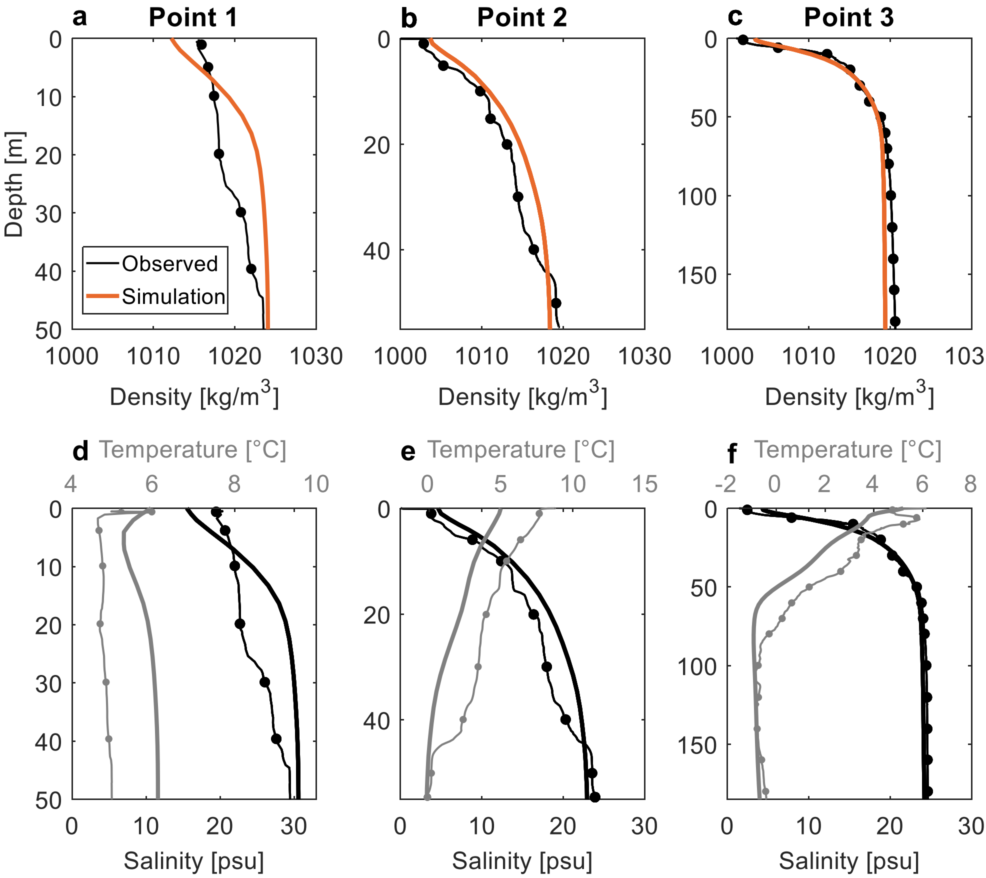

Figure 30. Results of the calibration of the MIKE 3 HD model. Subfigures (a-c) show the instantaneous vertical profiles of the density at the three locations in the fjord (see Figure 28). Subfigures (d-e) show the instantaneous vertical profiles of temperature (grey) and salinity (black) of the measurements (line with dots) and the simulation (solid line) at points 1, 2 and 3 for subfigures (d), (e) and (f), respectively. The profiles were extracted on 3 August 2005. The figure is taken from Monteban et al. (2020b).

4.3.3 Setup MIKE 21 Spectral Waves model

The MIKE 21 SW model was only implemented for the deep, inner part of the fjord, from the Sarfartoq River to the Watson River. All the boundaries are closed and, therefore, only locally generated wind-waves are considered. The input parameters that differ from the default values are provided in Table 2. The wind (speed and direction) is the most crucial input parameter, and this input was taken from the DMI weather station at the Kangerlussuaq airport (see Section 4.2.3). It is defined as the mean value over the 10-minute interval preceding the observation. The wind speed was adjusted for height (from 50 m to 10 m above mean sea level) using the wind profile power law (Shore Protection Manual, 1984). Moreover, the measured values were taken representative over the entire model domain.

Table 2. Overview of the input parameters and module choices for the MIKE 21 SW model.

Input Parameter	Value or model option
Horizontal mesh	Triangular grid cells of 300 m resolution
Time period	03.09.2013 – 02.10.2013
Maximum time step	120 s
Spectral formulation	Fully spectral
Spectral discretisation	Number of frequencies: 35 Number of directions: 16
Atmospheric forcing	Wind speed and direction
Air-sea interaction	Uncoupled formulation; Charnock parameter of 0.04

The MIKE 21 SW model was calibrated against the wave measurements (see Section 4.2.5) at point c (Figure 28). The results of the calibration of the model are presented in Figure 31. The main calibration parameter was the type of air-sea interaction, i.e., how the wind transfers its momentum to the waves. The uncoupled formulation, where the momentum transfer from the wind to the waves only depends on the wind speed and not on the sea-state roughness, was used as it gave the best results. Overall, the calibration showed satisfactory results. The model captures the peaks in the significant wave height well. However, the model overestimates some of the very small significant wave heights of approximately 0.2 m. This is most likely due to uncertainties in the wind input. The simplification of taking the wind speed and direction constant over the entire model domain will result in a loss of realism. Furthermore, the comparison of the peak period with the observations is satisfactory.

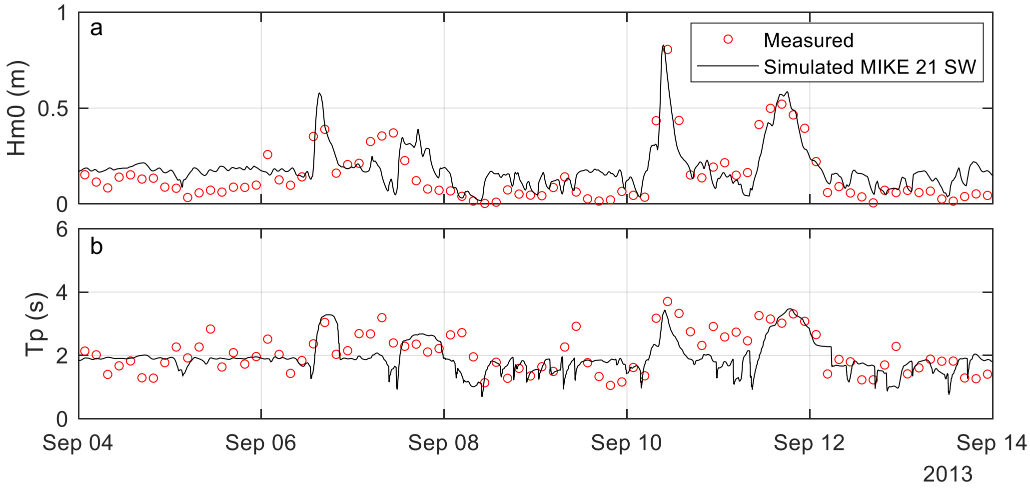

Figure 31. Results of the calibration of the MIKE 21 SW model of (a) the significant wave height (Hm0) and (b) the peak wave period (T_p). The measured significant wave height and peak period are computed using 3-hour intervals.

4.4 Physical oceanographic and wave conditions in the fjord

4.4.1 Currents

Rotational dynamics in the fjord are only minor, and thus the cross-fjord variations of the currents in the fjord are small. This causes the water to flow mainly in the along-fjord direction, and the circulation pattern in the fjord can be studied by looking at the along-fjord variations during a tidal cycle. In Figure 32, the instantaneous current speed is presented during flood tide (Figure 32a), slack tide (Figure 32b) and ebb tide (Figure 32c). Note that the tidal phase shown in the three subfigures of Figure 32 is defined at cross section length 60000 m. The tidal phase is not the same everywhere in the fjord, because it takes the tidal wave 3.5 hours to travel from the open ocean to the end of the fjord (point c in Figure 28). Very high current velocities are observed in the outer, shallow part of the fjord during flood tide (water flowing into the fjord) and during ebb tide (water flowing out of the fjord). These high current velocities in the shallow, outer part of the fjord are most likely the cause of the absence of sea ice during wintertime as can be seen from the S2 image shown in Figure 21b. The maximum instantaneous current speed observed over the entire simulation was 3.5 m/s. Furthermore, in the deep, inner part of the fjord, the current speed is always slow, with typical values around 0.05 m/s.

The time-averaged current speed over August 2005 is presented in Figure 33a. Additionally, in Figure 33b and Figure 33c, the temporal variations of two vertical profiles of the current speeds are given. Two distinct vertical current regimes can be distinguished at both locations of which one is present in the summertime and the other in wintertime. During summer, a net flow out of the fjord is observed in the surface layer, which is the light and freshwater coming from the meltwater rivers. The second regime is visible in wintertime, from approximately December to May. During this period, the vertical gradients are only minor as there is no more freshwater entering the fjord.

4.4.2 Water masses

The characteristics of the water masses in the fjord Kangerlussuaq were described by Nielsen et al. (2010), which was based on the two field surveys of the temperature and salinity presented in Section 4.2.2. In Monteban et al. (2020b) (Appendix F), a more comprehensive image of the water masses in the fjord is provided because the numerical MIKE 3 HD model allows the study of the development of the water masses over time.

The along fjord distributions of the temperature and salinity during winter and summer are presented in Figure 34. During summertime, the water masses include the coastal water from the West Greenland Current, a brackish surface layer and a deep-lying homogeneous water mass in the inner part of the fjord. The brackish surface layer is heavily influenced by the freshwater input from the meltwater rivers and occupies the upper 50-75 m in August (Figure 34c and Figure 34d). The deep-lying water mass is barely subject to any renewal in summer. The reason for this is twofold: 1) no strong wind mixing is observed that causes the deep-lying water mass to be effectively sheltered from the atmospheric conditions (Nielsen et al., 2010), and 2) the coastal water flowing through the fjord is significantly modified before it reaches the inner part of the fjord, which results in a density smaller than the density of the deep-lying water mass (D Monteban et al., 2020). Moreover, this causes the deep-lying water mass to be almost dynamically decoupled from the open ocean during summer. In wintertime, slow renewal of the deep-lying water mass takes place, which was found by a tracer investigation in Monteban et al. (2020b) (see Appendix F).

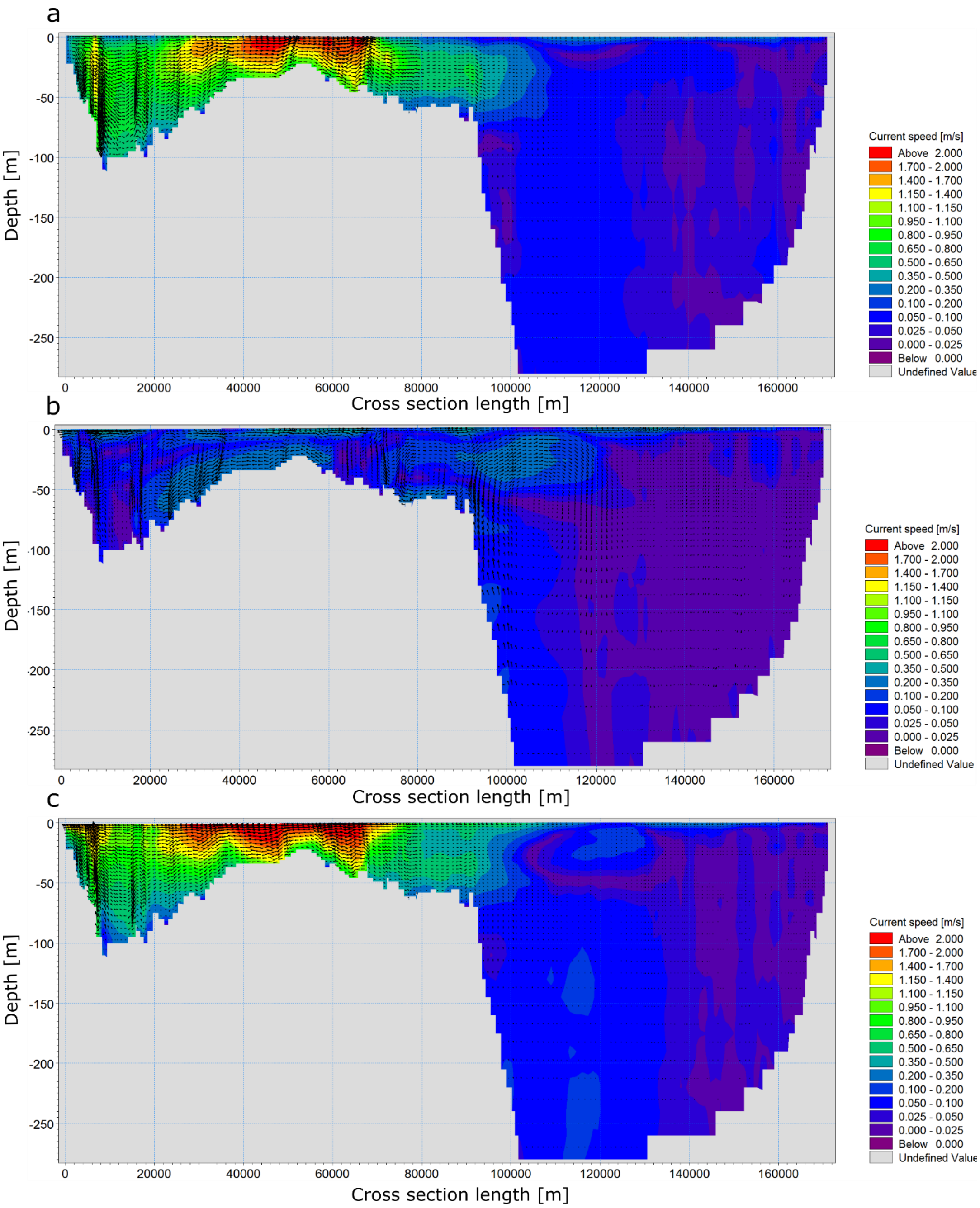

Figure 32. Cross sections of the instantaneous current speed along the fjord. The start and end points of the cross section are indicated in Figure 28 with the points IP1 and IP2, respectively. Subfigure (a) is given at flood tide, (b) at slack tide and (c) at ebb tide for a tidal cycle in August 2005. These tidal phases are defined at cross section length 60000 m.

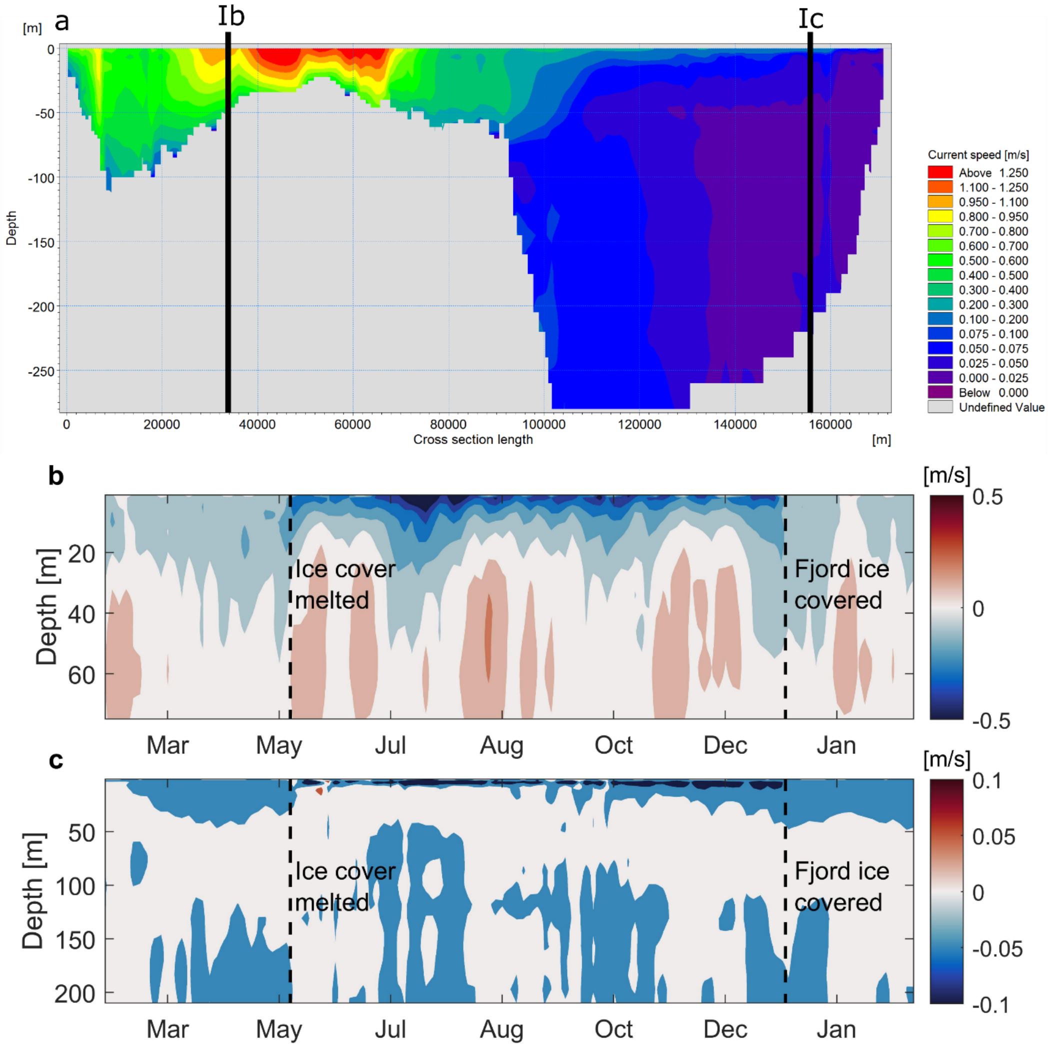

Figure 33. (a) Time-averaged current speed for August 2005 in along fjord direction. The start and end of the cross section are indicated in Figure 28 with the points IP1 and IP2, respectively. Subfigures (b) and (c) show the temporal variability of the current speed of the vertical profiles indicated in subfigure (a) by lines Ib and Ic, respectively. In subfigures (b) and (c), a positive value indicates a flow directed into the fjord. The figure is taken from Monteban et al. (2020b).

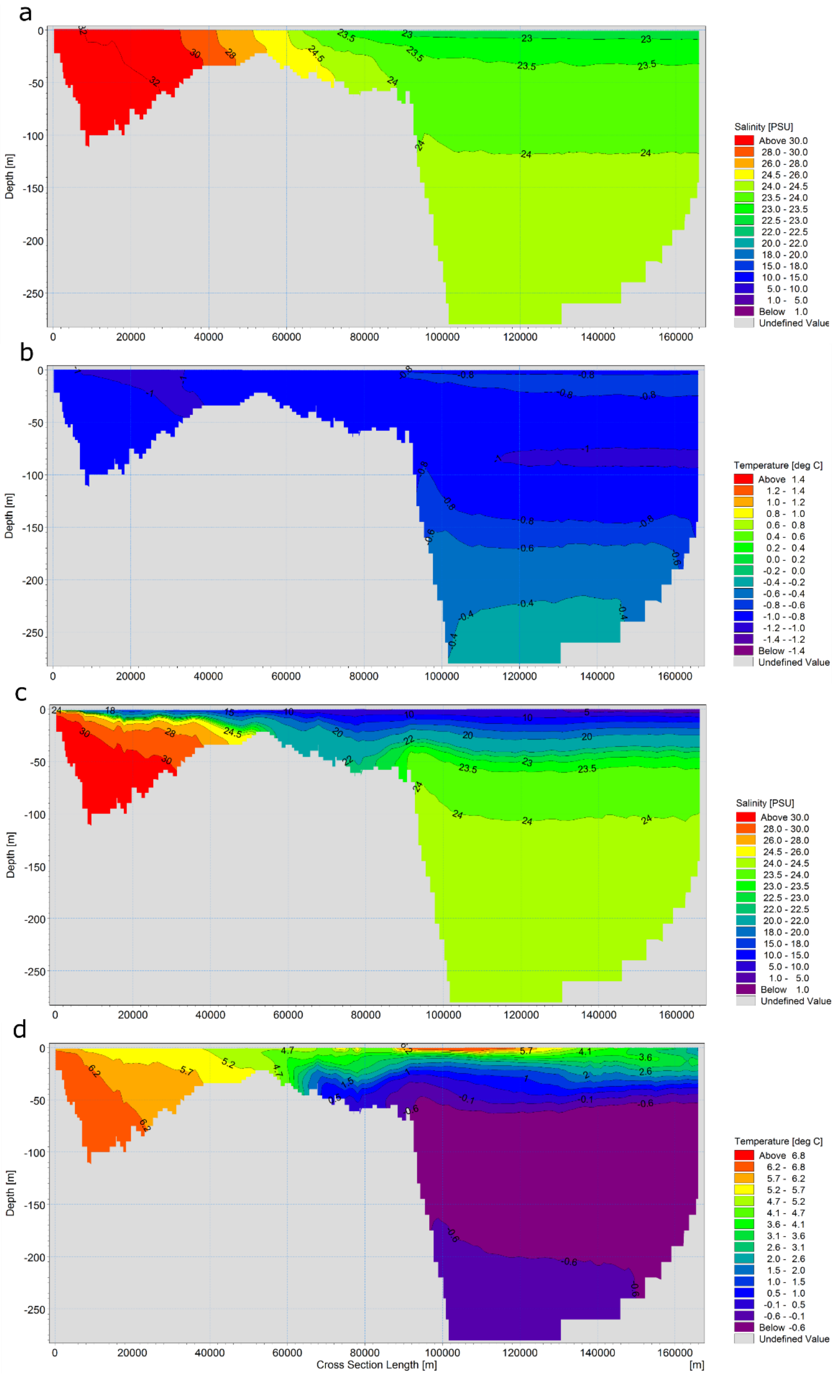

Figure 34. Vertical cross sections along the fjord. Subfigures (a) and (b) show the along fjord distributions of the temperature and salinity on 01 April 2005. Subfigures (c) and (d) show the along fjord distributions of the temperature and salinity on 01 August 2005. The mouth of the fjord is located at 0 m, at the left side of the figure. This figure is taken from Monteban et al. (2020b).

Furthermore, a strong stratification is observed in summer with large vertical gradients in the top 80 m of the water column. Notable, the water mass present in the depth range of 20-70 m is much denser (± 1016 kg/m^3) than the surface layer (± 1005 kg/m^3), but less dense than the deep-lying water mass (± 1019 kg/m^3). The origin of this water mass becomes clear by looking at Figure 35, where the temporal variability of a vertical profile in the inner, deep part of the fjord of the temperature, salinity and density is presented. The water mass is formed during spring and early summer when the meltwater runoff is small.

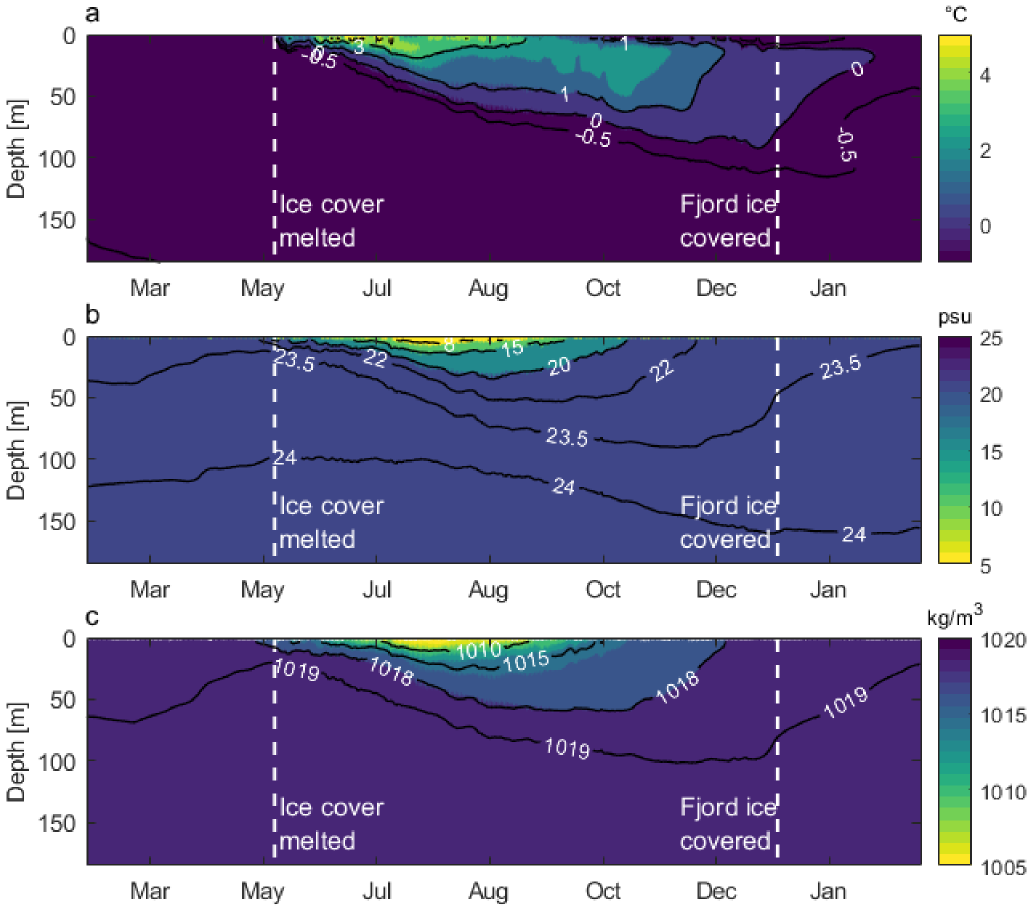

Figure 35. Temporal variability of a vertical profile at point c (Figure 28) of the temperature (a), salinity (b) and density (c). Subfigure (a) is taken from Monteban et al. (2020b).

On the contrary to the strong stratification observed during summertime, in wintertime, small vertical gradients are found with low temperatures and relatively high salinity in the inner part of the fjord (Figure 34a and Figure 34b). The temperature is close to the freezing point, which suggests that cooling and sea ice formation are dominant processes during wintertime. However, the MIKE 3 HD model lacks a sea ice module and therefore, processes such as ice formation, cooling, brine release and freshwater release during the melting of sea ice are not captured. This is the main drawback of using the model to investigate Arctic fjords.

4.4.3 Meltwater runoff sensitivity analysis

The fjord's response to changing meltwater forcing was investigated by performing three additional simulations. The three different simulations use either 50%, 200% or 400% of the meltwater discharge compared to the base case (discharge given in Section 4.2.4). The results are presented in Figure 36 for a point in the shallow, outer part of the fjord (point 1) and at a point in the inner, deep part of the fjord (point 3). At both locations, the deviation in temperature is only minor, with the variations between scenarios being less than 0.3 °C. On the other hand, different meltwater runoff forcing does have a substantial impact on the salinity, particularly in the inner part of the fjord. At point 3, the surface salinity increases by 1.8 psu for the 50% case, reduces by 2.3 psu for the 200% case and reduces by 5.5 psu for the 400% case. Beneath a depth of approximately 100 m, the effects are negligible for the 50% and 200% case, and only minor changes are observed for the 400% case (reduction of 0.5 psu and 0.2 psu at a depth of 150 m and 200 m, respectively). At point 1, the salinity changes over the entire water column and at the surface, an increase of 2.2 psu is found for the 50% case, and a reduction of 2.9 psu and 6.2 psu are observed for the 200% and 400% cases, respectively.

It was found by Lund-Hansen et al. (2010) that the freshwater entering the fjord from the meltwater rivers is the primary driver of variability in inorganic nutrients, optical conditions and primary production during summer. The meltwater rivers supply large amounts of sediments and nutrients into the fjord. Therefore, an increase in meltwater runoff will increase primary production as the availability of nutrients increases, and at the same time will decrease primary production as the increase in particles increases light attenuation. The net effect on the primary production and the ecosystems in the fjord can be investigated by including the ecological modelling module in MIKE 3, which would be very interesting for future work.

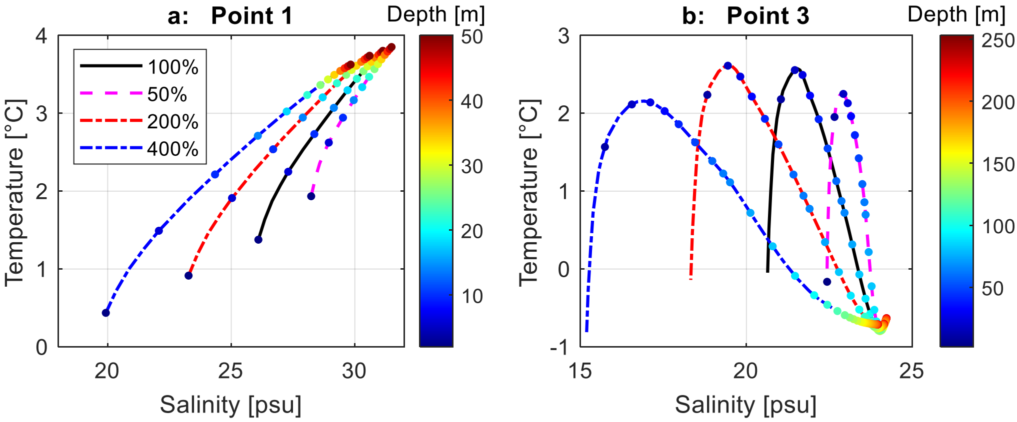

Figure 36. Temperature-salinity diagrams at point 1 and point 3 (for the locations see Figure 28) for the reference case (100%), the case with half the amount of meltwater (50%) and for the simulations with double (200%) or four times the amount of meltwater (400%). The vertical profiles are obtained on 1 November 2005. The colour-code of the dots indicate the depth.

4.4.4 50-year return period wave conditions

The MIKE 21 SW module was used to compute the 50-year return period significant wave height and peak wave period in the inner part of the fjord. These parameters can potentially be used for the design of a new harbour in the fjord.

The most severe waves are expected when the wind blows from the southwest direction as the fjord has the longest wave-generating fetch from this sector. Therefore, the 50-year return period wind speed is calculated for winds that come from the range between 215° to 240°, with respect to north. The annual maximum series is used, where the maximum value per year is extracted, and probability density functions are fitted to the data. The resulting non-exceedance probability plot is given in Figure 37. The best fit is obtained for the *Generalised Extreme Value* (GEV) distribution. From the fitted distribution, the 50-year return period is extracted and is 16.5 m/s.

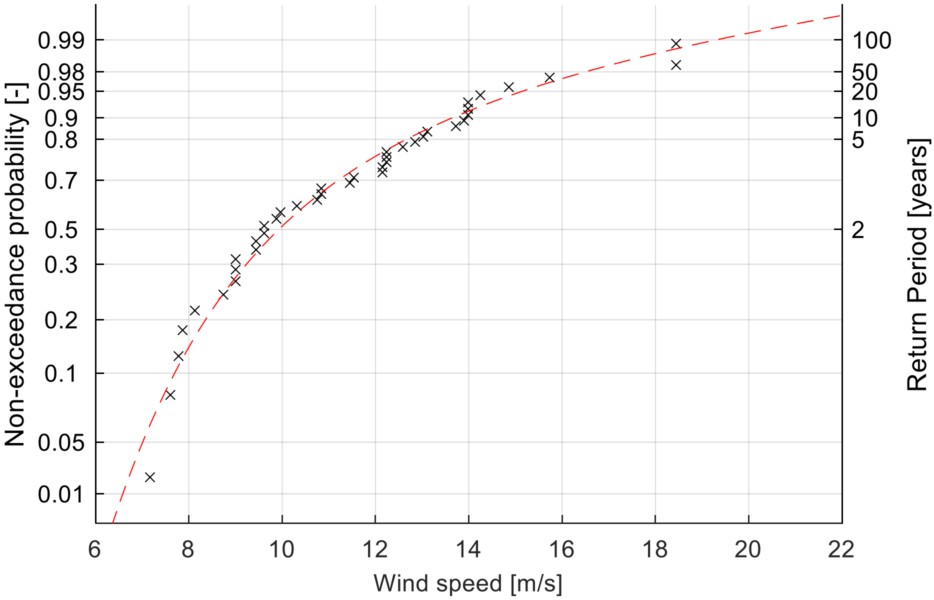

Figure 37. Non-exceedance probability plot of the annual maximum wind speeds coming from the southwest direction. The red line shows the fitted GEV distribution.

The 50-year significant wave height and peak wave period are computed by running the calibrated MIKE 21 SW model and forcing it with a constant wind speed of 16.5 m/s, coming from the southwest direction. A steady-state is reached after approximately four hours, and the spatial distribution of the steady-state significant wave height and peak wave period are presented in Figure 38 and Figure 39, respectively. The maximum value reached in the fjord is 1.8 m, close to the Watson River. The corresponding peak wave period is 5 s. More details regarding the location of the new proposed harbour and the extracted design conditions at this specific location can be found in Monteban et al. (2018), given in Appendix E.

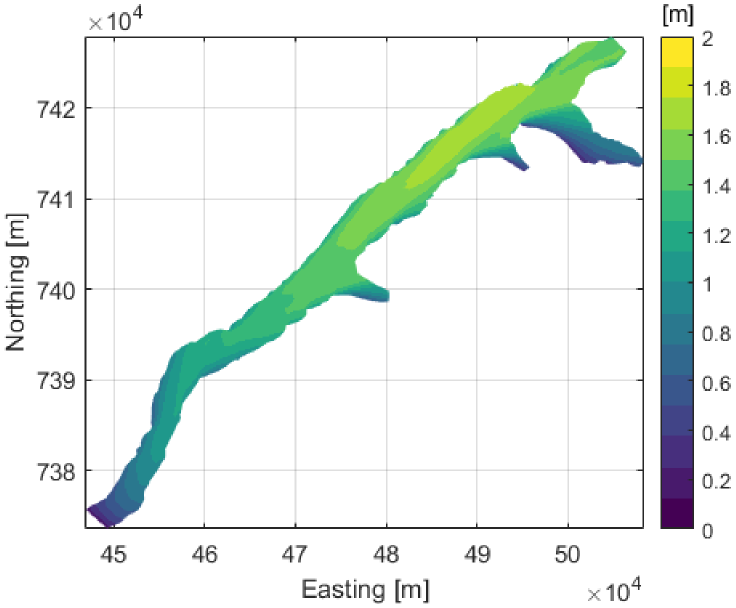

Figure 38. Spatial distribution of the significant wave height after 4-hour simulation time. The projection is given in UTM-22.

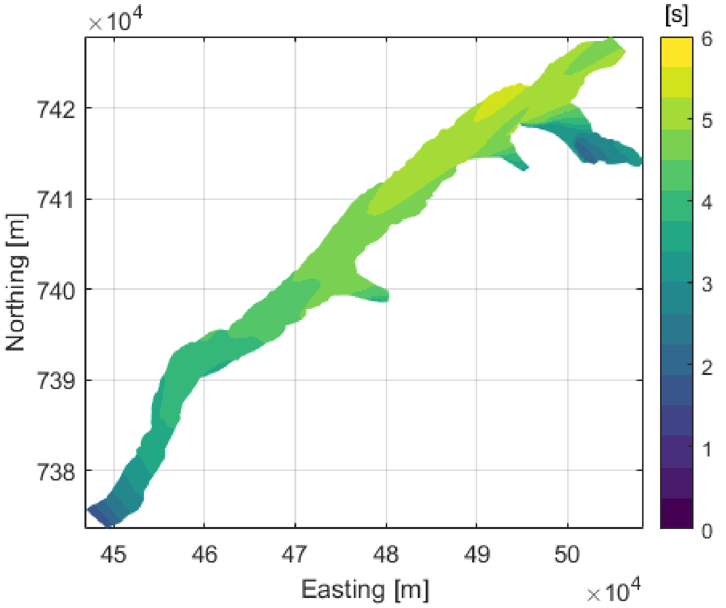

Figure 39. Spatial distribution of the peak wave period after 4-hour simulation time. The projection is given in UTM-22.

5 Iceberg drift modelling in the Barents Sea

As previously stated, the main objective of this thesis was to quantify the Arctic's physical environment through measurements and numerical modelling. So far, satellite remote sensing observations were used to study wave propagation through icy waters, and numerical modelling in combination with in-situ measurements were utilised to describe the physical oceanographic environment of the Arctic fjord Kangerlussuaq. In this chapter, both numerical modelling and satellite remote sensing observations are utilised to study another important aspect of the Arctic environment: iceberg conditions in the Barents Sea. This chapter is a summary of the paper by Monteban et al. (2020a), given in Appendix G.

Offshore developments and operations by the petroleum industry have moved further north into Arctic waters, which introduces new challenges in designing safe offshore structures and planning marine operations due to the potential presence of glacial ice. The objective of this chapter is to obtain the annual probability of iceberg occurrence in the Barents Sea, by using a numerical iceberg drift and deterioration model. The numerical model is taken from the literature (Eik, 2009; Keghouche et al., 2010; Wagner et al., 2017a). Moreover, it is a combination of the proposed models by the aforementioned references, and the model is described in Section 5.1.

One of the largest uncertainties in obtaining the probability of iceberg occurrence in the Barents Sea is the seeding of icebergs into the model. The characteristics of icebergs released at the sources include: 1) the number of icebergs released per year that drift freely into the Barents Sea and 2) their initial size distributions. Satellite remote sensing data were used to provide information on these two input parameters at the iceberg sources, which is described in Section 5.2. Finally, in Section 5.3, the numerical model is forced with the newly obtained data of the iceberg seeding to produce maps of the annual encounter frequency and the expected annual number of icebergs in the Barents Sea.

5.1 Numerical model of iceberg drift and deterioration

In this section, the numerical iceberg drift and deterioration model is described including the equations, the meteorological input data and all the other input parameters.

5.1.1 Equations

The used iceberg drift model is a combination of the models by Eik (2009), Keghouche et al. (2010) and Wagner et al. (2017a). Unless stated otherwise, the drift and deterioration equations presented here are taken from these studies.

The basic equation for the iceberg drift motion is Newton's second law and is given by (e.g., Kubat et al. (2005):

$$m\,(1 + C_m)\frac{d\boldsymbol{V}_i}{dt} = \boldsymbol{F}_a + \boldsymbol{F}_w + \boldsymbol{F}_{wd} + \boldsymbol{F}_c + \boldsymbol{F}_p + \boldsymbol{F}_{si} \tag{16}$$

with C_m the added mass coefficient; *m* is the iceberg mass; $\boldsymbol{V}_i$ is the iceberg velocity; *t* is the time; $\boldsymbol{F}_a$ is the air form drag; $\boldsymbol{F}_w$ is the current form drag; $\boldsymbol{F}_{wd}$ is the force due to the wave radiation stress; $\boldsymbol{F}_c$ is the Coriolis force; $\boldsymbol{F}_p$ is the pressure gradient force and $\boldsymbol{F}_{si}$ is forcing from the sea ice adjacent to the icebergs.

The force due to the wind is expressed as:

$$\boldsymbol{F}_a = \frac{1}{2}\,\rho_a\,C_a\,A_a\,|\boldsymbol{V}_a - \boldsymbol{V}_i|(\boldsymbol{V}_a - \boldsymbol{V}_i) \tag{17}$$

where ρ_a is the air density; C_a is the air form drag coefficient; A_a is the cross-sectional area on which the wind acts and $\boldsymbol{V}_a$ is the wind velocity. The forces due to the currents are given by:

$$\boldsymbol{F}_w = \frac{1}{2}\,\rho_w\,C_w\,A_w\,|\boldsymbol{V}_w - \boldsymbol{V}_i|(\boldsymbol{V}_w - \boldsymbol{V}_i) \tag{18}$$

with ρ_w the seawater density; C_w is the current form drag coefficient; A_w is the cross-sectional area on which the current velocity acts and $\boldsymbol{V}_w$ is the current speed. The cross-sectional areas A_w and A_a are defined as:

$$A_w = \frac{\rho_i}{\rho_w}\,\frac{2}{\pi}\,(L_i + W_i)\,H_i \tag{19}$$

$$A_a = \frac{\rho_w - \rho_i}{\rho_i}\,A_w \tag{20}$$

where ρ_i is the glacial ice density; L_i is the length of the iceberg, W_i is the iceberg width and H_i is the total height (draft + sail) of the iceberg.

The effects of the wave radiation stress force, $\boldsymbol{F}_{wd}$, on the icebergs are implicitly included in the wind drag coefficient (C_a). This coefficient is taken from the study by Keghouche et al. (2009). In their study, they calibrated the air and current drag coefficients against measurements of iceberg drift tracks in the Barents Sea, without using an explicit term of the wave radiation stress force. Moreover, they used in their calibration an added mass coefficient of 0, which was, therefore, also adopted in this study.

Further, the Coriolis force term reads:

$$\boldsymbol{F}_{cor} = -m\,\boldsymbol{f} \times \boldsymbol{V}_i \tag{21}$$

with the Coriolis parameters, $\boldsymbol{f}$, defined as:

$$\boldsymbol{f} = 1.45 \cdot 10^{-4}\,\sin(\varphi)\,\mathbf{k} \tag{22}$$

where φ is the geographic latitude position and $\mathbf{k}$ is the unit vector in the vertical direction. The pressure gradient force, $\boldsymbol{F}_p$, is approximated by the geostrophic current as done in many other studies (Gladstone et al., 2001; Wagner et al., 2017a) and this term reads:

$$\boldsymbol{F}_p = m\,\boldsymbol{f} \times \boldsymbol{V}_g \tag{23}$$

with $\boldsymbol{V}_g$ the geostrophic current taken from Slagstad et al. (1990). The forces due to the adjacent sea ice can be written as:

$$\begin{aligned} \boldsymbol{F}_{si} &= 0 && : C_i \leq 0.15 \\ \boldsymbol{F}_{si} &= \frac{1}{2}\,\rho_{si}\,C_{si}\,A_{si}\,|\boldsymbol{V}_{si} - \boldsymbol{V}_i|(\boldsymbol{V}_{si} - \boldsymbol{V}_i) && : 0.15 < C_i < 0.9 \\ \boldsymbol{F}_{si} &= -(\boldsymbol{F}_a + \boldsymbol{F}_w + \boldsymbol{F}_{cor} + \boldsymbol{F}_p) && : C_i \geq 0.9 \;\&\; \text{h} > h_{min} \end{aligned} \tag{24}$$

where C_i is the sea ice concentration; ρ_{si} is the sea ice density; C_{si} is the sea ice drag coefficient; $\boldsymbol{V}_{si}$ is the sea ice drift velocity; *h* is the sea ice thickness; h_{min} is the minimum sea ice thickness required to lock an iceberg into the sea ice and A_{si} is the cross-sectional area on which the sea ice acts, which reads:

$$A_{si} = \frac{2}{\pi}\,(L_i + W_i)\,h \tag{25}$$

The minimum ice thickness, h_{min}, is defined as:

$$h_{min} = \frac{P}{P^{*}\,\exp\left(-20\,(1 - C_i)\right)} \tag{26}$$

where *P* and P^{*} are the sea ice strength and sea ice coefficient, respectively.

It is assumed that the deterioration of icebergs in the model is driven by the three dominant processes of bottom melt (M_b), wave erosion (M_e) and buoyant convection along the iceberg sidewalls (M_v). The formulations of these terms are taken from the study by Wagner et al. (2017a) and Gladstone et al. (2001). The melt terms have units of metres per second, and the deterioration rates of the iceberg length (L_i), iceberg width (W_i) and total height (H_i) are given by:

$$\frac{d(L_i)}{dt} = \frac{d(W_i)}{dt} = -(M_e + M_v) \tag{27}$$

$$\frac{d(H_i)}{dt} = -M_b \tag{28}$$

The wave erosion term reads:

$$M_e = \frac{1}{86400}\left(\left[\frac{1}{6}(\tilde{T}_o + 2)\right] S_s \left[\frac{1}{2}\left(1 + \cos(C_i^3\pi)\right)\right]\right) \tag{29}$$

where $\tilde{T}_o$ is the sea surface temperature and S_s is the sea state defined as:

$$S_s = \frac{3}{2}|\boldsymbol{V}_a - \boldsymbol{V}_w|^{1/2} + \frac{1}{10}|\boldsymbol{V}_a - \boldsymbol{V}_w| \tag{30}$$

The rate of the bottom melt is given by:

$$M_b = a_1|\boldsymbol{V}_i - \boldsymbol{V}_w|^{0.8}\,\frac{\tilde{T}_o - \tilde{T}}{L_i^{0.2}} \tag{31}$$

with $\tilde{T}$ the effective iceberg temperature and $a_1 = 8.7 \times 10^{-6}\ m^{-0.4}s^{-0.2}$. The melt rate due to the buoyant convection along the sidewalls that is caused by the contrast in temperature between the ocean and the iceberg is defined as:

$$M_v = b_1\tilde{T}_o + b_2{\tilde{T}_o}^{2} \tag{32}$$

where $b_1 = 8.8 \times 10^{-8}\ ms^{-1}{}^{\circ}C^{-1}$ and $b_2 = 1.5 \times 10^{-8}\ ms^{-1}{}^{\circ}C^{-2}$. The iceberg length and iceberg width melt at different rates than the total iceberg height and therefore capsizing of icebergs need to be included to assure hydrostatic stability. The icebergs capsize when the width to height ratio falls below a critical value ε_c (Wagner et al., 2017b) as shown in Eq. (33). This critical value is defined in Eq. (34).

$$\varepsilon \equiv \frac{W_i}{H_i} < \varepsilon_c \tag{33}$$

$$\varepsilon_c = \sqrt{6\frac{\rho_i}{\rho_w}\left(1 - \frac{\rho_i}{\rho_w}\right)} \tag{34}$$

MATLAB's (The MathWorks, Inc., Natick, MA, USA) built-in solver ODE15S is used with a timestep of 2 hours to compute the tracks of the icebergs, $\boldsymbol{x}_i(t)$. The simulation of an iceberg ends when the total iceberg height becomes less than 1 m, or when the iceberg leaves the computational domain, which is defined between 0° and 90° longitude and 65° to 85° latitude.

5.1.2 Meteorological data and input parameters

The following meteorological and sea ice data are required to force the iceberg drift and deterioration model: wind, waves, currents, water temperature, sea ice concentration, sea ice drift and sea ice thickness. The source and resolution of these data, in addition to the specification of the used bathymetry, are given in Table 3. Some of the data have a temporal resolution of 24 hours. For these data, the value is kept constant for the 12 timesteps per day (timestep of 2 hours used in the model).

Table 3. Specifications of the bathymetry, metocean and sea ice data used to force the iceberg drift and deterioration model (Monteban et al., 2020a).

Parameter	**Spatial resolution**	**Temporal resolution**	**Model/ product name**	**Reference**
Bathymetry	1' × 1'	-	IBCAO	Jakobsson et al. (2012)
Wind	0.25° × 0.25°	2 hours	ERA5	Copernicus Climate Change Service (C3S) (2017)
Waves	0.25° × 0.25°	2 hours	ERA5	Copernicus Climate Change Service (C3S) (2017)
Currents	25 km × 25 km	Daily	TOPAZ	Bertino et al. (2008)
Temperature	25 km × 25 km	Daily	TOPAZ	Bertino et al. (2008)
Sea ice concentration	25 km × 25 km	Daily	TOPAZ	Bertino et al. (2008)
Sea ice thickness	25 km × 25 km	Daily	TOPAZ	Bertino et al. (2008)
Sea ice drift	25 km × 25 km	Daily	TOPAZ	Bertino et al. (2008)

All the remaining constants and input parameters used in the model are summarised in Table 4, together with their source if applicable.

Table 4. Constants used in the iceberg drift and deterioration model (Monteban et al., 2020a).

Parameter	Description	Value	Reference
ρ_w	Water density	1027 [kg/m^3]	
ρ_i	Glacial ice density	850 [kg/m^3]	
ρ_a	Air density	1.225 [kg/m^3]	
ρ_{si}	Sea ice density	900 [kg/m^3]	
C_w	Water drag coefficient	0.25 [-]	Keghouche et al. (2009)
C_a	Air drag coefficient	0.7 [-]	
C_{si}	Sea ice drag coefficient	1.0 [-]	Eik (2009)
P	Sea ice strength	660.9 [N/m]	Eik (2009)
P^*	Sea ice coefficient	20,000 [N/m^2]	
$\tilde{T}$	The effective iceberg temperature	-4 °C	Wagner et al. (2017a)

5.2 Iceberg release at the sources

The five main iceberg sources in the Barents Sea are: *Franz Josef Land* (FJL) East, FJL West, Edgeøya and Austfonna located at eastern Svalbard, and Novaya Zemlya, see Figure 40. FJL has 2600 km of tidewater ice cliffs (Løset et al., 2006) and is the most dominant source of icebergs. The secondary source of icebergs in the Barents Sea is the Svalbard archipelago, which has nearly 1030 km of tidewater ice cliffs (Dowdeswell, 1989). Icebergs are most frequently released in late summer and autumn (Løset, 1993), from approximately 1 July to 30 November (Kubyshkin et al., 2006). Moreover, this is also the period when icebergs are seeded into the numerical model and when the maximum iceberg extension occurs (Abramov, 1992).

Up till now, there is no estimate available in the literature on the annual number of icebergs that calve from glaciers and drift freely into the Barents Sea. Furthermore, information on the iceberg size characteristics in the Barents Sea is sparse. The most extensive iceberg campaign to date that focussed on the Barents Sea is the *Ice Data Acquisition Programme* (IDAP), which is the successor of the acquisition programme ICEBASE. Although IDAP provides valuable information regarding the iceberg size characteristics, it has some drawbacks for using it in numerical iceberg drift models. The observations of the icebergs were made in the vicinity of Svalbard and are, therefore (most likely) not valid for the other iceberg sources. In addition, the observations were generally not close to the iceberg producing glaciers, and because stereo photography was used from a plane, the observations are most likely biased towards larger icebergs.

It was shown by Monteban et al. (2020a) (Appendix G) that it is vital to have reliable data on the annual number of icebergs released at the sources and their initial size characteristics because the model output (expected number of icebergs) is approximately linearly dependent on both these input parameters.

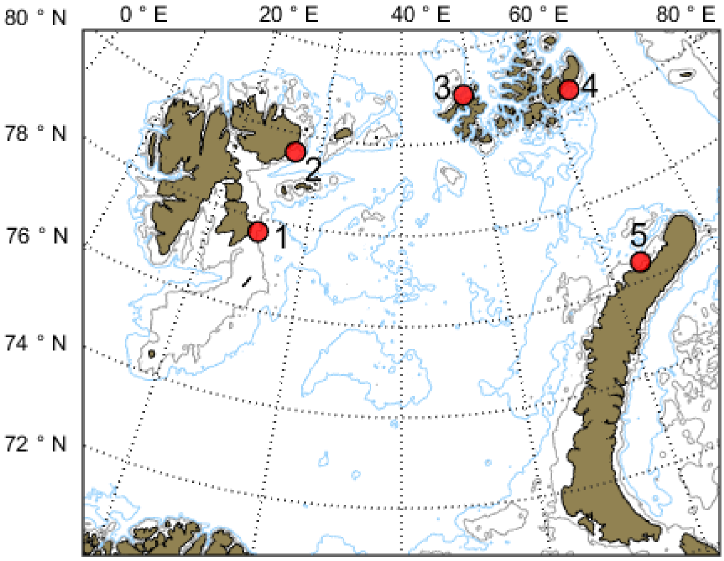

Figure 40. Locations of the five major iceberg sources in the Barents Sea: 1) Edgeøya, 2) Austfonna, 3) FJL West, 4) FJL East and 5) Novaya Zemlya. The grey and light blue contour lines are the isobaths at 100 and 200 m, respectively. The contour lines are based on bathymetry data taken from the International Bathymetry Chart of the Arctic Ocean (Jakobsson et al., 2012).

5.2.1 Iceberg size characteristics

The length and width of icebergs that calved from the glaciers at the five major sources in the Barents Sea were investigated using S2 optical imagery. Multiple images were collected for each source, and the images were manually processed using the QGIS software (QGIS Development Team, 2019). The major advantage of manual processing is that it leads to very accurate results, and for this study it was feasible as only a limited number of glaciers were studied. The studied locations are shown in Figure 41. For the two sources located at Svalbard (Austfonna and Edgeøya), only one major glacier is present, while for the other sources (FJL West, FJL East and Novaya Zemlya) two locations were identified as they contain multiple calving glaciers.

Icebergs larger than 30 m (3 pixels in the S2 images) were identified, and polygons were manually drawn around them. Next, a minimum box was fitted around each polygon with the QGIS built-in function “oriented minimum box” that is based on the rotating callipers algorithm (Toussaint, 1983). The iceberg length is defined as the longer side of the fitted minimum box. The width is then the shorter side of the box. An example of the processing is shown in Figure 42, and for more details on the selection of the S2 images, the reader is referred to Appendix G.

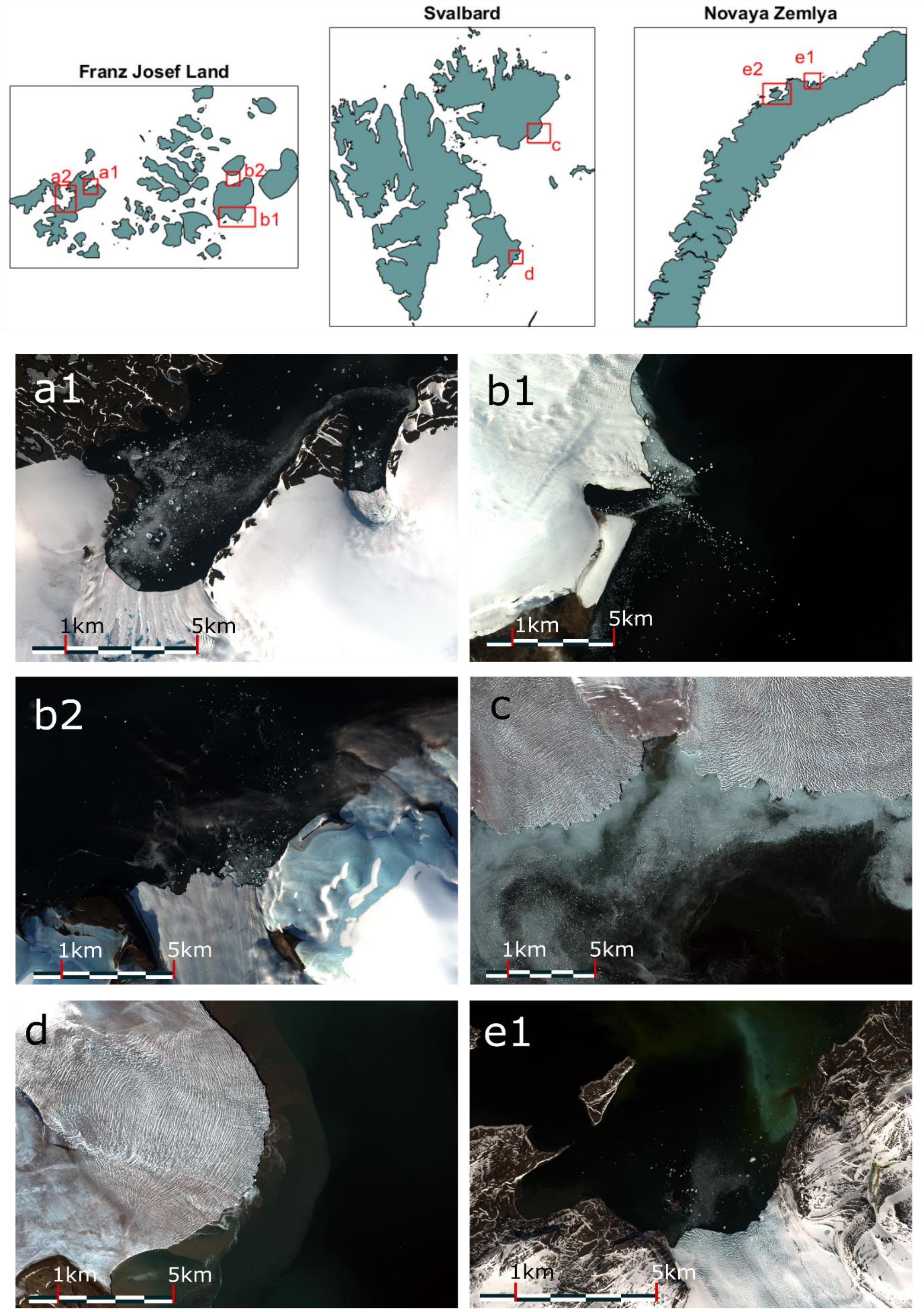

Figure 41. S2 images of the studied glaciers at the five major iceberg sources (Monteban et al., 2020a).

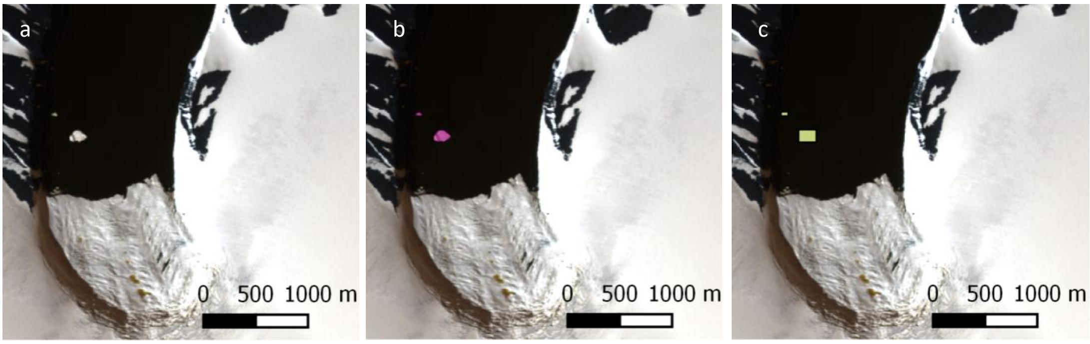

Figure 42. Example of the manual processing of the S2 optical images. (a) A glacier at the West side of FJL on 10 July 2016. (b) The icebergs are manually identified, and polygons are manually drawn around them. (c) A minimum box is fitted around the polygons from which the iceberg length (longest side of the box) and iceberg width (smallest side of the box) are obtained.

The number of identified icebergs for each source separately, in addition to the mean and maximum values of the iceberg length and iceberg width are presented in Table 5. Furthermore, the 3-parameter GEV distribution was found to be the best fit to the data and the fitted parameters for each iceberg source are also given in Table 5. In Figure 43, the fitted GEV distributions of the iceberg length at each iceberg source are shown. A satisfactory fit is obtained at all the different sources.

Table 5. The number of identified icebergs at the different iceberg sources, including the mean and maximum iceberg length and iceberg width. In addition, the values of the fitted GEV distribution (location μ, scale σ and shape k) for the iceberg length and iceberg width are given. This table is taken from Monteban et al. (2020a).

Geographical area	Number of icebergs	Iceberg length [m] (mean, max)	Iceberg width [m] (mean, max)	Iceberg length			Iceberg width		
				μ	σ	k	μ	σ	k
FJL East	3168	(61, 560)	(46, 215)	45.0	14.2	0.40	34.5	10.9	0.27
FJL West	6252	(62, 1016)	(45, 293)	46.5	15.6	0.25	36.1	11.4	0.20
Austfonna	7900	(52, 240)	(38, 147)	44.5	10.7	0.12	32.9	7.88	0.04
Edgeøya	785	(40, 121)	(30, 73)	34.6	5.86	0.22	27.3	4.86	0.02
Novaya Zemlya	4213	(50, 254)	(37, 148)	39.9	12.1	0.18	31.1	8.41	0.12
Total	22,318	(55, 1016)	(41, 293)						

The obtained iceberg lengths are plotted versus the iceberg widths in Figure 44 for the approximately 22,000 identified icebergs. In addition, an empirical relationship between the iceberg lengths and iceberg widths, taken from Dezecot and Eik (2015) and given in Eq. (35), is plotted. This relationship was found to fit the newly obtained data very well and, therefore, no new empirical formula was proposed. However, for the icebergs with a length larger than approximately 400 m, the empirical relationship predicts larger iceberg widths than found from the S2 images. It was however not found necessary to adjust the empirical relationship to capture these long, elongated icebergs. The reason for this is that these icebergs will most likely break up due to wave actions when they drift into more open water.

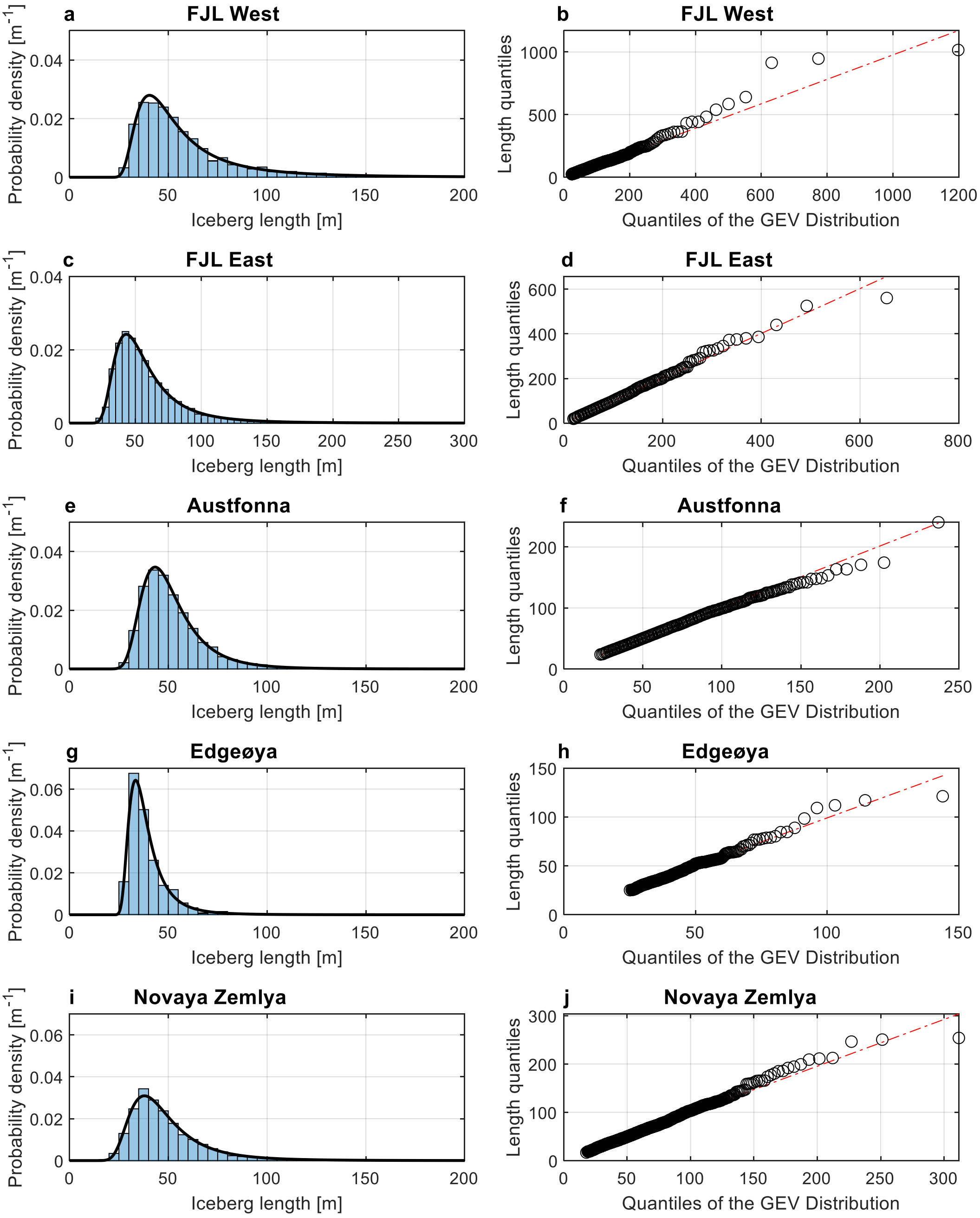

Figure 43. Distributions of the iceberg length at the five major iceberg sources shown in subfigures (a), (c), (e), (g), and (i), together with the fitted GEV distributions, indicated by the thick black lines. Also, the corresponding Q-Q plots comparing the iceberg length data with the fitted GEV distributions are provided in subfigures (b), (d), (f), (h) and (j).

Furthermore, Dezecot and Eik (2015) also provided an empirical relationship between the total heights (draft + sail) of icebergs and the iceberg lengths, which is presented in Eq. (36).

$$W_i = 0.7\, L_i\, exp(-0.00062\, L_i) \tag{35}$$

$$H_i = 0.3\, L_i\, exp(-0.00062\, L_i) \tag{36}$$

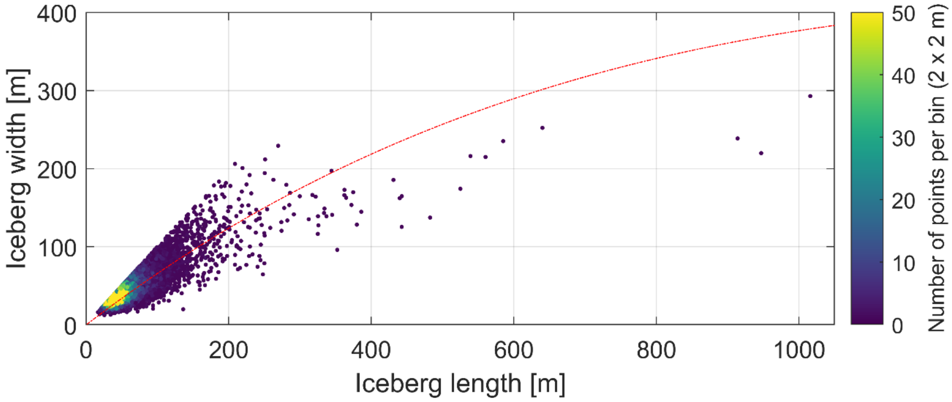

Figure 44. Scatter plot of the iceberg width versus the iceberg length of all the identified icebergs combined. The colour code indicates the number of data points within 2 × 2 m bins. In addition, the red line shows the empirical relationship provided in Eq. (35). This figure is taken from Monteban et al. (2020a).

The exceedance plot of the five iceberg sources is shown in Figure 45. This plot shows that the largest icebergs originate from the West side of FJL and the smallest icebergs come from Edgeøya. To compare, the iceberg length corresponding to a recurrence interval of 200 is 108 m for Edgeøya, 119 m for Austfonna, 159 m for Novaya Zemlya, 228 m for FJL East and 336 m for FJL West.

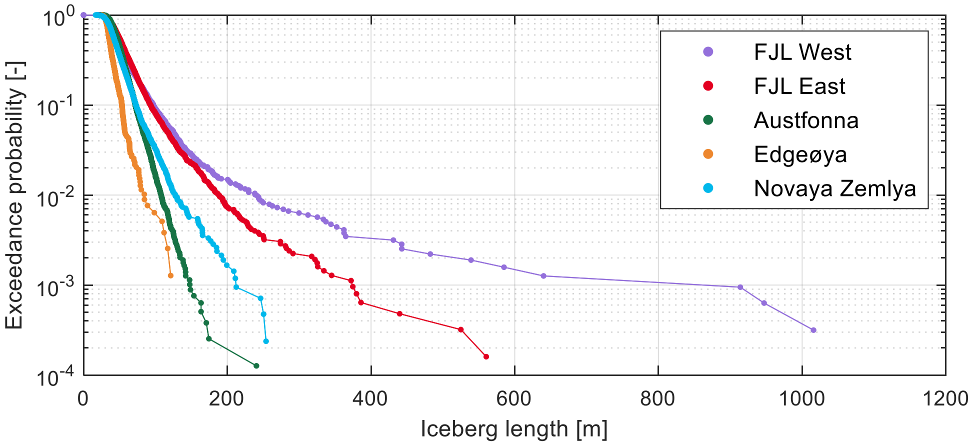

Figure 45. Exceedance probability of the iceberg length at the five major iceberg sources (Monteban et al., 2020a).

5.2.2 Number of icebergs released

No direct measurements of the number of icebergs released into the Barents Sea are available in the literature. One way to estimate this number is through the calving flux, q, that indicates the discharge volume per year. These calving fluxes were estimated by Keghouche et al. (2010) and are given in Table 6. Dividing the calving flux by the mean volume of the calved icebergs results in the number of calved icebergs. Keghouche et al. (2010) followed this approach by taking the mean iceberg volume from the IDAP campaign and found the number of released icebergs to be approximately 20,000. However, many of these icebergs will be bergy bits and growlers that will melt before reaching the southern part of the Barents Sea. Additionally, a portion of the icebergs will ground and melt close to the glacier and will never reach the open sea. This was accounted for in this study by assuming a percentage variable, P_{er}, which is the percentage of the total calved volume that turns into icebergs and drift freely into the Barents Sea. The number of icebergs that drift freely into the Barents Sea, $N_{Barents}$, is then estimated by:

$$N_{Barents} = P_{er} \frac{q}{(L_{mean}\, W_{mean}\, H_{mean})} \tag{37}$$

where L_{mean}, W_{mean}, and H_{mean} are the mean iceberg length, width and total height (draft + sail), respectively. Hansen et al. (2019) calibrated their iceberg drift model against the Abramov atlas (Abramov and Tunik, 1996), with the mean size characteristics taken from IDAP, and found a percentage P_{er} of 3%. However, as also mentioned by Hansen et al. (2019), the Abramov atlas has multiple sources of uncertainty, and the key problem is that its statistics cannot be taken as fully representative. This is because many icebergs were not detected, and it is unclear how this atlas accounted for this phenomenon. This shortcoming was overcome here by using satellite remote sensing data from the EU CMEMS Arctic Ocean – SAR sea iceberg concentration product (CMEMS, 2019), see Section 2.3.4. Data for 2016 and 2017 were used, and these observations are solely based on S1 measurements.

Table 6. Calving flux at the five major iceberg sources in the Barents Sea (Keghouche et al., 2010).

Geographical area	Calving location	Discharge rate (km^3 yr^{-1})
FJL East	80.5°N, 62.8°E	2.64
FJL West	81.0°N, 48.7°E	1.76
Austfonna	79.6°N, 27.0°E	2.7
Edgeøya	77.7°N, 25.0°E	0.6
Novaya Zemlya	76.4°N, 63.0°E	1.0

A major difficulty associated with the Copernicus iceberg number density dataset is the counting of duplicate icebergs. Data are provided with a temporal resolution of one day, but using all the data of subsequent days will result in double-counting of icebergs. Therefore, a time interval between the data is sought that is long enough to minimise duplicate icebergs and, at the same time, is short enough to minimise omitting icebergs. This time interval was estimated using two different methods. The first one was to compute the average residence time of icebergs in a grid cell of 100 km × 100 km using our numerical iceberg drift model. For the second method, the relation between the obtained number of icebergs and the time interval was studied. Both the methods resulted in a time interval of approximately six days (see Appendix G for the details).

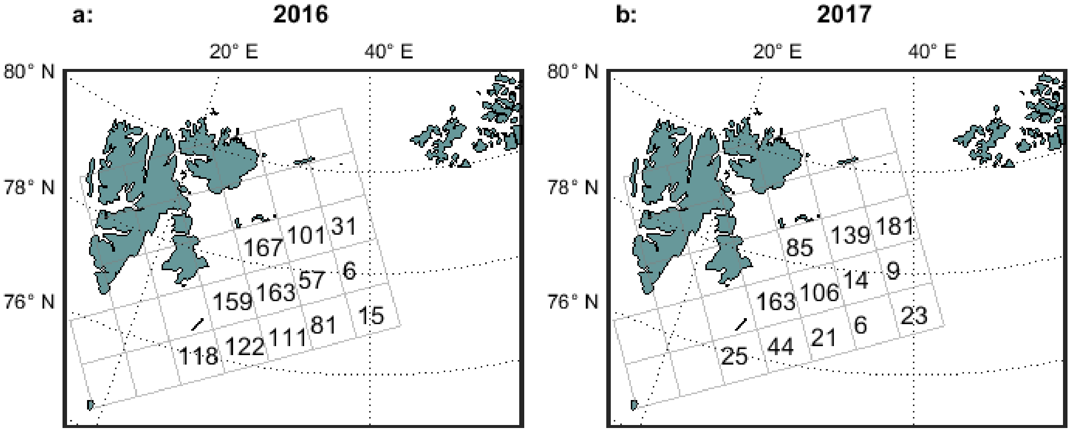

Figure 46. The iceberg number density for grid cells of size 100 km × 100 km for 2016 and 2017 for the period 01 July until 30 November. The time interval between the data is six days. This figure is taken from Monteban et al. (2020a).

The resulting number of icebergs for the period 1 July until 30 November using a 6-day time interval is presented in Figure 46. Grid cells that are close to land and include shallow areas are omitted because these areas will include many grounded icebergs that will be counted more than once, making the obtained values in those grid cells unreliable.

The percentage, P_{er}, was found by running the model and comparing the output with the Copernicus iceberg number density map (Figure 46). For the model simulations, the newly obtained size characteristics of the iceberg width and iceberg length (Table 5) were used, and the total height was computed from Eq. (36). The results for three percentages are shown in Figure 47. A direct comparison of the numbers in the cells was complicated as there are natural variations (model is partly probabilistic) when repeating a simulation. This is because the initial iceberg length is drawn from the fitted GEV distributions (Figure 43) and the icebergs are randomly released following a uniform distribution from 1 July till 30 November. Therefore, the focus was on the 50- and 200-iceberg contour lines. The best results were obtained for a percentage, P_{er}, of 1%, which equals 2600 icebergs released per year that drift freely into the Barents Sea. For this percentage, shown in Figure 47c and Figure 47d, the 200 contour line lies above the grid cells that have values between 100-180 icebergs. Moreover, the 50-contour line lies directly beneath these grid cells.

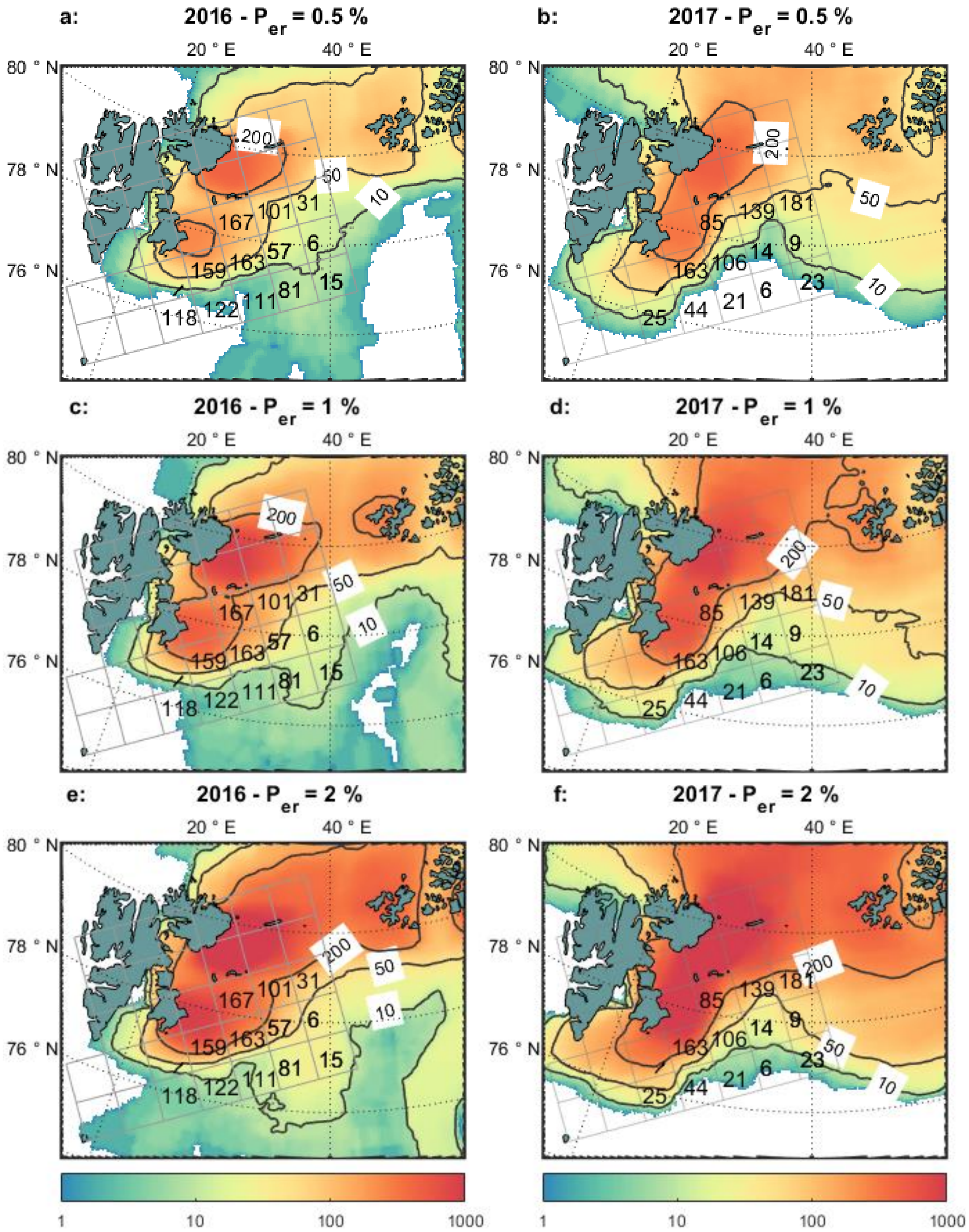

Figure 47. Results of the model simulation for the percentages, P_{er}, of 0.5% (a and b), 1% (c and d) and 2% (e and f). The coloured area indicates the computed number of icebergs. The overlaid grid indicates the number of icebergs found from the Copernicus iceberg number density product.

5.3 Iceberg occurrence in the Barents Sea

Finally, the numerical model described in Section 5.1 was used to compute the annual probability of iceberg occurrence (Figure 48) and the expected annual number of icebergs in the Barents Sea (Figure 49). The following specifications were used for the model simulation:

- The simulation extended a 27-year period (1991-2017) for which the metocean input data were available.
- Icebergs are randomly released from the five major sources in the Barents Sea (Figure 40) from 1 July to 30 November following a uniform distribution.
- Polygons are specified at the five major iceberg sources, and the icebergs are generated randomly within these polygons. See Lu et al. (2020) for the exact locations.
- The number of icebergs released from each source is computed from Eq. (37), using the calving fluxes from Table 6, the mean values of the iceberg width and iceberg length from Table 5, the mean total iceberg height computed from Eq. (36) and the estimated percentage value, P_{er}, of 1%.
- The initial length of an iceberg is drawn from the fitted GEV distributions shown in Figure 43 (values given in Table 5) for each source separately. The initial iceberg width and total height are computed from Eq. (35) and Eq. (36), respectively.

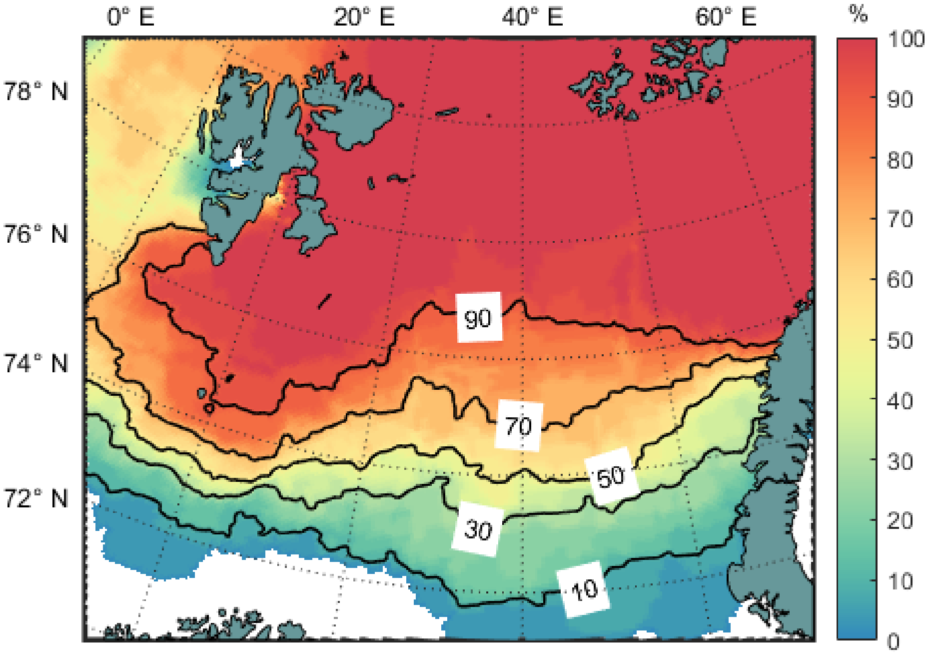

Figure 48. The annual probability of iceberg occurrence in the Barents Sea (Monteban et al., 2020a). The map is computed for icebergs entering a box of 100 km × 100 km.

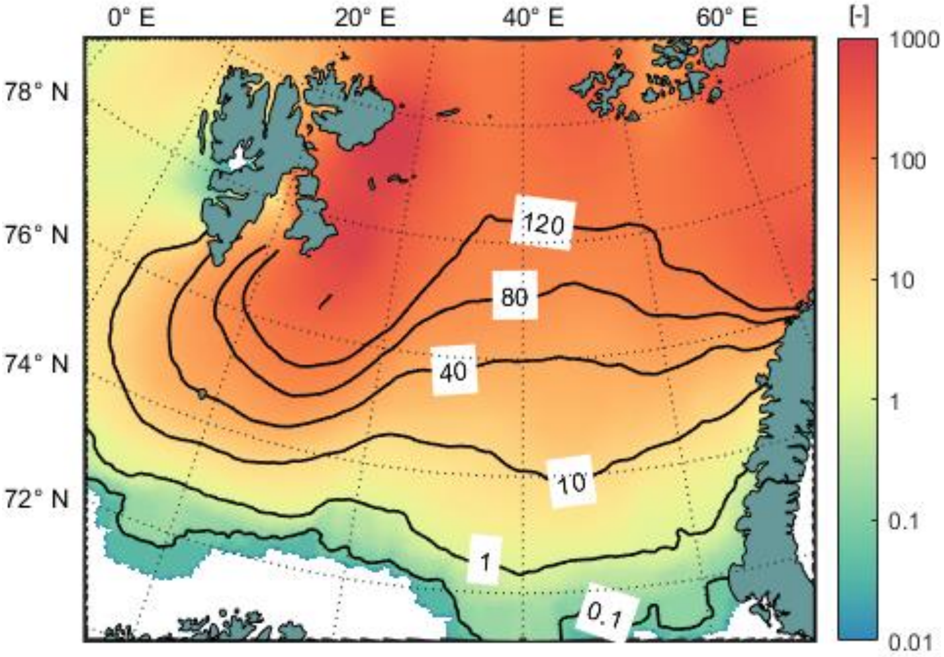

Figure 49. The expected annual number of icebergs in the Barents Sea (Monteban et al., 2020a). The map is computed for icebergs entering a box of 100 km × 100 km.

6 Conclusions and recommendations

The main objective of this PhD was to obtain a better understanding of the Arctic's physical environment through in-situ measured data, remote sensing techniques and numerical modelling. Many datasets are available of different Arctic properties that have proved to be essential to comprehend the ongoing changes in the Arctic due to, primarily, climate change. The most pronounced effects of the changing climate occur in the polar regions. Especially in the Arctic, which is warming much faster than the rest of the world. This has resulted in, among other things, a declining sea ice extent, thinning of sea ice and longer open water seasons. To predict the consequences of this Arctic transition, it is vital to have a thorough understanding of the physical environment of the Arctic. To this main objective, the PhD contributed to three particular Arctic phenomena/topics including:

1) Wave propagation through ice-covered oceans
2) The physical oceanographic environment of the Arctic fjord Kangerlussuaq
3) Iceberg drift modelling in the Barents Sea

The following conclusions are drawn corresponding to these studied topics:

1) Wave propagation through ice-covered oceans

- Satellite remote sensing data were used to study the propagation of waves within the sea ice. The primary focus was on how sea ice affects the waves. The Barents Sea was used as a study site as in-situ data were available here from the *Barents Sea Metocean and Ice Network* (BaSMIN) measurement programme. A literature review revealed that the most valuable remote sensing technique to study wave-ice interactions is *Synthetic Aperture Radar* (SAR) as this technique is mostly unaffected by clouds and does not require solar illumination. Furthermore, optical imagery provides high-resolution data. However, the polar regions are dark during winter and are often cloud-covered, which severely limits the amount of usable data from optical sensors. Altimetry data provides, amongst other things, information on the sea ice thickness and the significant wave height in the open water.
- SAR data were used to study the change in dominant wave direction, and peak wavelength as waves enter ice-covered waters. A shift in wave direction was found towards the normal, relative to the ice edge. This is partly due to refraction and due to an imaging artefact. The latter stems from the fact that the azimuth cutoff wavelength is much smaller within the sea ice than in the open ocean. This results in waves that were not visible in images over the open ocean to suddenly appear in images over the sea ice, which causes an apparent shift. Furthermore, a small increase in peak wavelength was observed that is due to the spatial dispersion of waves, and possibly enhanced by wave-ice interactions.
- A novel and innovative method was developed to derive the wave dispersion relation within sea ice from S1 data. The main advantages and results of this method are:
    - The method uses data from the spatial burst overlap area that is present due to the TOPSAR scanning technique of the S1 satellites. Using data from this area results in a larger time separation between subsequent images, which results in a higher-quality and less noisy imaginary spectrum in comparison to the spectra computed using data from the single-look area. This higher-quality imaginary spectrum allows for the derivation of the wave dispersion relation and, potentially, to determine the wave direction more accurately.
    - The modulation transfer function is not required as a linear ocean-to-SAR transform is assumed.

  - The availability of in-situ data of sea current speeds from the BaSMIN programme allowed the quantification of the influence of the currents on the wave dispersion relation, which is a significant improvement over previous studies as they lacked accompanying current data.
  - The derived wave dispersion relation within sea ice for long waves (peak wavelength within the range of 100-350 m and ice thickness less than 40 cm) is nearly identical to the theoretical open-water dispersion relation. This agrees with previous findings and provides confidence in the used assumption of a linear ocean-to-SAR regime for SAR images over the sea ice.
  - Presently, the spatial resolution of SAR data is too coarse to enable the study of the wave dispersion of short waves within the sea ice.

2) *The physical oceanographic environment of the Arctic fjord Kangerlussuaq*

- Two high-fidelity numerical models were set up using the commercially available MIKE software, including the MIKE 3 HD and the MIKE 21 SW models. These models were used to study the seasonal variations of the physical oceanographic conditions, the fjord's response to changing meltwater forcing and to estimate the 50-year return period wave parameters (significant wave height and peak wave period). Both the models were carefully calibrated against in-situ data.
- The tides in the inner part of the fjord are classified as semidiurnal, they have a tidal range of 3.5 m and they travel from the open ocean to the inner part of the fjord in approximately 3.5 hours.
- The across-fjord variations of the currents are minor as the fjord is too narrow to be significantly affected by the Earth's rotational dynamics. Therefore, the water flows primarily in along fjord direction. The current regime varies significantly between summertime and wintertime. During summer, there is a net outflow of freshwater in the surface layer, while in wintertime the vertical gradients in the current velocities are small. Furthermore, the currents are weak in the inner, deep part of the fjord as opposed to strong currents in the outer, shallow part. These strong currents are believed to be the cause of the absence of sea ice during wintertime in the outer part.
- Three different water masses are present in the summertime, including water from the West Greenland Current, a deep-lying homogeneous water mass and a freshwater influenced top layer. Additionally, a strong stratification is observed in the inner, deep part of the fjord. However, in the outer part, the strong tidal currents tend to break down stratification. In wintertime, the water mass in the inner, sea ice-covered part of the fjord is homogeneous.
- The water mass lying in the deep, inner part of the fjord below approximately 100 m is barely subject to renewal and appears dynamically decoupled from the open ocean in the summertime.
- A changing meltwater runoff forcing significantly influences the top 100 m of the water column in the inner, deep part of the fjord. In the outer part, the entire water column is affected.
- The estimated 50-year return period wave height and peak wave period are 1.8 m and 5 s, respectively. These values are observed at the end of the inner part of the fjord, close to the Watson River.
- A significant drawback of using the MIKE 3 HD model is the lack of a sea ice module. This prevents the model from taking essential processes such as cooling, brine release and freshwater release from sea ice melt into account.

3) *Iceberg drift modelling in the Barents Sea*

- A numerical iceberg drift and deterioration model was taken from the literature and was used to determine the iceberg occurrence in the Barents Sea.
- The output of the model (iceberg occurrence) is very sensitive towards two input parameters at the iceberg sources, which are 1) the annual number of icebergs released from the sources that drift

freely into the Barents Sea, and 2) the initial size characteristics of the released icebergs. However, there is no information available in the literature on the number of released icebergs, and the information on the iceberg size characteristics is sparse. Therefore, satellite remote sensing data were utilised to estimate these two input parameters.

- Sentinel-2 optical imagery was used to study the iceberg size characteristics of the five major iceberg sources in the Barents Sea, including Franz Josef Land West and East, Novaya Zemlya, Austfonna and Edgeøya. Over 22,000 icebergs were manually identified, and the most severe icebergs come from Franz Josef Land West, and the smallest icebergs originate from Edgeøya. For each of the five major iceberg sources, a generalised extreme value distribution was fitted to the data that were consequently used to sample the initial iceberg length of the icebergs seeded into the model. Furthermore, an empirical relationship between the lengths and widths of icebergs is provided.
- The annual number of icebergs released into the Barents Sea was estimated by comparing the output of the model with the Copernicus iceberg number density product. The best comparison was found for a percentage value of 1% of the total glacial calving flux of the five major iceberg sources in the Barents Sea. This corresponds to approximately 2600 icebergs released per year.
- A simulation extending 27 years was performed by forcing the model, among other things, with the newly obtained input data of the iceberg size characteristics and the annual number of released icebergs. This resulted in maps of the annual probability of iceberg occurrence and the annual expected number of icebergs in the Barents Sea.

Based on the work during this PhD study, it is evident that a comprehensive understanding of the Arctic physical environment is obtained only when combining data from different sources, i.e., in-situ measurements, remote-sensing techniques and numerical simulations, as they complement each other. Overall, it is therefore recommended to utilise and combine as many different data sources as possible. For the three studied topics, the following recommendations for future work are given:

1) *Wave propagation through ice-covered oceans*

- When higher resolution SAR data become available, the wave dispersion of short waves can most likely be derived using the newly developed method. Moreover, it is possible to back-calculate the ice thickness when accurate spatiotemporal information of short waves is retrieved.
- The new method using the spatial burst overlap area results in a higher-quality imaginary spectrum from which the wave direction can most likely be determined more accurately. It is recommended to investigate this further.

2) *The physical oceanographic environment of the Arctic fjord Kangerlussuaq*

- It is highly recommended to add a sea ice module to the MIKE 3 HD model. This will enable the model to take processes such as brine release, cooling and freshwater release into account, thereby making the model more suitable for studying sea ice-covered Arctic fjords.
- The net effect of changing meltwater runoff on the primary production in the fjord is unknown as an increasing meltwater runoff can either increase or decrease this production. Therefore, it is recommended to include the MIKE 3 ecological modelling module to investigate this net effect and hence, the impact on ecosystems.

3) *Iceberg drift modelling in the Barents Sea*

- The used Sentinel-2 images were manually processed to obtain iceberg size characteristics. For future studies, it is recommended to build an automated algorithm to detect icebergs. Much more images can then be processed, which will allow, for instance, the study of the seasonal dependency of iceberg sizes being calved from the glaciers.

- A methodology was presented to estimate the annual number of icebergs released from the sources as a percentage value from the total glacial flux. This percentage was assumed constant for all the iceberg sources. However, this percentage most likely differs from source to source, but it was not possible to get an estimate of each source separately due to the lack of sufficient validation data. It is recommended to estimate the number of icebergs released at each source separately when more satellite remote sensing data become available.
- It is recommended to quantify the accuracy and relative importance of the different forcing formulations. This can be done with the increasingly more satellite remote sensing data becoming available.
- Finally, it is recommended to study the effects of climate change on the iceberg occurrence in the Barents Sea. The numerical iceberg drift model used in this work appears a very suitable tool to do so.

7 Bibliography

Abramov, V., Tunik, A., 1996. Atlas of Arctic icebergs: The Greenland, Barents, East-Siberian and Chukchi Seas in the Arctic Basin, Backbone Publ. Co.

Abramov, V.A., 1992. Russian iceberg observations in the Barents Sea, 1933– 1990. Polar Res. 11, 93–97. https://doi.org/10.1111/j.1751-8369.1992.tb00415.x

Akbari, V., Lauknes, T.R., Rouyet, L., Negrel, J., Eltoft, T., 2018. Validation of SAR iceberg detection with ground-based radar and GPS measurements. Int. Geosci. Remote Sens. Symp. 2018-July, 4623–4626. https://doi.org/10.1109/IGARSS.2018.8517286

Alpers, W., Rufenach, C., 1979. The effect of orbital motions on synthetic aperture radar imagery of ocean waves. IEEE Trans. Antennas Propag. 27, 685–690. https://doi.org/10.1109/TAP.1979.1142163

Alpers, W.R., Ross, D.B., Rufenach, C.L., 1981. On the detectability of ocean surface waves by real and synthetic aperture radar. J. Geophys. Res. Ocean. 86, 6481–6498. https://doi.org/10.1029/JC086iC07p06481

AMAP, 2018. AMAP Assessment 2018: Arctic Ocean Acidification. Arctic Monitoring and Assessment Programme (AMAP). Tromsø, Norway.

Ardhuin, F., Collard, F., Chapron, B., Girard-Ardhuin, F., Guitton, G., Mouche, A., Stopa, J.E., 2015. Estimates of ocean wave heights and attenuation in sea ice using the SAR wave mode on Sentinel-1A. Geophys. Res. Lett. 42, 2317–2325. https://doi.org/10.1002/2014GL062940

Ardhuin, F., Stopa, J., Chapron, B., Collard, F., Smith, M., Thomson, J., Doble, M., Blomquist, B., Persson, O., Collins, C.O., Wadhams, P., 2017. Measuring ocean waves in sea ice using SAR imagery: A quasi-deterministic approach evaluated with Sentinel-1 and in situ data. Remote Sens. Environ. 189, 211–222. https://doi.org/10.1016/j.rse.2016.11.024

Armitage, T.W.K., Manucharyan, G.E., Petty, A.A., Kwok, R., Thompson, A.F., 2020. Enhanced eddy activity in the Beaufort Gyre in response to sea ice loss. Nat. Commun. 11, 761. https://doi.org/10.1038/s41467-020-14449-z

Bennetts, L.G., Alberello, A., Meylan, M.H., Cavaliere, C., Babanin, A. V., Toffoli, A., 2015. An idealised experimental model of ocean surface wave transmission by an ice floe. Ocean Model. 96, 85–92. https://doi.org/10.1016/j.ocemod.2015.03.001

Bertino, L., Lisæter, K.A., Scient, S., 2008. The TOPAZ monitoring and prediction system for the Atlantic and Arctic Oceans. J. Oper. Oceanogr. 1, 15–18. https://doi.org/10.1080/1755876X.2008.11020098

Beszczynska-Möller, A., Woodgate, R., Lee, C., Melling, H., Karcher, M., 2011. A Synthesis of Exchanges Through the Main Oceanic Gateways to the Arctic Ocean. Oceanography 24, 82–99. https://doi.org/10.5670/oceanog.2011.59

Booij, N., Ris, R.C., Holthuijsen, L.H., 1999. A third-generation wave model for coastal regions: 1. Model description and validation. J. Geophys. Res. Ocean. 104, 7649–7666. https://doi.org/10.1029/98JC02622

Born, G.H., Dunne, J.A., Lame, D.B., 1979. Seasat Mission Overview. Science (80-.). 204, 1405–1406. https://doi.org/10.1126/science.204.4400.1405

Broström, G., Christensen, K., 2008. Waves in sea ice. Norwegian Meteorological Institute met.no. Report no. 5/2008.

Bruck., M., 2015. Sea State measurements using TerraSAR-X/TanDEM-X data. PhD thesis, Fakultät der Christian-Albrechts-Universität, Kiel, Germany.

Buus-Hinkler, J., Hackett, B., Wettre, C., 2019. PRODUCT USER MANUAL - Iceberg Number Density - SEAICE_ARC_SEAICE_L4_NRT_OBSERVATIONS_011_007. Ref: CMEMS-SI-PUM-011-007.

Cappelen, J., 2016. DMI Report 16-08 Weather observations from Greenland - Observation data with description 1–31.

Carsey, F.D., Argus, S.A.D., Collins, M.J., Holt, B., Livingstone, C.E., Tang, C.L., 1989. Overview of LIMEX'87 ice observations. IEEE Trans. Geosci. Remote Sens. 27, 468–482.

https://doi.org/10.1109/TGRS.1989.35930

Cavalieri, D.J., Gloersen, P., Campbell, W.J., 1984. Determination of sea ice parameters with the Nimbus 7 SMMR. J. Geophys. Res. 89, 5355–5369. https://doi.org/10.1029/JD089iD04p05355

Cavalieri, D.J., St Germain, K.M., Swift, C.T., 1995. Reduction of weather effects in the calculation of sea-ice concentration with the DMSP SSM/I. J. Glaciol. 41, 455–464. https://doi.org/10.1017/S0022143000034791

Cheng, S., Rogers, W.E., Thomson, J., Smith, M., Doble, M.J., Wadhams, P., Kohout, A.L., Lund, B., Persson, O.P.G., Collins, C.O., Ackley, S.F., Montiel, F., Shen, H.H., 2017. Calibrating a Viscoelastic Sea Ice Model for Wave Propagation in the Arctic Fall Marginal Ice Zone. J. Geophys. Res. Ocean. 122, 8770–8793. https://doi.org/10.1002/2017JC013275

Cheng, Y., Andersen, O.B., 2010. Improvement in global ocean tide model in shallow water regions., in: Altimetry for Oceans & Hydrology OST-ST Meeting. Lisbon.

CMEMS, 2019. Arctic Ocean - SAR sea iceberg concentration product. Product Identifier: SEAICE_ARC_SEAICE_L4_NRT_OBSERVATIONS_011_007. E.U. Copernicus Marine Service Information.

CMEMS, 2018. Global Ocean Physical Reanalysis product. Product Identifier: GLOBAL_REANALYSIS_PHY_001_030. E.U. Copernicus Marine Service Information.

Collins, C., Doble, M., Lund, B., Smith, M., 2018. Observations of Surface Wave Dispersion in the Marginal Ice Zone. J. Geophys. Res. Ocean. 3336–3354. https://doi.org/10.1029/2018JC013788

Collins, C.O., Rogers, W.E., Lund, B., 2017. An investigation into the dispersion of ocean surface waves in sea ice. Ocean Dyn. 67, 263–280. https://doi.org/10.1007/s10236-016-1021-4

Collins, C.O., Rogers, W.E., Marchenko, A., Babanin, A. V, 2015. In situ measurements of an energetic wave event in the Arctic marginal ice zone. Geophys. Res. Lett. 42, 1863–1870. https://doi.org/10.1002/2015GL063063.Received

Copernicus Climate Change Service (C3S), 2017. ERA5: Fifth generation of ECMWF atmospheric reanalyses of the global climate. Copernicus Climate Change Service Climate Data Store (CDS), 01-03-2019. https://cds.climate.copernicus.eu/cdsapp#!/home.

Dewey, S., Morison, J., Kwok, R., Dickinson, S., Morison, D., Andersen, R., 2018. Arctic Ice-Ocean Coupling and Gyre Equilibration Observed With Remote Sensing. Geophys. Res. Lett. 45, 1499–1508. https://doi.org/10.1002/2017GL076229

Dezecot, C., Eik, K., 2015. Barents East blocks Metocean Design Basis, Statoil report. Document no.: ME2015-005.

DHI, 2017a. Spectral Wave Module - Scientific Documentation. DHI, Hørsholm, Denmark.

DHI, 2017b. MIKE 3 Flow Model - Scientific Documentation. DHI, Hørsholm, Denmark.

DHI, 2016. MIKE 21 & MIKE 3 Flow Model FM - Hydrodynamic and Transport Module - Scientific Documentation. DHI, Hørsholm, Denmark.

Dierking, W., 2010. Mapping of different sea ice regimes using images from sentinel-1 and ALOS synthetic aperture radar. IEEE Trans. Geosci. Remote Sens. 48, 1045–1058. https://doi.org/10.1109/TGRS.2009.2031806

Dowdeswell, J.A., 1989. On The Nature of Svalbard Icebergs. J. Glaciol. 35, 224–234. https://doi.org/10.3189/S002214300000455X

Eastwood, S., Karvonen, J., Dinessen, F., Fleming, A., Pedersen, L.T., Saldo, R., Buus-Hinkler, J., Hackett, B., Ardhuin, F., Kreiner, M.B., Wettre, C., 2019. QUALITY INFORMATION DOCUMENT For OSI TAC Sea Ice products 011-001, -002, -003, -004, -006, -007, -009, -010, -011, -012, -013. Ref: CMEMS-SI-QUID-011-001to007-009to013.

Eik, K., 2009. Iceberg drift modelling and validation of applied metocean hindcast data. Cold Reg. Sci. Technol. 57, 67–90. https://doi.org/10.1016/j.coldregions.2009.02.009

Engen, G., Johnsen, H., 1995. SAR-Ocean Wave Inversion Using Image Cross Spectra. IEEE Trans. Geosci. Remote Sens. 33, 1047–1056. https://doi.org/10.1109/36.406690

Fetterer, F., Knowles, K., Meier, W.N., Savoie, M., Windnagel, A.K., 2017. Updated daily. Sea Ice Index, Version 3. Boulder, Colorado USA. NSIDC: National Snow and Ice Data Center.

Gebhardt, C., Bidlot, J.R., Gemmrich, J., Lehner, S., Pleskachevsky, A., Rosenthal, W., 2016. Wave observation in the marginal ice zone with the TerraSAR-X satellite. Ocean Dyn. 66, 839–852. https://doi.org/10.1007/s10236-016-0957-8

Gill, R.S., 2001. Operational detection of sea ice edges and icebergs using SAR. Can. J. Remote Sens. 27, 411–432. https://doi.org/10.1080/07038992.2001.10854884

Gladstone, R.M., Bigg, G.R., Nicholls, K.W., 2001. Iceberg trajectory modeling and meltwater injection in the Southern Ocean. J. Geophys. Res. Ocean. 106, 19903–19915. https://doi.org/10.1029/2000jc000347

Goosse, H., Kay, J.E., Armour, K.C., Bodas-Salcedo, A., Chepfer, H., Docquier, D., Jonko, A., Kushner, P.J., Lecomte, O., Massonnet, F., Park, H.S., Pithan, F., Svensson, G., Vancoppenolle, M., 2018. Quantifying climate feedbacks in polar regions. Nat. Commun. 9. https://doi.org/10.1038/s41467-018-04173-0

Haas, C., 2004. Late-summer sea ice thickness variability in the Arctic Transpolar Drift 1991-2001 derived from ground-based electromagnetic sounding. Geophys. Res. Lett. 31, 1–5. https://doi.org/10.1029/2003GL019394

Haas, C., Beckers, J., King, J., Silis, A., Stroeve, J., Wilkinson, J., Notenboom, B., Schweiger, A., Hendricks, S., 2017. Ice and Snow Thickness Variability and Change in the High Arctic Ocean Observed by In Situ Measurements. Geophys. Res. Lett. 44, 10,462-10,469. https://doi.org/10.1002/2017GL075434

Haas, C., Gerland, S., Eicken, H., Miller, H., 1997. Comparison of sea-ice thickness measurements under summer and winter conditions in the Arctic using a small electromagnetic induction device. Geophysics 62, 749–757. https://doi.org/10.1190/1.1444184

Haas, C., Pfaffling, A., Hendricks, S., Rabenstein, L., Etienne, J.L., Rigor, I., 2008. Reduced ice thickness in Arctic Transpolar Drift favors rapid ice retreat. Geophys. Res. Lett. 35, 1–5. https://doi.org/10.1029/2008GL034457

Hansen, E., Borge, J., Arntsen, M., Olsson, A., Thomson, M., 2019. Estimating icebergs hazards in the Barents Sea using a numerical iceberg drift and deterioration model, in: Proceedings of the 25th International Conference on Port and Ocean Engineering under Arctic Conditions. Delft, Netherlands.

Hansen, J., Paulsen, H.H., 2014. Havnerapport Kangerlussuaq. Rambøll.

Hasholt, B., Bech Mikkelsen, A., Holtegaard Nielsen, M., Andreas Dahl Larsen, M., 2013. Observations of Runoff and Sediment and Dissolved Loads from the Greenland Ice Sheet at Kangerlussuaq, West Greenland, 2007 to 2010. Zeitschrift für Geomorphol. Suppl. Issues 57, 3–27. https://doi.org/10.1127/0372-8854/2012/S-00121

Hasselmann, K., Raney, R.K., Plant, W.J., Alpers, W., Shuchman, R.A., Lyzenga, D.R., Rufenach, C.L., Tucker, M.J., 1985. Theory of synthetic aperture radar ocean imaging: A MARSEN view. J. Geophys. Res. 90, 4659. https://doi.org/10.1029/JC090iC03p04659

Henderson, J., Loe, J., 2014. The Prospects and Challenges for Arctic Oil Development. The Oxford Institute for Energy Studies, Oxford. https://doi.org/10.26889/9781784670153

Herman, A., Cheng, S., Shen, H.H., 2019. Wave energy attenuation in fields of colliding ice floes - Part 1: Discrete-element modelling of dissipation due to ice-water drag. Cryosphere 13, 2887–2900. https://doi.org/10.5194/tc-13-2887-2019

Herman, Y., 1989. The Present Climate of the Arctic Ocean and Possible Past and Future States, in: THE ARCTIC SEAS- Climatology, Oceanography, Geology, and Biology. Springer US, Boston, MA. https://doi.org/10.1007/978-1-4613-0677-1

Holthuijsen, L.H., 2007. Waves in Oceanic and Coastal Waters, Oceanography. Cambridge University Press, Cambridge. https://doi.org/10.1017/CBO9780511618536

Hudson, B., Overeem, I., McGrath, D., Syvitski, J.P.M., Mikkelsen, A., Hasholt, B., 2014. MODIS observed increase in duration and spatial extent of sediment plumes in Greenland fjords. Cryosphere 8, 1161–1176. https://doi.org/10.5194/tc-8-1161-2014

Huntemann, M., Heygster, G., Kaleschke, L., Krumpen, T., Mäkynen, M., Drusch, M., 2014. Empirical sea ice thickness retrieval during the freeze-up period from SMOS high incident angle observations. Cryosphere 8, 439–451. https://doi.org/10.5194/tc-8-439-2014

Husson, R., 2012. Development and validation of a global observation-based swell model using wave mode operating Synthetic Aperture Radar. PhD thesis, Dep. of Earth Sciences, Univ. of Bretagne Occidentale, Brest, France.

Hwang, B., Ren, J., McCormack, S., Berry, C., Ben Ayed, I., Graber, H.C., Aptoula, E., 2017. A practical algorithm for the retrieval of floe size distribution of Arctic sea ice from high-resolution satellite Synthetic Aperture Radar imagery. Elem Sci Anth 5, 38. https://doi.org/10.1525/elementa.154

Ingeman-Nielsen, T., Nielsen, M.H., 2014. Seismiske undersøgelse for havneprojekt I kangerlussuaq. Technical report.

IPCC, 2013. Climate Change 2013: The Physical Science Basis. Contribution of Working Group I to the Fifth Assessment Report of the Intergovernmental Panel on Climate Change. [Stocker, T.F., D. Qin, G.-K. Plattner, M. Tignor, S.K. Allen, J. Boschung, A. Nauels, Y. Xia, V. Bex and P.M. Midgley (eds.)]. Cambridge University Press, Cambridge, United Kingdom and New York, NY, USA, 1535 pp.

Jackson, C.R., Apel, J.R., 2004. Synthetic Aperture Radar: Marine User's Manual.

Jakobsson, M., Mayer, L., Coakley, B., Dowdeswell, J.A., Forbes, S., Fridman, B., Hodnesdal, H., Noormets, R., Pedersen, R., Rebesco, M., Schenke, H.W., Zarayskaya, Y., Accettella, D., Armstrong, A., Anderson, R.M., Bienhoff, P., Camerlenghi, A., Church, I., Edwards, M., Gardner, J. V., Hall, J.K., Hell, B., Hestvik, O., Kristoffersen, Y., Marcussen, C., Mohammad, R., Mosher, D., Nghiem, S. V., Pedrosa, M.T., Travaglini, P.G., Weatherall, P., 2012. The International Bathymetric Chart of the Arctic Ocean (IBCAO) Version 3.0. Geophys. Res. Lett. 39, 1–6. https://doi.org/10.1029/2012GL052219

Johansson, A.M., Brekke, C., Spreen, G., King, J.A., 2018. X-, C-, and L-band SAR signatures of newly formed sea ice in Arctic leads during winter and spring. Remote Sens. Environ. 204, 162–180. https://doi.org/10.1016/j.rse.2017.10.032

Johnsen, H., Collard, F., 2009. Sentinel-1 ocean swell wave spectra (osw) algorithm definition.

Kaleschke, L., Maaß, N., Haas, C., Hendricks, S., Heygster, G., Tonboe, R.T., 2010. A sea-ice thickness retrieval model for 1.4 GHz radiometry and application to airborne measurements over low salinity sea-ice. Cryosphere 4, 583–592. https://doi.org/10.5194/tc-4-583-2010

Kaleschke, L., Tian-Kunze, X., Maas, N., Ricker, R., Hendricks, S., Drusch, M., 2015. Improved retrieval of sea ice thickness from SMOS and CryoSat-2. Int. Geosci. Remote Sens. Symp. 2015-Novem, 5232–5235. https://doi.org/10.1109/IGARSS.2015.7327014

Kaleschke, L., Tian-Kunze, X., Maaß, N., Mäkynen, M., Drusch, M., 2012. Sea ice thickness retrieval from SMOS brightness temperatures during the Arctic freeze-up period. Geophys. Res. Lett. 39, 1–5. https://doi.org/10.1029/2012GL050916

Keghouche, I., Bertino, L., Lisæter, K.A., 2009. Parameterization of an iceberg drift model in the barents sea. J. Atmos. Ocean. Technol. 26, 2216–2227. https://doi.org/10.1175/2009JTECHO678.1

Keghouche, I., Counillon, F., Bertino, L., 2010. Modeling dynamics and thermodynamics of icebergs in the Barents Sea from 1987 to 2005. J. Geophys. Res. Ocean. 115, 1–14. https://doi.org/10.1029/2010JC006165

Keller, J.B., 1998. Gravity waves on ice-covered water. J. Geophys. Res. Ocean. 103, 7663–7669. https://doi.org/10.1029/97JC02966

Kerbaol, V., Chapron, B., Vachon, P.W., 1998. Analysis of ERS-1/2 synthetic aperture radar wave mode imagettes. J. Geophys. Res. Ocean. 103, 7833–7846. https://doi.org/10.1029/97JC01579

Kohout, A.L., Williams, M.J.M., Toyota, T., Lieser, J., Hutchings, J., 2016. In situ observations of wave-induced sea ice breakup. Deep. Res. Part II Top. Stud. Oceanogr. 131, 22–27. https://doi.org/10.1016/j.dsr2.2015.06.010

Komen, G.J., Cavaleri, L., Donelan, M., Hasselmann, K., Hasselmann, S., Janssen, P.A.E.M., 1994. Dynamics and Modelling of Ocean Waves. Cambridge University Press, Cambridge. https://doi.org/10.1017/CBO9780511628955

Kramer, T., Johnsen, H., Brekke, C., Engen, G., 2018. Comparing SAR-based short time-lag cross correlation and doppler-derived sea ice drift velocities. IEEE Trans. Geosci. Remote Sens. 56, 1898–1908. https://doi.org/10.1109/TGRS.2017.2769222

Krumpen, T., Belter, H.J., Boetius, A., Damm, E., Haas, C., Hendricks, S., Nicolaus, M., Nöthig, E.M., Paul, S., Peeken, I., Ricker, R., Stein, R., 2019. Arctic warming interrupts the Transpolar Drift and affects long-range transport of sea ice and ice-rafted matter. Sci. Rep. 9, 1–9. https://doi.org/10.1038/s41598-019-41456-y

Kubat, I., Sayed, M., Savage, S.B., Carrieres, T., 2005. An operational model of iceberg drift. Proc. Int. Offshore Polar Eng. Conf. 2005, 752–758.

Kubyshkin, N. V., Buzin, I. V., Glazovsky, A.F., Skutin, A.A., 2006. Determination of the area of generation of big icebergs in the barents sea - Temperature distribution analysis. Proc. Int. Offshore Polar Eng. Conf. 634–638.

Kwok, R., 2018. Arctic sea ice thickness, volume, and multiyear ice coverage: Losses and coupled variability (1958-2018). Environ. Res. Lett. 13. https://doi.org/10.1088/1748-9326/aae3ec

Kwok, R., Cunningham, G.F., Wensnahan, M., Rigor, I., Zwally, H.J., Yi, D., 2009. Thinning and volume loss of the Arctic Ocean sea ice cover: 2003-2008. J. Geophys. Res. Ocean. 114, 2003–2008. https://doi.org/10.1029/2009JC005312

Kwok, R., Rignot, E., Holt, B., Onstott, R., 1992. Identification of sea ice types in spaceborne synthetic aperture radar data. J. Geophys. Res. 97, 2391–2402. https://doi.org/10.1029/91JC02652

Kwok, R., Spreen, G., Pang, S., 2013. Arctic sea ice circulation and drift speed: Decadal trends and ocean currents. J. Geophys. Res. Ocean. 118, 2408–2425. https://doi.org/10.1002/jgrc.20191

Langhorne, P.J., Squire, V.A., Fox, C., Haskell, T.G., 1998. Break-up of sea ice by ocean waves. Ann. Glaciol. 27, 438–442. https://doi.org/10.3189/S0260305500017869

Laxon, S.W., Giles, K.A., Ridout, A.L., Wingham, D.J., Willatt, R., Cullen, R., Kwok, R., Schweiger, A., Zhang, J., Haas, C., Hendricks, S., Krishfield, R., Kurtz, N., Farrell, S., Davidson, M., 2013. CryoSat-2 estimates of Arctic sea ice thickness and volume. Geophys. Res. Lett. 40, 732–737. https://doi.org/10.1002/grl.50193

Leppäranta, M., 2011. The Drift of Sea Ice. Springer. https://doi.org/10.1007/978-3-642-04683-4

Li, H., Lubbad, R., Monteban, D., 2018. Review of wave-ice interaction studies, in: 24th IAHR International Symposium on Ice. Vladivostok, Russia, pp. 533–543.

Lindsay, R., Schweiger, A., 2015. Arctic sea ice thickness loss determined using subsurface, aircraft, and satellite observations. Cryosphere 9, 269–283. https://doi.org/10.5194/tc-9-269-2015

Liu, A.K., Holt, B., Vachon, P.. W., 1991a. Wave propagation in the marginal ice zone: Model predictions and comparisons with buoy and synthetic aperture radar data. J. Geophys. Res. Ocean. 96, 4605–4621. https://doi.org/10.1029/90JC02267

Liu, A.K., Martin, S., Kwok, R., 1997. Tracking of ice edges and ice floes by wavelet analysis of SAR images. J. Atmos. Ocean. Technol. 14, 1187–1198. https://doi.org/10.1175/1520-0426(1997)014<1187:TOIEAI>2.0.CO;2

Liu, A.K., Vachon, P.W., Peng, C.Y., 1991b. Observation of wave refraction at an ice edge by Synthetic Aperture Radar. J. Geophys. Res. 96, 4803–4808. https://doi.org/10.1029/90JC02546

Liu, A.K., Vachon, P.W., Peng, C.Y., Bhogal, A.S., 1992. Wave attenuation in the marginal ice zone during limex. Atmos. - Ocean 30, 192–206. https://doi.org/10.1080/07055900.1992.9649437

Liu, J., Scott, K.A., Gawish, A., Fieguth, P., 2016. Automatic detection of the ice edge in SAR imagery using curvelet transform and active contour. Remote Sens. 8, 1–16. https://doi.org/10.3390/rs8060480

Løset, S., 1993. Thermal energy conservation in icebergs and tracking by temperature. J. Geophys. Res. 98, 10001. https://doi.org/10.1029/93JC00138

Løset, S., Carstens, T., 1996. Sea ice and iceberg observations in the western Barents Sea in 1987. Cold Reg. Sci. Technol. 24, 323–340. https://doi.org/10.1016/0165-232X(95)00029-B

Løset, S., Shkhinek, K.N., Gudmestad, O.T., Høyland, K. V, 2006. Actions from ice on Arctic offshore and coastal structures.

Lu, W., Yu, Z., van den Berg, M., Monteban, D., Lubbad, R., Hornes, V., Amdahl, J., Sveinung, L., Ekaterina, K., 2020. Report--Loads, Design and Operations of Floaters in the North (Nord ST20).

Lund-Hansen, L.C., Andersen, T.J., Nielsen, M.H., Pejrup, M., 2010. Suspended Matter, Chl-a, CDOM, Grain Sizes, and Optical Properties in the Arctic Fjord-Type Estuary, Kangerlussuaq, West Greenland During Summer. Estuaries and Coasts 33, 1442–1451. https://doi.org/10.1007/s12237-010-9300-7

Lund-Hansen, L.C., Hawes, I., Holtegaard Nielsen, M., Dahllöf, I., Sorrell, B.K., 2018. Summer meltwater and spring sea ice primary production, light climate and nutrients in an Arctic estuary, Kangerlussuaq, west Greenland. Arctic, Antarct. Alp. Res. 50. https://doi.org/10.1080/15230430.2017.1414468

Lund-Hansen, L.C., Hawes, I., Sorrell, B.K., Nielsen, M.H., 2014. Removal of snow cover inhibits spring growth of Arctic ice algae through physiological and behavioral effects. Polar Biol. 37, 471–481. https://doi.org/10.1007/s00300-013-1444-z

Lyzenga, D.R., Shuchman, R. a., Lyden, J.D., 1985. SAR Imaging of Waves in Water and Ice : Evidence for Velocity Bunching. J. Geophys. Res. 90, 1031–1036. https://doi.org/10.1029/JC090iC01p01031

Maslanik, J., Stroeve, J., Fowler, C., Emery, W., 2011. Distribution and trends in Arctic sea ice age through spring 2011. Geophys. Res. Lett. 38, 2–7. https://doi.org/10.1029/2011GL047735

McKenna, R.F., Crocker, G.B., 1992. Ice-floe collisions interpreted from acceleration data during limex ‘89. Atmos. - Ocean 30, 246–269. https://doi.org/10.1080/07055900.1992.9649440

Melling, H., Johnston, P.H., Riedel, D.A., 1995. Measurements of the Underside Topography of Sea Ice by Moored Subsea Sonar. J. Atmos. Ocean. Technol. https://doi.org/10.1175/1520-0426(1995)012<0589:motuto>2.0.co;2

Meredith, M., Sommerkorn, M., Cassotta, S., Derksen, C., Ekaykin, A., Hollowed, A., Kofinas, G., Mackintosh, A., Melbourne-Thomas, J. Muelbert, M.M.C., Ottersen, G., Pritchard, H., Schuur, E.A.G., 2019. Polar Regions, in: IPCC Special Report on the Ocean and Cryosphere in a Changing Climate. [H.-O. Pörtner, D.C. Roberts, V. Masson-Delmotte, P. Zhai, M. Tignor, E. Poloczanska, K. Mintenbeck, A. Alegría, M. Nicolai, A. Okem, J. Petzold, B. Rama, N.M. Weyer (eds.)]. In press.

Mikkelsen, A.B., Hasholt, B., 2013. Sediment Transport to the Kangerlussuaq Fjord , West Greenland. Int. North. Res. basins Symp. Work. Alaska. USA 19, 1–10.

Mikkelsen, A.B., Hasholt, B., Knudsen, N.T., Nielsen, M.H., 2013. Jökulhlaups and sediment transport in Watson River, Kangerlussuaq, West Greenland. Hydrol. Res. 44, 58. https://doi.org/10.2166/nh.2012.165

Monteban, D., Johnsen, H., Lubbad, R., 2019a. Spatiotemporal observations of wave dispersion within sea ice using Sentinel-1 SAR TOPS mode. J. Geophys. Res. Ocean. https://doi.org/10.1029/2019JC015311

Monteban, D., Lubbad, R., Johnsen, H., 2019b. Sentinel-1 SAR observations of peak wavelength and wave direction in the marginal ice zone of the Barents Sea, in: Proceedings of the 25th International Conference on Port and Ocean Engineering under Arctic Conditions. Delft, Netherlands.

Monteban, D., Lubbad, R., Pedersen, J.O.P., 2019c. Use of satellite remote sensing to study wave-ice interactions in the marginal ice zone - A review, in: Proceedings of the 25th International Conference on Port and Ocean Engineering under Arctic Conditions. Delft, Netherlands.

Monteban, Dennis, Lubbad, R., Samardzija, I., Løset, S., 2020a. Enhanced iceberg drift modelling in the Barents Sea with estimates of the release rates and size characteristics at the major glacial sources using Sentinel-1 and Sentinel-2. Cold Reg. Sci. Technol. 175, 103084. https://doi.org/10.1016/j.coldregions.2020.103084

Monteban, D, Pedersen, J.O.P., Nielsen, M.H., 2020b. Physical oceanographic conditions and a sensitivity study on meltwater runoff in a West Greenland fjord: Kangerlussuaq. Oceanologia. Manuscript submitted for publication.

Monteban, D., Pedersen, J.O.P., Nielsen, M.H., Ingeman-nielsen, T., 2018. Modelling of hydrodynamic and wave conditions for a new harbor in Søndre Strømfjord (Kangerlussuaq), in: AIC 2018 Transportation Infrastructure Engineering in Cold Regions. Sisimiut, Greenland, pp. 28–29.

Mosig, J.E.M., Montiel, F., Squire, V.A., 2015. Comparison of viscoelastic-type models for ocean wave attenuation in ice-covered seas. J. Geophys. Res. Ocean. 120, 6072–6090. https://doi.org/10.1002/2015JC010881

Müller, F.L., Dettmering, D., Bosch, W., Seitz, F., 2017. Monitoring the arctic seas: How satellite altimetry can be used to detect openwater in sea-ice regions. Remote Sens. 9. https://doi.org/10.3390/rs9060551

Myers, P.G., Kulan, N., Ribergaard, M.H., 2007. Irminger water variability in the West Greenland Current. Geophys. Res. Lett. 34, 2–7. https://doi.org/10.1029/2007GL030419

Nielsen, M.H., Erbs-Hansen, D.R., Knudsen, K.L., 2010. Water masses in Kangerlussuaq, a large fjord in West Greenland: the processes of formation and the associated foraminiferal fauna. Polar Res. 29, 159–175. https://doi.org/10.1111/j.1751-8369.2010.00147.x

Olason, E., Notz, D., 2014. Drivers of variability in Arctic sea-ice drift speed. J. Geophys. Res. Ocean. 119, 5755–5775. https://doi.org/10.1002/2014JC009897

Onarheim, I.H., Eldevik, T., Smedsrud, L.H., 2018. Seasonal and Regional Manifestation of Arctic Sea Ice Loss. J. Clim. 31, 4917–4932. https://doi.org/10.1175/JCLI-D-17-0427.1

Onstott, R.G., Shuchman, R. a., 2004. Chapter 3. SAR Measurements of Sea Ice, in: SAR Marine User's Manual. pp. 81–115.

Park, J.-W., Korosov, A., Babiker, M., Won, J.-S., Hansen, M., Kim, H.-C., 2019. Classification of Sea Ice Types in Sentinel-1 SAR images. Cryosph. Discuss. 1–23. https://doi.org/10.5194/tc-2019-127-RC3

Pizzolato, L., Howell, S.E.L., Dawson, J., Laliberté, F., Copland, L., 2016. The influence of declining sea ice on shipping activity in the Canadian Arctic. Geophys. Res. Lett. 43, 12,146-12,154. https://doi.org/10.1002/2016GL071489

Pizzolato, L., Howell, S.E.L., Derksen, C., Dawson, J., Copland, L., 2014. Changing sea ice conditions and marine transportation activity in Canadian Arctic waters between 1990 and 2012. Clim. Change 123, 161–173. https://doi.org/10.1007/s10584-013-1038-3

Polvani, L.M., Previdi, M., England, M.R., Chiodo, G., Smith, K.L., 2020. Substantial twentieth-century Arctic warming caused by ozone-depleting substances. Nat. Clim. Chang. 2020 10, 1–4. https://doi.org/10.1038/s41558-019-0677-4

Power, D., Youden, J., Lane, K., Randell, C., Flett, D., 2001. Iceberg detection capabilities of radarsat synthetic aperture radar. Can. J. Remote Sens. 27, 476–486. https://doi.org/10.1080/07038992.2001.10854888

Prinsenberg, S., Holladay, S., 2009. Ice thickness measurements with a miniature electromagnetic sensor sled. Proc. Int. Offshore Polar Eng. Conf. 1, 666–671.

Proshutinsky, A., Krishfield, R., Barber, D., 2009a. Preface to special section on Beaufort Gyre climate system exploration studies: Documenting key parameters to understand environmental variability. J. Geophys. Res. Ocean. 114. https://doi.org/10.1029/2008JC005162

Proshutinsky, A., Krishfield, R., Timmermans, M.-L., Toole, J., Carmack, E., McLaughlin, F., Williams, W.J., Zimmermann, S., Itoh, M., Shimada, K., 2009b. Beaufort Gyre freshwater reservoir: State and variability from observations. J. Geophys. Res. 114, 1–25. https://doi.org/10.1029/2008jc005104

QGIS Development Team, 2019. QGIS Geographic Information System. Open Source Geospatial Foundation Project. http://qgis.osgeo.org.

Rampal, P., Weiss, J., Marsan, D., 2009. Positive trend in the mean speed and deformation rate of Arctic sea ice, 1979-2007. J. Geophys. Res. Ocean. 114, 1–14. https://doi.org/10.1029/2008JC005066

Raney, R.K., Vachon, P.W., De Abreu, R.A., Bhogal, A.S., 1989. Airborne SAR observations of ocean surface waves penetrating floating ice. IEEE Trans. Geosci. Remote Sens. 27, 492–500. https://doi.org/10.1109/TGRS.1989.35932

Richter-Menge, J., Overland, J.E., Mathis, J.T., Osborne, E., 2017. Arctic Report Card 2017. https://www.arctic.noaa.gov/Report-Card.

Ricker, R., Hendricks, S., Helm, V., Skourup, H., Davidson, M., 2014. Sensitivity of CryoSat-2 Arctic sea-ice freeboard and thickness on radar-waveform interpretation. Cryosphere 8, 1607–1622. https://doi.org/10.5194/tc-8-1607-2014

Ricker, R., Hendricks, S., Kaleschke, L., Tian-Kunze, X., King, J., Haas, C., 2017. A weekly Arctic sea-ice thickness data record from merged CryoSat-2 and SMOS satellite data. Cryosphere 11, 1607–1623. https://doi.org/10.5194/tc-11-1607-2017

Rigor, I.G., Wallace, J.M., Colony, R.L., 2002. Response of sea ice to the Arctic Oscillation. J. Clim. 15, 2648–2663. https://doi.org/10.1175/1520-0442(2002)015<2648:ROSITT>2.0.CO;2

Rothrock, D.A., Wensnahan, M., 2007. The accuracy of sea ice drafts measured from U.S. Navy submarines. J. Atmos. Ocean. Technol. 24, 1936–1949. https://doi.org/10.1175/JTECH2097.1

Sandven, S., Johannessen, O.M., Kloster, K., 2006. Sea Ice Monitoring by Remote Sensing, Encyclopedia of

Analytical Chemistry. https://doi.org/10.1002/9780470027318.a2320

Schulz-Stellenfleth, J., Lehner, S., 2002. Spaceborne synthetic aperture radar observations of ocean waves traveling into sea ice. J. Geophys. Res. 107, 3106. https://doi.org/10.1029/2001JC000837

Schweiger, A.J., Wood, K.R., Zhang, J., 2019. Arctic Sea Ice volume variability over 1901-2010: A model-based reconstruction. J. Clim. 32, 4731–4752. https://doi.org/10.1175/JCLI-D-19-0008.1

Screen, J.A., Simmonds, I., 2010. The central role of diminishing sea ice in recent Arctic temperature amplification. Nature 464, 1334–1337. https://doi.org/10.1038/nature09051

Shen, H., Perrie, W., Hu, Y., He, Y., 2018. Remote Sensing of Waves Propagating in the Marginal Ice Zone by SAR. J. Geophys. Res. Ocean. 123, 189–200. https://doi.org/10.1002/2017JC013148

Shen, H.H., 2017. Wave-Ice Interactions, in: Encyclopedia of Maritime and Offshore Engineering. John Wiley & Sons, Ltd, pp. 1–14.

Shen, H.H., Squire, V.A., 1998. Wave Damping in Compact Pancake Ice Fields Due to Interactions Between Pancakes. Antarctic Sea Ice: Physical Processes, Interactions and Variability. https://doi.org/10.1029/AR074p0325

Shokr, M., Sinha, N.K., 2015. Sea Ice Physics and Remote Sensing. Wiley, New Jersey.

Shore Protection Manual, 1984. Shore Protection Manual. US Army Corps of Engineergs, Washington DC.

Shuchman, R. a., Rufenach, C.L., Johannessen, O.M., 1994. Extraction of marginal ice zone thickness using gravity wave imagery. J. Geophys. Res. 99, 901. https://doi.org/10.1029/93JC01956

Skriver, H., Dierking, W., 2004. Knowledge-based sea ice classification by polarimetric SAR. Int. Geosci. Remote Sens. Symp. 1, 204–207. https://doi.org/10.1109/igarss.2004.1368995

Slagstad, D., Støle-Hansen, K., Loeng, H., 1990. Density driven currents in the Barents Sea calculated by a numerical model, Modeling, Identification and Control 11, 181–190.

Squire, V.A., 2020. Ocean Wave Interactions with Sea Ice: A Reappraisal. Annu. Rev. Fluid Mech. 52. https://doi.org/10.1146/annurev-fluid-010719-060301

Squire, V.A., 2018. A fresh look at how ocean waves and sea ice interact. Philos. Trans. R. Soc. A Math. Phys. Eng. Sci. 376, 20170342. https://doi.org/10.1098/rsta.2017.0342

Squire, V.A., 2007. Of ocean waves and sea-ice revisited. Cold Reg. Sci. Technol. 49, 110–133. https://doi.org/10.1016/j.coldregions.2007.04.007

Squire, V.A., Duggan, J.P., Wadhams, P., Rottier, P.J., Liu, A.J., 1995. Of ocean waves and sea ice. Annu. Rev. Fluid Mech. 27, 115–168. https://doi.org/10.1146/annurev.fl.27.010195.000555

Stokes, G.G., 1847. On the Theory of Oscillatory Waves, in: Transactions of the Cambridge Philosophical Society. https://doi.org/10.1017/cbo9780511702242.013

Stopa, J.E., Ardhuin, F., Thomson, J., Smith, M.M., Kohout, A., Doble, M., Wadhams, P., 2018a. Wave Attenuation Through an Arctic Marginal Ice Zone on 12 October 2015. 1. Measurement of Wave Spectra and Ice Features From Sentinel 1A. J. Geophys. Res. Ocean. 123, 3619–3634. https://doi.org/10.1029/2018JC013791

Stopa, J.E., Sutherland, P., Ardhuin, F., 2018b. Strong and highly variable push of ocean waves on Southern Ocean sea ice. Proc. Natl. Acad. Sci. U. S. A. 237, 1–5. https://doi.org/10.1073/pnas.1802011115

Storms, J.E.A., de Winter, I.L., Overeem, I., Drijkoningen, G.G., Lykke-Andersen, H., 2012. The Holocene sedimentary history of the Kangerlussuaq Fjord-valley fill, West Greenland. Quat. Sci. Rev. 35, 29–50. https://doi.org/10.1016/j.quascirev.2011.12.014

Straneo, F., Cenedese, C., 2015. The Dynamics of Greenland's Glacial Fjords and Their Role in Climate. Ann. Rev. Mar. Sci. 7, 89–112. https://doi.org/10.1146/annurev-marine-010213-135133

Stroeve, J., Notz, D., 2018. Changing state of Arctic sea ice across all seasons. Environ. Res. Lett. 13. https://doi.org/10.1088/1748-9326/aade56

Stroeve, J.C., Markus, T., Boisvert, L., Miller, J., Barrett, A., 2014. Changes in Arctic melt season and implications for sea ice loss. Geophys. Res. Lett. 41, 1216–1225. https://doi.org/10.1002/2013GL058951

Stroeve, J.C., Maslanik, J., Serreze, M.C., Rigor, I., Meier, W., Fowler, C., 2011. Sea ice response to an extreme negative phase of the Arctic Oscillation during winter 2009/2010. Geophys. Res. Lett. 38, 1–6.

https://doi.org/10.1029/2010GL045662

Stuecker, M.F., Bitz, C.M., Armour, K.C., Proistosescu, C., Kang, S.M., Xie, S.P., Kim, D., McGregor, S., Zhang, W., Zhao, S., Cai, W., Dong, Y., Jin, F.F., 2018. Polar amplification dominated by local forcing and feedbacks. Nat. Clim. Chang. 8, 1076–1081. https://doi.org/10.1038/s41558-018-0339-y

Sutherland, D.A., Pickart, R.S., 2008. The East Greenland Coastal Current: Structure, variability, and forcing. Prog. Oceanogr. 78, 58–77. https://doi.org/10.1016/j.pocean.2007.09.006

Swanson, P.N., Riley, A.L., 1980. The Seasat Scanning Multichannel Microwave Radiometer (SMMR): Radiometric Calibration Algorithm Development and Performance. IEEE J. Ocean. Eng. 5, 116–124. https://doi.org/10.1109/JOE.1980.1145452

Tateyama, K., Shirasawa, K., Uto, S., Kawamura, T., Toyota, T., Enomoto, H., 2006. Standardization of electromagnetic-induction measurements of sea-ice thickness in polar and subpolar seas. Ann. Glaciol. 44, 240–246. https://doi.org/10.3189/172756406781811484

Thompson, D.W.J., Wallace, J.M., 1998. The Arctic oscillation signature in the wintertime geopotential height and temperature fields. Geophys. Res. Lett. 25, 1297–1300. https://doi.org/10.1029/98GL00950

Tilling, R.L., Ridout, A., Shepherd, A., 2018. Estimating Arctic sea ice thickness and volume using CryoSat-2 radar altimeter data. Adv. Sp. Res. 62, 1203–1225. https://doi.org/10.1016/j.asr.2017.10.051

Tolman, H.L., 1991. A Third-Generation Model for Wind Waves on Slowly Varying, Unsteady, and Inhomogeneous Depths and Currents. J. Phys. Oceanogr. 21, 782–797. https://doi.org/10.1175/1520-0485(1991)021<0782:ATGMFW>2.0.CO;2

Toussaint, G.T., 1983. Solving Geometric Problems With the “Rotating Calipers”. Proc. IEEE MELECON’83.

Tschudi, M., Fowler, C., Maslanik, J., Stroeve, J., 2010. Tracking the Movement and Changing Surface Characteristics of Arctic Sea Ice. IEEE J. Sel. Top. Appl. Earth Obs. Remote Sens. 3, 536–540. https://doi.org/10.1109/JSTARS.2010.2048305

Tschudi, M., Meier, W.N., Stewart, S.J., Fowler, C., Maslanik, J., 2019. EASE-Grid Sea Ice Age, Version 4. Boulder, Colorado USA. NASA National Snow and Ice Data Center Distributed Active Archive Center.

UNESCO, 1987. International oceanographic tables. Unesco Tech. Pap. Mar. Sci. 3, 195.

van As, D., Hasholt, B., Ahlstrøm, A.P., Box, J.E., Cappelen, J., Colgan, W., Fausto, R.S., Mernild, S.H., Mikkelsen, A.B., Noël, B.P.Y., Petersen, D., van den Broeke, M.R., 2018. Reconstructing Greenland Ice Sheet meltwater discharge through the Watson River (1949–2017). Arctic, Antarct. Alp. Res. 50. https://doi.org/10.1080/15230430.2018.1433799

Vihma, T., Tisler, P., Uotila, P., 2012. Atmospheric forcing on the drift of Arctic sea ice in 1989-2009. Geophys. Res. Lett. 39, 1–6. https://doi.org/10.1029/2011GL050118

Wadhams, P., 1986. The Seasonal Ice Zone, in: The Geophysics of Sea Ice. pp. 825–991. https://doi.org/10.1007/978-1-4899-5352-0_15

Wadhams, P., Aulicino, G., Parmiggiani, F., Persson, P.O.G., Holt, B., 2018. Pancake Ice Thickness Mapping in the Beaufort Sea From Wave Dispersion Observed in SAR Imagery. J. Geophys. Res. Ocean. 123, 2213–2237. https://doi.org/10.1002/2017JC013003

Wadhams, P., Holt, B., 1991. Waves in frazil and pancake ice and their detection in Seasat synthetic aperture radar imagery. J. Geophys. Res. 96, 8835–8852. https://doi.org/10.1029/91JC00457

Wadhams, P., Parmiggiani, F., de Carolis, G., 2002. The Use of SAR to Measure Ocean Wave Dispersion in Frazil–Pancake Icefields. J. Phys. Oceanogr. 32, 1721–1746. https://doi.org/10.1175/1520-0485(2002)032<1721:TUOSTM>2.0.CO;2

Wadhams, P., Parmiggiani, F.F., De Carolis, G., Desiderio, D., Doble, M.J., 2004. SAR imaging of wave dispersion in Antarctic pancake ice and its use in measuring ice thickness. Geophys. Res. Lett. 31, L15305. https://doi.org/10.1029/2004GL020340

WAFO-group, 2000. WAFO - A Matlab Toolbox for Analysis of Random Waves and Loads - A Tutorial. Math. Stat., Center for Math. Sci., Lund Univ., Lund, Sweden. ISBN XXXX, URL http://www.maths.lth.se/matstat/wafo.

Wagner, T.J.W., Dell, R.W., Eisenman, I., 2017a. An analytical model of iceberg drift. J. Phys. Oceanogr. 47, 1605–1616. https://doi.org/10.1175/JPO-D-16-0262.1

Wagner, T.J.W., Stern, A.A., Dell, R.W., Eisenman, I., 2017b. On the representation of capsizing in iceberg models. Ocean Model. 117, 88–96. https://doi.org/10.1016/j.ocemod.2017.07.003

Walsh, J.E., Chapman, W.L., Fetterer, F., Stewart, J.S., 2019. Gridded Monthly Sea Ice Extent and Concentration, 1850 Onward, Version 2. Boulder, Colorado USA. NSIDC: National Snow and Ice Data Center. https://doi.org/https://doi.org/10.7265/jj4s-tq79

Walsh, J.E., Fetterer, F., Scott Stewart, J., Chapman, W.L., 2017. A database for depicting Arctic sea ice variations back to 1850. Geogr. Rev. 107, 89–107. https://doi.org/10.1111/j.1931-0846.2016.12195.x

Wang, J., Ikeda, M., 2000. Arctic oscillation and Arctic Sea-Ice oscillation. Geophys. Res. Lett. 27, 1287–1290. https://doi.org/10.1029/1999GL002389

Wang, R., Shen, H.H., 2010. Gravity waves propagating into an ice-covered ocean: A viscoelastic model. J. Geophys. Res. Ocean. 115, 1–12. https://doi.org/10.1029/2009JC005591

Weitz, M., Keller, J.B., 1950. Reflection of water waves from floating ice in water of finite depth. Commun. Pure Appl. Math. 3, 305–318. https://doi.org/10.1002/cpa.3160030306

Wesche, C., Dierking, W., 2012. Iceberg signatures and detection in SAR images in two test regions of the Weddell Sea, Antarctica. J. Glaciol. 58, 325–339. https://doi.org/10.3189/2012J0G11J020

Wingham, D.J., Francis, C.R., Baker, S., Bouzinac, C., Brockley, D., Cullen, R., de Chateau-Thierry, P., Laxon, S.W., Mallow, U., Mavrocordatos, C., Phalippou, L., Ratier, G., Rey, L., Rostan, F., Viau, P., Wallis, D.W., 2006. CryoSat: A mission to determine the fluctuations in Earth's land and marine ice fields. Adv. Sp. Res. 37, 841–871. https://doi.org/10.1016/j.asr.2005.07.027

Winton, M., 2006. Surface albedo feedback estimates for the AR4 climate models. J. Clim. 19, 359–365. https://doi.org/10.1175/JCLI3624.1

Woodgate, R.A., Aagaard, K., Weingartner, T.J., 2005. Monthly temperature, salinity, and transport variability of the Bering Strait through flow. Geophys. Res. Lett. 32, 1–4. https://doi.org/10.1029/2004GL021880

World Metrological Organization, 1970. WMO Sea-Ice Nomenclature. Vol 1: Terminology and codes. Report 259, Geneva, Switzerland.

Yde, J.C., Anderson, N.J., Post, E., Saros, J.E., Telling, J., 2018. Environmental change and impacts in the Kangerlussuaq area, west Greenland. Arctic, Antarct. Alp. Res. 50. https://doi.org/10.1080/15230430.2018.1433786

Zan, F. De, Guarnieri, A.M., 2006. TOPSAR: Terrain Observation by Progressive Scans. IEEE Trans. Geosci. Remote Sens. 44, 2352–2360. https://doi.org/10.1109/TGRS.2006.873853

Zhang, J., Schweiger, A., Steele, M., Stern, H., 2015. Sea ice floe size distribution in the marginal ice zone: Theory and numerical experiments. J. Geophys. Res. Ocean. 120, 3484–3498. https://doi.org/10.1002/2015JC010770

Zhao, X., Shen, H.H., Cheng, S., 2015. Modeling ocean wave propagation under sea ice covers. Acta Mech. Sin. Xuebao 31, 1–15. https://doi.org/10.1007/s10409-015-0017-5

Zubov, N.N., 1963. Arctic Ice. U.S. Navy, San Diego, California.

Appendix A Review of wave-ice interactions

This paper is published in the 24th IAHR International Symposium on Ice, 4-9 June 2018, Vladivostok, Russia.

Li, H., Lubbad, R., Monteban, D., 2018. Review of wave-ice interaction studies, in: 24th IAHR International Symposium on Ice. Vladivostok, Russia, pp. 533–543.

International Association for Hydro-Environment Engineering and Research
Supported by Spain Water and IWHR, China

24th IAHR International Symposium on Ice
Vladivostok, Russia, June 4 to 9, 2018

Review of wave-ice interaction studies

Hongtao Li, Raed Lubbad, Dennis Monteban
1) Sustainable Arctic Marine and Coastal Technology (SAMCoT),
Centre for Research-based Innnovation (CRI),
Norwegian University of Science and Technology, Trondheim, Norway
Høgskoleringen 7A, 7491 Trondheim, Norway
hongtao.li@ntnu.no

In the past several decades, sea-ice cover in the Arctic Ocean advances later than usual in the autumns and retreats earlier in the springs due to climate change. Concomitantly, total area of ice cover reduces and average ice thickness decreases. Consequently, open water areas increase and wave climate exacerbates. The interaction between waves and ice is strongly coupled and highly nonlinear. Ice refracts, attenuates, and scatters the waves. Reciprocally, waves bend, break and transport the ice around. From 1950s onwards, considerable scientific efforts have been made to study wave propagation in ice-covered waters. This paper summarizes the theoretical models, available in the open literature, for wave-ice interactions. Here, we discuss the assumptions, application ranges and limitations of these models. Moreover, we discuss the use of these theoretical models in operational wave models like WAVEWATCH III and present concerns about the parameterizations of the ice effects. Additionally, some applications of Synthetic Aperture Radar (SAR) remote sensing for studying ice effects on waves are presented. Finally, we identify the knowledge gaps in studying wave-ice interactions.

Introduction

Global climate change has complex implications for the Arctic Oceans. One example is the fiercer wave climates in the Arctic (Thomson et al., 2016). These severe waves are mainly attributed to the increasing fetch (Thomson and Rogers, 2014), which is a result of the reduction in the ice cover extent over the last decades (Vizcarra, 2018). Waves are one of the determinants for the spatial and temporal evolutions of sea ice. Waves break the ice (Kohout et al., 2016), transport it, accelerate its melting and induce collisions between the ice floes (McKenna and Crocker, 1990). On the other hand, ice refracts the waves (Squire et al., 1995), changes their dispersion relation, scatters and attenuates them (Wadhams et al., 1988).

In this study, we focus only on the effects of sea ice on the waves. Firstly, we list the different mechanisms that contribute to the wave attenuation. Then we provide a summary of the theoretical models, available in the open literature, for wave-ice interactions. Thereafter, we investigate the assumptions, application ranges and limitations of these models. Some of these models are recently implemented in the operational wave model WAVEWATCH III (henceforth WW3). In this paper, we also present a comparison of the implemented models along with other models. Additionally, Synthetic Aperture Radar (SAR) applications in studying change of waves due to ice are included. Finally, we discuss some of the knowledge gaps in the studies of wave-ice interaction.

Mechanisms to attenuate waves

Waves are attenuated due to scattering (Shen and Squire, 1998), turbulence (Shen and Squire, 1998, Squire and Shen, 1997), over-washing (Bennetts et al., 2015, Nelli et al., 2017), inelastic collisions between ice floes (McKenna and Crocker, 1992), inelastic bending of ice (thus fatigue) (Erber et al., 1993, Langhorne et al., 1998) and fracture of ice (Zhang et al., 2015). Among them, only wave scattering is a conservative process, which implies that the total wave energy is a constant, while forward-going wave energy reduces. The other processes, on the other hand, are all dissipative.

Theoretical models for wave-ice interaction

There have been intermittent efforts to develop theoretical models for wave-ice interaction since 1950s. These models are summarized in Table 1. The principal assumptions of each model are presented in the third and fourth columns (from left to right) of the same table. Abbreviations of these models, which are used in the remainder of this paper, are provided in the second column.

It is worthwhile to identify other assumptions of each model. WK neglects draughts of discrete mass points. GW model uses linear wave theory and thin elastic plate theory. Implicitly, plain strain state (see e.g. Logan (2012)) is assumed for the thin plate. Furthermore, small plate thickness relative to wavelength assumption leads to small normal stress in water depth direction that can be neglected. Lastly, it is assumed that the bottom of the plate is in contact with water all the time. Detailed derivation of resultant constitutive relation of the GW model can be found in Marchenko (2016). Regarding the viscous models (VSK, VSDD and VSLM), they are two-layer type models, in which the former two assume that the two layers are immiscible fluids. Same as for the GW model, all viscous and viscoelastic models assume upper layer always stays in contact with water. Note that Marchenko (2016) neglects inertia effect of ice when deriving the

VCM model. One common assumption of these models is small amplitude waves with small steepness.

Table 1. Wave-ice interaction models

Wave – ice interaction model		Ice	Water	Damping of wave energy from	Included in WW3	Selected wave number (Criteria)
Mass loading model	WK[1]	Discrete mass point	Inviscid	Scattering	No	2 real[12] (Geophysics relevant)
Thin plate model	GW[2]	Thin elastic plate	Inviscid	Scattering	No	2 real[13] (Geophysics relevant)
Viscous layer model	VSK[3]	Viscous fluid layer	Inviscid	Viscous damping in ice	No	1 complex (least damped wave mode)[3]
	VSLM[4]	Thin elastic plate	Viscous	Viscous damping in water	Yes[10]	1 complex
	VSDD[5]	Viscous fluid layer	Viscous	Viscous damping in ice and water	No	1 complex (closest to open-gravity wave with least attenuation)[14]
Viscoelastic model	VCWS[6]	Viscoelastic fluid layer (Voigt model)	Inviscid	Viscous damping in ice (linear dashpot)	Yes[10]	1 complex (closest to open-gravity wave with least attenuation)[6]
	VCFS[7]	Viscoelastic solid beam (Voigt model)	Inviscid	Viscous damping in ice (linear dashpot)	Yes[11]	2 complex (in first quadrant of complex plane)[15]
	VCRP[8]	Thin elastic beam	Inviscid	Damping forces due to vertical velocity of beam	No	2 complex (in first quadrant of complex plane)[15]
	VCM[9]	Viscoelastic solid (Maxwell model)	Inviscid	Viscous damping in ice (nonlinear dashpot)	No	1 complex (close to wave number of gravity wave)[16]

1. Weitz and Keller (1950), 2. Greenhill (1886) and Wadhams (1986), 3. Keller (1998), 4. Liu and Mollo-Christensen (1988), 5. De Carolis and Desiderio (2002), 6. Wang and Shen (2010), 7. Mosig et al. (2015), Li et al. (2015) and Fox and Squire (1994), 8. Mosig et al. (2015) and Robinson and Palmer (1990), 9. Marchenko (2016), 10. The WAVEWATCH III® Development Group (WW3DG) (2016), 11. Rogers (2017), 12. Squire et al. (1995), 13. Squire (1993) and Wadhams (1981), 14. De Carolis (2018), 15. Mosig et al. (2015), 16. Marchenko (2018).

Limitations of the theoretical models

WK fails to reproduce the progressive decay of waves, due to the lack of damping mechanisms in the ice-covered regions (see e.g. Squire et al. (1995)). In the GW model, viscous dissipation is absent. Thus the WK and GW models are applicable for sparse pancakes field and intact ice sheet, respectively (Zhao et al., 2015). The VSK and VSDD models are suitable for grease ice (Newyear and Martin, 1999, De Carolis and Desiderio, 2002). The VCWS model should, in principle, work for all the aforementioned ice types (Wang and Shen, 2010). The VSLM model appears to be more suitable for ice fields with high concentration (Liu et al., 1991). The VCFS model seems more applicable for low concentration ice fields (Squire, 2018), which is probably also true for the VCRP model.

The VSLM model adopts eddy viscosity to parameterize turbulence in the viscous boundary layer. Eddy viscosity is not measurable and it is usually used as tuning parameter to best-fit model results to field measurements (Liu et al., 1991). Undesirably, this parameter obtained from best-fit varies greatly for different field measurements. Similarly, the VCWS and VCFS models contain immeasurable quantities, i.e. equivalent viscosity and elasticity. Up to now, these two input model parameters are determined by inverse methods. Specifically, based on available measurements, they are estimated by minimizing the discrepancy between model results and corresponding measured quantities, such as total wave energy (Rogers et al., 2016), significant wave height (Li et al., 2017), wave attenuation coefficients (Li et al., 2015, Mosig et al., 2015) and complex wave number (Cheng et al., 2017). However, there are many limitations in using inverse method, such as possible interdependency among parameters, multiple solutions, measurement errors and low sensitivity of measurable output to input model parameters (Li et al., 2015). Another major limitation is that the roots selection criteria are not well defined, see Mosig et al. (2015) and Rogers et al. (2016) for VCWS and Collins et al. (2017) for VCWS and VCFS.

One common limitation of all available models is that they are based on linear theory, which implies that over-washing, rafting, ridging and collisions between ice floes are not accounted for explicitly. Owing to the utilization of linear wave theory, the above mentioned models only predict exponential attenuation (Squire, 2018). However, Squire (2018) and Kohout et al. (2014) found a distinct attenuation behaviour for large waves in western Arctic and Southern Ocean, respectively.

WW3 operational wave model

WW3 is a third generation spectral wave model that has been developed continuously to include wave-ice interaction effects (see The WAVEWATCH III® Development Group (WW3DG) (2016) and the sixth column of Table 1). The governing equation of this model is (presented here using the same concise form as in Cheng et al. (2017))

$$\frac{\partial E(f,\vec{x},\theta)}{\partial t} + \nabla_x \cdot c_g E(f,\vec{x},\theta) = (1-C)(S_{in}+S_{ds}) + S_{nl} + CS_{ice} \qquad \mathbf{[1]}$$

where $E(f,\vec{x},\theta)$ is the wave spectral density, f is the wave frequency, $\vec{x}$ is the spatial coordinate, θ is the wave propagation direction, t is time, c_g is wave group velocity, C is ice concentration, S_{in}, S_{ds}, S_{nl} and S_{ice} represent wind-wave interaction, wave energy dissipation due to white-capping, nonlinear interactions between different wave components and wave damping due to ice, respectively.

S_{ice} includes a dissipative term ($S_{ice,dis}$) resulting from friction and viscosity, and a conservative damping ($S_{ice,sc}$) induced by scattering (Zhao et al., 2015).

Comparisons of different theoretical models

Viscous and viscoelastic models for wave–ice interaction in principle address directly $S_{ice,dis}$ and c_g. $S_{ice,dis} = -2c_g k_i E$ (Rogers and Orzech, 2013), where k_i is the imaginary wave number. Both k_i and c_g can be obtained from the dispersion relations of these models. In contrast, WK and GW models conceptually deal with $S_{ice,sc}$ and c_g.

The viscoelastic models (VCWS, VCFS and VCRP) were compared by Mosig et al. (2015). They found that the dispersion relations of the VCFS and the VCRP models are analytically invertible for elasticity and viscosity. Hence, there is only one result of the inverse analysis for these models. Similarly, it is possible to show that the dispersion relation of VCM can be analytically inverted for the tuning parameter - creep constant. In contrast, the rheological parameter in the VCWS model can only be numerically found and non-unique solutions exist using the inverse analysis (Mosig et al., 2015).

Among all the previously mentioned models, only the VSLM model reproduces rollover. This phenomenon is a special wave attenuation behaviour, in which spatial wave attenuation coefficient increases first with frequency prior to decreasing steadily afterwards.

The theoretical models can be divided, based on their usage in real life, into two groups, i.e. 1) physics based models and 2) effective media continuum models (see Squire (2018) and references therein). The GW model belongs to first group, whereby physics are simulated to most extent for each solitary ice floe in ice field. Normally, the GW model is applied along with scattering theory to study wave attenuation and wave induced ice break-up (Kohout and Meylan, 2008, Dumont et al., 2011). Other models fall into the second category, where detailed physics are omitted and heterogeneous ice field is studied as a single entity. Effective media approach lumps together all attenuation mechanisms, scattering and dissipation, into effective viscosity. Nonlinear dissipation mechanisms such as collisions and ridging are accounted for in a linear manner in the second type model (Squire, 2018).

The comparisons of other features of the different models are summarized in Table 1. It is seen that only VCM includes a nonlinear term.

Mode-swap phenomenon inherited in VCWS model may explain the abrupt change of wave number profile with frequency, as shown in Figure 3 of Mosig et al. (2015), Figure 9 of Rogers et al. (2016) and Figure 7 of Collins et al. (2017). This behaviour was investigated extensively in Zhao et al. (2017). They found that outside the mode-swap region, gravity waves contribute most to the vertical motion. Following this, Cheng et al. (2017) selected the least damped propagating gravity wave. However, the efficiency of this root selection criterion should be further investigated. As demonstrated in Collins et al. (2017), the VCFS model displays similar discontinuity in the wave number profile.

Although the root finding criteria are not well-established yet, the VCFS and VCWS models have been implemented in WW3. The VCWS and the VCFS models together with the VSLM model that are embedded in WW3, awaits to be validated. To date, these models are not calibrated sufficiently against full-scale data for various ice types. This suggests that more field experiments including comprehensive ice property survey (such as ice thickness, elastic modulus and viscosity of ice, etc.) are needed (see e.g. Collins et al., 2017, Squire, 2018). In addition, concurrent and collocated measurements of wave height, wave period, wavelength and wave direction are necessary, in order to improve the calibration of these models. Recent progress in sensor technology makes it feasible, e.g. by applying stereo-imaging, SAR (see section 7 for details) and wave buoys in conjunction with marine radar (see Collins et al. (2017) and references therein).

As for WW3, many researchers questioned the current parameterization of S_{ice}, S_{ds}, S_{nl} and S_{in}. Li et al. (2017) questioned the validity of scaling down S_{in} and S_{ds} using fraction of open water. In addition to be suspicious of the current scaling of S_{in}, Rogers et al. (2016) claimed that present parameterization of S_{nl} in ice-covered waters requires in depth examination. Using physical arguments, Squire (2018) maintained that it is inappropriate to simply use ice concentration to scale S_{ice}. It can be seen that parameterizations of these parameters in WW3 are not resolved yet.

Apart from these issues, the debate on whether the rollover phenomenon does physically exist or not is still ongoing. Not all field studies report rollover and no laboratory experiment has yet captured this phenomenon (see Rogers et al. (2016), Li et al. (2017) and references therein). Although this question is not appropriately answered yet, researchers started to investigate the mechanisms, which contribute to this phenomenon. Wadhams et al. (1988) hypothesized that S_{in} and S_{nl} result in rollover. This is corroborated by study of Li et al. (2017) and references therein. However, little consensus is reached at this stage. Therefore, solid theoretical proof for the existence of rollover and lab test designed for this purpose are desired to understand the physical processes, which induce this behaviour.

SAR remote sensing used in ice-covered waters

Synthetic aperture radar (SAR) shows great potential for studying waves interacting with sea ice as it can be used day and night, independent of the weather and it covers large spatial areas. Wadhams et al. (1986) already mentioned the great potential SAR has and since then, SAR imagery was used to study wave parameter modulation in the marginal ice zone.

Some of the first spatial observations of ocean swell in sea ice by SAR were performed in the late 1980s during the Labrador Ice Margin Experiment (LIMEX). From the collected data, Liu et al. (1991, 1992) studied wave evolution in the marginal ice zone in terms of wave attenuation, refraction and dispersion. They found the characteristic rollover at high wave numbers from the

SAR-derived attenuation. Schulz- Stellenfleth and Lehner (2002) used ERS-2 SAR data to study wave damping of ocean waves by sea ice. A detailed theoretical analysis is provided, showing that the dominant wavelength and wave direction can be obtained. Wadhams et al. (2002) also used ERS-2 SAR data to study the wave-dispersion relation in frazil and pancake ice.

The quantitative analysis of SAR imagery in ice-covered regions could only provide an estimation of dominant wave direction and wavelength, until a study by Ardhuin et al. (2015) which estimated wave heights in sea ice in the presence of two ocean swell systems.

New operational satellites in service (e.g. Sentinel 1, TerraSAR-X) provide new opportunities to study the interactions of waves with sea ice due to their high spatial resolutions (e.g. Sentinel-1A wave mode products have a resolution of 4 m on the earth surface). Ardhuin et al. (2017) proposed an algorithm to determine elevation spectra and hence wave parameters. Their algorithm is supposed to work best when short waves are absent, i.e. beyond some tens of kilometers into the sea ice.

Gebhardt et al. (2016) utilized TerraSAR-X satellite scenes to analyze variations in peak wavelength of waves passing through marginal ice zone at the East coast of Greenland. They found an increase in peak wavelength, and the dispersion of waves is the same as in deep waters. Shen et al. (2018) used RADARSAT-2 SAR imagery for the same storm event and found that when waves travel into the marginal ice zone, the dominant wavelength increases, wave energy is attenuated and a shift in mean wave direction. Therefore, SAR imagery is consistent with in situ field observations and attenuation theory.

SAR imagery can provide wave information on a large scale, while in situ measurements provide limited spatial and finer temporal scale observations. A combination of these two provides a more detailed picture and shows great potential for studying wave-ice interactions. From SAR imagery, the dominant wavelength and wave direction can be determined in ice-covered oceans, while the retrieval of wave height is possible, though limited.

Conclusions

From this study, following conclusions are drawn:

1. The VSLM, VCWS and VCFS models appears to be the most desired models to simulate ice effects on ocean surface waves.
2. Large waves are attenuated differently from small and intermediate amplitude waves, which follow exponential attenuation law.
3. Wave mode selection criteria for the VCWS and the VCFS models urgently need improvement.
4. Ice property (such as viscosity, density and elastic modulus) and other oceanographic measurements (such as temperature and salinity profiles along water depth) are necessary to be measured in field campaign for studying wave propagation in ice cover.
5. Field and laboratory experiments are indispensable to conclude whether rollover physically exists and the mechanisms promote it.
6. Calibration and validation work is instrumental in ascertaining the fidelity of using the VSLM, VCWS and VCFS models in wave climate forecast in ice-infested waters.

7. Improved determination methodology for the tuning parameters, eddy viscosity used in viscous model, equivalent elasticity and viscosity, creep constant used in viscoelastic model, is required to reduce uncertainty in inverse analysis problem.
8. Exact effect of ice on S_{in}, S_{ds} and S_{nl} should be thoroughly examined.
9. Validation of scaling S_{ice} with ice concentration is required.
10. SAR remote sensing is an indispensable supplement to in situ measurements to provide a complete picture of the wave-ice interactions process.
11. SAR imagery from satellites can provide the dominant wavelength, wave direction and up to some extent wave heights in ice covered oceans.

Acknowledgement

The authors feel grateful towards the discussions with Knut Høyland, Aleksey Marchenko and Jens Olaf Pepke Pedersen. The authors wish to acknowledge the support from the Research Council of Norway through the Centre for Research-Based Innovation SAMCoT and the support from all SAMCoT partners.

References

Ardhuin, F., Collard, F., Chapron, B., Girard- Ardhuin, F., Guitton, G., Mouche, A. & Stopa, J. E. (2015). Estimates of ocean wave heights and attenuation in sea ice using the SAR wave mode on Sentinel- 1A. Geophysical Research Letters, 42, 2317-2325.

Ardhuin, F., Stopa, J., Chapron, B., Collard, F., Smith, M., Thomson, J., Doble, M., Blomquist, B., Persson, O., Collins, C. O. & Wadhams, P. (2017). Measuring ocean waves in sea ice using SAR imagery: A quasi-deterministic approach evaluated with Sentinel-1 and in situ data. Remote Sensing of Environment, 189, 211-222.

Bennetts, L. G., Alberello, A., Meylan, M. H., Cavaliere, C., Babanin, A. V. & Toffoli, A. (2015). An idealised experimental model of ocean surface wave transmission by an ice floe. Ocean Modelling, 96, 85-92.

Cheng, S., Rogers, W. E., Thomson, J., Smith, M., Doble, M., Wadhams, P., Kohout, A. L., Lund, B., Persson, O., Collins, C. O., Ackley, S. F., Montiel, F. & Shen, H. H. (2017). Calibrating a Viscoelastic Sea Ice Model for Wave Propagation in the Arctic Fall Marginal Ice Zone. Journal of Geophysical Research: Oceans [Online]. Available: http://dx.doi.org/10.1002/2017JC013275 [Accessed October 21, 2017].

Collins, C. O., Rogers, W. E. & Lund, B. (2017). An investigation into the dispersion of ocean surface waves in sea ice. Ocean Dynamics, 67, 263-280.

De Carolis, G. April 02, 2018 2018. RE: Questions regarding your paper - Dispersion and attenuation of gravity waves in ice: a two-layer viscous fluid model with experimental data validation. Type to LI, H.

De Carolis, G. & Desiderio, D. (2002). Dispersion and attenuation of gravity waves in ice: a two-layer viscous fluid model with experimental data validation. Physics Letters A, 305, 399-412.

Dumont, D., Kohout, A. & Bertino, L. (2011). A wave- based model for the marginal ice zone including a floe breaking parameterization. Journal of Geophysical Research: Oceans, 116.

Erber, T., Guralnick, S. & Michels, S. (1993). Hysteresis and fatigue. Annals of Physics, 224, 157-192.

Fox, C. & Squire, V. A. (1994). On the oblique reflexion and transmission of ocean waves at shore fast sea ice. Philosophical Transactions of the Royal Society of London A: Mathematical, Physical and Engineering Sciences, 347, 185-218.

Gebhardt, C., Bidlot, J.-R., Gemmrich, J., Lehner, S., Pleskachevsky, A. & Rosenthal, W. (2016). Wave observation in the marginal ice zone with the TerraSAR-X satellite. Ocean Dynamics, 66, 839-852.

Greenhill, A.-G. (1886). Wave motion in hydrodynamics. American Journal of Mathematics, 62-96.

Keller, J. B. (1998). Gravity waves on ice- covered water. Journal of Geophysical Research: Oceans, 103, 7663-7669.

Kohout, A., Williams, M., Dean, S. & Meylan, M. (2014). Storm-induced sea-ice breakup and the implications for ice extent. Nature, 509, 604.

Kohout, A., Williams, M., Toyota, T., Lieser, J. & Hutchings, J. (2016). In situ observations of wave-induced sea ice breakup. Deep Sea Research Part II: Topical Studies in Oceanography, 131, 22-27.

Kohout, A. L. & Meylan, M. H. (2008). An elastic plate model for wave attenuation and ice floe breaking in the marginal ice zone. Journal of Geophysical Research: Oceans, 113.

Langhorne, P. J., Squire, V. A., Fox, C. & Haskell, T. G. (1998). Break-up of sea ice by ocean waves. Annals of Glaciology, 27, 438-442.

Li, J., Kohout, A. L., Doble, M. J., Wadhams, P., Guan, C. & Shen, H. H. (2017). Rollover of Apparent Wave Attenuation in Ice Covered Seas. Journal of Geophysical Research: Oceans, 122, 8557-8566.

Li, J., Mondal, S. & Shen, H. H. (2015). Sensitivity analysis of a viscoelastic parameterization for gravity wave dispersion in ice covered seas. Cold Regions Science and Technology, 120, 63-75.

Liu, A. K., Holt, B. & Vachon, P. W. (1991). Wave propagation in the marginal ice zone: Model predictions and comparisons with buoy and synthetic aperture radar data. Journal of Geophysical Research: Oceans, 96, 4605-4621.

Liu, A. K. & Mollo-Christensen, E. (1988). Wave propagation in a solid ice pack. Journal of physical oceanography, 18, 1702-1712.

Liu, A. K., Vachon, P. W., Peng, C. Y. & Bhogal, A. (1992). Wave attenuation in the marginal ice zone during LIMEX. Atmosphere-Ocean, 30, 192-206.

Logan, D. L. (2012). A first course in the finite element method, Stamford, Conn, Cengage Learning.

Marchenko, A. Damping of surface waves propagating below solid ice. The 26th International Ocean and Polar Engineering Conference, 2016. International Society of Offshore and Polar Engineers.

Marchenko, A. 2018. RE: Question regarding your paper - Damping of surface waves propagating below solid ice. Type to LI, H.

Mckenna, R. F. & Crocker, G. B. (1990). Wave Energy and Floe Collisions in Marginal Ice Zones. In: MURTHY, T., PAREN, J., SACKINGER, W. & WADHAMS, P. (eds.) International Conference on Ice Technology. Downing College, Cambridge University, UK: Computational Mechanics Publications.

Mckenna, R. F. & Crocker, G. B. (1992). Ice- floe collisions interpreted from acceleration data during LIMEX ‘89. Atmosphere-Ocean, 30, 246-269.

Mosig, J. E., Montiel, F. & Squire, V. A. (2015). Comparison of viscoelastic- type models for ocean wave attenuation in ice- covered seas. Journal of Geophysical Research: Oceans, 120, 6072-6090.

Nelli, F., Bennetts, L., Skene, D., Monty, J., Lee, J., Meylan, M. & Toffoli, A. (2017). Reflection and transmission of regular water waves by a thin, floating plate. Wave Motion, 70, 209-221.

Newyear, K. & Martin, S. (1999). Comparison of laboratory data with a viscous two-layer model of wave propagation in grease ice. Journal of Geophysical Research: Oceans, 104, 7837-7840.

Robinson, N. J. & Palmer, S. C. (1990). A modal analysis of a rectangular plate floating on an incompressible liquid. Journal of Sound and Vibration, 142, 453-460.

Rogers, W. & Orzech, M. (2013). Implementation and testing of ice and mud source functions in WAVEWATCH III, NRL Memorandum Report. NRL/MR/7320-13-9462.

Rogers, W. E. (2017). Wave forecasting for the Marginal Ice Zone [Online]. Available: http://www.waveworkshop.org/15thWaves/index.htm [Accessed November 29 2017].

Rogers, W. E., Thomson, J., Shen, H. H., Doble, M. J., Wadhams, P. & Cheng, S. (2016). Dissipation of wind waves by pancake and frazil ice in the autumn Beaufort Sea. Journal of Geophysical Research: Oceans, 121, 7991-8007.

Schulz-Stellenfleth, J. & Lehner, S. (2002). Spaceborne synthetic aperture radar observations of ocean waves traveling into sea ice. Journal of Geophysical Research: Oceans, 107.

Shen, H., Perrie, W., Hu, Y. & He, Y. (2018). Remote Sensing of Waves Propagating in the Marginal Ice Zone by SAR. Journal of Geophysical Research: Oceans, 123, 189-200.

Shen, H. H. & Squire, V. A. (1998). Wave damping in compact pancake ice fields due to interactions between pancakes, Wiley Online Library.

Squire, V. A. (1993). A comparison of the mass-loading and elastic plate models of an ice field. Cold Regions Science and Technology, 21, 219-229.

Squire, V. A. (2018). A fresh look at how ocean waves and sea ice interact.

Squire, V. A., Dugan, J. P., Wadhams, P., Rottier, P. J. & Liu, A. K. (1995). Of ocean waves and sea ice. Annual Review of Fluid Mechanics, 27, 115-168.

Squire, V. A. & Shen, H. H. Ice floe collisions: a neglected attribute of wave dissipation in ice fields. The Seventh International Offshore and Polar Engineering Conference, 1997. International Society of Offshore and Polar Engineers.

The WAVEWATCH III® Development Group (WW3DG) (2016). User manual and system documentation of WAVEWATCH III® version 5.16, Tech. Note 329, NOAA/NWS/NCEP/MMAB, 329+ Appendices, Tech. Rep.

Thomson, J., Fan, Y., Stammerjohn, S., Stopa, J., Rogers, W. E., Girard-Ardhuin, F., Ardhuin, F., Shen, H., Perrie, W., Shen, H., Ackley, S., Babanin, A., Liu, Q., Guest, P., Maksym, T., Wadhams, P., Fairall, C., Persson, O., Doble, M., Graber, H., Lund, B., Squire, V., Gemmrich, J., Lehner, S., Holt, B., Meylan, M., Brozena, J. & Bidlot, J.-R. (2016). Emerging trends in the sea state of the Beaufort and Chukchi seas. Ocean Modelling, 105, 1-12.

Thomson, J. & Rogers, W. E. (2014). Swell and sea in the emerging Arctic Ocean. Geophysical Research Letters, 41, 3136-3140.

Vizcarra, N. (2018). Arctic sea ice maximum at second lowest in the satellite record [Online]. National Snow and Ice Data Center. Available: http://nsidc.org/arcticseaicenews/2018/03/arctic-sea-ice-maximum-second-lowest/ [Accessed March 29, 2018].

Wadhams, P. (1981). The ice cover in the Greenland and Norwegian Seas. Reviews of geophysics, 19, 345-393.

Wadhams, P. (1986). The seasonal ice zone. The geophysics of sea ice. Springer.

Wadhams, P., Parmiggiani, F. & De Carolis, G. (2002). The use of SAR to measure ocean wave dispersion in frazil–pancake icefields. Journal of physical oceanography, 32, 1721-1746.

Wadhams, P., Squire, V. A., Ewing, J. & Pascal, R. (1986). The effect of the marginal ice zone on the directional wave spectrum of the ocean. Journal of physical oceanography, 16, 358-376.

Wadhams, P., Squire, V. A., Goodman, D. J., Cowan, A. M. & Moore, S. C. (1988). The attenuation rates of ocean waves in the marginal ice zone. Journal of Geophysical Research: Oceans, 93, 6799-6818.

Wang, R. & Shen, H. H. (2010). Gravity waves propagating into an ice- covered ocean: A viscoelastic model. Journal of Geophysical Research: Oceans [Online], 115. Available: http://dx.doi.org/10.1029/2009JC005591 [Accessed September 04, 2017].

Weitz, M. & Keller, J. B. (1950). Reflection of water waves from floating ice in water of finite depth. Communications on Pure and Applied Mathematics, 3, 305-318.

Zhang, J., Schweiger, A., Steele, M. & Stern, H. (2015). Sea ice floe size distribution in the marginal ice zone: Theory and numerical experiments. Journal of Geophysical Research: Oceans, 120, 3484-3498.

Zhao, X., Cheng, S. & Shen, H. H. (2017). Nature of Wave Modes in a Coupled Viscoelastic Layer over Water. Journal of Engineering Mechanics, 143, 04017114.

Zhao, X., Shen, H. H. & Cheng, S. (2015). Modeling ocean wave propagation under sea ice covers. Acta Mechanica Sinica, 31, 1-15.

Appendix B Sentinel-1 SAR observations of peak wavelength and dominant wave direction in the marginal ice zone of the Barents Sea

This paper is published in the Proceedings of the 25th International conference on Port and Ocean Engineering under Arctic conditions, 9-13 June 2019, Delft, Netherlands.

Monteban, D., Lubbad, R., Johnsen, H., 2019b. Sentinel-1 SAR observations of peak wavelength and wave direction in the marginal ice zone of the Barents Sea, in: Proceedings of the 25th International Conference on Port and Ocean Engineering under Arctic Conditions. Delft, Netherlands.

Proceedings of the 25th International Conference on
Port and Ocean Engineering under Arctic Conditions
June 9-13, 2019, Delft, The Netherlands

Sentinel-1 SAR observations of peak wavelength and dominant wave direction in the marginal ice zone of the Barents Sea

Dennis Monteban[1,2], Raed Lubbad[2], Harald Johnsen[3]
[1] DTU Space, Technical University of Denmark, Lyngby, Denmark
[2] The Norwegian University of Science and Technology (NTNU), Trondheim, Norway
[3] Norut (Northern research Institute), Tromsø, Norway

ABSTRACT

Synthetic aperture radar (SAR) has proven to be a very important source of data in the Polar regions because it covers large areas continuously, independent of the weather and time of day. In this study, we make use of Sentinel-1 Interferometric wide (IW) swath SAR images to study the change in peak wavelength and dominant wave direction of long waves traveling through icy waters in the Barents Sea. We verify our estimates of the open water peak wavelength and dominant wave direction by comparing the results from the Sentinel-1 SAR with in-situ buoy measurements, which are part of the *Barents Sea Metocean and Ice Network* (BaSMIN) measurement campaign.

We find that the peak wavelength increases as waves propagate into the sea ice. This agrees well with our knowledge of wave penetration into the MIZ, where the sea ice acts as a natural low pass filter on the ocean waves. A consequence of this is the disappearance of the high frequency waves from SAR images over the sea ice especially at a distance from the ice edge. Since the presence of high frequency waves blur the SAR images, SAR images in sea ice become of higher quality compared to images over the open ocean. As a result, the spread in observations of the peak wavelength is much larger in the open water than within the sea ice.

Further, the dominant wave direction changes towards the normal, relative to the ice edge. This can be motivated by Snell's law and agrees with findings from previous studies. A large shift of the dominant wave direction is found in the vicinity of the ice edge, which is partly physical due to wave refraction and is partly an imaging artefact. The latter stems from that fact that the azimuth cut-off (i.e., loss of spatial resolution along track) is much smaller in the sea ice than in open water and thus waves that were not visible in images over the open water may appear in images over the sea ice. This causes an apparent shift in wave direction close to the ice edge that is purely due to SAR imaging. We demonstrate this effect with our processed images.

KEY WORDS: SAR; Sentinel-1, Marginal Ice Zone, Ocean waves, Sea ice; BaSMIN measurement programme

Introduction

Due to climate change, the Polar regions are experiencing dramatic sea ice reductions. The reduced sea ice cover gives rise to longer open water seasons and will lead to increased commercial activities in the Arctic. For safety reasons it is extremely important to forecast the wave-climate. However, to accurately predict the wave climate in ice-covered oceans, we need to have a proper understanding of the interactions between ocean waves and sea ice.

Sea ice can be classified based on its position to land as: landfast ice zone, shear zone and the marginal ice zone (MIZ). The MIZ is closest to the open water and depending on time and location, a continuous ice sheet, floe aggregates, pancake ice, brash ice and grease ice can be found in this zone (e.g., Zhao et al., 2015). Further, it is the most dynamic and complex zone, as the sea ice is affected by ocean waves through for instance ice breakup (Kohout et al., 2016) ice drift (Perrie and Hu, 1997) and rafting (Dai et al., 2004). Not only do waves affect the sea ice cover, but also the ice has a strong impact on the waves, making the study of wave-ice interactions a two-way coupled problem. Waves propagating through ice-covered oceans show a reduction in amplitude due to wave scattering and dissipation (e.g., Squire 2018). Scattering redistributes the energy and is a conservative process, i.e., no energy is lost. Dissipation on the other hand removes energy from the waves. The ice also affects the waves by refraction, reflection and it changes the dispersion relation (e.g., Squire et al., 1995).

The propagation of ocean waves into the MIZ has been studied by remote sensing for a few decades. Especially synthetic aperture radar (SAR) satellite images are capable of wave measurements in icy waters. In this study, we make use of Sentinel-1 SAR imagery and focus on the change in peak wavelength and dominant wave direction for waves propagating within sea ice in the Barents Sea.

SAR observations have been used to study ocean waves within sea ice, see the review by Monteban et al. (2019). These observations have proven to be a valuable source of information because SAR can operate day and night, independent of the weather, and it can cover a vast area at once. One of the mechanisms that allow the imaging of ocean waves by SAR is velocity bunching (e.g., Alpers et al., 1981). The velocity bunching of short waves blurs the image and results in the well-known azimuth cut-off effect (e.g., Kerbaol et al., 1998). This effect becomes much smaller in sea ice, because the ice cover acts as a low pass filter on the waves and the short wavelengths of wind driven sea are the dominant contribution to the azimuth cut-off. The difference in azimuth cut-off wavelength causes an apparent shift in dominant wave direction close to the ice edge. This happens when comparing an image over open water (with a high azimuth cut-off) with its adjacent image over the sea ice (with a lower azimuth cut-off). Thus, the anticipated change in dominant wave direction from SAR images when waves enter the sea ice is not entirely based on physical processes, but part of it is an imaging effect (Schulz-stellenfleth and Lehner, 2002). A good example of this is given in (Stopa et al., 2018), their Figure 1d, where a significant change in wave direction between an open water area and an ice-covered area can be seen.

The first detailed study on wave refraction at the ice edge was done by Liu et al. (1991), using aircraft SAR. They argued that the critical angle which determines if waves are reflected or refracted, can be found by Snell's law and they showed that it was in agreement with the SAR observations. Shen et al. (2018) studied long waves propagating from the open water into the MIZ with the RADARSAT-2 SAR satellite at the East side of Greenland. They found a lengthening of the peak wavelength in the MIZ and a change in dominant wave direction. Moreover, they reported that the dominant wave direction changes towards the normal direction, relative to the ice edge. The same storm system as studied by Shen et al. (2018) was studied by Gebhardt et al. (2016) using the TerraSAR-X satellite. The TerraSAR-X satellite orbits at an altitude of ~500 km, which is lower than the Sentinel-1 (~700 km) and RADARSAT-2 (~800 km). The low altitude of the TerraSAR-X satellite is advantageous against the non-linear imaging effects of ocean waves (Gebhardt et al., 2015), and has for instance a smaller azimuth cut-off. Gebhardt et al. (2016) looked at the change in peak wavelength for waves travelling long distances (in the order of 1000 km). They found that the observed wavelengths from the TerraSAR-X images are consistent with the spatial dispersion of waves on the open water. The largest increase of the peak wavelength was found in the MIZ, which is most likely due to wave-ice interactions. The study of Stopa et al. (2018) reported, amongst others, the change in wave direction when waves enter the sea ice in the Beaufort Sea. A change of 20-30° is found at the ice edge and further into the ice pack another large change in wave direction is observed. The authors expect that the large change in wave direction is due to refraction, either at the ice edge or due to a change in ice thickness.

In this study we make use of Sentinel-1 SAR imagery and focus on the change in peak wavelength and dominant wave direction when waves propagate within the sea ice. The peak wavelength and dominant wave direction are in this study inferred from the wavenumber and direction associated with the maxima of the image cross spectrum as will be shown later. We study a wave event with long waves captured by the Sentinel-1A satellite, which took place on the 4th of April 2017 in the Barents Sea. We present also new in situ data, which are part of the *Barents Sea Metocean and Ice network* (BaSMIN) measurement campaign. This in situ data are used to verify our derived peak wavelength and dominant wave direction from Sentinel-1 in the open water. The measurement campaign and the studied wave event are introduced in the next section. The wave parameters are derived from the real part of the cross spectrum directly, without applying a modulation transfer function. The cross spectrum is derived using the method of Johnsen & Collard (2009) and the main parts are described in this paper. The obtained peak wavelength and dominant wave direction show an increased peak wavelength and a wave direction change towards the normal as waves penetrate the MIZ.

BaSMIN measurement programme

The BaSMIN field campaign took place from October 2015 until October 2018. This campaign was undertaken by Fugro GEOS Ltd on behalf of Equinor (former Statoil). Five wave scan moorings and five ice profiling moorings were deployed. The wave scan moorings measured current speed and direction, seawater temperature, salinity, wave parameters, atmospheric pressure and temperature, and relative humidity. The ice profile moorings measured ice draft, ice velocity, current velocity, sea water temperature, salinity and pressure. The measurement locations are shown in Figure 2. The relevant in situ data for this project are the wave data collected at wave scan mooring three (WS3). The wave rose and the relation between significant wave height and mean wave period are presented in Figure 1. The dominant direction where the waves come from is west-southwest. Moreover, the highest and longest waves are coming from this direction. This is to be expected, as this is the directional sector which has the largest wave generating fetch.

We studied a wave event that occurred on the 4th of April 2017. This event is characterized by long waves, with a significant wave height of roughly 5 meters and a peak wavelength of 163 meter, measured at wave buoy WS3. The waves propagate approximately from east to west. Sentinel-3 altimetry and Sentinel-1 SAR data were collected during this event. In Figure 2, a Sentinel-3 altimetry track provides the significant wave height and matches the observations at the wave scan moorings well (not shown here). Further, a Sentinel-1 Extra-Wide swath (EW) image is provided. The brighter regions indicate the ice and the darker regions the open water. From this image the approximate location of the ice edge can be seen, and all the ice mooring stations are circumpassed by the sea ice. During this wave event, the ice draft measured at the five ice moorings are in the range of 0.2 – 0.4 m and the ice is therefore thin ice.

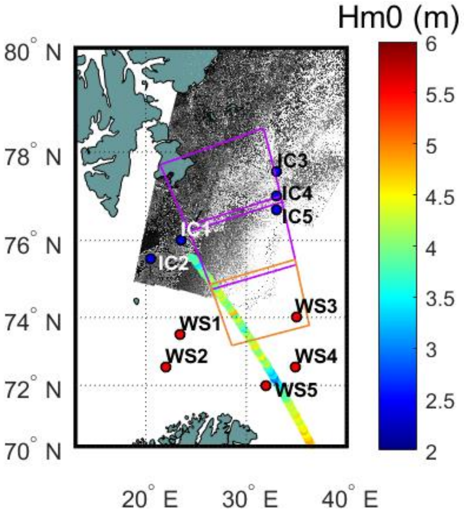

Figure 2. Overview of the BaSMIN measurement locations in the Barents Sea. The red dots indicate the wavescan moorings (WS) and the blue dots the ice mooring locations (IC). A Sentinel-1 EW image is plotted in gray scale, where the lighter areas indicate sea ice. Further, a Sentinel-3 altimetry track is overlaid with the significant wave height (Hm0) given in colour code. The purple and orange rectangles show the extent of Sentinel-1 IW images used to derive the peak wavelength and dominant wave direction. All the satellite data is acquired on the 4th of April 2017.

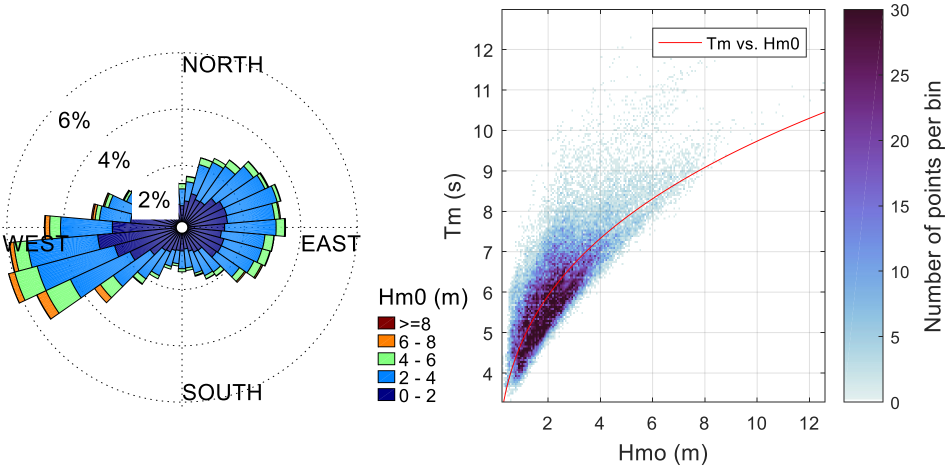

Figure 1. Left figure presents a wave rose and shows the direction from where the waves come from. The right figure shows a scatter plot of the significant wave height (Hm0) vs mean wave period (Tm). The red line is a fit through the data. Both figures show data from wavescan location 3 (WS3) for the entire period of the BaSMIN measurement campaign.

Sentinel-1 data and processing

In this study, we used data collected by ESA's Sentinel-1A satellite. The Sentinel-1 constellation consists of two polar orbiting satellites, carrying a C-band SAR instrument with a frequency of 5.4 GHz. The instrument supports both single and dual polarization. Further, it can operate in four different acquisitions modes that include Stripmap (SM), Interferometric Wide swath (IW), Extra-Wide swath (EW) and Wave (WV). The incidence angle varies between 30° and 46°. We used data collected on the 4th of April 2017, acquired in the IW

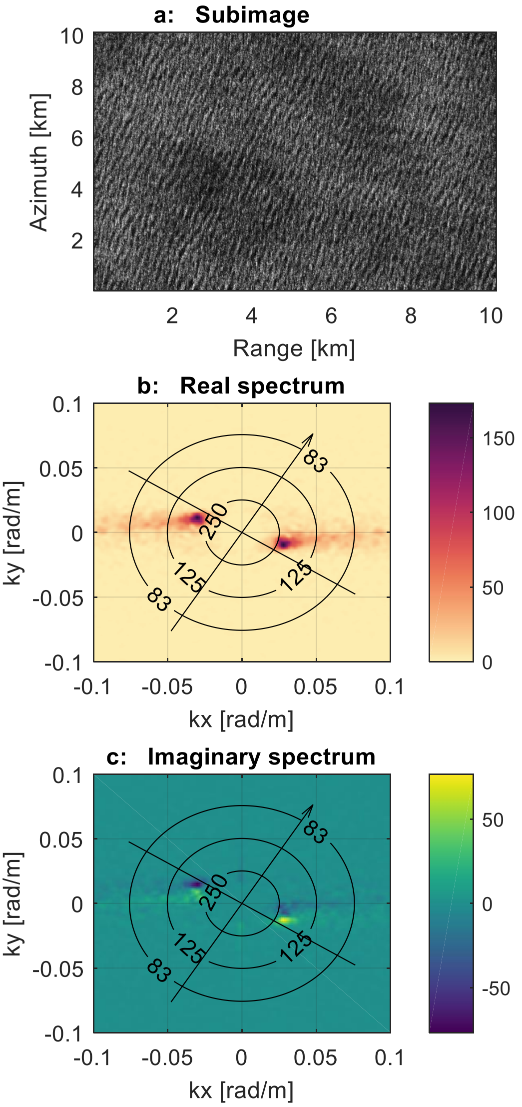

Figure 3. (a) Typical fragment of the Sentinel-1 IW radar scene acquired on the 4th of April 2017, used for the calculation of the cross spectrum. The cross spectrum consists of a real part (panel b) and an imaginary part (panel c). k_x is the wavenumber in range direction and k_y is the wavenumber in azimuth. The arrow points towards north and the overlaid circles indicate the wavelength.

acquisition mode and both HH and HV polarization were available. Throughout this study, we used the HH polarization. The data are a level-1 Single Look Complex (SLC) product that can freely be downloaded from ESA's Sentinel Data Hub. For this data product, the phase information is preserved. This phase information allows us to produce multi looks from which the cross spectrum is calculated (Engen and Johnsen, 1995). The resolution of the data is approximately 3.5 by 14 meter, in range (perpendicular to flight path) and azimuth (along the flight path), respectively. The extent of the data acquired can be seen in Figure 2, indicated by the purple and orange rectangles. Each rectangle is the extent of one data product.

To calculate the peak wavelength and dominant wave direction, we use images of roughly 10 x 10 km. An example is given in Figure 3a, where the normalized intensity is plotted. This complex subimage is first processed into three different sub looks and the cross spectrum is computed between them, following the method of Johnsen & Collard (2009). The resulting real part and imaginary part of the cross spectrum computed from the image in Figure 3a are given in Figure 3b and Figure 3c, respectively. Waves longer than 300 meters are removed from the spectrum by masking out the centre.

From the real part of the cross spectrum, we can find the peak wavelength and the dominant wave direction from the direction and wavenumber of the maximum of the spectrum, but only to within a sign. This is referred to as the 180° wave ambiguity, i.e., it is not clear if the waves come from approximately east or west in this example. This had been a fundamental difficulty in SAR imaging, because traditional SAR images did not include phase information and thus provided a snapshot of the sea surface. With the applied cross-spectral method here, originally developed by Engen & Johnsen (1995), we can solve the 180° wave ambiguity problem. The obtained imaginary part of the cross spectrum has a positive and a negative peak. When the peak in the real part of the cross spectrum matches the positive peak in the imaginary part, this is where the waves are coming from (e.g., Bao & Alpers 1998). Therefore, for the example given in Figure 3, the waves propagate from almost east to west.

The obtained real part of the cross spectrum, also called the image intensity spectrum, is connected to the ocean wave spectra by a Modulation Transfer Function (MTF). This relation is expressed as (e.g., Hasselmann et al., 1985):

$$P(k) = S(k) * R^{SAR}(k)^{2} \tag{1}$$

where $P(k)$ and $S(k)$ are the image intensity spectrum and the ocean wave spectrum, respectively, and $R^{SAR}(k)$ is the MTF. The MTF is a combination of tilt and hydrodynamic modulation in addition to velocity bunching (e.g., Alpers et al., 1981). The MTF has in general a limited effect on the derived peak wavelength and wave direction (e.g., Gebhardt et al., 2016) for range traveling waves and for long waves, not affected by the azimuth cut-off. For our studied wave event, the waves travel near range and are relatively long waves. Therefore, we directly obtain these wave parameters from the image intensity spectrum and do not use an MTF.

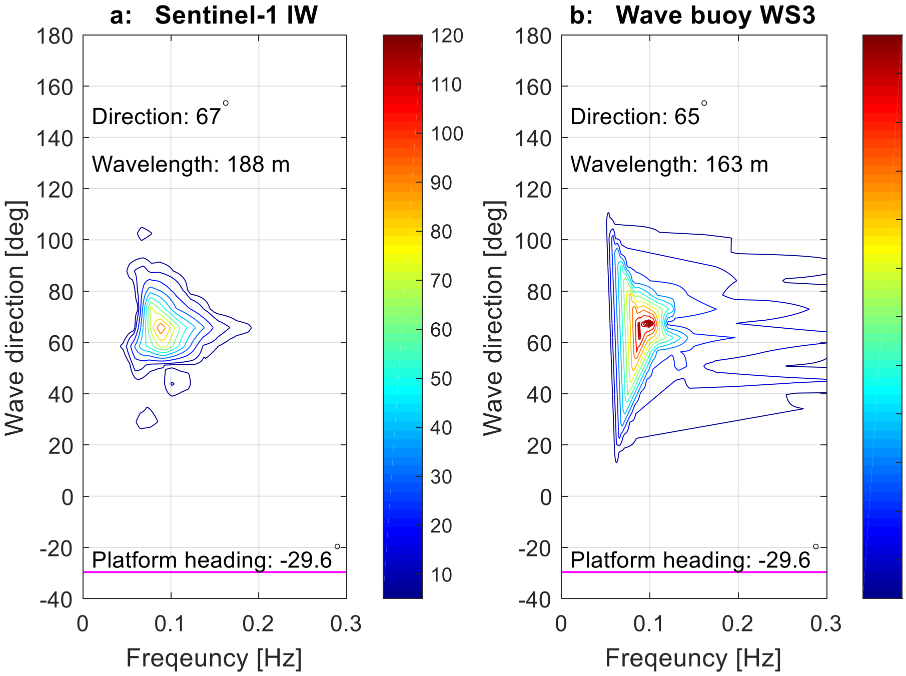

Figure 4. (a) The intensity image spectrum as computed from the Sentinel-1 IW subimage of 10 x 10 km over wave scan mooring WS3. The 180° ambiguity has already been removed and the wave direction indicates the direction the waves are coming from, with respect to north (0° on the y-axis). The frequency spectrum given in panel (a) is calculated from the wavenumber spectrum and using the open water dispersion relation. In addition, the platform heading is shown with the magenta line and indicates the range direction. (b) The wave spectrum obtained at wave buoy WS3. Note that the two plotted spectra are fundamentally different and cannot be directly compared. The relation between the two spectra is given in Eq. (1).

Results

In this section, we present the results of the processed Sentinel-1 IW imagery obtained on the 4th of April 2017. First, we verify our obtained wave parameters in the open ocean with measurements from wave buoy WS3. Then we present the estimated peak wavelength and dominant wave direction in the open water and within the ice-covered ocean. Finally, we demonstrate the azimuth cut-off effect by studying a wave system traveling in azimuth direction and entering the sea ice.

Comparison of the peak wavelength and dominant wave direction with wave buoy WS3

A subimage of the radar scene of roughly 10 x 10 km over buoy WS3 (extent of radar scene is shown with an orange rectangle in Figure 2) is processed and the derived peak wavelength and dominant wave direction are compared with in-situ data from buoy WS3. The image intensity spectrum as obtained from Sentinel-1 and the ocean wave spectrum acquired by wave buoy WS3 are shown in Figure 4. For a one-to-one comparison of the two spectra, one would have to convert the intensity image spectrum from the Sentinel-1 imagery to the wave spectrum using Eq. (1). However, we are only interested in the peak wavelength and dominant wave direction, so we did not do this conversion. The obtained values of the peak wavelength and dominant wave direction from the Sentinel-1 image are 188 m and 67°, respectively. This is satisfactory when compared with the measured wavelength of 163 m and dominant wave direction of 65° from the wave buoy.

Peak wavelength and dominant wave direction

The peak wavelength and dominant wave direction are estimated on subimages of 10 x 10 km, both in the open water and in the sea ice. This is done for two Sentinel-1 IW data products; the extent is shown with the purple rectangles given in Figure 2. The derived wave parameters are plotted in Figure 6 on top of the Sentinel-1 IW images. Each arrow is the average of four different subimages, so it represents an area of roughly 20 x 20 km. The direction of the arrows is very consistent over the range direction. Moreover, the waves are travelling in the open water almost in range direction. This corresponds to waves travelling from east-northeast. The wave direction clearly changes upon entering the sea ice. To better demonstrate the change, we plotted the dominant wave direction in the azimuth direction for fixed range locations in Figure 5b. In addition, the change in dominant wave direction over azimuth, averaged over range, is also plotted in the same figure. We see that the waves come from roughly 70°, with respect to north, in the open water. At the location of the ice edge we see a large shift in direction of roughly 30°. In the sea ice we see a gradual change in wave direction and over approximately 220 km the waves show a directional change of roughly 22°.

The colour of the arrows in Figure 6 indicates the peak wavelength. The derived peak wavelength shows quite some variation over the range direction and it is hard to see the change for waves entering the sea ice from this figure directly. In Figure 5a, the change of the peak wavelength in the azimuth direction is plotted for subimages with a fixed range position. Two things are evident from this figure. The first is that the spread in the estimated peak wavelength is much larger in the open water than within the sea ice. Second, the change of the peak wavelength in azimuth, when averaged over range direction, clearly shows an increase in peak wavelength from the ice edge to roughly 220 km into the ice pack. The peak wavelength for waves that just entered the ice is 210 m, while the peak wavelength 220 km into the sea ice is roughly 231 m.

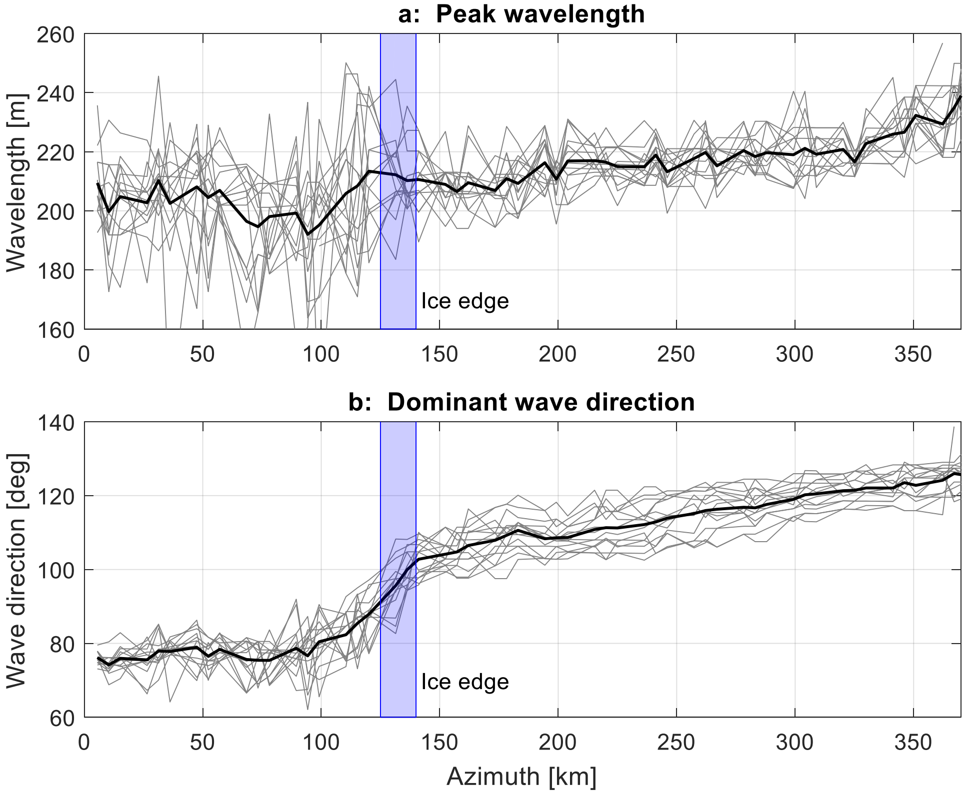

Figure 5. The top figure (a) shows the peak wavelength and the bottom figure (b) displays the dominant wave direction, derived from subimages of 10 x 10 km. The light gray lines show the result of all the subimages in azimuth direction, for a fixed range coordinate. The range positions are 10 km apart. The solid black line shows the results averaged over range direction, i.e., the mean of the light gray lines. The start of ice edge is indicated with the coloured area and is estimated from Figure 6.

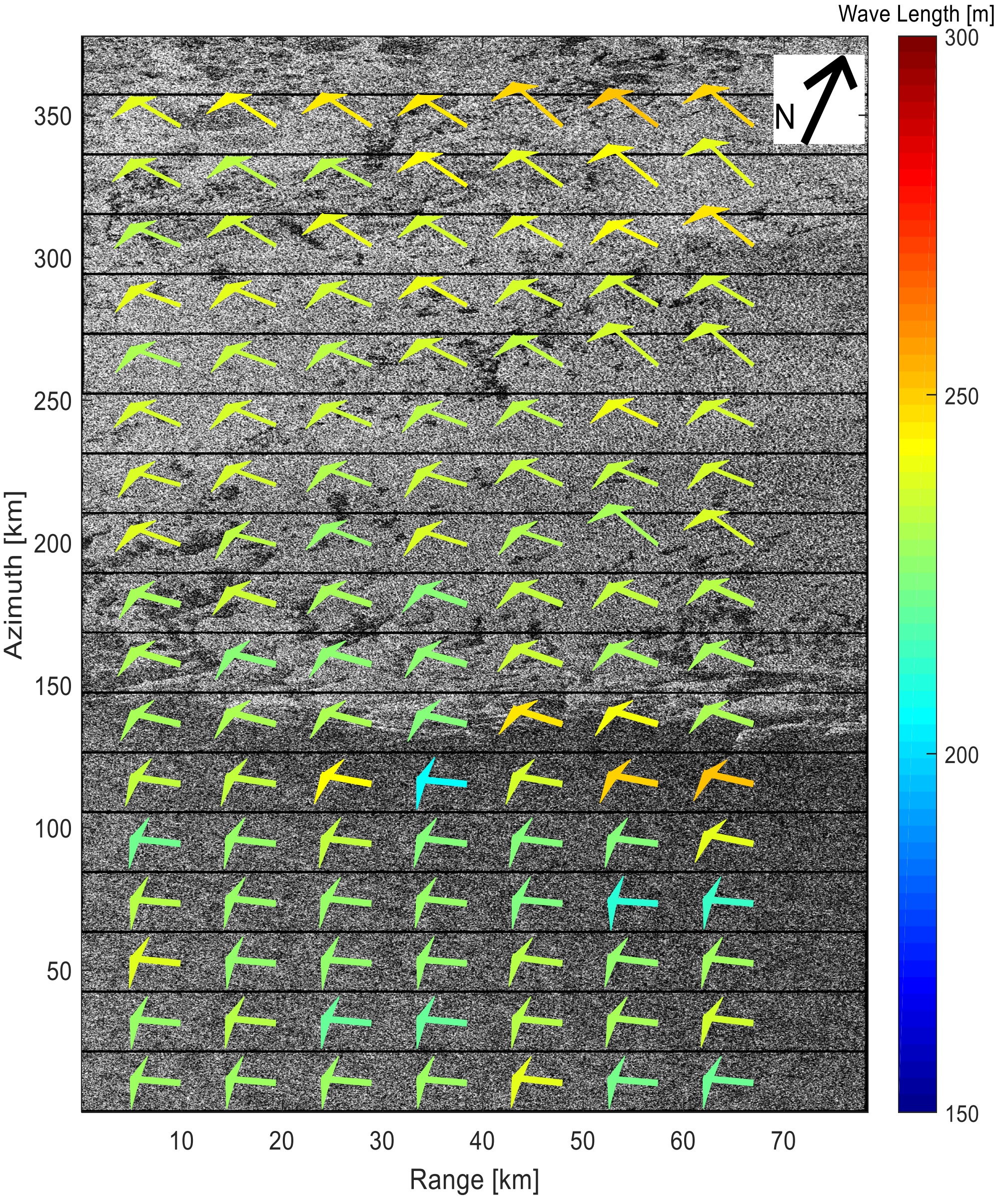

Figure 6. Sentinel-1 IW normalized intensity map (gray scale). The extent is shown in Figure 2 with the two purple rectangles. The brighter regions indicate sea ice, while the darker regions are open water. The ice edge starts around 130-140 km in azimuth direction. The overlaid arrows show the derived peak wavelength and dominant wave direction for subimages of approximately 20 x 20 km. The arrows point in the direction the waves are moving towards and the colour indicates the peak wavelength.

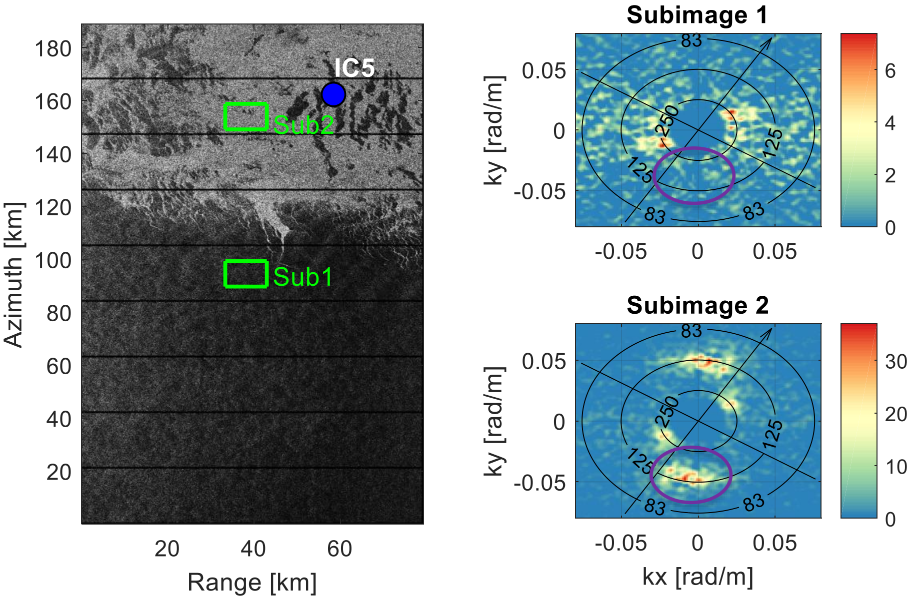

Figure 7. Illustration of the azimuth cut-off effect. The left figure shows a normalised intensity map (gray scale), acquired by Sentinel-1 IW on the 22nd of April 2017. The two image intensity spectra plotted on the right are calculated from the two subimages indicated by the green squares. Note that the 180° wave ambiguity is not removed from the spectra. k_x is the wavenumber in range direction and k_y is the wavenumber in azimuth. The arrow points towards north and the overlaid circles indicate the wavelength.

Azimuth cut-off: open water versus sea ice

The azimuth cut-off effect can nicely be demonstrated when comparing SAR imagery over the open ocean compared to imagery over the sea ice. This is demonstrated in Figure 7. A wave event was captured on the 22nd of April 2017, where two wave systems are present. One swell system traveling close to the range direction and another swell system traveling in the azimuth direction. The image intensity spectra are computed for a subimage over the open ocean (subimage 1) and over the sea ice (subimage 2). The swell system traveling in azimuth direction is not visible in the open ocean but does appear in the sea ice (compare the area in the purple ovals). This is because the azimuth cut-off wavelength is much smaller in the sea ice compared to the open ocean.

Discussion and Conclusions

In this paper we have demonstrated the change in peak wavelength and dominant wave direction of long waves entering the MIZ in the Barents Sea. We used Sentinel-1 SAR imagery, acquired on the 4th of April 2017. The peak wavelength and dominant wave direction are directly inferred from the direction and wavenumber associated with the maxima of the image intensity spectrum, i.e., from the real part of the image cross spectrum. This approach to directly infer the peak wavelength and dominant wave direction from the image spectrum, without applying an MTF, was also applied by Gebhardt et al. (2016) on TerraSAR-X imagery. This approach implies an assumption of a linear relationship between the image intensity spectrum and wave spectrum (Gebhardt et al., 2015) and was validated by Bruck & Lehner (2012) using the TerraSAR-X satellite. This relationship holds for waves traveling near range, or for very long waves that are not affected by the azimuth cut-off. Further, when there is a linear relationship, the maximum value of the image intensity spectrum is not significantly altered by the MTF. For our studied wave event, the waves travel near range and are long waves, suggesting a linear relationship. We verified our derived peak wavelength and dominant wave direction from Sentinel-1 with buoy measurements. The derived values are in good agreement with the measurements, giving confidence in the obtained values for the studied wave event.

The derived peak wavelengths show an increase as the waves enter the MIZ. At the ice edge the peak wavelength is roughly 210 m, while further into the ice pack it is increased to 231 m. This increase in peak wavelength agrees with our understanding of wave penetration into the MIZ. The sea ice found in the MIZ scatters and dissipates the high frequency ocean waves, thereby acting as a low pass filter (Collins et al., 2015). However, part of the increase in peak wavelength can be attributed to the spatial dispersion of waves in the open water (e.g., Gebhardt et al. (2016). Furthermore, the spread in derived peak wavelength in the open water is much larger than for sea ice, see Figure 5a. This can be attributed to the fact that the high frequency waves are not present in the sea ice. The random motions of the short waves blur the image (Alpers and Rufenach, 1979) and the absence of short waves enhances wave visibility in the sea ice (Lyzenga et al., 1985). Therefore, the derived values of the peak wavelength show less spread in the sea ice as the quality of the image is better than in the open ocean.

The dominant direction of the waves coming from the open ocean is roughly 70°, with respect to north. Upon entering the sea ice, a large shift in wave direction of roughly 30° is found. Further in the sea ice the change is small and gradual. The change in dominant wave direction at the ice edge is the largest and in the earliest studies with SAR (e.g., Liu et al., 1991; Shuchman et al., 1994), this change was solely attributed to refraction. However, due to the damping of short waves by the ice, the azimuth cut-off is much smaller in the sea ice compared to the open ocean, as is nicely demonstrated in Figure 7, where waves that are not visible in the open ocean do appear in the image over the sea ice. Therefore, part of the change in dominant wave direction is an imaging artefact, as was demonstrated by Schulz-stellenfleth & Lehner (2002). The result is that the large shift of 30° at the ice edge is partly an imaging artefact and can partly be attributed to refraction. The azimuth cut-off is largest for waves traveling in azimuth direction and it disappears for waves traveling in range direction (e.g., Alpers et al., 1981). Because the waves travel almost in range direction in the open water, we expect that the large change in dominant wave direction at the ice edge is mainly due to refraction. Further, the change in dominant wave direction is towards the normal, relative to the ice edge. This can be motivated by Snell's law, which is in agreement with the results of Liu et al. (1991). This change in wave direction results in wave convergence when the ice edge has a circular shape, potentially leading to a region of increased wave energy and may contribute to ice break up (Shen et al., 2018).

The observations provided in this paper can be used to validate theoretical models such as the viscous layer model or the scattering model, as was for instance done in the study of Shen et al. (2018). Furthermore, the results once again show the great potential of SAR. The availability of freely downloadable data from ESA's Sentinel missions will most certainly improve the understanding of the complex interactions between ocean waves and sea ice.

Acknowledgements

We would like to thank and acknowledge Equinor (former Statoil) and the other BaSMIN JIP members for kindly making the data recorded in the Barents Sea available for this study. The Sentinel-1 and Sentinel-3 data are provided by the European Space Agency (ESA) and can freely be downloaded from ESA's Sentinel data hub. Further we would like to acknowledge the support from the SAMCoT CRI through the Research Council of Norway and all the SAMCoT partners.

References

Alpers, W., Rufenach, C., 1979. The effect of orbital motions on synthetic aperture radar imagery of ocean waves. IEEE Trans. Antennas Propag. 27, 685–690. https://doi.org/10.1109/TAP.1979.1142163

Alpers, W.R., Ross, D.B., Rufenach, C.L., 1981. On the detectability of ocean surface waves by real and synthetic aperture radar. J. Geophys. Res. Ocean. 86, 6481–6498. https://doi.org/10.1029/JC086iC07p06481

Bao, M., Alpers, W., 1998. On the cross spectrum between individual-look synthetic aperture radar images of ocean waves. IEEE Trans. Geosci. Remote Sens. 36, 922–932. https://doi.org/10.1109/36.673683

Bruck, M., Lehner, S., 2012. Sea state measurements using TerraSAR-X data. Geosci. Remote Sens. Symp. (IGARSS), 2012 IEEE Int. 7609–7612. https://doi.org/10.1109/IGARSS.2012.6351866

Collins, C.O., Rogers, W.E., Marchenko, A., Babanin, A. V, 2015. in the Arctic marginal ice zone. Geophys. Res. Lett. 42, 1863–1870. https://doi.org/10.1002/2015GL063063.Received

Dai, M., Shen, H.H., Hopkins, M.A., Ackley, S.F., 2004. Wave rafting and the equilibrium pancake ice cover thickness. J. Geophys. Res. C Ocean. 109, 1–9. https://doi.org/10.1029/2003JC002192

Engen, G., Johnsen, H., 1995. SAR-Ocean Wave Inversion Using Image Cross Spectra. IEEE Trans. Geosci. Remote Sens. 33, 1047–1056. https://doi.org/10.1109/36.406690

Gebhardt, C., Bidlot, J.R., Gemmrich, J., Lehner, S., Pleskachevsky, A., Rosenthal, W., 2016. Wave observation in the marginal ice zone with the TerraSAR-X satellite. Ocean Dyn. 66, 839–852. https://doi.org/10.1007/s10236-016-0957-8

Gebhardt, C., Pleskachevsky, A., Rosenthal, W., Lehner, S., Hoffmann, P., Kieser, J., Bruns, T., 2015. Comparing wavelengths simulated by the coastal wave model CWAM and TerraSAR-X satellite data. Ocean Model. 103, 133–144. https://doi.org/10.1016/j.ocemod.2015.10.003

Hasselmann, K., Raney, R.K., Plant, W.J., Alpers, W., Shuchman, R.A., Lyzenga, D.R., Rufenach, C.L., Tucker, M.J., 1985. Theory of synthetic aperture radar ocean imaging: A MARSEN view. J. Geophys. Res. 90, 4659. https://doi.org/10.1029/JC090iC03p04659

Johnsen, H., Collard, F., 2009. Sentinel-1 ocean swell wave spectra (osw) algorithm definition.

Kerbaol, V., Chapron, B., Vachon, P.W., 1998. Analysis of ERS-1/2 synthetic aperture radar wave mode imagettes. J. Geophys. Res. Ocean. 103, 7833–7846. https://doi.org/10.1029/97JC01579

Kohout, A.L., Williams, M.J.M., Toyota, T., Lieser, J., Hutchings, J., 2016. In situ observations of wave-induced sea ice breakup. Deep. Res. Part II Top. Stud. Oceanogr. 131, 22–27. https://doi.org/10.1016/j.dsr2.2015.06.010

Liu, A.K., Vachon, P.W., Peng, C.Y., 1991. Observation of wave refraction at an ice edge by Synthetic Aperture Radar. J. Geophys. Res. 96, 4803–4808. https://doi.org/10.1029/90JC02546

Lyzenga, D.R., Shuchman, R. a., Lyden, J.D., 1985. SAR Imaging of Waves in Water and Ice : Evidence for Velocity Bunching. J. Geophys. Res. 90, 1031–1036. https://doi.org/10.1029/JC090iC01p01031

Monteban, D., Lubbad, R., Pedersen, J.O.P., 2019. Use of satellite remote sensing to study wave-ice interactions in the marginal ice zone - A review, in: POAC Port and Ocean Engineering under Arctic Conditions. Delft.

Perrie, W., Hu, Y.C., 1997. Air-ice-ocean momentum exchange. Part II: Ice drift. J. Phys. Oceanogr. 27, 1976-1996--. https://doi.org/10.1175/1520-0485(1997)027<1976:AIOMEP>2.0.CO;2

Schulz-stellenfleth, J., Lehner, S., 2002. Spaceborne synthetic aperture radar observations of ocean waves traveling into sea ice. Geophys. Res. Lett. 107, 1–19.

Shen, H., Perrie, W., Hu, Y., He, Y., 2018. Remote Sensing of Waves Propagating in the Marginal Ice Zone by SAR. J. Geophys. Res. Ocean. 123, 189–200. https://doi.org/10.1002/2017JC013148

Shuchman, R. a., Rufenach, C.L., Johannessen, O.M., 1994. Extraction of marginal ice zone thickness using gravity wave imagery. J. Geophys. Res. 99, 901. https://doi.org/10.1029/93JC01956

Squire, V.A., 2018. A fresh look at how ocean waves and sea ice interact. Philos. Trans. R. Soc. A Math. Phys. Eng. Sci. 376, 20170342. https://doi.org/10.1098/rsta.2017.0342

Squire, V.A., Duggan, J.P., Wadhams, P., Rottier, P.J., Liu, A.J., 1995. Of ocean waves and sea ice. Annu. Rev. Fluid Mech. 27, 115–168. https://doi.org/10.1146/annurev.fl.27.010195.000555

Stopa, J.E., Ardhuin, F., Thomson, J., Smith, M.M., Kohout, A., Doble, M., Wadhams, P., 2018. Wave Attenuation Through an Arctic Marginal Ice Zone on 12 October 2015. 1. Measurement of Wave Spectra and Ice Features From Sentinel 1A. J. Geophys. Res. Ocean. 123, 3619–3634. https://doi.org/10.1029/2018JC013791

Zhao, X., Shen, H.H., Cheng, S., 2015. Modeling ocean wave propagation under sea ice covers. Acta Mech. Sin. Xuebao 31, 1–15. https://doi.org/10.1007/s10409-015-0017-5

Appendix C Use of satellite remote sensing to study wave-ice interactions in the marginal ice zone – A review

This paper is published in the Proceedings of the 25th International conference on Port and Ocean Engineering under Arctic conditions, 9-13 June 2019, Delft, Netherlands.

Monteban, D., Lubbad, R., Pedersen, J.O.P., 2019c. Use of satellite remote sensing to study wave-ice interactions in the marginal ice zone - A review, in: Proceedings of the 25th International Conference on Port and Ocean Engineering under Arctic Conditions. Delft, Netherlands.

Proceedings of the 25th International Conference on
Port and Ocean Engineering under Arctic Conditions
June 9-13, 2019, Delft, The Netherlands

Use of satellite remote sensing to study wave-ice interactions in the marginal ice zone – A review

Dennis Monteban[1,2], Raed Lubbad[2], Jens Olaf Pepke Pedersen[1]
[1] Technical University of Denmark (DTU), Space department, Lyngby, Denmark
[2] The Norwegian University of Science and Technology (NTNU), Trondheim, Norway

Abstract

Predicting the wave climate in the Polar regions is vital for navigation and offshore operation safety. These predictions are nowadays made using numerical models based on different theories for wave-ice interactions. To date, hardly any field measurements exist that can be used to validate the proposed theoretical models. Remote sensing observations, on the other hand, have a great potential and they are gaining a widespread interest due to the large amounts of data that can be collected continuously over an extensive area.

In this study, we discuss the use of satellite remote sensing to improve our understanding of wave-ice interactions. Three different types of satellite remote sensing are reviewed, including optical, altimetry and synthetic aperture radar (SAR). We present examples of such data over the Barents Sea, where new in situ data are available. These in situ data, which were collected during the *Barents Sea Metocean and Ice Network* (BaSMIN) field campaign, are used to illuminate the review.

Optical data provide high quality and high-resolution images. However, just a small portion of such data are useful to study wave-ice interactions because only images acquired with daylight and cloud free conditions can be processed. Imagery over our study site reveal a tremendous amount of detail of the sea ice, including a diffusive and compact ice edge. Altimetry data provide accurate wave height information up to the ice edge. Wave height data are collected over our study site and validated with buoy measurements. Since the Polar regions are often dark and cloud covered, active microwave sensors such as SAR are the most valuable source of information in these regions. Four different applications of SAR are reviewed: imaging of ocean waves within the ice cover and determination of the ice edge, ice type and floe size distribution. Regarding ocean waves in sea ice, SAR can provide information on wave attenuation, the change in peak wavelength and the shift in dominant wave direction.

KEY WORDS: Marginal ice zone; Sea ice; Remote sensing; Sentinel missions; BaSMIN measurement programme

1. Introduction

Consequences of a warmer climate and warmer sea temperatures are thawing of permafrost, decreasing sea ice extent and increasing ice sheet melt causing changes in relative sea level. The longer open water seasons and increasing storminess will result in an increased rate of coastal erosion in the Arctic (Solomon, 2005). This increasing rate of coastal erosion is further enhanced by thawing of permafrost leaving many coastal communities and facilities exposed to higher risks. Due to a reduced sea ice cover it is also very likely that commercial activities in the Arctic such as marine transport and access to and recovery of resources (e.g., oil) increases (ACIA, 2004).

For safe marine transport in the Arctic and safe offshore operations, accurate predictions of the wave climate are of utmost importance. Hindcasts and forecasts of the wave climate are nowadays often made using numerical wave models. These models have had a long development history (Komen et al., 1994), but with a focus on mid-latitudes. Due to retreat of the sea ice cover, the economic interest in the Arctic has increased and hence, a numerical wave model that can be applied in ice-covered oceans is vital. To be able to apply wave models in the Arctic, the interaction between sea ice and ocean waves needs to be considered. Including wave-ice interactions is not straightforward as it is a strongly coupled problem: the ice affects the waves by refraction, reflection, attenuation, scattering and changes the dispersion relation (e.g., Squire et al. 1995; Squire 2007). On the other hand, the waves also alter the sea ice cover, for instance by ice breakup (e.g., Kohout et al., 2016).

A major obstacle for the development of ice modules in operational numerical wave models, is the need of validation data (Broström and Christensen, 2008). Data of ocean waves propagating into the marginal ice zone (MIZ) can be collected during measurement campaigns, acquired by remote sensing or simulated in the laboratory. Laboratory experiments have the advantage that many environmental parameters can be controlled and therefore isolate the variables of interest. However, only high frequency waves can be generated, and the scaling effects make the generalization of the results extremely difficult (Collins et al., 2017). In situ data collected in the field does not have scaling issues due to its natural setting and typically provides time series, i.e., the temporal domain. However, the acquired data are sparse and have proved to be challenging and costly to collect in the harsh environment of the Polar regions. Remote sensing, on the other hand, provides continuous data acquired over a large area, i.e., in the spatial domain. Moreover, the cost of collecting these data is limited compared to in situ measurements.

This study focusses on the use of satellite remote sensing observations to study the interaction between ocean waves and sea ice. A review is presented and in addition, we use remote sensing data that were acquired over the Barents Sea. New in situ data is available here that was collected during the *Barents Sea Metocean and Ice network* (BaSMIN) measurement campaign, which will be introduced in Section 2. The additional remote sensing data is used to illuminate the review and by combining with in-situ data, a better picture of the study site is obtained. Moreover, the remote sensing observations can be verified and validated with the in-situ measurements. All the satellite data presented here are acquired by the Sentinel missions from the European Space Agency (ESA), which can freely be downloaded from ESA's Sentinel Data Hub. Three different satellite remote sensing techniques are presented herein including optical, altimetry and synthetic aperture radar (SAR) techniques. Optical imagery obtained by the Sentinel-2 constellation is presented in Section 3. Sentinel-3 altimetry data are presented in Section 4 and validated with buoy measurements. SAR is introduced in Section 5 and four of its applications are presented, including imaging of ocean waves (in the open ocean and within the sea ice) and the determination of the ice edge, ice type and floe size distribution. In addition, some Sentinel-1 SAR data are presented as an example. Finally, a conclusion is given in Section 6.

2. BaSMIN measurement programme

The BaSMIN field campaign took place from October 2015 until October 2018 and was executed by Fugro GEOS Ltd on behalf of Equinor (former Statoil). The bathymetry of the Barents Sea and the measurement locations are presented in Figure 1. In total, there were five wavescan moorings, one seabed mooring and five ice profiling moorings. The wavescan moorings measured the seawater and atmospheric temperature, salinity, atmospheric pressure and humidity, and wave parameters. At the ice mooring locations, the ice and current velocity, ice draft, seawater temperature, salinity and pressure were measured. For this project, we used the significant wave height from the buoys to compare with the values derived from altimetry. The measured ice draft at the ice mooring stations is used to see whether ice is present, which is compared with the sea ice edge determination from SAR data.

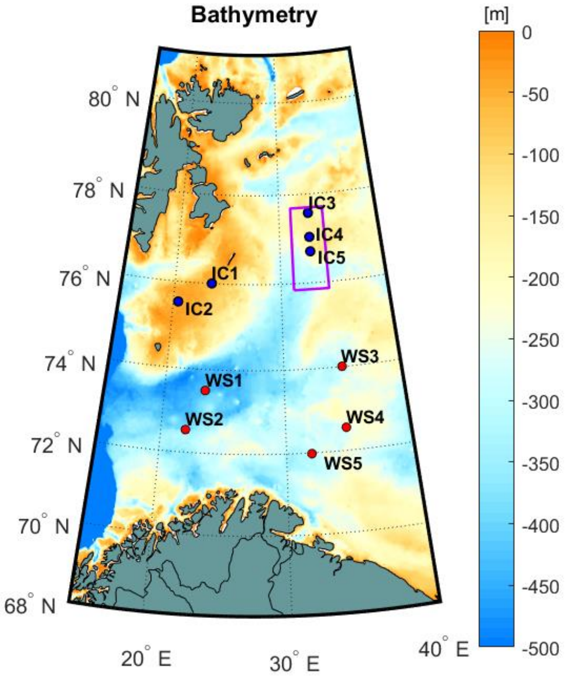

Figure 1. Bathymetry map of the Barents Sea, where the BaSMIN measurement programme took place. The wavescan (WS) moorings are indicated with the red dots and the ice profiling moorings (IC) are shown with the blue dots. The purple rectangle is the extent of the Sentinel-2 imagery, presented in Figure 2. The bathymetry data is taken from the International Bathymetric Chart of the Arctic Ocean (Jakobsson et al., 2012).

3. Optical (Sentinel-2)

The Sentinel-2 constellation consists of twin satellites that follow the same orbit and are phased at 180°. The satellites carry a Multispectral Instrument (MSI) and have the objective of providing high-resolution images at a high revisit frequency (Drusch et al., 2012). The revisit frequency of the twin satellites combined is 5 days. Furthermore, the Sentinel-2 has 13 different spectral bands at a resolution of 10, 20 and 60 meters, depending on the spectral band. A major limitation of the multispectral instrument is that it requires daylight and cloud-free conditions. This severely limits the amount of good and useful images and caused the development of optical techniques to be quite limited (Kudryavtsev et al., 2017).

The high-resolution optical images from Sentinel-2 can be used to observe the ice from above, as illustrated in Figure 2 for our study site. The figure shows Sentinel-2 images of the ice edge close to ice moorings IC3, IC4 and IC5 (see Figure 1), with a resolution of 10 meter. The ice edge is shown on the 2nd of April 2017 in Figure 2a and on the 9th of April 2017 in Figure 2b. The image acquired on the 2nd of April is a good example of a diffuse ice edge, which is characterised by a poorly defined ice edge, an area of dispersed ice and is usually observed at the leeward side. The wind was blowing roughly from north-west for more than 4 days straight before the satellite passed, causing the area of ice to be on the leeward side. Figure 2b shows an example of a compact ice edge. There is a clearly defined ice edge that is compacted by the wind. The wind came from the southeast for approximately 2 days before the image was acquired and therefore the ice edge is on the windward side. Furthermore, Figure 2 provides

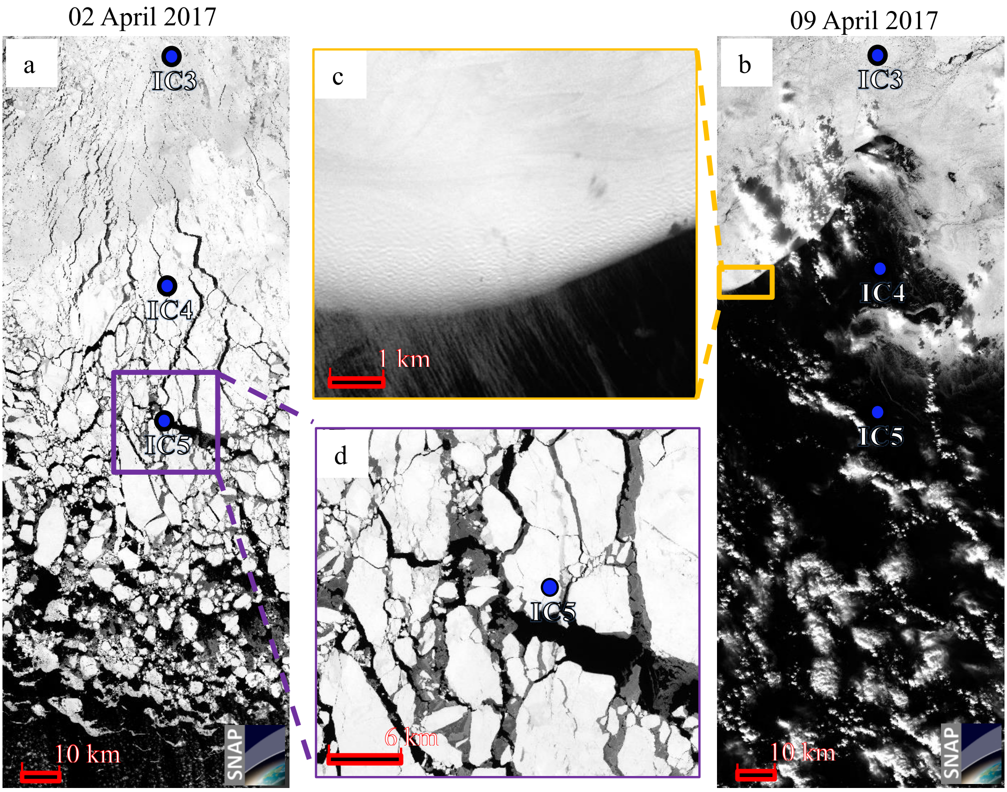

Figure 2. Sentinel-2 imagery (spectral band B4) of the ice edge on the 2nd of April 2017 (panel a) and the 9th of April 2017 (panel b). The extent of panel a and b is indicated in Figure 1. Panel c shows a magnification of the ice edge on the 9th of April. Panel d is a magnification around ice mooring IC5 on the 2nd of April 2017.

magnified images at two locations where a significant amount of detail can be observed. In Figure 2c, waves are visible within the ice at the ice edge. Figure 2d shows the area around ice mooring IC5 and here we can see an example of ice break-up, resulting in ice floes of different sizes, with newly formed ice in between.

Beside the qualitative analysis of the images to observe and understand the ice conditions, a method was developed by Kudryavtsev et al. (2017) to quantitatively retrieve two-dimensional ocean wave spectra from sun glitter imagery. This method uses reflected sunlight (brightness) from the water surface, converted into sea surface elevations in order to perform spectral analysis. However, the method requires a good alignment of the sun, the ocean surface and the satellite. This condition is only met at mid latitudes and not at the high latitude of the Barents Sea.

4. Altimetry (Sentinel-3)

The Sentinel-3 constellation also consists of twin satellites. Sentinel-3 has the objective to deliver operational land and ocean observations. Some of the products that are provided are: sea surface height, ocean surface wind speed, sea surface temperature, significant wave height and land ice/snow surface temperature (European Space Agency, 2013). The satellite carries four main instruments: Ocean and Land Colour Instrument (OLCI), Sea and Land Surface Temperature Instrument (SLSTR), SAR Radar Altimeter (SRAL) and Microwave Radiometer (MWR).

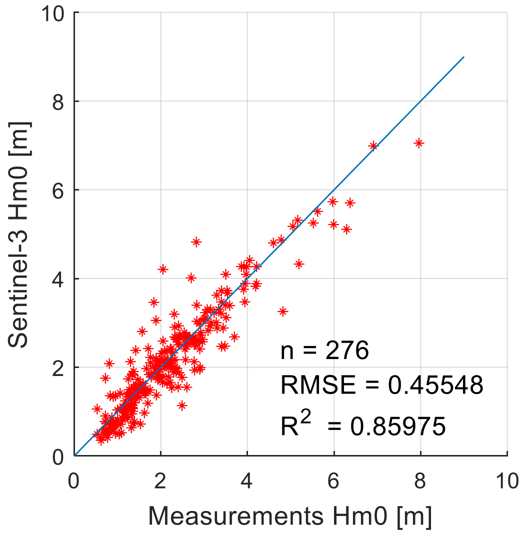

Figure 3. Comparison of the derived significant wave height (Hm0) by the Sentinel-3 constellation and the buoy measurements. Data is included for the period 01-01-2018 until 01-10-2018 from the five wavescan moorings (WS 1-5). Satellite altimetry tracks that pass the wave buoys within 20 km are used, which resulted in 276 observations.

The significant wave height is provided along the track of the satellite from the SRAL instrument. The inter-track distance is 54 km for the two satellites combined. Further, the nadir resolution of the SRAL is more than 2 km and the revisit time is 27 days. The SRAL instrument on the Sentinel-3 satellite can measure significant wave heights within the range of 0.5-20 m, with an error of approximately 4%. (European Space Agency, 2012). In Figure 3 the observations of the Sentinel-3 are plotted against the measurements at the wavescan moorings WS1 to WS5 for the year 2018. Tracks are considered if they pass a wave buoy within 20 km. A total of 276 tracks met this criterion and the observations of the Sentinel-3 are in good agreement with the measurements. A root mean square error (RMSE) of 0.46 and an R-squared value fit to the x=y regression line is 0.86. The information from satellite altimetry has proven to be very accurate (e.g., Vu et al. 2018) and provides additional wave height data over a larger spatial scale than provided by the wave buoys, although the data are still quite sparse. More altimetry satellites are available (e.g., Envisat, SARAL, CryoSat) whose data can be utilised.

In addition to providing information on the ocean waves, altimetry has also been used to estimate sea ice thickness (e.g., Guerreiro et al., 2017; Tilling et al., 2018) and detect open water areas in sea-ice regions (Müller et al., 2017). The estimation of the ice thickness is based on observations of the sea-ice freeboard. The main uncertainty involved when using the freeboard is the presence of snow as it influences the freeboard to a great extent.

5. Synthetic aperture radar (Sentinel-1)

The first SAR satellite was Seasat, which was launched in 1978 (Born et al., 1979). Since then, SAR satellites have provided a tremendous amount of data to study ocean related phenomena, such as surface waves, sea ice, internal waves, currents and wind. The great advantage of SAR over for instance optical imagery is that it operates at wavelengths that are generally unaffected by the cloud cover. Also, it does not require solar illumination, meaning it can operate day and night. Another advantage is that factors such as the frequency, incident angle, polarization, swath width and spatial resolution can be controlled. SAR is an active microwave remote sensing technique. A microwave is sent to an object and the radar measures the intensity backscatter and phase. Standard frequencies of the SAR sensors are X-, C-, S-, L- and P-bands, equivalent to a wavelength of 3 – 75 cm. SAR determines its along-track (azimuth) position by the instantaneous Doppler shift of the reflected signal (e.g., Massonnet & Souyris 2008). This is where SAR differs from real aperture radar (RAR). The major limitation of RAR is that its azimuth resolution is directly proportional to the physical length of the antenna.

5.1. Imaging of ocean waves in open water

Ocean surface imaging by SAR is undoubtedly the least understood and most complex data produced by remote sensing (Holt, 2004). This is because the imaging process is sensitive to a numerous number of parameters, including the motion of the ocean waves, the geometry and properties of the SAR instrument itself.

A SAR image over the ocean consists of a backscatter map and the reflectivity of the radar return is called the Normalized Radar Cross Section (NRCS). The main processes that are responsible for the backscatter depend on the incidence angle. For small incidence angles (< 20°), specular reflection dominates. This reflection is identical to an ordinary mirror, where the angle of the reflected signal is the same as the angle of incidence (Thompson, 2004). However, SAR satellites such as the Sentinel-1 typically operates at incidence angles between 25 and 45°, where Bragg scattering dominates (Valenzuela, 1978). Under Bragg scattering, also referred to as resonance scattering, the radar signal is scattered back by short, wind generated wave components whose wavelength is close to the radar frequency (Holt, 2004).

As mentioned, Bragg scattering mainly reflects the emitted signal. This backscatter is however modulated by three processes which are: hydrodynamic modulation, tilt modulation, and velocity bunching (see for instance: Alpers & Rufenach, 1979; Alpers et al., 1981; Alpers, 1983; Hasselmann et al., 1985). The hydrodynamic modulation is a result of the orbital velocities of long waves. These velocities have different directions along the wave, creating zones of convergence (crest) and divergence (trough). Therefore, on the crest of long waves, the short waves are compressed, and Bragg scattering is increased. The long waves do not only modify the dynamics of the short waves, but also change the local orientation (tilt). This is referred to as tilt modulation. Velocity bunching is caused by the motion of the ocean waves relative to the motion of the satellite. The sea surface motion introduces an extra Doppler shift, which is used to determine its azimuth position and hence, the scatterer or echoes will be misplaced. The periodic motion of the long waves causes an apparent increase and decrease in scatter density, allowing long waves to be visible in SAR imagery. The velocity bunching of short waves also cause random position shifts in azimuth direction and results in an apparent blurring of the SAR image (e.g., Raney 1981). The degraded azimuth resolution results in the well-known azimuth cut-off (Kerbaol et al., 1998). SAR does not sense waves that are shorter than the azimuth cut-off wavelength. It is important to note that velocity bunching modulation is largest for waves traveling in azimuth and disappears for waves traveling in range direction. An example of ocean wave imaging by Sentinel-1 SAR is given in Figure 4. Wave diffraction around Bear Island can be seen. The waves enter the image at the bottom right corner and travel towards the top left corner, i.e., the propagation direction is in between range and azimuth. At the top left of the figure, the waves have diffracted around the island and now travel in range direction. These waves appear much clearer in the image than the waves in the bottom right corner, which is due to

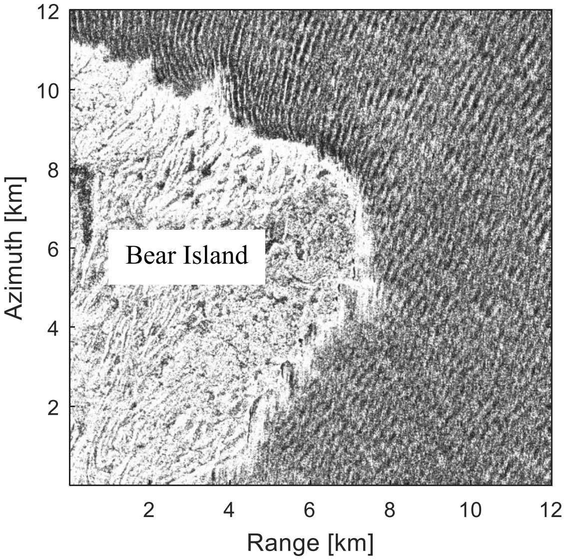

Figure 4. SAR imagery of ocean waves diffracting around Bear Island, located in the Barents Sea. The normalized intensity from a Sentinel-1 GRD product is shown, acquired on the 15th of January 2018 at 05:35:26 UTC.

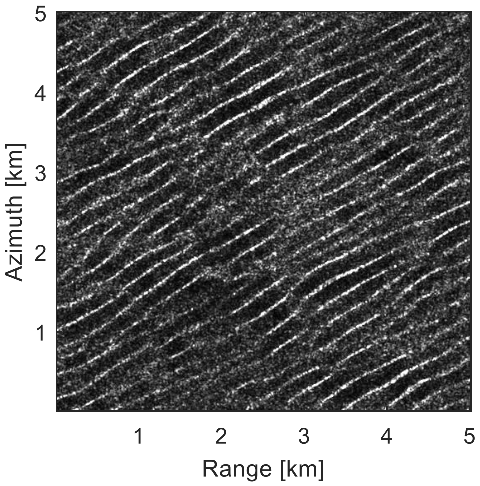

Figure 5. Typical image of long waves within the sea ice. The image is acquired on the 4th of April 2017 at 15:03:19 UTC, just East of Svalbard.

the difference in the velocity bunching modulation for waves traveling in range and azimuth direction.

It is possible to compute the 2D wave spectrum from SAR imagery for waves that are larger than the cut-off wavelength. Following spectral analysis, the intensity variance spectrum can directly be obtained from SAR images. However, to obtain the real wave spectrum one would have to correct for the three modulation mechanisms and the function that does this is called the modulation transfer function (e.g., Vachon et al., 2004). For a more detailed introduction to ocean wave imaging by SAR see for instance (Bruck, 2015; Husson, 2012; Jackson and Apel, 2004).

5.2. Imaging of ocean waves in sea ice

SAR has shown to be able to detect ocean wind waves and swell waves within the sea ice cover. The first observations were made by airborne SAR in the late 1980's and beginning 1990's (Lyzenga et al., 1985; Carsey et al., 1989; Raney et al., 1989; Liu et al., 1991a). The first SAR images obtained from satellites came from Seasat (Fu and Holt, 1982) and one of the most recent launched SAR satellites is the Sentinel-1 constellation.

Ocean waves create patterns in SAR images over the sea ice such as shown in Figure 5. When these patterns are visible in the imagery, the peak wavelength and dominant wave direction can be determined from the image intensity spectrum (Liu et al., 1991a; Schulz-Stellenfleth & Lehner 2002). Multiple studies investigated the change in peak wavelength and dominant wave direction as ocean waves propagate into the MIZ (Gebhardt et al., 2016; A. K. Liu et al., 1991; Monteban et al., 2019; Shen et al., 2018). The peak wavelength increases because the ice cover acts as a low pass filter, damping out the high frequency waves. The dominant wave direction changes due to refraction at the ice edge. However, part of the change in dominant wave direction at the ice edge is an imaging artifact of SAR (Monteban et al., 2019; Schulz-Stellenfleth and Lehner, 2002).

The study of Lyzenga et al. (1985) used SAR imagery of sea ice to show that velocity bunching is the dominant mechanism for waves to be visible within the sea ice. They showed that due to velocity bunching, straight lines such as the ice edge appear as oscillating lines in the images. Ardhuin et al. (2015) used the periodical displacement that results in bright oscillating lines in the ice pack to estimate the orbital velocities, which can be related to the significant wave height when two swell systems are present. Ardhuin et al. (2017) extended this to a methodology to derive the wave spectra, by relating wave patterns visible in the SAR imagery (e.g., Figure 5) to orbital velocities. This method was applied by Stopa et al. (2018a), together with a homogeneity test, based on the homogeneity parameter of (Koch, 2004). A storm event in the Beaufort Sea was captured by Sentinel-1 IW and the wave evaluation over a length of 400 km into the MIZ was studied. They found that wave heights have an attenuation coefficient that varies spatially, which suggest that ice modules in numerical wave models should have multiple wave decay mechanisms. Furthermore, these measurements from SAR were used by Ardhuin et al. (2018) to validate the operational numerical wave model WAVEWATCH III and to test multiple processes that affect ocean waves within the sea ice. The largest dataset of wave attenuation up to date is given by Stopa et al. (2018b) obtained at the Southern Ocean using the

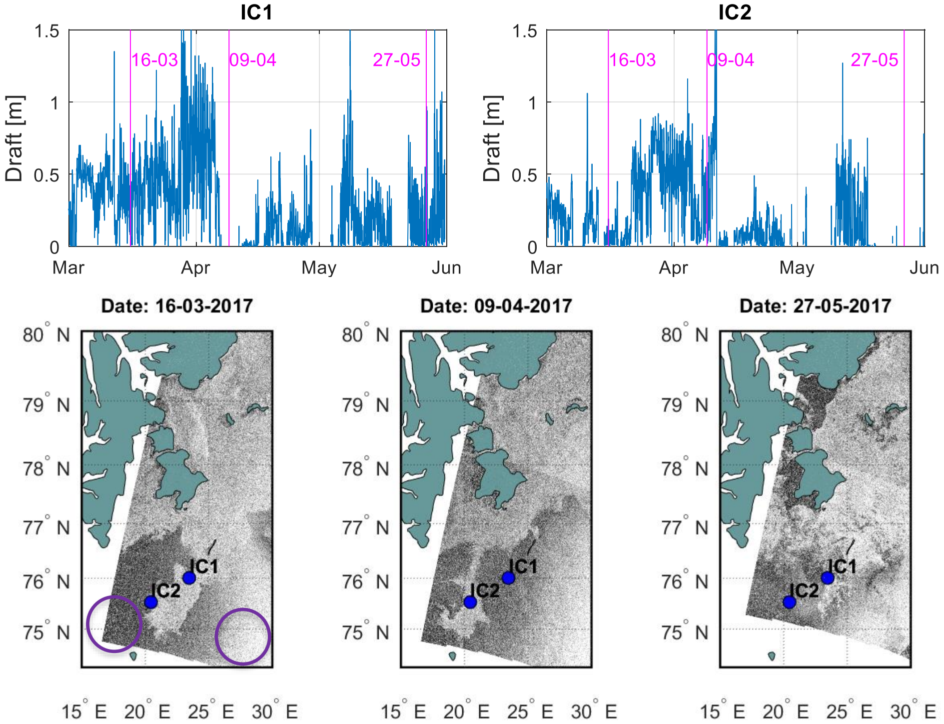

Figure 6. Comparison of the ice draft data at the ice mooring stations IC1 and IC2 with Sentinel-1 EW imagery for three different dates in the year 2017. The Sentinel-1 EW images show the normalized intensity in gray scale.

method of Ardhuin et al., (2015, 2017) and Stopa et al., (2018a). There is in general a weaker attenuation for long waves and a very large scatter (up to 3 orders of magnitude) is observed.

Sea ice affects the ocean waves by, amongst others, changes in the dispersion relation (e.g., Collins et al., 2017). Many different formulations of the wave dispersion relation exist in the literature, but all are a function of the ice thickness. With SAR observations, it is possible to estimate the ice thickness by inverting the wave dispersion relation. This was first done using the mass loading model (Wadhams et al., 2002; Wadhams and Holt, 1991). However, a severe overestimation was found. Later, the viscous layer model was used and good estimates of the ice thickness were obtained (Wadhams et al., 2018, 2004).

5.3. Ice edge

The sea ice terrain is most complex since there are many possible forms of ice and because sea ice properties and the structure are constantly altered by ocean and atmospheric processes. The amount of backscatter from sea ice depends, amongst others, on the surface parameters and is naturally different from the open ocean. The difference in intensity backscatter between the open water and the sea ice can be used to determine the position of the ice edge. Multiple algorithms have been written that automatically find the location of the ice edge (e.g., Liu et al., 1997; Liu et al., 2016; Similä et al., 2013). In Figure 6, we qualitatively show the position of the ice edge around the BaSMIN study site using Sentinel-1 Extra Wide (EW) swath images, acquired on three different dates. The sea ice appears brighter than the open ocean and the ice edge can straightforward be observed. For instance, on the 9th of April 2017, we can see that ice mooring IC2 is circumpassed by the sea ice while ice mooring IC1 is not. This agrees with the ice draft data at these mooring stations as shown in the upper panel of Figure 6. Further, when looking at the Sentinel-1 EW image on the 16th of April 2017, we can see that the brightness on the open water is larger at the east side than on the west side (compare the

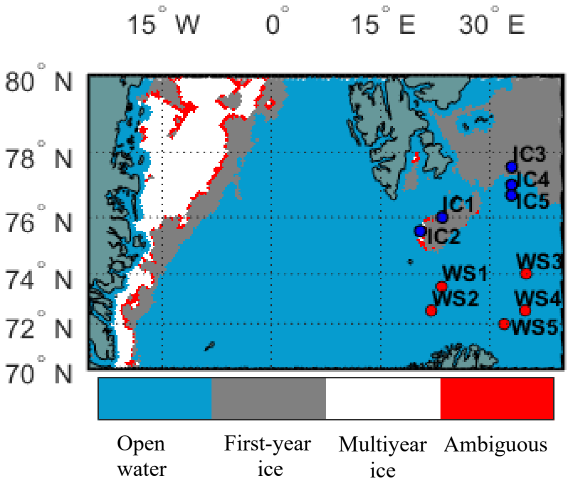

Figure 7. Ice type map for the 1st of March 2018. The data are taken from the dataset Sea ice type product of the EUMETSAT Ocean and Sea Ice Satellite Application Facility (OSI SAR, www.osi-saf.org).

brightness in the purple circles in Figure 6). This is because the incidence angle on the east side is much smaller and some specular reflection occurs here.

5.4. Floe size distribution

To understand the complex dynamics of the Arctic MIZ it is essential to have floe size distribution data. However, floe size distribution data from satellites are quite rare due to the lack of reliable algorithms (Hwang et al., 2017). Some of the challenges encountered include: variability in intensity backscatter, high level of noise, presence of melt ponds, and lack of a method to properly distinguish between adjacent floes in contact. Recently, an algorithm was developed by Hwang et al. (2017) to semi-automatically retrieve floe size distributions from SAR data. Their algorithm performs well for floe sizes larger than 100 m in diameter. Floe sizes smaller than 100 m diameter are usually not detected by the algorithm. With the increasing coverage and spatial resolution of SAR satellites nowadays, it is only to be expected that these algorithms will improve in the future. It will be very interesting to understand the coupling between certain wave events and the floe size distribution. This will be possible in the future when the algorithms improve, and a large dataset becomes available.

5.5. Ice type

The backscatter from sea ice varies, as the characteristics of the illuminated area are different, i.e., different ice forms and properties. Backscatter response is different during winter and summer times and there are four surface parameters that affect the scattering characteristics: the surface roughness, the dielectric constant, dielectric discontinuities (e.g., gas bubbles) and the orientation of the sea ice (Onstott and Shuchman, 2004). Therefore, the intensity backscatter consists of surface and volume scattering. Furthermore, the appearance of sea ice in SAR images is also affected by: the frequency of the SAR sensor, the polarization, the incidence angle, the noise level and the spatial resolution (Dierking, 2013). Considerable efforts have been dedicated over the last few decades to understand the sensitivity of the radar backscatter for various ice properties and different SAR sensor configurations (frequency, polarization, etc.). For instance, surface scattering dominates the backscatter from first-year ice and can be very low if the ice is formed under calm conditions and is therefore very smooth (specular reflection). Multi-year ice is less saline and has a greater microwave penetration depth, i.e., volume scattering dominates. This leads to a higher backscatter return than for first-year ice (Onstott and Shuchman, 2004).

Combining data from different satellite sensors made it possible to produce maps giving the type of ice. An example of an ice type map that includes the study site of the BaSMIN programme is given in Figure 7. It has a resolution of 10 km and is among other things based on the sensors: ASCAT, AMSR-2 and SSMIS. From the figure, it can be seen that on this date there is only first-year ice around the study site. Multi-year ice can be observed at the east side of Greenland.

6. Conclusions

In this study we reviewed three different types of satellite remote sensing, including optical, altimetry and SAR. To illuminate the review, we used remote sensing data acquired by ESA's Sentinel missions over the BaSMIN study site. We show how in situ data can be used in combination with remote sensing observations to provide a clearer picture. Moreover, the in-situ data can be used to validate multiple remote sensing observations, and hence increase the confidence we have in them.

Optical imagery can provide high resolution and high-quality images, up to 10-meter resolution for Sentinel-2. However, optical sensors require solar illumination and cloud free conditions. This severely limits the number of usable images, especially in the Polar regions.

Altimetry data provides, amongst others, very accurate significant wave height data in the open ocean. In this study we used Sentinel-3 wave height data and compared it with the buoy measurements obtained during the BaSMIN programme. We used satellite tracks that are within a radius of 20 km of the wave buoys, which resulted in 276 observations for the year 2018. The comparison shows very good results with an RMSE of 0.46 and an R^2 value of 0.86. In addition, altimetry can provide information regarding the sea ice freeboard, which can be used to calculate the ice thickness.

SAR data are the most useful source of information in the Polar regions as it provides information over large spatial scales and does not require solar illumination or cloud free conditions. SAR has been used to study wave propagation within the sea ice and an increase in peak wavelength, change in dominant wave direction and wave attenuation have been reported in literature. Furthermore, SAR can be used to determine the position of the ice edge and distinguish between ice type (e.g., first and multi-year ice). Floe size distributions can be estimated, but the algorithms so far are not very reliable and only work for large floe sizes.

Overall, satellite remote sensing observations are a very valuable source in order to study wave-ice interactions. Data over large spatial areas can be obtained for a relatively low cost. It should however be combined with in situ data as much as possible. In this way, information in the temporal domain and spatial domain are combined, which provide the clearest picture of the processes at play.

Acknowledgements

We would like to thank and acknowledge Equinor (former Statoil) and the other BaSMIN JIP members for kindly making the data recorded in the Barents Sea available for this project. The Sentinel-1, Sentinel-2 and Sentinel-3 data are provided by the European Space Agency (ESA) and can freely be downloaded from ESA's Sentinel data hub. Further we would like to acknowledge the support from the SAMCoT CRI through the Research Council of Norway and all the SAMCoT partners.

References

ACIA, 2004. Impacts of a Warming Arctic: Arctic Climate Impact Assessment. ACIA Overv. Rep. 140. https://doi.org/10.2277/0521617782

Alpers, W., 1983. Monte Carlo Simulations for Studying the Relationship Between Ocean Wave and Synthetic Aperture Radar Image Spectra. J. Geophys. Res. 88, 1745–1759.

Alpers, W., Rufenach, C., 1979. The effect of orbital motions on synthetic aperture radar imagery of ocean waves. IEEE Trans. Antennas Propag. 27, 685–690. https://doi.org/10.1109/TAP.1979.1142163

Alpers, W.R., Ross, D.B., Rufenach, C.L., 1981. On the detectability of ocean surface waves by real and synthetic aperture radar. J. Geophys. Res. Ocean. 86, 6481–6498. https://doi.org/10.1029/JC086iC07p06481

Ardhuin, F., Boutin, G., Stopa, J., Girard-Ardhuin, F., Melsheimer, C., Thomson, J., Kohout, A., Doble, M., Wadhams, P., 2018. Wave Attenuation Through an Arctic Marginal Ice Zone on 12 October 2015. 2. Numerical Modeling of Waves and Associated Ice Breakup. J. Geophys. Res. Ocean. 1–17. https://doi.org/10.1029/2018JC013791

Ardhuin, F., Collard, F., Chapron, B., Girard-Ardhuin, F., Guitton, G., Mouche, A., Stopa, J.E., 2015. Estimates of ocean wave heights and attenuation in sea ice using the SAR wave mode on Sentinel-1A. Geophys. Res. Lett. 42, 2317–2325. https://doi.org/10.1002/2014GL062940

Ardhuin, F., Stopa, J., Chapron, B., Collard, F., Smith, M., Thomson, J., Doble, M., Blomquist, B., Persson, O., Collins, C.O., Wadhams, P., 2017. Measuring ocean waves in sea ice using SAR imagery: A quasi-deterministic approach evaluated with Sentinel-1 and in situ data. Remote Sens. Environ. 189, 211–222. https://doi.org/10.1016/j.rse.2016.11.024

Born, G.H., Dunne, J.A., Lame, D.B., 1979. Seasat Mission Overview. Am. Assoc. Adv. Sci. 204, 1405–1406.

Broström, G., Christensen, K., 2008. Waves in sea ice. Met.No Rep.

Bruck, M., 2015. Sea State measurements usiong TerraSAR-X/TanDEM-X data (PhD Thesis). Kiel.

Carsey, F.D., Argus, S.A.D., Collins, M.J., Holt, B., Livingstone, C.E., Tang, C.L., 1989. Overview of LIMEX’87 ice observations. IEEE Trans. Geosci. Remote Sens. 27, 468–482. https://doi.org/10.1109/TGRS.1989.35930

Collins, C.O., Rogers, W.E., Lund, B., 2017. An investigation into the dispersion of ocean surface waves in sea ice. Ocean Dyn. 67, 263–280. https://doi.org/10.1007/s10236-016-1021-4

Dierking, W., 2013. Sea Ice Monitoring by Synthetic Aperture Radar. Oceanography 26, 100–111. https://doi.org/10.5670/oceanog.2013.33

Drusch, M., Del Bello, U., Carlier, S., Colin, O., Fernandez, V., Gascon, F., Hoersch, B., Isola, C., Laberinti, P., Martimort, P., Meygret, A., Spoto, F., Sy, O., Marchese, F., Bargellini, P., 2012. Sentinel-2: ESA’s Optical High-Resolution Mission for GMES Operational Services. Remote Sens. Environ. 120, 25–36. https://doi.org/10.1016/j.rse.2011.11.026

European Space Agency, 2013. Sentinel-3 User Handbook. https://doi.org/GMES-S1OP-EOPG-TN-13-0001

European Space Agency, 2012. Sentinel-3: ESA’s Global Land and Ocean Mission for GMES Operational Services. Esa Sp-1322/3 97.

Fu, L., Holt, B., 1982. Seasat views oceans with synthetic-aperture radar. JPL Publ. 81-120 204. https://doi.org/10.1111/j.1365-2133.2012.11180.x

Gebhardt, C., Bidlot, J.R., Gemmrich, J., Lehner, S., Pleskachevsky, A., Rosenthal, W., 2016. Wave observation in the marginal ice zone with the TerraSAR-X satellite. Ocean Dyn. 66, 839–852. https://doi.org/10.1007/s10236-016-0957-8

Guerreiro, K., Fleury, S., Zakharova, E., Kouraev, A., Rémy, F., Maisongrande, P., 2017. Comparison of CryoSat-2 and ENVISAT radar freeboard over Arctic sea ice: Toward an improved Envisat freeboard retrieval. Cryosphere 11, 2059–2073. https://doi.org/10.5194/tc-11-2059-2017

Hasselmann, K., Raney, R.K., Plant, W.J., Alpers, W., Shuchman, R.A., Lyzenga, D.R., Rufenach, C.L., Tucker, M.J., 1985. Theory of synthetic aperture radar ocean imaging: A MARSEN view. J. Geophys. Res. 90, 4659. https://doi.org/10.1029/JC090iC03p04659

Holt, B., 2004. Chapter 2. SAR Imaging of the Ocean Surface, in: Synthetic Aperture Radar Marine User’s Manual. pp. 25–79.

Husson, R., 2012. Development and validation of a global observation-based swell model using wave mode operating Synthetic Aperture Radar. Université de Bretagne, Brest.

Hwang, B., Ren, J., McCormack, S., Berry, C., Ben Ayed, I., Graber, H.C., Aptoula, E., 2017. A practical algorithm for the retrieval of floe size distribution of Arctic sea ice from high-resolution satellite Synthetic Aperture Radar imagery. Elem Sci Anth 5, 38. https://doi.org/10.1525/elementa.154

Jackson, C.R., Apel, J.R., 2004. Synthetic Aperture Radar: Marine User's Manual. https://doi.org/10.1016/S0165-4101(01)00024-6

Jakobsson, M., Mayer, L., Coakley, B., Dowdeswell, J.A., Forbes, S., Fridman, B., Hodnesdal, H., Noormets, R., Pedersen, R., Rebesco, M., Schenke, H.W., Zarayskaya, Y., Accettella, D., Armstrong, A., Anderson, R.M., Bienhoff, P., Camerlenghi, A., Church, I., Edwards, M., Gardner, J. V., Hall, J.K., Hell, B., Hestvik, O., Kristoffersen, Y., Marcussen, C., Mohammad, R., Mosher, D., Nghiem, S. V., Pedrosa, M.T., Travaglini, P.G., Weatherall, P., 2012. The International Bathymetric Chart of the Arctic Ocean (IBCAO) Version 3.0. Geophys. Res. Lett. 39, 1–6. https://doi.org/10.1029/2012GL052219

Kerbaol, V., Chapron, B., Vachon, P.W., 1998. Analysis of ERS-1/2 synthetic aperture radar wave mode imagettes. J. Geophys. Res. Ocean. 103, 7833–7846. https://doi.org/10.1029/97JC01579

Koch, W., 2004. Directional analysis of SAR images aiming at wind direction. IEEE Trans. Geosci. Remote Sens. 42, 702–710. https://doi.org/10.1109/TGRS.2003.818811

Kohout, A.L., Williams, M.J.M., Toyota, T., Lieser, J., Hutchings, J., 2016. In situ observations of wave-induced sea ice breakup. Deep. Res. Part II Top. Stud. Oceanogr. 131, 22–27. https://doi.org/10.1016/j.dsr2.2015.06.010

Komen, G., Cavaleri, L., Donelan, M., Hasselmann, K., Hasselmann, S., Janssen, P., 1994. Dynamics and Modelling of Ocean Waves. Cambridge University Press, Cambridge.

Kudryavtsev, V., Yurovskaya, M., Chapron, B., Collard, F., 2017. Sun glitter imagery of surface waves. Part 2:Waves transformation on ocean currents. J. Geophys. Res. 1384–1399. https://doi.org/10.1002/2016JC012425.Sun

Liu, A.K., Holt, B., Vachon, P.W., 1991a. Wave propagation in the marginal ice zone: Model predictions and comparisons with buoy and synthetic aperture radar data. J. Geophys. Res. Ocean. 96, 4605–4621. https://doi.org/10.1029/90JC02267

Liu, A.K., Martin, S., Kwok, R., 1997. Tracking of ice edges and ice floes by wavelet analysis of SAR images. J. Atmos. Ocean. Technol. 14, 1187–1198. https://doi.org/10.1175/1520-0426(1997)014<1187:TOIEAI>2.0.CO;2

Liu, A.K., Vachon, P.W., Peng, C.Y., 1991b. Observation of wave refraction at an ice edge by Synthetic Aperture Radar. J. Geophys. Res. 96, 4803–4808. https://doi.org/10.1029/90JC02546

Liu, J., Scott, K.A., Gawish, A., Fieguth, P., 2016. Automatic detection of the ice edge in SAR imagery using curvelet transform and active contour. Remote Sens. 8, 1–16. https://doi.org/10.3390/rs8060480

Lyzenga, D.R., Shuchman, R. a., Lyden, J.D., 1985. SAR Imaging of Waves in Water and Ice : Evidence for Velocity Bunching. J. Geophys. Res. 90, 1031–1036. https://doi.org/10.1029/JC090iC01p01031

Massonnet, D., Souyris, J.-C., 2008. Imaging with Synthetic Aperture Radar.

Monteban, D., Lubbad, R., Johnsen, H., 2019. Sentinel-1 SAR observations of peak wavelength and wave direction in the marginal ice zone of the Barents Sea, in: POAC Port and Ocean Engineering under Arctic Conditions.

Müller, F.L., Dettmering, D., Bosch, W., Seitz, F., 2017. Monitoring the arctic seas: How satellite altimetry can be used to detect openwater in sea-ice regions. Remote Sens. 9. https://doi.org/10.3390/rs9060551

Onstott, R.G., Shuchman, R. a., 2004. Chapter 3. SAR Measurements of Sea Ice, in: SAR Marine User's Manual. pp. 81–115.

Raney, R.K., 1981. Wave Orbital Velocity Fade & Sar Response To Azimuth Waves. IEEE J. Ocean. Eng. OE-6, 140–146. https://doi.org/10.1109/JOE.1981.1145495

Raney, R.K., Vachon, P.W., Abreu, R.A., Bhogal, A.S., 1989. Airborne SAR Observations of

Ocean Surface Waves Penetrating Floating Ice. IEEE Trans. Geosci. Remote Sens. 27, 492–500.

Schulz-Stellenfleth, J., Lehner, S., 2002. Spaceborne synthetic aperture radar observations of ocean waves traveling into sea ice. Geophys. Res. Lett. 107, 1–19.

Shen, H., Perrie, W., Hu, Y., He, Y., 2018. Remote Sensing of Waves Propagating in the Marginal Ice Zone by SAR. J. Geophys. Res. Ocean. 123, 189–200. https://doi.org/10.1002/2017JC013148

Similä, M., Dinessen, F., Hughes, N.E., Mäkynen, M., 2013. Ice Edge Detection With Dual-polarized Sar Data. POAC'13 Proc.

Solomon, S.M., 2005. Spatial and temporal variability of shoreline change in the Beaufort-Mackenzie region, northwest territories, Canada. Geo-Marine Lett. 25, 127–137. https://doi.org/10.1007/s00367-004-0194-x

Squire, V.A., 2007. Of ocean waves and sea-ice revisited. Cold Reg. Sci. Technol. 49, 110–133. https://doi.org/10.1016/j.coldregions.2007.04.007

Squire, V.A., Duggan, J.P., Wadhams, P., Rottier, P.J., Liu, A.J., 1995. Of ocean waves and sea ice. Annu. Rev. Fluid Mech. 27, 115–168. https://doi.org/10.1146/annurev.fl.27.010195.000555

Stopa, J.E., Ardhuin, F., Thomson, J., Smith, M.M., Kohout, A., Doble, M., Wadhams, P., 2018a. Wave Attenuation Through an Arctic Marginal Ice Zone on 12 October 2015. 1. Measurement of Wave Spectra and Ice Features From Sentinel 1A. J. Geophys. Res. Ocean. 123, 3619–3634. https://doi.org/10.1029/2018JC013791

Stopa, J.E., Sutherland, P., Ardhuin, F., 2018b. Strong and highly variable push of ocean waves on Southern Ocean sea ice. Proc. Natl. Acad. Sci. U. S. A. 237, 1–5. https://doi.org/10.1073/pnas.1802011115

Thompson, D.R., 2004. Chapter 4. Microwave Scattering from the Sea, in: Synthetic Aperture Radar Marine User's Manual. pp. 117–138.

Tilling, R.L., Ridout, A., Shepherd, A., 2018. Estimating Arctic sea ice thickness and volume using CryoSat-2 radar altimeter data. Adv. Sp. Res. 62, 1203–1225. https://doi.org/10.1016/j.asr.2017.10.051

Vachon, P.W., Monaldo, F.M., Holt, B., Lehner, S., 2004. Chapter 5. Ocean Surface Waves and Spectra, in: SAR Marine User's Manual. pp. 139–169.

Valenzuela, G.R., 1978. Theories for the interaction of electromagnetic and oceanic waves - A review. Boundary-Layer Meteorol. 13, 61–85. https://doi.org/10.1007/BF00913863

Vu, P.L., Frappart, F., Darrozes, J., Ramillien, G., Marieu, V., Blarel, F., Bonnefond, P., 2018. Jason-3 and Sentinel-3A Altimeter Validation Along the French Atlantic Coast in the Southern Bay of Biscay. IGARSS 2018 - 2018 IEEE Int. Geosci. Remote Sens. Symp. 3793–3796. https://doi.org/10.1109/IGARSS.2018.8519532

Wadhams, P., Aulicino, G., Parmiggiani, F., Persson, P.O.G., Holt, B., 2018. Pancake Ice Thickness Mapping in the Beaufort Sea From Wave Dispersion Observed in SAR Imagery. J. Geophys. Res. Ocean. 123, 2213–2237. https://doi.org/10.1002/2017JC013003

Wadhams, P., Holt, B., 1991. Waves in frazil and pancake ice and their detection in Seasat synthetic aperture radar imagery. J. Geophys. Res. 96, 8835–8852. https://doi.org/10.1029/91JC00457

Wadhams, P., Parmiggiani, F., de Carolis, G., 2002. The Use of SAR to Measure Ocean Wave Dispersion in Frazil–Pancake Icefields. J. Phys. Oceanogr. 32, 1721–1746. https://doi.org/10.1175/1520-0485(2002)032<1721:TUOSTM>2.0.CO;2

Wadhams, P., Parmiggiani, F.F., De Carolis, G., Desiderio, D., Doble, M.J., 2004. SAR imaging of wave dispersion in Antarctic pancake ice and its use in measuring ice thickness. Geophys. Res. Lett. 31, L15305. https://doi.org/10.1029/2004GL020340

Appendix D Spatiotemporal Observations of Wave Dispersion Within Sea Ice Using Sentinel-1 SAR TOPS Mode

This paper is published in the Journal of Geophysical Research: Oceans.

Monteban, D., Johnsen, H., Lubbad, R., 2019a. Spatiotemporal Observations of Wave Dispersion Within Sea Ice Using Sentinel-1 SAR TOPS Mode. J. Geophys. Res. Ocean. 124, 8522–8537. https://doi.org/10.1029/2019JC015311.

JGR Oceans

RESEARCH ARTICLE
10.1029/2019JC015311

Key Points:
- An innovative use of Sentinel-1 (TOPS mode) data allows us to estimate the wave dispersion relationship within the sea ice
- The dispersion relation is derived for wavelengths of 100–350 m within thin ice (<40 cm), and it agrees with the open-water relationship
- Higher-resolution synthetic aperture radar data are required to study the wave dispersion of short waves within sea ice

Correspondence to:
D. Monteban,
dmont@space.dtu.dk

Citation:
Monteban, D., Johnsen, H., & Lubbad, R. (2019). Spatiotemporal Observations of Wave Dispersion Within Sea Ice Using Sentinel-1 SAR TOPS Mode. *Journal of Geophysical Research: Oceans*, *124*, 8522–8537. https://doi.org/10.1029/2019JC015311

Received 21 MAY 2019
Accepted 10 NOV 2019
Accepted article online 18 NOV 2019
Published online 3 DEC 2019

Spatiotemporal Observations of Wave Dispersion Within Sea Ice Using Sentinel-1 SAR TOPS Mode

Dennis Monteban[1,2], **Harald Johnsen**[3], **and Raed Lubbad**[2]

[1]DTU space, Technical University of Denmark, Lyngby, Denmark, [2]Department of Civil and Environmental Engineering, Norwegian University of Science and Technology, Trondheim, Norway, [3]NORCE Norwegian Research Center AS, Tromsø, Norway

Abstract In this paper, we derive the dispersion relation for waves within ice-covered waters from the Sentinel-1 Interferometric Wide swath mode by using an innovative new implementation of the method proposed by Johnsen and Collard (2009). We apply this method to the spatial burst overlap area that is present due to the *terrain observations with progressive scans* (TOPS) technique. The advantage of this implementation is the use of a larger time separation between subsequent images that results in a less noisy and higher-quality imaginary spectrum, which allows us to obtain spatiotemporal information of the dispersion relation. We studied seven wave events in the Barents Sea, where we have accompanying in situ data of sea currents and sea ice draft, available from the *Barents Sea Metocean and Ice Network* measurement program. Having simultaneous data on the currents is a significant improvement over previous studies and allows us to quantify these data's influence on the dispersion relation. The derived dispersion relation from Sentinel-1 is derived for long waves propagating through icy waters (peak wavelengths 100–350 m), and it does not deviate from the theoretical open-water dispersion relation. At present, however, the spatial resolution of synthetic aperture radar (SAR) data is too coarse and does not enable the study of the dispersion relation for short waves within sea ice.

Plain Language Summary In the open ocean, there is a well-known relationship between the length and the frequency of ocean waves: the open-water dispersion relation. This relationship changes when waves enter ice-covered oceans. Knowledge about this altered relationship is vital for computer simulations that predict, for instance, the climate and the wave conditions in the polar regions. In this paper, we derive the dispersion relationship for waves in ice-covered oceans by using the Sentinel-1 satellite and by introducing an innovative implementation of a known method. The new implementation benefits from the steering of the satellite antenna in a certain mode to allocate overlapping images of the ocean surface, which have not been previously used. Further, our study area is located in the Barents Sea, where we have data on, among others, the ocean currents. Having these data is an improvement in and of itself, as many previous studies lacked data that were collected on site. Our results show that we can study the wave dispersion relationship for long waves within the sea ice and, for some cases, in open water. At present, short waves cannot be studied with satellite imagery because the amount of details the satellite can capture is insufficient.

1. Introduction

The rapid change in sea ice extent (e.g., Comiso et al., 2017) and sea ice thickness (e.g., Renner et al., 2014) in the Arctic region provides a clear sign of climate change. The shrinkage in sea ice cover has led to longer open-water seasons, increased wave intensity (Thomson et al., 2018), new shipping routes (Melia et al., 2016), and the growth of offshore operations. To reduce the risks and hazards of coastal and offshore operations, it is of the utmost importance to accurately forecast the wave climate. However, in the polar regions, wave prediction is problematic due to the presence of sea ice. Not only do the waves influence the ice cover through, for instance, ice breakup (Collins et al., 2015; Kohout et al., 2016) and by compacting ice edges (Stopa, Sutherland, et al., 2018), but the ice also impacts waves by refraction, shoaling, reflection, scattering, dissipation, and changing the dispersion relation (e.g., Squire, 2007; Squire et al., 1995). Therefore, waves propagating through icy waters show amplitude attenuation and have a different propagation speeds compared to waves traveling in open water. Both the change in the wave speed and the attenuation of the wave amplitude can be described by a dispersion relation, for which various mathematical formulae exist throughout the literature (see section 2). It is common to express the wave number in these formulae using complex notation, which allows the description of the amplitude attenuation (the imaginary part) together with changes in the wavelength (the real part). In this paper, we obtain the real part of such dispersion relations from Sentinel-1 (S1) Interferometric Wide (IW) swath mode in the marginal ice zone (MIZ), where waves have been observed by synthetic aperture radar (SAR) hundreds of kilometers into the ice pack (e.g., Ardhuin et al., 2015; Carsey et al., 1989).

A major challenge in validating the theoretical formulae of the wave dispersion in icy waters and for determining the model parameters is the need for data. The data can be collected from either in situ measurements or remote sensing. The complication of retrieving observations of the dispersion relation is that both the temporal and spatial measurements are simultaneously required. In situ measurements from buoys provide time series, that is, in the temporal domain, while observations from remote sensing provide information in the spatial domain. Furthermore, the data collected from in situ measurements are sparse, are typically available for a limited amount of time, and have proved to be challenging and expensive to collect in the harsh environment of the polar regions. With its large and continuous day and night coverage, in addition to its outstanding performance in all weather conditions, SAR onboard the S1 constellation is a valuable source of wave information in ice-covered oceans (e.g., Ardhuin et al., 2017; Stopa, Ardhuin, et al., 2018).

The study by Collins et al. (2017) gives an overview of available observations (visual, in situ, remote sensing, and laboratory) of wave dispersion in the polar regions. From these observations, both lengthening and shortening of waves in pancake and brash ice are observed. All previous studies on remote sensing observations of wave dispersion use airborne or satellite SAR imagery to investigate the change in the two-directional spectrum for waves entering icy waters (Liu et al., 1991; Shuchman et al., 1994; Wadhams & Holt, 1991). As noted in these studies, the analysis of SAR imagery to retrieve the wave number spectrum is nontrivial. A modulation transfer function (MTF) is required, which in open water consists of tilt modulation, hydrodynamic modulation, and velocity bunching (e.g., Alpers et al., 1981; Hasselmann et al., 1985). The method presented in this study does not require the use of the MTF because we assume a linear ocean-to-SAR transform and we directly retrieve the dispersion relation from the SAR image cross-spectrum (see section 4.5). Furthermore, in our analysis, we include the effects of sea currents on the wave dispersion relation by using in situ measurements. This addition is a significant improvement over previous studies since a major drawback of all the previous studies on the change in wave number in the MIZ is the lack of simultaneous current measurements (Collins et al., 2017).

The Arctic Sea State field experiment is a measurement campaign that was recently conducted in the western Arctic region (Thomson et al., 2018). Wave buoys and shipboard X-band marine radar were used to derive the dispersion relation for waves in icy waters. From these observations, it was concluded that the dispersion of long waves in sea ice does not deviate significantly from the theoretical open-water dispersion relation (Cheng et al., 2017, their Figure 2). Collins et al. (2018) performed the most comprehensive study on the dispersion relation for waves in sea ice to date by using the *Arctic Sea State field experiment* data. For wave frequencies lower than 0.3 Hz, the measurements were close to the theoretical open-water dispersion relation. For wave frequencies in the range of 0.3 to 0.5 Hz, a deviation between measurements and the theoretical open-water dispersion relation was found. Collins et al. (2018) claimed that this deviation is consistent with the mass-loading model (see section 2) but did not follow the contour lines exactly.

While the latest study by Collins et al. (2018) presented detailed observations of the dispersion relation from in situ measurements, the aim of this study is to present and validate an approach to retrieve the wave dispersion relation from satellite SAR imagery. We use an innovative implementation of the method proposed by Johnsen and Collard (2009) on the spatial burst overlap area of S1 IW data. We analyze seven S1 IW images taken over the Barents Sea during the period of the *Barents Sea Metocean and Ice network* (BaSMIN) measurement program. This measurement campaign, together with the studied wave events, is introduced in section 3. Our method to derive the wave dispersion relation is described in section 4. Section 5 presents the results and is divided into three parts: (1) a comparison between the derived wave dispersion relation in open water and the one obtained in ice-covered seas, (2) the validation of the dispersion relation for relatively long waves, and (3) the derived dispersion relation for the shortest observed wavelengths within the sea ice. Finally, the results are summarized in section 6 before we draw the main conclusions.

2. Wave Dispersion

Wave dispersion (or frequency dispersion) refers to the difference in the wave speeds of wave components with different frequencies: Waves with different wavelengths propagate at dissimilar speeds and therefore disperse (Snodgrass et al., 1966). The derivation of the theoretical open-water wave dispersion relation is based on the assumptions of irrotational fluid motion, inviscid water, and incompressibility. It relates the spatial and temporal wave kinematics and is defined by

$$\omega = \sqrt{gktanhkd} + kUcos\alpha, \tag{1}$$

where ω and k denote the angular frequency and the wave number expressed in a fixed frame of reference, respectively, g is the gravitational acceleration, d is the water depth, U is the current velocity, and α is the angle between the direction of the mean current and the wave propagation. When waves propagate through ice-covered oceans, equation (1) will be altered in such a way that causes changes in the wavelength, the phase and group velocities, the wave direction, and the wave height while keeping the frequency and action unchanged (Collins et al., 2017). Greenhill (1887) was the first to propose a modification to the theoretical open-water dispersion relation to make it applicable to ice-covered waters; over the past few decades, substantial effort has been put into the development of theoretical models to derive dispersion relations for waves in icy waters. These models include the mass-loading model (Weitz & Keller, 1950), the viscous layer model (Keller, 1998), and the viscoelastic model (Wang & Shen, 2010). All these models are based on different assumptions of the ice and water layers. Therefore, it is unlikely that one formulation can be used for all types of ice. Following the notation of Meylan et al. (2018), the general dispersion relation for waves traveling in *deep water* in the presence of sea ice and the absence of sea currents may be written as

$$\omega^2 = gk(1 + Q(k,\omega)), \tag{2}$$

where the factor $Q(k,\omega)$ is the modification of the theoretical open-water dispersion relation. If no ice is present, $Q(k,\omega)$ is zero, and the theoretical open-water dispersion relation is restored. As an example, the simplest dispersion relationship for waves traveling in ice waters is the mass-loading model, for which the factor becomes

$$Q(k,\omega) = -\frac{1}{g}\frac{\rho_{ice}}{\rho_w}ch\omega^2, \tag{3}$$

where ρ_{ice} and ρ_{w} are the ice and the water densities, respectively, c is the ice concentration, and h is the ice thickness. For other wave dispersion formulae and the corresponding $Q(k,\omega)$, see, for instance, Meylan et al. (2018).

One useful application of wave dispersion relations valid for icy waters is the estimation of the sea ice thickness. A method was first developed by Wadhams and Holt (1991), who used the mass-loading model to estimate the ice thickness in the MIZ. By observing the ice concentration, wave number and angular frequency, the ice thickness can be computed from equations (2) and (3). Wadhams et al. (2002) extensively tested this method and obtained the wave number in sea ice, k_{i}, by deriving the directional wave number spectrum in ice with the Hasselmann inversion scheme (Hasselmann & Hasselmann, 1991) and the cross-spectral inversion scheme (Engen & Johnsen, 1995). The wave number in open water, k_{ow}, was acquired from the directional wave number spectrum in open water, and by using the theoretical open-water dispersion relation ($\omega^2 = gk_{\mathrm{ow}}$), the angular frequency, ω, was found. Wadhams et al. (2002) found that the derived ice thickness was overestimated. According to Collins et al. (2017), a possible explanation is that the spatial resolution of the SAR is too poor, so a shift of one wave number bin already results in a large change in the wavelength. In later studies by Wadhams et al. (2004) and Wadhams et al. (2018) , the viscous layer model by Keller (1998) was used, and good agreement with in situ measurements of pancake ice was found.

3. Site Description, BaSMIN Measurement Program, and Studied Wave Events

To assess the results from our method to retrieve the wave dispersion relation from satellite SAR imagery, we used in situ data collected during the BaSMIN measurement program. This 3-year metocean and ice

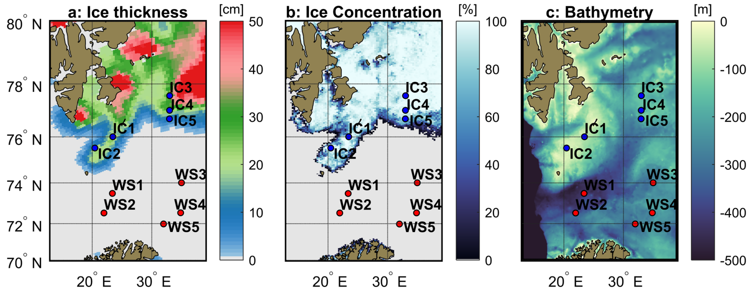

Figure 1. Overview of the BaSMIN measurement locations and ice conditions during an S1 satellite pass on 4 April 2017. The wavescan moorings are indicated by red dots and the abbreviation "WS"; the ice profilers are shown as blue dots and are referred to by "IC." (a) The ice thickness as derived by SMOS. (b) The ice concentration taken from AMSR2. (c) The bathymetry of the Barents Sea, taken from the International Bathymetric Chart of the Arctic Ocean (Jakobsson et al., 2012).

measurement campaign took place from October 2015 until October 2018. It is a joint industry project led by Equinor, and the measurement campaign was conducted by Fugro GEOS Ltd. The data were kindly made available for academic research, and this is the first time the data are being published. During this field campaign, five wave-scan moorings and five ice profilers were deployed, and their locations are indicated in Figure 1. The wave-scan moorings measured the wave parameters, near-surface currents, seawater temperature, seawater salinity, and meteorological parameters. The ice profilers measured the ice draft, seawater temperature, ice drift speed, and current velocity.

The bathymetry of the Barents Sea is shown in Figure 1c. The Ice Moring Stations IC3, IC4, and IC5 are located at water depths of 157, 139, and 173 m, respectively. Therefore, when using the deep-water limit ($H > 0.5 \cdot L$, where H is the water depth and L is the wavelength), waves with wavelength smaller than approximately 300 m can be considered deep-water waves. The Ice Mooring Stations IC1 and IC2 are placed at water depths of 52 and 68 m, respectively. For most wave events, this depth range can be classified as intermediate water. For this reason, we only looked at satellite passes close to IC3–IC5, as they are in deep water.

In Figure 1a, the ice thickness is provided for the date 4 April 2017 (Tian-Kunze et al., 2018) as taken from the Soil Moisture Ocean Salinity Earth Explorer mission (Kaleschke et al., 2012). The ice thickness in Figure 1a is between 20 and 40 cm around the ice mooring stations, which is consistent with the measured ice draft at locations IC3–IC5 but is slightly underestimated at IC1 and IC2 (not shown). The ice concentration (Figure 1b) is from Advanced Microwave Scanning Radiometer 2 (Spreen et al., 2008) for the same date. From both the Soil Moisture Ocean Salinity ice thickness and ASMR2 ice concentration, there is an ice tongue extending south, encompassing Ice Mooring Stations IC1 and IC2. This ice tongue follows the Spitsbergen Bank because of the limited water depth, where ice forms more rapidly than in deeper water, and because of the sea ice drift. The sea ice drift has a directional trend toward the southwest, and its magnitude is on average larger for IC1 and IC2 than for IC3–IC5, which is in agreement with the general surface circulation in the Barents Sea (e.g., Oziel et al., 2016).

The relevant data collected during the measurement campaign for this study are the current speed and the ice draft. The current speed is necessary to calculate the wave dispersion (see equation (1)). At IC1 and IC2, they generally vary between 0.05 and 0.3 m/s and, at IC3–IC5, between 0.2 and 0.8 m/s. The maximum current speed observed during the entire campaign was 1.06 m/s, observed at IC1. For the 3 years of the measurement campaign, ice was mostly recorded from March to May. The ice was typically thin with a mean ice draft varying between 0.1 and 0.5 m. According to the sea ice nomenclature (World Metrological Organization, 1970), which relates the ice thickness to ice categories, young ice and first year thin ice are found. Furthermore, by studying some Sentinel-2 optical images, we found that the ice close to the ice edge is usually inhomogeneous, with ice floes and some open-water patches present.

Seven wave events were selected to test and validate our proposed method to derive the wave dispersion relation from S1. An overview is provided in Table 1, and these events were selected, so they cover a wide range of peak wavelengths. For the events with long waves (#1–4), the dispersion relation in sea ice is expected to

Table 1
Overview of the Wave Events Processed in This Paper

Event no.	Date	Hs (m)	L_{ws} (m)	W_{ad} (°)	W_{is} (m/s)	W_{id} (°)	h_{ice} (m)	U (m/s)
1	16-02-2018	3.70	352	250	4.30	72	—	0.11
2	04-04-2017	5.50	194	64	10.66	71	0.28	0.14
3	22-04-2017	1.86	99	147	5.74	88	0.36	0.16
4	28-04-2017	1.52	118	285	9.02	294	0.32	0.20
5	16-05-2017	1.17	72	290	4.10	60	0.21	0.03
6	11-04-2018	1.38	75	225	4.69	257	0.40	0.08
7	29-04-2018	1.52	56	296	4.70	256	0.32	0.15

Note. The wave and wind parameters are taken from wavescan mooring WS3. Hs = significant wave height; L_{ws} = wavelength; W_{ad} = wave direction “coming from,” relative to north and positive clockwise; W_{is} = wind speed; W_{id} = wind direction “coming from,” relative to north and positive clockwise; h_{ice} = daily mean ice thickness computed as the average from Ice Mooring Stations IC3–IC5; U = current speed averaged over Ice Mooring Stations IC3–IC5.

be identical to the open-water dispersion relation (Collins et al., 2018), and hence, these events are used to validate our algorithm. The Events 5–7 have peak wavelengths in the range of 55–70 m and are in the remainder of this paper referred to as short waves. These waves were the shortest observed peak wavelength where the waves were still visible within the sea ice.

4. Method Description

The method described here results in spatiotemporal observations of the wave dispersion, that is, simultaneous measurements of the wave number and the angular frequency. Our method is based on the S1 WV Level-2 algorithm proposed by Johnsen and Collard (2009), which is innovatively adapted to S1 TOPS mode *Single Look Complex* (SLC) data. The traditional processing technique to estimate the cross-spectra (Engen & Johnsen, 1995) from strip-map data is performed on single-look data. This methodology usually solves the 180° wave ambiguity and removes the speckle noise bias. However, it results in a noisy and poor-quality imaginary cross-spectrum when applied to TOPS SLC data. Therefore, we propose to apply the cross-spectra estimation method proposed by Johnsen and Collard (2009) on the burst overlap area, which leads to a higher-quality imaginary cross-spectrum. This method can be used to more reliably determine the wave direction.

The burst overlap area is present because the S1 constellation uses the *Terrain Observation with Progressive Scans SAR* (TOPSAR) technique (Zan & Guarnieri, 2006) in its IW and Extra Wide swath modes. In addition to beam steering across the range direction, as with the traditional scanning SAR acquisition, the antenna beam is also steered in the azimuth direction, which results in a single-look area and a burst overlap area for each subswath. The scanning geometry is sketched in Figure 2, and the single-look and burst overlap areas are indicated.

The well-established method by Engen and Johnsen (1995) is commonly used to produce multiple independent looks from the SLC image of the single-look area and to consequently compute the cross-spectrum. The different sublooks that are produced have a maximum separation time of approximately half the integration time (≈0.4 s). Applying this technique to TOPS SLC data results in a poor-quality imaginary part of the cross-spectrum because the progressive sweep of the antenna results in a dwell time of only 0.15 s. Moreover, the phase change (introduced by wave propagation) between the resulting subsequent looks is small and, therefore, noisy. In this study, we overcome this challenge by using two intensity images from the burst overlap area, in which we have two looks of the same area that are separated in time by approximately 1.8–2.1 s, depending on the subswath and the range location. The phase change between subsequent images is now significantly larger and less noisy. Therefore, the quality of the computed imaginary part of the cross-spectrum via our method is much better than that calculated using the

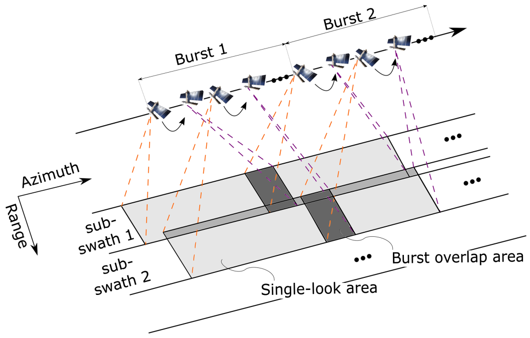

Figure 2. Acquisition geometry of the S1 TOPSAR technique (adapted from Park et al., 2018). There are three subswaths for the Interferometric Wide swath mode, and the burst cycle time is approximately 2.6 s. During each burst, the antenna beam is steered forward in the azimuth direction (orange dotted line to the purple dotted line) for each subswath. Overlap areas occur between the subswaths and between the bursts for each subswath. The overlap area between the bursts of a subswath, used in the processing, is indicated in the figure.

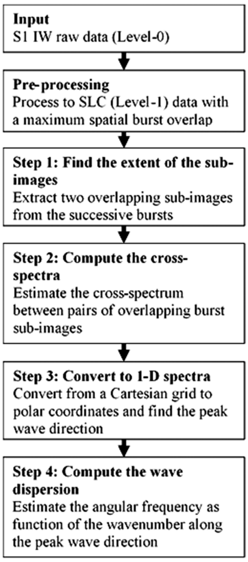

Figure 3. Successive steps of the proposed method

standard processing technique, which is necessary for the accurate estimation of the wave dispersion relation. In addition, the wave direction can be resolved more accurately than the standard processing of the single-look area.

In Figure 3, we present a flow chart that shows the steps of the proposed method. In the next few sections, the different steps are explained in detail. Finally, we present an example case to illustrate the results.

4.1. SAR Input Data and Preprocessing

We use data acquired from the S1 constellation operating in IW swath mode. S1 carries a C-band radar instrument and has an incidence angle that ranges from 29° to 46°. Multiple polarization options are available, but throughout this study, we use the HH polarization. The total swath width is approximately 250 km, and it consists of three subswaths. We use the raw Level 0 data that can freely be downloaded from the European Space Agency's Sentinel Data Hub. These data are processed to Level 1 SLC data product with the same method that the European Space Agency (2013) uses but without merging the bursts in the azimuth direction and the subswaths in the range direction. This preprocessing step results in standard SLC images with a maximum spatial overlap between the bursts and swaths.

4.2. Step 1: Find the Extent of the Sub-images

After the preprocessing of the data, the next step is to define multiple sub-images with the spatial overlap area of consecutive bursts. We first find the area where the two bursts overlap at the azimuth time. However, we cannot use the entire overlap area because the targets located at the beginning and at the end of each burst are not illuminated by the entire antenna pattern. Therefore, we find the length of the subscene in the azimuth direction by plotting the normalized intensity averaged over the range for both overlapping bursts. The length of the sub-image in the azimuth direction (y direction) is then found using the following criterion:

$$\left|\hat{I}^{n+1}(\mathrm{y})-\hat{I}^{n}(y)\right|<0.5, \tag{4}$$

where $\hat{I}^{n+1}(\mathrm{y})$ and $\hat{I}^{n}(y)$ are the normalized intensities averaged over the range for burst $n+1$ and burst n, respectively. The limit of 0.5 is a compromise between using as many points in the azimuth direction as possible while excluding the part where the intensities fade out at the beginning and at the end of each burst. For all the images, this step results in approximately 320 points in the azimuth direction. In the range direction, we used 1,000 points for each sub-image. The resolution of the SLC data in the azimuth and range directions is approximately 14 and 5 m, respectively, resulting in a total sub-image area of approximately 4.5 × 5 km. The number of bursts used for each wave event differs. Bursts are manually selected for processing when waves are visible. Therefore, for events with long waves, more bursts are used as the waves propagate further into the ice pack. For each burst, we used multiple sub-images in the range direction, with 50% overlap, which typically results in 30 sub-images for each burst. A sub-image is manually processed when ocean waves are visible within the sea ice.

4.3. Step 2: Compute the Cross-Spectra

The image cross-spectrum between two overlapping images from two different bursts is computed following the method proposed by Johnsen and Collard (2009). The cross-spectrum ($P^{(n,n+1)}$) is defined by

$$P^{(n,n+1)}(\underline{k},\tau)=\frac{1}{\left\langle I^{(n)}\right\rangle\left\langle I^{(n+1)}\right\rangle}\left\langle I^{(n)}\left(\underline{k},\frac{\tau}{2}\right)I^{(n+1)^{*}}\left(\underline{k},-\frac{\tau}{2}\right)\right\rangle, \tag{5}$$

where $I^{(n)}$ and $I^{(n+1)}$ are the two overlapping intensity sub-images of burst n and burst $n+1$, respectively. The two images are separated by the look separation time τ, and $\underline{k}=\left(k_x,k_y\right)$ is the wave number domain (k_x in the range direction and k_y in the azimuth direction). The asterisk (*) denotes the complex conjugate, and < > represents ensemble averaging over the sub-images. Next, the inverse of the cross-spectrum is computed, which is referred to as the cross-variance function, $\rho^{(n,n+1)}$ and is given by

$$\rho^{(n,n+1)}(\underline{x},\tau)=\frac{1}{(2\pi)^2}\int d\underline{k}P^{(n,n+1)}(\underline{k},\tau)e^{-i\underline{k}\cdot\underline{x}}, \tag{6}$$

where $\underline{x}$ is the target pixel (with range and azimuth values). The cross-variance function is smoothed with a Hanning window, h, raised to the power of β. Throughout this study, we used a value of 2 for β. The final cross-spectrum is computed as the Fourier transform of the smoothed cross-variance function according to

$$P^{(n,n+1)}(\underline{k},\tau)=\int d\underline{k}h(\underline{x})^{\beta}\rho^{(n,n+1)}(\underline{x},\tau)\ e^{i\underline{k}\cdot\underline{x}}. \tag{7}$$

Finally, wavelengths larger than 500 m are filtered out by masking the middle of the cross-spectrum.

4.4. Step 3: Convert to a 1-D Spectra

To obtain the 1-D cross-spectra, we first compute the real part, $P_{\text{real}}(\underline{k})$, and imaginary part, $P_{\text{imag}}(\underline{k})$, of the cross-spectrum (equations (8) and (9)).

$$P_{\text{real}}(\underline{k})=Re\left\{P^{(n,n+1)}(\underline{k},\tau)\right\}, \tag{8}$$

$$P_{\text{imag}}(\underline{k})=Im\left\{P^{(n,n+1)}(\underline{k},\tau)\right\}. \tag{9}$$

We then convert from a Cartesian wave number grid into polar coordinates: $\{\underline{k}=(k_x,k_y)\rightarrow\underline{k}=(k,\theta)\}$. The dominant wave direction is identified where the maximum value in the real part of the cross-spectrum matches the maximum value of the imaginary part of the cross-spectrum (e.g., Bao & Alpers, 1998). The 1-D spectra are found by integrating over the angular coordinate of the maximum value of the imaginary cross-spectrum θ_{max}, with a range of ±5°, using trapezoidal numerical integration:

$$P_{\text{real}}(k)=\int_{\theta_{\text{max}}-5}^{\theta_{\text{max}}+5}d\theta\ P_{\text{real}}(k,\theta),$$

(10)

$$P_{\text{imag}}(k)=\int_{\theta_{\text{max}}-5}^{\theta_{\text{max}}+5}d\theta\ P_{\text{imag}}(k,\theta). \tag{11}$$

We integrate over a range of 10° angular coordinates, and the resolution of the wave number, k, is set to 0.0015. The choice of both the wave number resolution and the range in the angular coordinate should be as small as possible, so we only look at one set of waves. At the same time, the range should be large enough to smooth the noise as much as possible. After some trial and error, we found that the chosen values provided acceptable results.

4.5. Step 4: Compute the Wave Dispersion

The nature of the ocean-to-SAR transform depends on the imaging regime, which can be linear, quasi-linear, and nonlinear (Krogstad, 1992). In the linear imaging regime, the 2-D SAR image cross-spectrum is related to the ocean wave spectrum through (Engen et al., 2000)

$$P(k,\theta,\tau)\approx T^2(k,\theta)\cdot S(k,\theta)\cdot e^{i\varphi(k,\tau)}, \tag{12}$$

where $T(k,\theta)$ is the MTF and $S(k,\theta)$ the ocean wave spectrum. The linear regime does not occur very often in the open ocean as it requires a low significant wave height (and hence, a low azimuth cutoff) and relatively long waves. Within the sea ice, however, the azimuth cutoff is much smaller because the short wavelengths of wind-driven seas, which are the dominant contribution to the azimuth cutoff effect, are mainly absent because the ice cover acts as a low-pass filter (Collins et al., 2015). Therefore, we argue that SAR images taken over the sea ice are in the linear imaging regime. With this assumption, we can compute the phase

Table 2
Look Separation Time, τ (s)

Swath	Near range	Far range
IW1	2.1124	2.1396
IW2	1.8782	1.9156
IW3	2.1073	2.1356

spectrum, $\varphi(k, \tau)$, from the imaginary part and real part of the 1-D cross-spectrum given in equations (10) and (11). In this case, the MTF from equation (12) cancels out, and we get

$$\varphi(k) = \tan^{-1}\frac{\langle P_{\text{imag}}(k)\rangle}{\langle P_{\text{real}}(k)\rangle}. \tag{13}$$

Both the imaginary part and the real part are smoothed using the moving average filter. The relation between the phase spectrum and the angular wave frequency, $\omega(k)$, is

$$\omega(k) = \frac{\varphi(k)}{\tau}. \tag{14}$$

The look separation time between the images, τ, depends on the subswath and the range coordinate (see Table 2). For a certain range coordinate, the look separation time is found by a linear interpolation between the near and far range coordinates.

4.6. Test Case

To demonstrate the abovementioned steps of our proposed method, we give an example within the sea ice of the wave event that occurred on 4 April 2017. This event is characterized by relatively long waves (peak wavelength of 190 m; see Table 1). Two subsequent bursts for the same subswath are presented in Figures 4a and 4b. The red line in Figures 4a and 4b is found from the azimuth time and indicates where the next burst starts and where the previous burst ends, respectively. In Figure 4c, the normalized intensity averaged over the range is plotted for two overlapping bursts. It can be clearly seen that the intensity of a burst fades at the beginning and at the end of each burst. The length between the two thick black lines satisfies the criterion given in equation (4) and is the number of pixels in the azimuth direction. A typical obtained sub-image is presented in Figure 4d, which is the result of Step 2 in Figure 3.

The real part and the imaginary part of the cross-spectrum from two sub-images (the green rectangles in Figures 4a and 4b) are shown Figures 4e and 4f, respectively. The resolution of the cross-spectrum in the range direction $\left(dk_x = \frac{2\pi}{1000\cdot 5}\right)$ is 0.0013 and 0.0015 [rad/m] in the azimuth direction $\left(dk_y = \frac{2\pi}{300\cdot 14}\right)$. The resolution in the azimuth direction is slightly different from burst to burst, as the number of points used in azimuth differ slightly for each sub-image. In Figure 4g, the phase spectrum is given, computed with equation (13). The resulting 1-D real and imaginary image spectra are presented in Figure 4h, which is the result of Step 3. In addition, the computed angular frequencies from Step 4 are plotted and compared with the theoretical open-water dispersion relation, which uses data on the currents collected from Ice Mooring Stations IC3–IC5 at a depth of 8 m (Table 1). For this example, the computed angular frequency from S1 is almost identical to the theoretical open-water angular frequency in the range where the wave energy is located (between approximately $k = 0.025$ and 0.04).

The portion of the imaginary and the real parts of the cross-spectrum that is used to calculate the phase, equation (13), does include noise. Therefore, we can rewrite equation (13) as

$$\varphi(k) = tan^{-1}\frac{\langle P_{imag}(k) + ImNoise\rangle}{\langle P_{real}(k) + ReNoise\rangle}. \tag{15}$$

We estimated the noise of the imaginary spectrum (*ImNoise*) and the noise of the real spectrum (*ReNoise*) by calculating the variance in a small area of the cross-spectrum, far away from the area of interest. For example, in the event shown in Figure 4, we estimated the variance in the area: k_x between 0.6 and 0.65 and k_y between 0.2 and 0.25. For all the cases considered in this paper, the estimated noise was less than 1% of the peak values of the cross-spectrum, and hence, noise did not greatly influence the results of the wave dispersion.

To illustrate the advantage of our proposed method in which the burst overlap area is used compared to the single-look area, we compute the imaginary spectrum for the case within the sea ice as presented in Figure 4 using the single-look area. The result is presented in Figures 5a and 5b. The quality of the spectrum derived

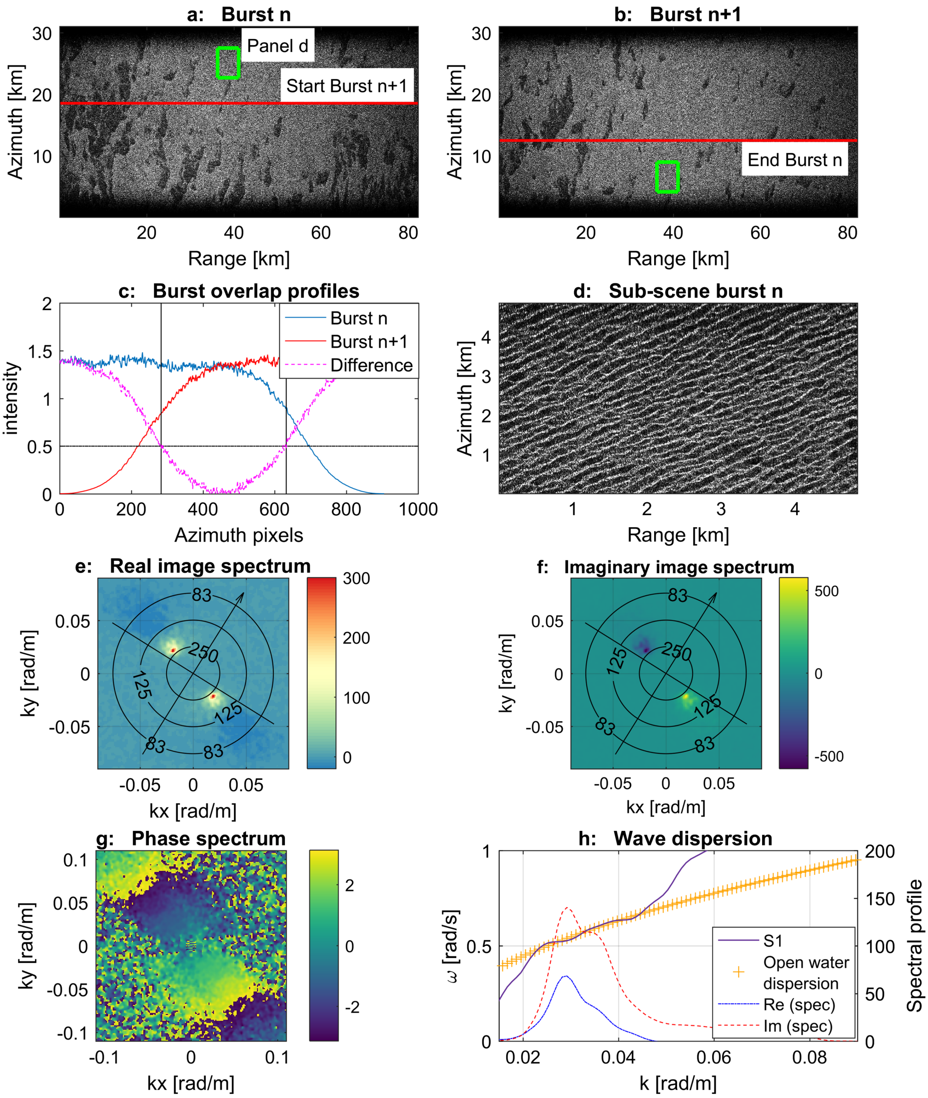

Figure 4. (a) Normalized intensity image of burst n. The red line indicates where burst n + 1 starts, and the green rectangle is the extent of (d). (b) Normalized intensity image of burst n + 1. The red line shows where burst n ends, and the green rectangle is the same spatial area as the one given in (a). (c) Normalized intensity of burst n and burst n + 1 averaged over a range, together with the absolute difference. The overlap area is defined where the difference is less than 0.5, resulting in the two thick, vertical black lines. (d) One of the two sub-images used from the burst overlap area to estimate the cross-spectrum. (e) The real part and (f) the imaginary part of the cross-spectrum. The black arrows in (e) and (f) indicates north, and the black circles indicate a wavelength of 83, 125 and 250 m from the outer to the inner circle. (g) Phase spectrum. (h) The 1-D imaginary and real parts of the cross-spectrum are plotted against the right y axis. The open-water dispersion relation including currents and the estimated dispersion relation from S1 are plotted against the y axis on the left.

from the burst overlap area is much better and less noisy. For this example, the wave direction can still be seen from the spectrum of the single-look area. However, in the open ocean, the imaginary spectrum becomes even more noisy, making it sometimes impossible to derive the wave direction accurately from the single-look area. This result can be greatly improved by using the burst overlap area instead, where

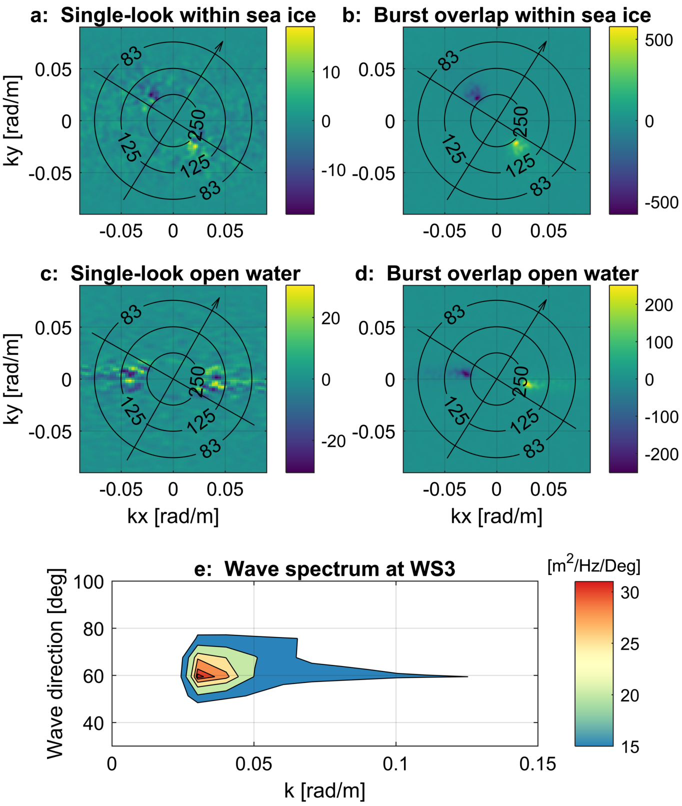

Figure 5. Imaginary spectra derived from the single-look area and the burst overlap area for the wave event on 4 April 2017 within the sea ice given in (a) and (b) and in the open water shown in (c) and (d). The black arrow indicates the north, and the circles show the wavelength. Note that the imaginary spectrum of the burst overlap area within the sea ice (b) is identical to the one presented in Figure 4. In (e), the measured 2-D wave spectrum measured at wavescan mooring WS3 is presented.

we have a larger time separation that results in a better-quality imaginary spectrum. An example in the open water is presented in Figures 5c and 5d, which shows the imaginary spectrum at the location of Wavescan Mooring WS3. The measured 2-D wave spectrum at this location is given in Figure 5e. The imaginary spectrum of the single-look area (Figure 5c) is in this case too noisy to extract the wave direction and wavelength. However, these wave parameters can be retrieved from the imaginary spectrum from the burst overlap area (Figure 5d) and have values of 67° and 217 m for the mean wave direction and the peak wavelength, respectively. These values are close to the ones obtained from the measured 2-D wave spectrum (Figure 5e), which has a mean wave direction of 64° and a peak wavelength of 193 m.

5. Results and Discussion

5.1. Applicability of the Method—Linear and Nonlinear Imaging Regime

Among the wave events considered in this paper, the angular frequency as a function of the wave number, that is, the wave dispersion relation, is underestimated in open water, except for Wave Event 1. We believe that this underestimation may be attributed to nonlinear imaging effects caused by the random motions of short waves. These random motions blur the image and lead to the azimuth cutoff effect (e.g., Kerbaol et al., 1998). Linearity of ocean-to-SAR transform is assumed when computing the phase from equation (13) in our method, and therefore, we do not expect our method to work in the nonlinear imaging regime.

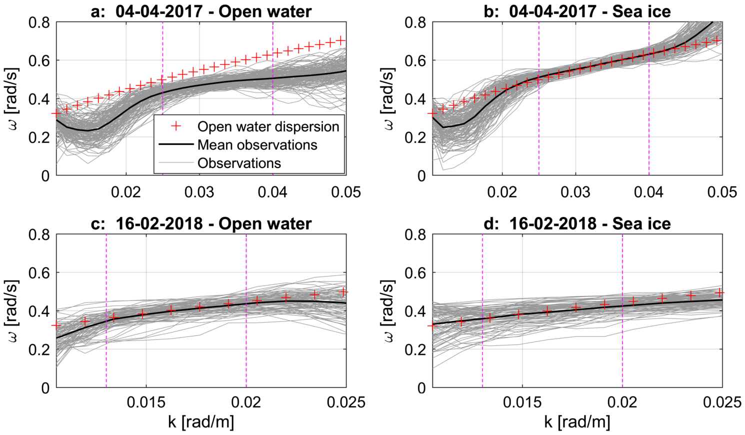

Figure 6. Comparison of the computed angular frequency (ω), as function of the wave number (k), in open water (a and c) and within the sea ice (b and d) for two different wave events, which occurred on 4 April 2017 and on 16 February 2018. Both events include sub-images of Swath IW3, and 150 and 90 sub-images are included for the event on 4 April 2017 and 16 February 2018, respectively. The thick black line is the average of the observations, and the dashed magenta lines indicate where most of the energy of the spectrum is located, which is found by normalizing the 1-D real part of the cross-spectrum and finding values larger than 0.5. The azimuth cutoff wavelength is roughly 306 m for the 4 April 2017 event and approximately 260 m for the 16 February 2018 event.

To demonstrate this, we apply our proposed method to waves propagating from open water into sea ice, which allows us to derive and compare the wave dispersion relations for linear and nonlinear cases. We present the derived wave dispersion relations both in the open water and within the sea ice for two wave events in Figure 6. These two wave events are characterized by long waves and occurred on 4 April 2017 and on 16 February 2018 (Events 1 and 2 in Table 1). The derived values of the angular frequency are compared with the theoretical open-water dispersion relation, which is calculated using in situ data of the currents. Note that the comparison by means of the theoretical open-water dispersion relation is also valid for images taken over the sea ice since the dispersion of long waves within the sea ice is nearly identical to the theoretical open-water dispersion relation (Cheng et al., 2017; Collins et al., 2018). In Figure 6, the wave dispersion obtained from S1 is in good agreement with the theoretical open-water dispersion relation for images taken over the sea ice for both events. However, the obtained angular frequencies in the open water show an underestimation for the 4 April 2017 event, while again, a good agreement is found for the 16 February 2018 case.

Factors that could lead to differences between the results from S1 and the theoretical open-water dispersion relation could be a too noisy imaginary spectrum. This is, for instance, the case when instead of the burst overlap area, the single-look area is used. Another factor could be that our assumption of linearity of the ocean-to-SAR transform is violated, which is the case for the 4 April 2017 event in the open water. To illustrate this, we estimated the linearity for both cases by calculating the nonlinearity coefficient, equation (16), proposed by Alpers et al. (1981), which was used in the study by Shen et al. (2018) to show linear conditions. This is the case when the value is equal or smaller than 0.3.

$$C = \frac{R}{V} \cdot a \cdot {k_p}^{3/2} \cdot g^{1/2} \cdot cos\varphi_p \cdot cos\vartheta, \tag{16}$$

with R, V, and ϑ the radar parameters that are the target range, platform velocity, and the radar incidence angle, respectively, a is the wave amplitude, k_p the peak wave number, and φ_p the peak wave direction relative to the azimuth direction. The computed nonlinearity coefficient is 0.1 for the 16 February 2018 event and 0.65 for the 4 April 2017 event. Hence, only the 16 February 2018 event can be considered linear in the open water. Furthermore, we estimated the azimuth cutoff in the open ocean for both wave events by minimizing the error of a fitted Gaussian function to the normalized azimuth profile of the cross-covariance function. This method minimizes the function (Johnsen & Collard, 2009):

$$\varepsilon = \int dy \left\{ \rho^{n,n+1}(y) - e^{-\left(\frac{\pi y}{\lambda_c}\right)^2} \right\}, \tag{17}$$

where λ_c is the estimated azimuth cutoff wavelength. This method has been indicated to give reasonable results over the open ocean (Kerbaol et al., 1998; Stopa et al., 2015). The computed azimuth cutoff wavelength is approximately 306 m for the 4 April 2017 event and approximately 260 m for the 16 February 2018 event. On 4 April 2017, there was a higher wind speed and a larger significant wave height, resulting in a higher value. For the 16 February 2018 event, the peak wavelength (350 m) is well above the azimuth cutoff wavelength. In contrast, for the 4 April 2017 event, the peak wavelength (160 m) is smaller than the azimuth cutoff wavelength, and the peak wavelength is distorted by the cutoff. As stated in section 4.5, we argue that the images taken over the sea ice are in the linear regime. Most of the short waves are not present in images taken over the sea ice because the sea ice scatters and dissipates the high-frequency waves. For that reason, waves appear clearer in images taken over the sea ice than in images taken over the open ocean (Lyzenga et al., 1985) and that the azimuth cutoff wavelength is much smaller in the sea ice than in the open water. As a result, only the images taken over the open water for the 4 April 2017 event, presented in Figure 6a, are in the nonlinear imaging regime, and the peak wavelength is distorted by the azimuth cutoff. Therefore, we conclude that our method does not work when the assumption of linearity is violated. The good results of the open water case for the 16 February 2018 event (Figure 6c) and the cases within the sea ice, Figures 6b and 6d, give us confidence in the validity of our method when we are in the linear regime.

5.2. Analysis of the Derived Wave Dispersion Relations for Long Waves Within Sea Ice

We validate our method by comparing the obtained angular frequencies with the values from the theoretical open-water dispersion relation because the wave dispersion of long waves within sea ice is nearly identical to the open-water wave dispersion relation. We use three different wave events with long waves, that is, Wave Events 2–4 in Table 1. The results are shown in Figure 7. The results are in good agreement with the theoretical open-water dispersion relation in the area where the wave energy is located. We evaluated the performance by calculating the mean absolute error and the mean absolute percentage error (MAPE). These errors are defined as follows:

$$MAE = \frac{1}{n}\sum_{i=1}^{n} |\omega s1 - \omega ow|, \tag{18}$$

$$MAPE = \frac{1}{n}\sum_{i=1}^{n} \left| \left(\frac{\omega s1}{\omega ow} - 1 \right) \cdot 100 \right|, \tag{19}$$

where $\omega s1$ is the angular frequency computed from S1 and ωow is the angular frequency calculated from the theoretical open-water dispersion relation. The MAPE for the three wave events, based on the average of the observations, is approximately 1%. However, quite a large spread in the observations can be observed. This spread is roughly ±7% when looking at the right panels of Figure 7. Nonetheless, the good agreement with the theoretical open-water dispersion relation gives us confidence in the validity of our method.

An advantage of this study is the availability of in situ data on the currents. We investigated the influence of the currents by comparing the three wave events presented in Figure 7 with the theoretical open-water dispersion relation, without using the currents. The MAPE, when including currents, is approximately 1–2% lower compared to the case without currents. For these specific cases, the error does not change substantially because the magnitude of the currents is quite weak, with values between 0.1 and 0.2 m/s. Having stronger currents will modify the open-water wave dispersion considerably. To demonstrate this, we computed the MAPE for a theoretical case using the maximum observed current speed of 1.06 m/s. The MAPE is then up to 11% higher than the case with the actual observed current speeds, which clearly shows it is vital to have accompanying data on the currents.

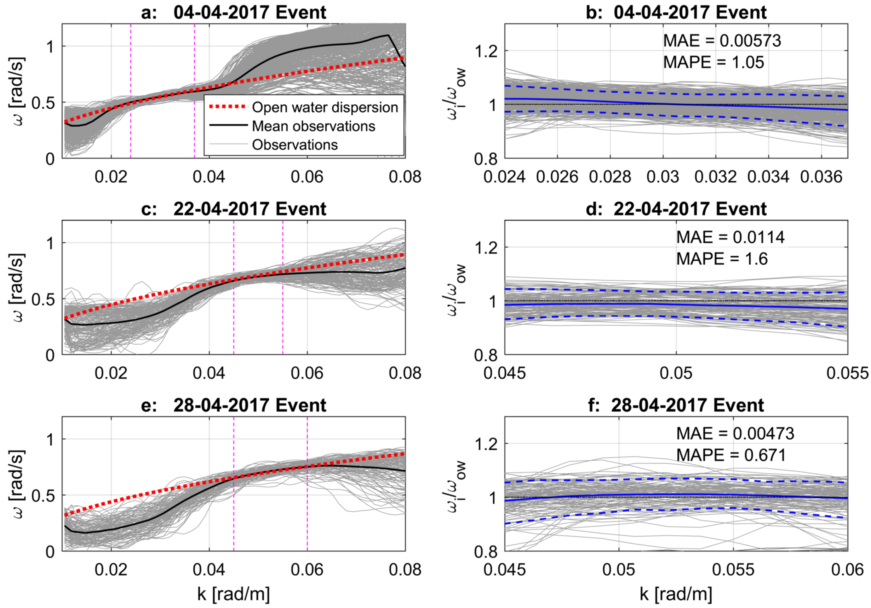

Figure 7. Comparison of the wave dispersion within sea ice for three wave events with long waves. The peak wavelength measured at Wave Buoy WS3 for the events given in (a), (c), and (e) are 194, 99, and 118 m, respectively. The magenta lines indicate where most of the energy of the 1-D real part of the cross-spectrum is located. (b), (d), and (f) show the ratio of the S1 estimated (ω_i) and open water angular frequency (ω_{ow}) between the magenta lines. The thick blue line is the average of the observations, and the dashed blue lines enclose 90% of the observations. The mean absolute error (MAE) and the mean absolute percentage error (MAPE) are calculated for the area between the magenta lines.

5.3. Analysis of Derived Wave Dispersion Relations for Short Waves Within Sea Ice

The obtained dispersion relations of the three wave events with the shortest waves observed, that is, Wave Events 5–7 in Table 1, are plotted in Figure 8. The different wave events shown here include fewer observations than the ones with long waves because there are significantly fewer sub-images in which waves are visible within the sea ice. Furthermore, the spread in observations is larger compared to the events with long waves (Figure 7) because all the sub-images of the events with short waves are close to the ice edge. The ice here is very inhomogeneous; for example, broken-up ice and resulting ice floes in addition to patches of open water are found here. Nevertheless, the average of the observations does show a small deviation from the open-water dispersion relation. Recall that the derived dispersion relationship for long waves within the thin ice did not deviate from the open-water dispersion relation, which is consistent with findings in literature.

In addition to comparing the derived dispersion relation with the theoretical open-water dispersion relation, we attempted to back-calculate the ice thickness by looking at the simplest dispersion relation model, including sea ice, that is, the mass-loading model. To do so, we plotted this mass-loading model as a function of the ice thickness in addition to the derived dispersion relation from S1 in Figure 8. The ice thickness at Mooring Stations IC3–IC5 is approximately 0.2–0.5 m. For such a small ice thicknesses, we can see that the deviation from the theoretical open-water dispersion relation is minor according to the mass-loading model. It is evident from Figure 8 that the desired small deviation from the theoretical open-water dispersion cannot be sensed by the satellite, and we cannot use these observations to quantitatively extract the ice thickness.

To obtain a deviation sufficiently large from the theoretical open-water dispersion relation that can be sensed by S1, we would need to study even shorter waves. Collins et al. (2018) found that the deviation from the open-water dispersion relation for frequencies larger than 0.3 Hz (corresponding to a wavelength of

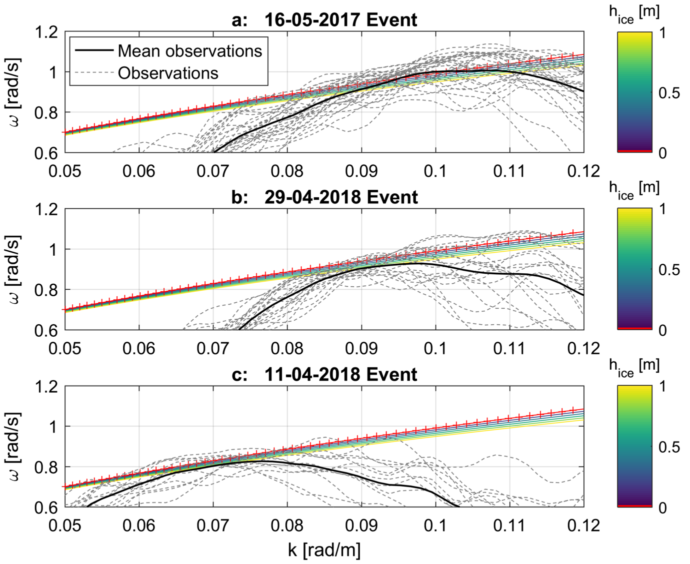

Figure 8. S1-calculated angular frequency (ω) as function of the wave number (k) for the three events with the shortest observed waves. The peak wavelength obtained at Wave Buoy WS3 are 72, 56 and 75 m for (a), (b), and (c), respectively. The theoretical open water dispersion relation is plotted as the red line with crosses. The mass-loading model is plotted as a function of the ice thickness (h_{ice}), which is given as a color-code spectrum. The mean ice thickness at the wave events given in (a), (b), and (c) are 0.21, 0.32, and 0.4 m, respectively.

approximately 14 m) was significant. Therefore, we would need to measure in this range of wavelengths to obtain a substantial deviation that can be sensed by S1. However, these measurements are not currently possible because the spatial resolution of S1 is too coarse. Having higher-resolution data will not only allow the study of shorter waves but will also lead to a better accuracy in determining the wave dispersion. The reason for this is that we can average more over the same spatial area, which will lead to a less noisy imaginary spectrum and therefore a better estimate of the phase and the wave dispersion.

6. Conclusions

In this study, we present a new method for retrieving spatiotemporal observations of ocean waves from the S1 constellation. We propose a new and innovative implementation of the method proposed by Johnsen and Collard (2009) on the spatial burst overlap area, which is present due to the S1 TOPS acquisition mode. The advantage of this method is that the time separation between two individual looks (images) is significantly larger, and, therefore, a larger phase change is present. This method leads to a less noisy and better-quality imaginary spectrum, which can potentially be used for a better determination of the wave direction. Furthermore, the proposed method does not require the MTF because we assume a linear ocean-to-SAR transform within the sea ice. The assumption is based on the fact that the ice cover acts as a low-pass filter, attenuating high-frequency waves. Short wavelengths of wind-driven seas are the dominant contributors to the azimuth cutoff; hence, this cutoff is much smaller within the sea ice.

We used seven wave events in the Barents Sea to test and validate our method. For this study site, we have accompanying in situ measurements of the sea currents and the ice draft. The use of the current measurements is a major advantage, as many previous studies that focused on the change in the wave number in the MIZ lacked simultaneous data on the currents. For our studied cases, the use of the currents generally improved the results by reducing the MAPE by 1–2%. This relatively small contribution of the currents is because the current speed during our studied events are low. However, it is evident that strong currents significantly modify the wave dispersion relation and can lead to considerable errors if not included.

The computed wave dispersion within the sea ice for long waves (peak wavelengths larger than approximately 100 m) is in good agreement with the theoretical open-water dispersion relation. This agreement gives us confidence in the validity of our assumption of linearity and confirms that the dispersion relation is not altered for these waves, which agrees with previous findings. In the open water, the estimated angular frequency, as function of the wave number, is underestimated for almost all the studied wave events. We show that the reason for this is that the assumption of linearity is violated in these cases.

Three wave events were studied with peak wavelengths in the range of 50–70 m, which were the smallest wavelengths we found where waves were visible within the sea ice. We investigated whether it is possible to back-calculate the ice thickness using the mass-loading model. However, the combination of the small ice thickness observed at the ice mooring stations and the range of wavelengths studied causes the deviation from the theoretical open-water dispersion relation to be minor. This deviation is too small to be able to be sensed by S1. Moreover, the observations from S1 show quite a large spread due to the inhomogeneous ice cover close to the ice edge. Broken-up ice and resulting ice floes, as well as open-water patches, are present. For the deviation to be sensible by the satellite, we would have to study waves with a wavelength of approximately 10–20 m, which requires higher-resolution data. Besides being able to study shorter waves, having higher-resolution data allows more averaging over the same spatial area, which eventually will lead to an accuracy sufficient to detect the effects of thin ice on the wave dispersion of short waves.

Acknowledgments
This project is based on Sentinel-1 raw data, which are kindly made available by the ESA and can freely be downloaded from the ESA's Sentinel data hub (https://scihub.copernicus.eu/). We would like to thank Yngvar Larsen at Norut for helping us with the SAR processing of the raw TOPS data. Furthermore, we would like to thank Equinor and the other BaSMIN JIP members for kindly providing in situ data which are presented in Table 1 and Figure 5e. The AMSR2 ice concentration data are available online (https://ghrc.nsstc.nasa.gov/uso/ds_details/inactive/A2_SI12_NRT_v0.html). The SMOS sea ice concentration data can be obtained online (https://icdc.cen.uni-hamburg.de/1/daten/cryosphere/l3c-smos-sit.html). Finally, we would like to acknowledge the support from the SAMCoT CRI through the Research Council of Norway, all the SAMCoT partners, and the support from CIRFA (funded by the Research Council, RCN Grant 237906).

References

Alpers, W. R., Ross, D. B., & Rufenach, C. L. (1981). On the detectability of ocean surface waves by real and synthetic aperture radar. *Journal of Geophysical Research, Oceans*, *86*(C7), 6481–6498. https://doi.org/10.1029/JC086iC07p06481

Ardhuin, F., Collard, F., Chapron, B., Girard-Ardhuin, F., Guitton, G., Mouche, A., & Stopa, J. E. (2015). Estimates of ocean wave heights and attenuation in sea ice using the SAR wave mode on Sentinel-1A. *Geophysical Research Letters*, *42*, 2317–2325. https://doi.org/10.1002/2014GL062940

Ardhuin, F., Stopa, J., Chapron, B., Collard, F., Smith, M., Thomson, J., et al. (2017). Measuring ocean waves in sea ice using SAR imagery: A quasi-deterministic approach evaluated with Sentinel-1 and in situ data. *Remote Sensing of Environment*, *189*, 211–222. https://doi.org/10.1016/j.rse.2016.11.024

Bao, M., & Alpers, W. (1998). On the cross spectrum between individual-look synthetic aperture radar images of oceanwaves. *IEEE Transactions on Geoscience and Remote Sensing*, *36*, 922–932. https://doi.org/10.1109/36.673683

Carsey, F. D., Argus, S. A. D., Collins, M. J., Holt, B., Livingstone, C. E., & Tang, C. L. (1989). Overview of LIMEX'87 ice observations. *IEEE Transactions on Geoscience and Remote Sensing*, *27*, 468–482. https://doi.org/10.1109/TGRS.1989.35930

Cheng, S., Rogers, W. E., Thomson, J., Smith, M., Doble, M. J., Wadhams, P., et al. (2017). Calibrating a viscoelastic sea ice model for wave propagation in the Arctic Fall Marginal Ice Zone. *Journal of Geophysical Research: Oceans*, *122*, 8770–8793. https://doi.org/10.1002/2017JC013275

Collins, C., Doble, M., Lund, B., & Smith, M. (2018). Observations of surface wave dispersion in the marginal ice zone. *Journal of Geophysical Research: Oceans*, *123*(5), 3336–3354. https://doi.org/10.1029/2018JC013788

Collins, C. O., Rogers, W. E., & Lund, B. (2017). An investigation into the dispersion of ocean surface waves in sea ice. *Ocean Dynamics*, *67*, 263–280. https://doi.org/10.1007/s10236-016-1021-4

Collins, C. O., Rogers, W. E., Marchenko, A., Babanin, A. V. (2015). In situ measurements of an energetic wave event in the Arctic marginal ice zone. *Geophysical Research Letters 42*, 1863–1870. https://doi.org/10.1002/2015GL063063.Received

Comiso, J. C., Meier, W. N., & Gersten, R. (2017). Variability and trends in the Arctic Sea ice cover: Results from different techniques. *Journal of Geophysical Research: Oceans*, *122*, 6883–6900. https://doi.org/10.1002/2017JC012768

Engen, G., & Johnsen, H. (1995). SAR-ocean wave inversion using image cross spectra. *IEEE Transactions on Geoscience and Remote Sensing*, *33*(4), 1047–1056. https://doi.org/10.1109/36.406690

Engen, G., Vachon, P. W., Johnsen, H., & Dobson, F. W. (2000). Retrieval of ocean wave spectra and RAR MTF's from dual-polarization SAR data. *IEEE Transactions on Geoscience and Remote Sensing*, *38*(1), 391–403. https://doi.org/10.1109/36.823935

European Space Agency (2013). Sentinel-1 user handbook (Tech. Rep. GMES-S1OP-EOPG-TN-13-0001).

Greenhill (1887). Wave motion in hydrodynamics. *American Journal of Mathematics*, *9*, 62–96.

Hasselmann, K., & Hasselmann, S. (1991). On the nonlinear mapping of an ocean wave spectrum into a synthetic aperture radar image spectrum and its inversion. *Journal of Geophysical Research*, *96*(C6), 10713. https://doi.org/10.1029/91JC00302

Hasselmann, K., Raney, R. K., Plant, W. J., Alpers, W., Shuchman, R. A., Lyzenga, D. R., et al. (1985). Theory of synthetic aperture radar ocean imaging: A MARSEN view. *Journal of Geophysical Research*, *90*, 4659. https://doi.org/10.1029/JC090iC03p04659

Jakobsson, M., Mayer, L., Coakley, B., Dowdeswell, J. A., Forbes, S., Fridman, B., et al. (2012). The International Bathymetric Chart of the Arctic Ocean (IBCAO) Version 3.0. *Geophysical Research Letters*, *39*, L12609. https://doi.org/10.1029/2012GL052219

Johnsen, H., & Collard, F. (2009). Sentinel-1 ocean swell wave spectra (OSW) algorithm definition.

Kaleschke, L., Tian-Kunze, X., Maaß, N., Mäkynen, M., & Drusch, M. (2012). Sea ice thickness retrieval from SMOS brightness temperatures during the Arctic freeze-up period. *Geophysical Research Letters*, *39*, L05501. https://doi.org/10.1029/2012GL050916

Keller, J. B. (1998). Gravity waves on water. *Journal of Geophysical Research*, *103*(C4), 7663–7669. https://doi.org/10.1029/97JC02966

Kerbaol, V., Chapron, B., & Vachon, P. W. (1998). Analysis of ERS-1/2 synthetic aperture radar wave mode imagettes. *Journal of Geophysical Research, Oceans*, *103*(C4), 7833–7846. https://doi.org/10.1029/97JC01579

Kohout, A. L., Williams, M. J. M., Toyota, T., Lieser, J., & Hutchings, J. (2016). In situ observations of wave-induced sea ice breakup. *Deep Sea Research Part II: Topical Studies in Oceanography*, *131*, 22–27. https://doi.org/10.1016/j.dsr2.2015.06.010

Krogstad, H. E. (1992). A simple derivation of Hasselmann's nonlinear ocean-synthetic aperture radar transform. *Journal of Geophysical Research*, *97*(C2), 2421–2425. https://doi.org/10.1029/91JC03010

Liu, A. K., Vachon, P. W., & Peng, C. Y. (1991). Observation of wave refraction at an ice edge by synthetic aperture radar. *Journal of Geophysical Research*, *96*(C3), 4803–4808. https://doi.org/10.1029/90JC02546

Lyzenga, D. R., Shuchman, R. a., & Lyden, J. D. (1985). SAR imaging of waves in water and ice: Evidence for velocity bunching. *Journal of Geophysical Research*, *90*(C1), 1031–1036. https://doi.org/10.1029/JC090iC01p01031

Melia, N., Haines, K., & Hawkins, E. (2016). Sea ice decline and 21st century trans-Arctic shipping routes. *Geophysical Research Letters*, *43*, 9720–9728. https://doi.org/10.1002/2016GL069315

Meylan, M. H., Bennetts, L. G., Mosig, J. E. M., Rogers, W. E., Doble, M. J., & Peter, M. A. (2018). Dispersion relations, power laws, and energy loss for waves in the marginal ice zone. *Journal of Geophysical Research: Oceans*, *123*(5), 3322–3335. https://doi.org/10.1002/2018JC013776

Oziel, L., Sirven, J., & Gascard, J. C. (2016). The Barents Sea frontal zones and water masses variability (1980–2011). *Ocean Science*, *12*(1), 169–184. https://doi.org/10.5194/os-12-169-2016

Park, J.-W., Korosov, A. A., Babiker, M., Sandven, S., & Won, J.-S. (2018). Efficient thermal noise removal for Sentinel-1 TOPSAR Cross-Polarization Channel. *IEEE Transactions on Geoscience and Remote Sensing*, *56*(3), 1555–1565. https://doi.org/10.1109/TGRS.2017.2765248

Renner, A. H. H., Gerland, S., Haas, C., Spreen, G., Beckers, J. F., Hansen, E., et al. (2014). Evidence of Arctic sea ice thinning from direct observations. *Geophysical Research Letters*, *41*, 5029–5036. https://doi.org/10.1002/2014GL060369

Shen, H., Perrie, W., Hu, Y., & He, Y. (2018). Remote sensing of waves propagating in the marginal ice zone by SAR. *Journal of Geophysical Research: Oceans*, *123*(1), 189–200. https://doi.org/10.1002/2017JC013148

Shuchman, R. a., Rufenach, C. L., & Johannessen, O. M. (1994). Extraction of marginal ice zone thickness using gravity wave imagery. *Journal of Geophysical Research*, *99*(C1), 901. https://doi.org/10.1029/93JC01956

Snodgrass, F. E., Groves, G. W., Hasselmann, K. F., Miller, G. R., Munk, W. H., & Powers, W. H. (1966). Propagation of ocean swell across the Pacific. *Philosophical Transactions of the Royal Society A - Mathematical Physical and Engineering Sciences*, *259*(1103), 431–497. https://doi.org/10.1098/rsta.1966.0022

Spreen, G., Kaleschke, L., & Heygster, G. (2008). Sea ice remote sensing using AMSR-E 89-GHz channels. *Journal of Geophysical Research, Oceans*, *113*(C2), 1, C02S03–14. https://doi.org/10.1029/2005JC003384

Squire, V. A. (2007). Of ocean waves and sea-ice revisited. *Cold Regions Science and Technology*, *49*(2), 110–133. https://doi.org/10.1016/j.coldregions.2007.04.007

Squire, V. A., Duggan, J. P., Wadhams, P., Rottier, P. J., & Liu, A. J. (1995). Of ocean waves and sea ice. *Annual Review of Fluid Mechanics*, *27*, 115–168. https://doi.org/10.1146/annurev.fl.27.010195.000555

Stopa, J. E., Ardhuin, F., Chapron, B., & Collard, F. (2015). Estimating wave orbital velocity through the azimuth cutoff from space-borne satellites. *Journal of Geophysical Research: Oceans*, *120*, 7616–7634. https://doi.org/10.1002/2015JC011275

Stopa, J. E., Ardhuin, F., Thomson, J., Smith, M. M., Kohout, A., Doble, M., & Wadhams, P. (2018). Wave attenuation through an Arctic marginal ice zone on 12 October 2015. 1. Measurement of wave spectra and ice features from Sentinel 1A. *Journal of Geophysical Research: Oceans*, *123*(5), 3619–3634. https://doi.org/10.1029/2018JC013791

Stopa, J. E., Sutherland, P., & Ardhuin, F. (2018). Strong and highly variable push of ocean waves on Southern Ocean sea ice. *Proceedings of the National Academy of Sciences of the United States of America*, *237*, 1–5. https://doi.org/10.1073/pnas.1802011115

Thomson, J., Ackley, S., Girard-Ardhuin, F., Ardhuin, F., Babanin, A., Boutin, G., et al. (2018). Overview of the Arctic sea state and boundary layer physics program. *Journal of Geophysical Research: Oceans*, *123*(12), 8674–8687. https://doi.org/10.1002/2018JC013766

Tian-Kunze, X., Kaleschke, L., & Maass, N. (2018). SMOS Daily sea ice thickness version 3, 04-04-2017. University of Hamburg, Germany, Digital medio.

Wadhams, P., Aulicino, G., Parmiggiani, F., Persson, P. O. G., & Holt, B. (2018). Pancake ice thickness mapping in the Beaufort Sea from wave dispersion observed in SAR imagery. *Journal of Geophysical Research: Oceans*, *123*(3), 2213–2237. https://doi.org/10.1002/2017JC013003

Wadhams, P., & Holt, B. (1991). Waves in frazil and pancake ice and their detection in Seasat synthetic aperture radar imagery. *Journal of Geophysical Research*, *96*(C5), 8835–8852. https://doi.org/10.1029/91JC00457

Wadhams, P., Parmiggiani, F., & de Carolis, G. (2002). The use of SAR to measure ocean wave dispersion in frazil–pancake icefields. *Journal of Physical Oceanography*, *32*(6), 1721–1746. https://doi.org/10.1175/1520-0485(2002)032<1721:TUOSTM>2.0.CO;2

Wadhams, P., Parmiggiani, F. F., De Carolis, G., Desiderio, D., & Doble, M. J. (2004). SAR imaging of wave dispersion in Antarctic pancake ice and its use in measuring ice thickness. *Geophysical Research Letters*, *31*, L15305. https://doi.org/10.1029/2004GL020340

Wang, R., & Shen, H. H. (2010). Gravity waves propagating into an ice-covered ocean: A viscoelastic model. *Journal of Geophysical Research, Oceans*, *115*(C6), 1, C06024–12. https://doi.org/10.1029/2009JC005591

Weitz, M., & Keller, J. B. (1950). Reflection of water waves from floating ice in water of finite depth. *Communications on Pure and Applied Mathematics*, *3*(3), 305–318. https://doi.org/10.1002/cpa.3160030306

World Metrological Organization (1970). *WMO Sea-Ice Nomenclature*, *Terminology and codes. Report 259* (Vol. 1). Geneva: Switzerland.

Zan, F. D., & Guarnieri, A. M. (2006). TOPSAR: Terrain observation by progressive scans. *IEEE Transactions on Geoscience and Remote Sensing*, *44*(9), 2352–2360. https://doi.org/10.1109/TGRS.2006.873853

Appendix E Modelling of hydrodynamic and wave conditions for a new harbour in Søndre Strømfjord (Kangerlussuaq)

This paper was prepared for the AIC 2018 – Transportation Infrastructure Engineering in Cold Regions conference, 1-3 May 2018, Sisimiut, Greenland.

Monteban, D., Pedersen, J.O.P., Nielsen, M.H., Ingeman-Nielsen, T., 2018. Modelling of hydrodynamic and wave conditions for a new harbor in Søndre Strømfjord (Kangerlussuaq), in: AIC 2018 Transportation Infrastructure Engineering in Cold Regions. Sisimiut, pp. 28-29

Modelling of hydrodynamic and wave conditions for a new harbor in Søndre Strømfjord (Kangerlussuaq).

Dennis Monteban[1]*, Jens Olaf Pepke Pedersen[1], Morten Holtegaard Nielsen[2] and Thomas Ingeman-Nielsen[3]

[1] DTU Space, Technical University of Denmark, Diplomvej, 371, 2800 Kgs. Lyngby, Denmark
[2] Marine Science & Consulting, Peder Lykkes Vej 8, 4. th. 2300 Copenhagen, Denmark
[3] Department of Civil Engineering, Technical University of Denmark, Brovej, 118, 2800 Kgs. Lyngby, Denmark
* Speaker, e-mail: dmont@space.dtu.dk

Introduction

Søndre Strømfjord (Kangerlussuaq fjord) is located at the West coast of Greenland, Figure 1. There are three large river systems which transport glacial sediments into the fjord, i.e. the Watson River, Umivit River and Sarfartoq River. The Watson River enters the fjord at the North Eastern head and a well-developed delta is found at its outlet. The existing harbour in Kangerlussuaq is located at this outlet and experiences major sedimentation problems. Deposited sediments have reduced the water depth and hinders cruise- and large container ships from entering the harbour. In order to enter the port, small vessels transport passengers and cargo from the ships which are anchored further out in the fjord. The result is an inefficient operation and high maintenance cost for the municipality. Therefore, a new harbour location was proposed by Stenstad et al. (2015) 10 km further out the fjord near Hancock Pynt (HP), see Figure 1. The new location was selected based on seismic data and it was found that the onshore area is well suited for a harbour support area. The offshore sediments are mainly fine grained and not suitable as support for foundations. In addition, to reach the required water depth a significant amount of sediments need to be removed. The focus of this paper is to set up numerical models of the fjord system and provide the hydrodynamic, wind and wave conditions for the new proposed harbour location.

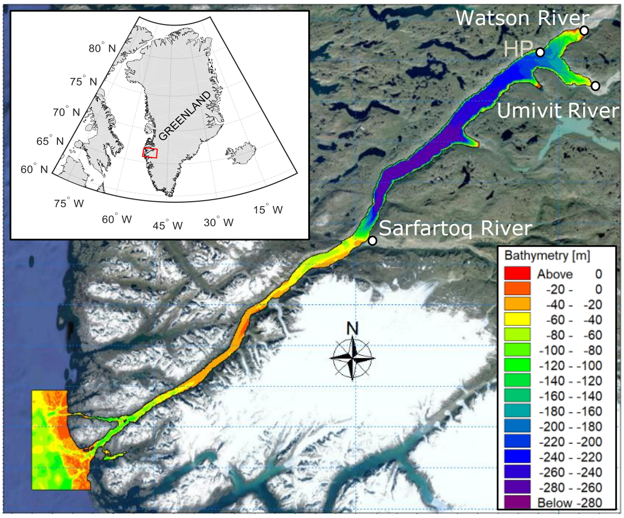

Figure 1. Top left figure is an overview map of Greenland showing the extent of the main map of Kangerlussuaq fjord. The bathymetry of the fjord is shown with a colour code which is also the model extent used in MIKE 21 FM. The new proposed harbour location Hancock Pynt (HP) and the three main rivers are indicated with white circles.

Regional settings

Kangerlussuaq fjord is roughly 180 km long and has two distinct parts: the inner part which is broad (4-6 km) and deep (up to 280 m), and the shallow outer part which is roughly 100 km long, about 1 km wide and has a depth of 20-80 m. This shallow outer part is unusual for Arctic fjords because of its length and causes the water mass in the inner deep part of the fjord to be almost decoupled from the open ocean (Nielsen et al., 2010). The initial formation of ice in the inner part of the fjord system generally starts at the end of November. The sea ice expands all the way to the outer part of the fjord, close to Sarfartoq River, where the tidal currents are too strong for sea ice to form. In the inner part of the fjord, the sea ice reaches a thickness of about 1 m (Nielsen et al., 2010). An analysis of MODIS images show that at the end of May the last ice floats melt and open water is expected. The ice free period extents from the beginning of June till the end of November.

Approach

Two different numerical models were set up of the fjord system using the MIKE 21 software developed by DHI. The first numerical model is the MIKE 21 Flow Model hydrodynamic module. It simulates water level and flow variations by solving the depth-integrated incompressible Reynolds averaged Navier-Stokes equations (DHI, 2016). The fjord was surveyed by the Danish Geodata Agency in the summer of 2012 and the model bathymetry (Figure 1) was constructed from this data. The computational mesh has a resolution of 440 m outside the fjord and 300 m inside the fjord. There are three open boundaries located outside the fjord. The tides at these boundaries were predicted from a tidal constituents map constructed from the DTU global tide model (Cheng and Andersen, 2010). It includes 10 tidal constituents and has a resolution of 0.125 degrees. The model was calibrated against water level measurements which were collected in the summer of 2011 at multiple locations throughout the fjord. The main calibration parameter is the bed friction and the best fit was obtained by applying a varying Manning number depending on the water depth. The second numerical model is the MIKE 21 Spectral Wave (SW) module. It is a spectral-wind wave model and is able to simulate growth, decay and the transformation of wind-generated and swell waves. The model extent only covers the inner part of the fjord until Sarfartoq River. A computational mesh with resolution of 300 m was used and the model does not include any open boundaries. The wind input was obtained at Kangerlussuaq airport from 1976-2016 (Cappellen, 2017) and was adjusted for height and location. The model was calibrated against wave height measurements at a location close to Hancock Pynt for the period September-October 2013. The main calibration parameter was the type of air-sea interaction, i.e. how the momentum is transferred from the wind to the waves. The 'uncoupled' formulation, where the momentum transfer solely depends on the wind speed resulted in the best calibrated model. An extreme value analysis was performed on the wind data in order to find the wind speed with a return period of 50 years. This was done for two different sectors with the largest fetch, South-West and South-East. The obtained wind speed for each sector was used as input for the MIKE 21 SW model to find the corresponding wave height and peak period.

Results and conclusions

The hydrodynamic, wind and wave conditions found by analysing the wind data and from the numerical model simulations are summarised in Table 1. The tidal wave takes 3.5 hours to travel from the beginning of the fjord to Hancock Pynt. At Hanock Pynt there is a mean spring tidal range of about 3.5 meter and therefore it has a meso-tidal regime (mean spring tidal range between 2-4 meters). The tidal character can be determined from the four major tidal constituents which are at Hancock Pynt: K1 = 0.2575, O1 = 0.1252, M2 = 1.1935 and S2 = 0.3358. The form factor, F = (K1+1)/(M2+S2), is used to classify the tidal characteristics and has a value of 0.2503. Hence, the tide is mixed, mainly semidiurnal. The maximum flood current speed observed is 0.2 m/s and the maximum ebb current speed is 0.148 m/s. The 50 year return period wind speed, wave height and peak wave period for the South-West and South-East sector are shown in Table 1. It can be seen that the wave height coming in from the South-West is larger than the one coming in from the South-East. Though, the waves from both directions should be taken into account when designing the layout of the harbour. Beside the wind, current and wave conditions which are provided in this paper, further investigations regarding the ice forces and sediment transport are needed in order to come up with a suitable harbour design. Currently, a MIKE 3 model is under construction which will give a more detailed picture of the (3D) current field in the fjord.

Table 1. Wind, wave and hydrodynamic conditions at Hancock Pynt.

Parameter	**Value**	**Unit**
Lowest astronomical tide (LAT)	-1.74	m
Highest astronomical tide (HAT)	1.89	m
Maximum tidal current speed	0.2	m/s
50 year return period wind speed (South-West)	16.5	m/s
50 year return period wave height (South-West)	1.8	m
50 year return period peak wave period (South-West)	5	s
50 year return period wind speed (South-East)	16.1	m/s
50 year return period wave height (South-East)	1.18	m
50 year return period peak wave period (South-East)	3.95	s

References

Cappelen, J. (2017). *Weather observations from Greenland 1958-2016 - Observation data with description*. Copenhagen: Danish Meteorological Institute. Retrieved from http://www.dmi.dk/laer-om/generelt/dmi-publikationer/

Cheng, Y., Andersen, O. B. (2009). *Improvement in global ocean tide model in shallow water regions.* Poster, SV.1-68 45, OSTST, Lisbon, Oct.18-22.

DHI (2016), *MIKE 21 Flow Model, Scientific Documentation*, Hørsholm, Denmark

Nielsen, M. H., Erbs-Hansen, D. R., & Knudsen, K. L. (2010). Water masses in Kangerlussuaq, a large fjord in West Greenland: the processes of formation and the associated foraminiferal fauna. *Polar Research*, *29*(2), 159–175

Stenstad, J. G., Kjetil, G., & Ingeman-Nielsen, T. (2015). New Harbor in Kangerlussuaq, Western Greenland: Field Investigations and Utilization of Existing Materials. Proceeding of the 23th International Conference on Port and Ocean Engineering under Arctic Conditions.

Appendix F Physical oceanographic conditions and a sensitivity study on meltwater runoff in a West Greenlandic fjord: Kangerlussuaq

This paper is submitted to the Oceanologia journal. Presently, it is in the second round of the reviewing process.

Monteban, D., Pedersen, J.O.P., Nielsen, M.H., 2020b. Physical oceanographic conditions and a sensitivity study on meltwater runoff in a West Greenland fjord: Kangerlussuaq. Oceanologia. Manuscript submitted for publication.

Physical oceanographic conditions and a sensitivity study on meltwater runoff in a West Greenland fjord: Kangerlussuaq

Dennis Monteban[1,2], Jens Olaf Pepke Pedersen[1] and Morten Holtegaard Nielsen[3]

[1]DTU Space, Technical University of Denmark, Lyngby, Denmark

[2]Norwegian University of Science and Technology, Trondheim, Norway

[3]Marine Science & Consulting ApS, Copenhagen, Denmark

Corresponding author: Dennis Monteban dmont@space.dtu.dk

Highlights:

- A hydrodynamic model was set up for the fjord Kangerlussuaq
- The circulation pattern is primarily along the fjord direction, with weak currents in the inner part of the fjord as opposed to very strong tidal currents in the outer part
- Two distinct vertical current structures are present, with a strong outflow of freshwater in the upper layer during summertime and small vertical gradients observed during wintertime
- The deep-lying water mass in the inner part of the fjord is barely subject to renewal and is nearly dynamically decoupled from the open ocean during summertime
- A sensitivity study of meltwater runoff provides insight into the potential effects, with the most significant changes observed in the upper 100 m

Abstract

In this paper, we discuss the first setup of a hydrodynamic model for the fjord-type estuary Kangerlussuaq, located in West Greenland. Such a high-fidelity numerical model is important because it allows us to fill in the temporal and spatial gaps left by in situ data and it allows us to investigate the effects of perturbations in the model's forcing data. The numerical model is calibrated against in situ data, and a one-year simulation was performed to study the seasonal variability in the physical oceanographic environment and the fjord's response to changing meltwater runoff. The fjord consists of two distinct parts, namely, a deep inner part that is 80 km long with weak currents and a shallow part that covers the outer 100 km of the fjord connected to the ocean. The outer part has very strong currents, which are most likely the cause of the absence of sea ice during wintertime. The circulation pattern is primarily in the along-fjord direction, and during summertime, the freshwater inflow from the meltwater rivers causes a net outflow of the fjord in the upper layer. Furthermore, a comprehensive analysis of the water masses is provided, which shows that the deep-lying water mass is almost dynamically decoupled from the open ocean and hardly subject to any renewal during summertime. Finally, a sensitivity study on the changing meltwater runoff was performed, showing that the most severe impacts of increasing freshwater runoff are in the upper 100 m of the deep, inner part of the fjord.

Keywords: Arctic fjord, Hydrodynamic model, MIKE 3, Water masses, Meltwater runoff, Kangerlussuaq fjord

1 Introduction

The largest ice mass in the Northern Hemisphere, the *Greenland Ice Sheet* (GIS), experienced an increase in mass loss over the past two decades (Hanna et al., 2008; Shepherd et al., 2012), which is expected to continue because the most pronounced effects of future climate change are projected to occur in the Arctic region (Kattsov et al., 2005). The freshwater discharged from the GIS mostly transits through fjords, where the freshwater can be significantly modified before reaching the ocean. Therefore, it is essential to have a detailed understanding of fjord dynamics, as they are considered to be a vital link between inland ice and the ocean (Straneo and Cenedese, 2015). Moreover, an improved understanding of fjord circulation is required to explain regional climate changes in Greenland and predict future changes in the climate system (Straneo et al., 2013).

Previous studies on Arctic fjords were primarily conducted because fjords contain information on past ice sheet variability and sedimentary records (e.g., Storms et al., 2012). Another motivation was also that fjord systems contain complex marine ecosystems and because local communities are dependent on fjords for fishing and hunting (e.g., Born and Böcher, 2001). It was relatively recently that the physical oceanographic environment of fjords has been the main focus (Cottier et al., 2010), and such knowledge will allow for a better interpretation of fjord-related research.

The most accurate method to obtain the physical conditions in Arctic fjords is by collecting in situ measurements. However, because of the harsh Arctic environment, it is logistically difficult and expensive to collect large amounts of in situ data that are representative of the whole fjord and extend over large timescales. Therefore, a major limitation in the Arctic is the lack of in situ data. Another approach to obtain an understanding of the physical state of a fjord is modelling. Although numerical models are a simplification of reality, they can act as an additional tool to fill in the spatial and temporal gaps in in situ data and consequently understand the physical processes at work.

A growing body of literature has studied Greenlandic fjord systems (see Rignot et al. (2012) for an overview of study areas). These studies have looked at fjords from two different perspectives. The first perspective is that the fjord is a mixing zone where the relevant flow transports heat into the fjord and directly towards the glacier terminus (Holland et al., 2008; Mortensen et al., 2011; Rignot et al., 2010; Sutherland et al., 2014), which affects glacial melting. The other view also regards fjords as mixing zones, but the focus is on the transformation and export of meltwater runoff from the GIS towards the ocean (Bendtsen et al., 2014; Straneo et al., 2011), potentially influencing shelf circulation (e.g., Murray et al., 2010).

In this paper, we focus on the fjord Kangerlussuaq, located in West Greenland. This fjord receives large quantities of freshwater from meltwater rivers each year. Van As et al. (2018) found that the average discharge of the main meltwater river flowing into the fjord, i.e., the

Watson River, increased by 46 percent between 2003-2017 compared to the 1949-2002 average. Moreover, the interannual variability in the meltwater runoff increased considerably. An increase in the annual volume of freshwater runoff from the GIS influences the physical structure of the water column (Kjeldsen et al., 2014; Mortensen et al., 2013) and the structure of ecosystems (e.g., Arendt et al., 2010; Dziallas et al., 2013). The latter is because turbid meltwater has a large light attenuation coefficient that reduces photosynthesis and therefore reduces primary production (Piwosz et al., 2009; Retamal et al., 2008). To understand the fjord's response to changing meltwater runoff and the physical oceanographic conditions in general, a hydrodynamic model was established in this study.

The paper is structured as follows: in Section 2, the study area is described together with the available measurements and observations. In Section 3, the setup of the numerical model is presented, and all the model parameters and parameterizations, the model domain and the boundary conditions are described. Next, the calibration procedure is described in Section 4. A one-year simulation was performed, and the main outputs of the model are presented and discussed in Section 5, which is divided into three parts: 1) the circulation pattern in the fjord, 2) the seasonal dynamics of the water masses and 3) a sensitivity study towards meltwater runoff. Finally, some concluding remarks are presented in Section 6.

2 Study area and observations

2.1 Regional setting

The fjord Kangerlussuaq (also called Søndre Strømfjord) is a large fjord located at the Arctic circle in West Greenland (Figure 1). This fjord is classified as a fjord-type estuary (Lund-Hansen et al., 2010) and has a surface area of approximately 490 km^2. The fjord is 180 km long, and there are two branches at the mouth of the fjord that connect the fjord with the open ocean. Further west from the mouth of the fjord at the continental slope, the West Greenland Current is found. The West Greenland Current is a continuation of the East Greenland Current and the Irminger Current, which are governed by cold and relatively fresh water of Arctic origin and warm and salty water that originated in the Atlantic, respectively (Myers et al., 2007; Sutherland and Pickart, 2008).

In Figure 3, the bathymetry of the fjord Kangerlussuaq, which was surveyed by the Danish Geodata Agency, is presented. The fjord can be divided into two distinct parts: the outer part of the fjord, which covers the first 100 km, is characterized by a limited water depth (between approximately 30 and 60 m) and a small width. The inner part is much deeper (up to 300 m) and wider. A steep slope defines the transition between the two parts where the bottom rises approximately 215 m over 13 km and is located close to the mouth of the Sarfartoq River.

2.2 Freshwater sources

The fjord receives freshwater from snowmelt, sea ice melt, precipitation, local glaciers and the GIS. Large quantities of freshwater runoff enter the fjord in the summertime primarily from three rivers; the Watson River (66°57′54″ N, 50°51′50″ W) flows into the northeast head of the fjord, the Umivit River (66°50′2″ N, 50°48′37″ W) enters at the southeast head of the fjord and the Sarfartoq River (66°29′30″ N, 52°1′30″ W), which enters in approximately the middle of the fjord. The rivers drain meltwater from the GIS and the Sukkertoppen ice cap (Figure 1). Hudson et al. (2014) estimated the catchment area based on the surface and basal topography, and this area is 3639 km^2, 6320 km^2 and 5385 km^2 for the Watson River, the Umivit River and the Sarfartoq River, respectively. The catchment area of the Watson River was also determined in multiple previous studies, and this value differs significantly from one study to the other. For instance, catchment areas of 9743 km^2 (Hasholt et al., 2013), 6130 km^2 (Mernild et al., 2010), 12547 km^2 (Van As et al., 2012) and 12000 km^2 (Lindbäck et al., 2015) were reported. Furthermore, the area of Kangerlussuaq is exceptionally dry because of orographic shielding by the Sukkertoppen ice cap (Box et al., 2006), and this dryness, together with water losses from evaporation, causes the contribution of precipitation to be minimal compared to the ice sheet runoff (Hasholt et al., 2013). Field measurements of the discharge of the Watson River were conducted by Hasholt et al. (2013) from 2007 to 2010. The peak discharge is usually observed in July/August, and a peak flow of 1620 m^3 s^{-1} was measured. The flow in the rivers is almost zero from October/November until April/May, and during 2007-2010, the average annual discharge was 1070 km^3. In the measurements, certain characteristic spikes of high magnitude discharge were observed that are related to Jökulhlaups, which occur in this glaciated area (Carrivick et al., 2018; Mikkelsen et al., 2013; Russell et al., 2011).

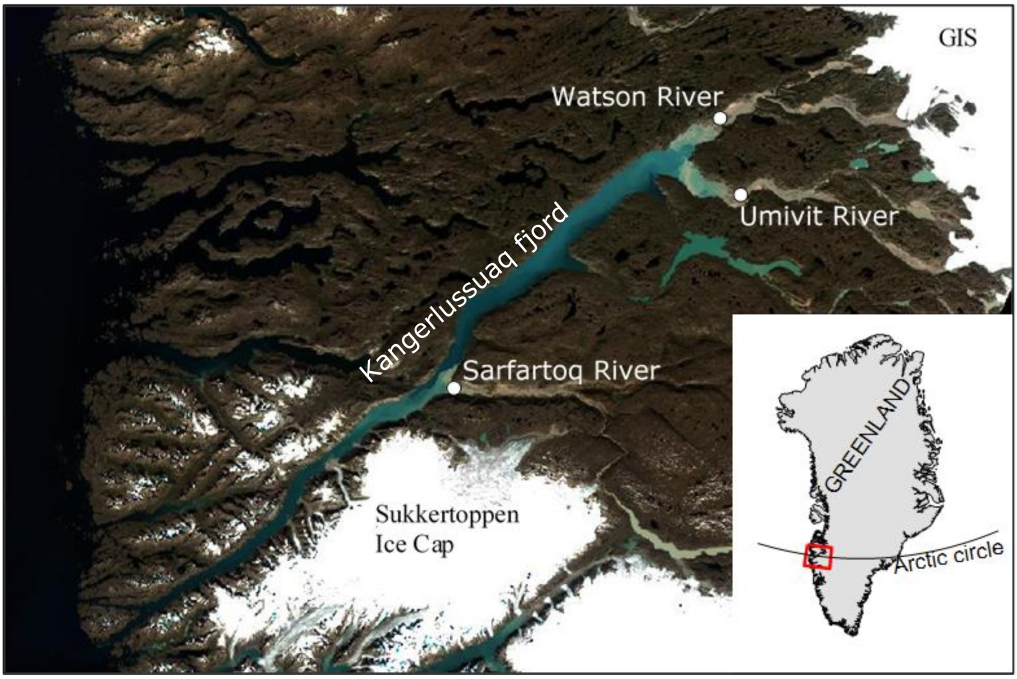

Figure 1. Sentinel-2 image of the fjord Kangerlussuaq, acquired 31 July 2017. The locations where the three main meltwater rivers enter the fjord are indicated.

2.3 Atmospheric and sea ice observations

Meteorological observations at an elevation of 50 m are obtained from the *Danish Meteorological Institute* (DMI) weather station, located at the airport of Kangerlussuaq (67°01′ N, 50°42′ W), which includes the wind speed and direction, relative humidity, cloud cover and air temperature (Cappelen, 2016). The wind measurements are corrected for height (from 50 m to 10 m above mean sea level) using the wind profile power law (e.g., Shore Protection Manual, 1984). The data were sampled every 1 hour, and the data used to force the model are presented in

Figure 2 for the period of March 2005 to March 2006.

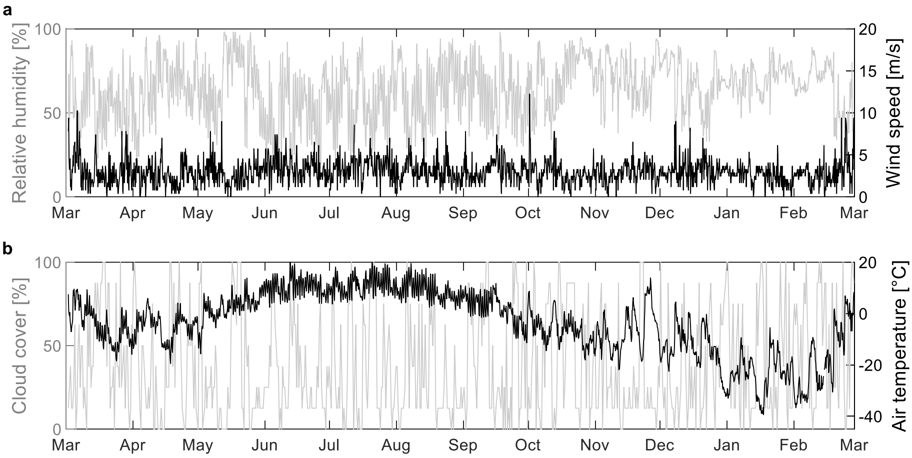

Figure 2. Observations from the DMI weather station, located at the airport of Kangerlussuaq. (a) The relative humidity (gray line) and the wind speed corrected to a height of 10 m above mean sea level (black line). (b) The cloud cover (gray line) and the dry bulb air temperature (black line). The data are taken from Cappelen (2016).

The mean corrected wind speed is approximately 3 m/s, but some relatively strong winds up to 12.2 m/s were observed. The dominant wind direction is from the northeast, which corresponds to the wind blowing out of the fjord. Typical values for the relative humidity are approximately 70%. The cloud cover varies substantially with cloud-free days (0%) and days with 100% cloud cover. The recorded air temperature varied between approximately +20 °C in summer and -38 °C in winter. The air temperature dropped below zero degrees around October and was negative until approximately the start of May.

Sea ice formation and breakup were studied using optical imagery collected by the *Moderate-resolution Imaging Spectroradiometer* (MODIS) onboard the Terra and Aqua satellites from the NASA Worldview application during the 2009-2017 period. For the winter of 2005/2006, observations were available from the Envisat satellite. Generally, initial sea ice formation starts in mid-November, and the fjord is sea ice free beginning in June. The sea ice covers only the inner part of the fjord, up to the Sarfartoq River, as these currents are most likely too strong for sea ice to form (see Section 5.1). The ice thickness reaches up to approximately 1 metre in the inner part of the fjord (Hawes et al., 2012; Nielsen et al., 2010). For the winter of 2005/2006, sea ice formation started in the beginning of December 2005 and reached its maximum areal extent at the end of December. The last sea ice floes were observed on 23 May 2006.

2.4 Water level and CTD measurements

Measurements of the water level at several locations throughout the fjord (points a, b and c in Figure 3) were conducted from June 2011 until mid-September 2011 using Solinst Levelogger Gold recording devices (Solinst Canada Ltd, Georgetown, Ontario, Canada). These devices were placed under the waterline during low tide, and they measured the pressure at 5 min intervals. The water levels are computed from the pressure difference as the tidal wave passes, and a mean spring tidal range of 3.5 metres was found. Moreover, the tidal wave travels in approximately 3.5 hours from the seaside (point a in Figure 3) to the end of the inner part of the fjord (point c in Figure 3). The tidal character may be defined by the form factor, F, which is the sum of the two main diurnal components (K_1, O_1) divided by the sum of the two main semidiurnal components (S_2, M_2) and reads as follows (Courtier, 1939):

$$F = \frac{(K_1 + O_1)}{(M_2 + S_2)} \tag{1}$$

Four different types of tides are distinguished based on the form factor. At the inner part of the fjord, the form factor has a value of 0.24, which means that the tidal character is classified as semidiurnal.

Conductivity, temperature and pressure data were collected during two surveys that were carried out on 3-5 August 2005 and on 26-27 February 2006. These measurements are described in Nielsen et al. (2010). During the survey in August, a total of 16 vertical profiles were made along the entire fjord using a 19plus SEACAT Profiler (Sea-bird Electronics, Bellevue, WA, USA). The survey in February includes 6 different vertical profiles that were made on the sea ice-covered part of the fjord; hence, only the inner part of the fjord was visited.

3 Model description

The numerical model of the fjord Kangerlussuaq was implemented using the commercially available three-dimensional MIKE 3 Flow Model (2016 version) software. The MIKE 3 model is well documented, and a comprehensive description can be found in DHI (2016). An overview of all the input parameters, the choice of the different modules in MIKE 3 and the sources of the boundary and initial conditions used in the simulations are summarized in Table 1. The model setup is described in detail in the remainder of this chapter.

3.1 Model setup

The MIKE 3 model numerically solves the *Reynolds-averaged Navier-Stokes* (RANS) equations with the assumptions of Boussinesq and hydrostatic pressure using a cell-centred finite volume method. The RANS equations are closed with a turbulent scheme by adopting the eddy viscosity concept, where the vertical and horizontal eddy viscosities are represented by the standard k-ε model (Rodi, 1984) and the Smagorinsky formulation (Smagorinsky, 1963), respectively.

The bathymetry of the modelled fjord, the model domain and the horizontal computational mesh are presented in Figure 3. The computation mesh is a combination of triangular elements and quadrangular grid cells. There is a pre-dominant water flow direction along the fjord direction, i.e., there is limited across-fjord variability (see Section 5.1). Therefore, we used quadrangular grid cells in the main part of the fjord that allow for a coarser resolution in the along-fjord direction than in the across-fjord direction; hence, the number of elements and the computational time are reduced. Moreover, the quadrangular cells simulate the flow more accurately compared to the triangular elements in this case because the elongated quadrangular cells favour water flow along the element, while the triangular elements enhance divergence in the water flow (DHI, 2016a). The computational mesh has 1984 elements (computational cells) in the surface layer. The smallest element has a characteristic length of approximately 160 m, and the largest cell has a dimension of approximately 1000 m, which is directed along the long axis. The vertical domain was discretized using 40 vertical layers with a resolution of 1 m at the surface layer down to 15 m at the bottom. The first 5 vertical layers starting at the surface are terrain-following sigma layers. The remaining vertical layers are z-layers, which do not follow the bottom terrain and are defined at fixed depths.

Table 1. Overview of the input parameters and module options used in the MIKE 3 model.

Input Parameter	**Value or module option**
Horizontal mesh	Resolution (min, max) = (160, 1000) m
Vertical mesh	Combined sigma/z-level; 5 sigma layers to a depth of 10 m and 35 z-layers. Resolution (min, max) = (1, 15) m
Time period	01.03.2005-01.03.2006
Maximum time step	300 s
Solution technique	Higher order scheme
Eddy viscosity	Horizontal eddy viscosity: Smagorinsky formulation Vertical eddy viscosity: k-ε model
Bed resistance	Constant roughness height: 0.05 m
Dispersion	Horizontal dispersion coefficient: 1 Vertical dispersion coefficient: 0.1
Coriolis forcing	Constant in domain
Atmospheric forcing	Observations available from the DMI weather station located at the airport of Kangerlussuaq and includes - Wind speed and direction - Air temperature - Cloud cover - Humidity
Ice coverage	Sea ice coverage derived from Envisat satellite imagery Sea ice roughness: 0.01 m
Initial conditions	Water level 0 m Velocities 0 m s^{-1} Salinity From February 2006 measurements (Nielsen et al., 2010) Temperature From February 2006 measurements (Nielsen et al., 2010)
Boundary conditions	Rivers Average discharge of 2007-2010 observations (Hasholt et al., 2013) Sea Water levels from DTU global tide model Sea Salinity and temperature from the Global Ocean Physics Reanalysis product (Copernicus)

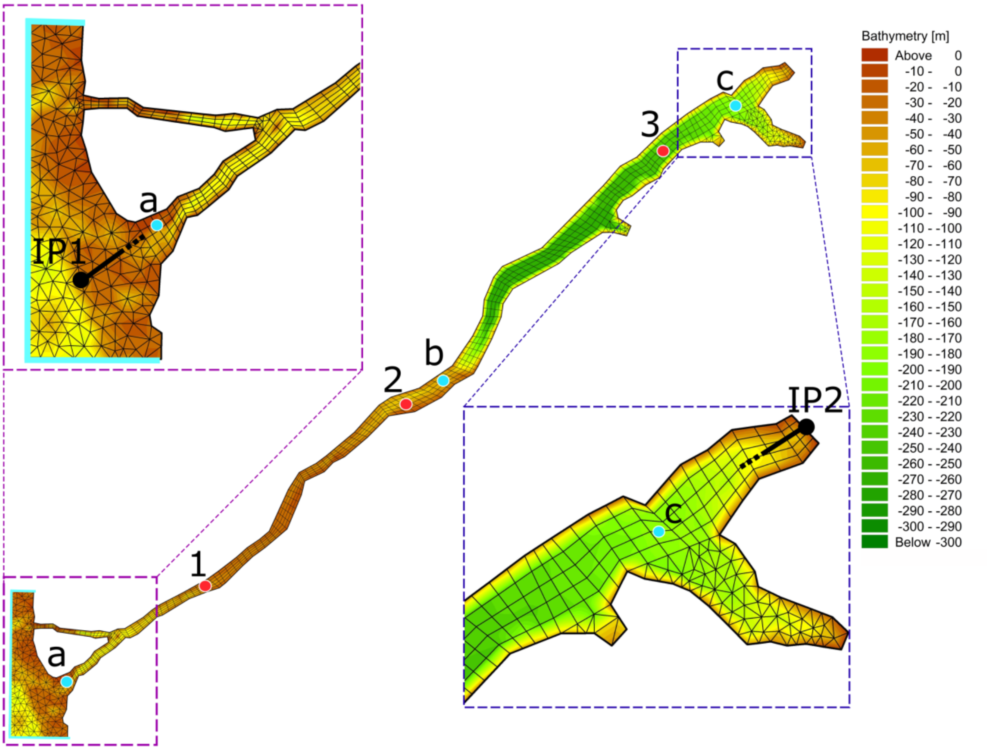

Figure 3. The model domain, bathymetry and horizontal computational mesh. The three red dots (points 1, 2 and 3) indicate the positions of the calibration points for the baroclinic part, and the three blue dots (points a, b and c) show the calibration points of the barotropic part. The IP1 and IP2 points shown in the magnifications of the fjord show the beginning and end of the vertical cross sections, which are shown in multiple figures in this paper, respectively. Furthermore, the solid light blue line at the mouth of the fjord depicts the seaside open boundary.

3.2 Initial and boundary conditions

The initial conditions (simulation started on 01 March 2005) were obtained from the CTD profiles taken on 26 February 2006. Although these measurements are from a different year, we used them because the temperature and salinity distributions throughout the fjord in wintertime are very homogeneous and relatively similar from year to year (Nielsen et al., 2010). The initial conditions in the outer, shallow part of the fjord were obtained by interpolating between the measurements of the vertical profiles in the inner part of the fjord and the values at the seaside open boundary. Potential discrepancies in the initial conditions of the outer part of the fjord would be adjusted by the model before summertime. Nevertheless, the model simulation does not substantially change the values of the initial conditions during wintertime, which gives us confidence in the representability of the applied initial conditions. The lateral boundary condition located outside the mouth of the fjord combines the water level, current velocities, temperature and salinity. This boundary is indicated by the solid light blue line in Figure 3. The hydrodynamic part was specified using Flather's boundary condition, which is a combination of the water level and sea water velocities. The water velocities are not necessary to force the model but are imposed for stability reasons. Furthermore, the temperature and salinity were defined as Dirichlet boundary conditions. For this study, two different sources of data were used. The water level was predicted based on tidal constituents from the DTU10 global ocean tide model (Cheng and Andersen, 2010). This model includes 10 tidal constituents and has a resolution of 0.125° × 0.125°. The output of the DTU10 global ocean tide model compares well with the water level measurements at the mouth of the fjord, with the difference generally being less than 10 cm. The sea water velocities, temperature and salinity were taken from the E.U. *Copernicus Marine Environment Monitoring Service* (CMEMS) global ocean physics reanalysis product (CMEMS, 2019). This product has a horizontal resolution of 1/12°, 50 vertical layers down to a depth of 5500 metres and provides daily mean values.

The following atmospheric data were included in the model: wind speed and direction, dry bulb air temperature, cloudiness and relative humidity. Observations of these parameters were obtained from the DMI weather station (Figure 2), and these observations are taken as representative values for the entire fjord. The validity of this assumption was checked by comparing the atmospheric data obtained at the Kangerlussuaq airport with those at the Sisimiut airport, which is located further north and closer to the ocean (the comparison is not shown here). Because the inland climate is different from the coastal climate, using values from the Kangerlussuaq airport for the entire fjord may lead to a loss of realism for the atmospheric input data close to the coast. Precipitation and evaporation are neglected because they are assumed to be negligible for our study area because of the orographic shielding by the Sukkertoppen ice cap. An input file of the ice concentration was prepared based on Envisat satellite observations. This file defines the location of the sea ice (ice concentration of 100%) and covers the inner, deep part of the fjord to approximately the Sarfartoq River from December to May.

3.3 Freshwater input

The three meltwater rivers were represented in the model as point sources, which are placed in the surface layer. The 'simple source' option was used where the source discharge only contributes to the continuity equation (DHI, 2017). The salinity was set to 0 psu (practical salinity unit) (UNESCO, 1987), and the runoff temperature was set to 1 °C. The temperature as well as the discharge of the Watson River has some small-scale fluctuations resulting from warm and colder periods and from the day and night cycle. The temperature of the Watson River typically varies between 0 °C and 2 °C (unpublished data). However, because we are interested in the general circulation pattern in the fjord system, we neglected all the high frequency variations found in the meltwater runoff. The discharge in the Watson River was estimated based on the average accumulated annual discharge during 2007-2010 (Hasholt et al., 2013) and is presented in Figure 4. The peak discharge is assumed to occur in late July (Julian day 200) and has a value of 1070 m^3 s^{-1}. The average accumulated annual discharge of the Watson River is 3.7 km^3. There are no data on the discharges of the Umivit and Sarfartoq Rivers. Therefore, we assumed the same shape as the Watson River discharge (Figure 4), but we scaled the values based on the catchment areas given by Hudson et al. (2014). Therefore, the discharge of the Watson River is multiplied by factors (6320/3639) and (5385/3639) for the Umivit River and the Sarfartoq River, respectively. The resulting total annual accumulated discharge of the Umivit River is 6.4 km^3 and 5.5 km^3 for the Sarfartoq River.

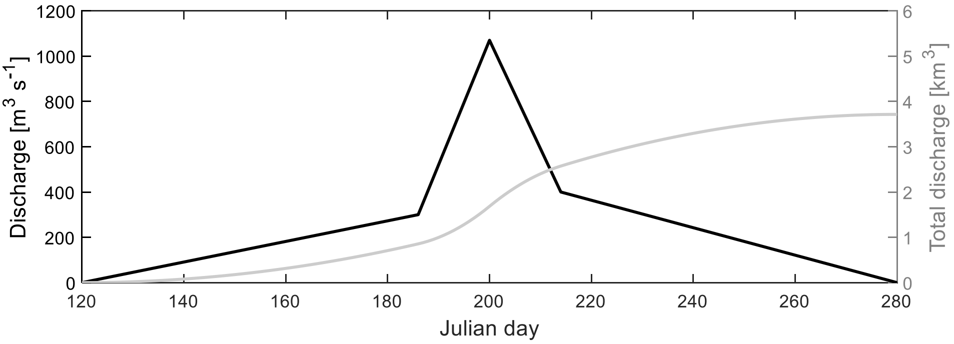

Figure 4. Estimated discharge from the Watson River used as input to the model. The solid black line shows the discharge per second, and the gray solid line shows the accumulated discharge.

4 Model calibration

The model calibration was divided into barotropic and baroclinic parts. It was not possible to perform a full validation procedure because of the lack of adequate in situ data.

4.1 Barotropic part

For the barotropic part, the simulated surface elevation was calibrated against the water level measurements. However, these measurements (30 July 2011 to 01 September 2011) are not available for our simulated time period (March 2005 to March 2006). Therefore, we performed an additional simulation for the period when the water level measurements were taken. The model setup, sources of the boundary conditions and sources of the atmospheric forcing for the new time period were all the same (Table 1). New input data for the boundary conditions and the atmospheric forcing were generated, but the initial conditions of the salinity and the temperature were kept identical to the 2006 observations. The potential differences in the vertical profiles of salinity and temperature between the simulation periods have a very small influence on the water level variation. This was checked by running the same simulation but with a constant initial temperature of 0 °C and salinity of 24 psu. The difference in water level between these simulations was less than 0.02 m overall.

The resolution of the horizontal computational mesh was the main parameter altered during the calibration of the barotropic part. A sufficiently fine mesh was required to obtain the correct water levels in the fjord. The influence of the bed roughness was found to be minor and therefore kept as the default value. The model simulation is compared with the observations at validation points a, b and c in Figure 3. The model simulation is in good agreement with the observations (Figure 5), with a root mean square error of 0.12 m at point c. The phase of the tidal wave is very well reproduced throughout the fjord, meaning we have a good representation of the bathymetry, as this is the main contributor to the phase of the simulated tidal wave. Some discrepancies are present, with a small overestimation during spring tide and an underestimation during neap tide. These same minor discrepancies are observed when comparing the input of the model (from the DTU10 global ocean tide model) at the seaside boundary with measurements taken outside the fjord (results not shown here). Therefore, the small errors are due to the input of the model at the seaside boundary, and the model itself reproduces the tides very well.

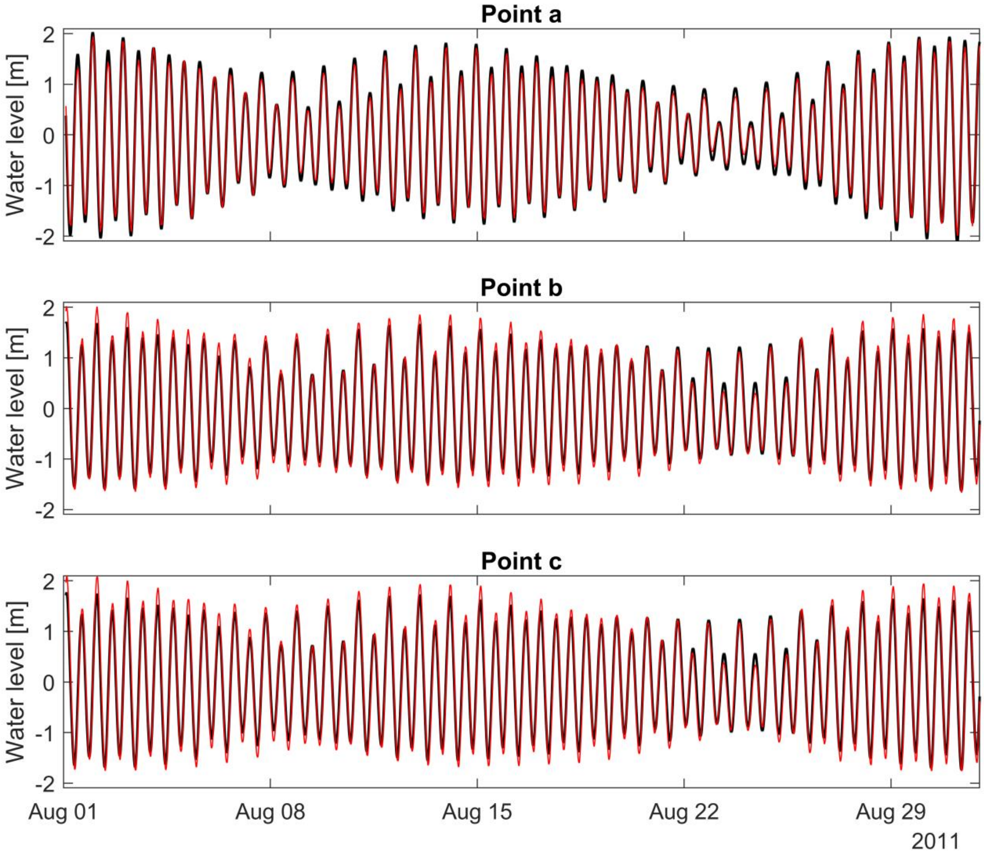

Figure 5. Observed water level (black line) and simulated water level using MIKE 3 (red line) at validation points a, b and c, as indicated in Figure 3, for a one-month period.

4.2 Baroclinic part

The second step of the calibration involved comparing the vertical profiles of the density, salinity and temperature at three validation points (points 1, 2 and 3 in Figure 3). Two main parameters were altered during this part of the calibration: the type and resolution of the vertical mesh and the vertical dispersion coefficient. Only a few terrain-following sigma layers were adopted because using more of these layers resulted in too much mixing in the deep inner part of the fjord. The reason for this mixing is the very steep slope between the outer and inner parts of the fjord. If such a steep slope is represented with terrain-following sigma layers, the grid cells are directed almost vertically, which causes significant mixing errors and results in unrealistic flows (DHI, 2016b). This phenomenon is demonstrated in Figure 6, where the temperature variation along the fjord is shown in August for a simulation with only sigma layers. Significantly unrealistic vertical mixing is observed at the vertical steep slope (around cross section length 100000 m) with a water temperature of approximately 0.5 °C found at the bottom of the fjord. Furthermore, we reduced the vertical dispersion coefficient to a value of 0.1. This low value was required to limit the amount of vertical mixing, which was found to be too large when using the default value of 1. The necessity of this low dispersion coefficient suggests that there is too much vertical mixing by default in the model.

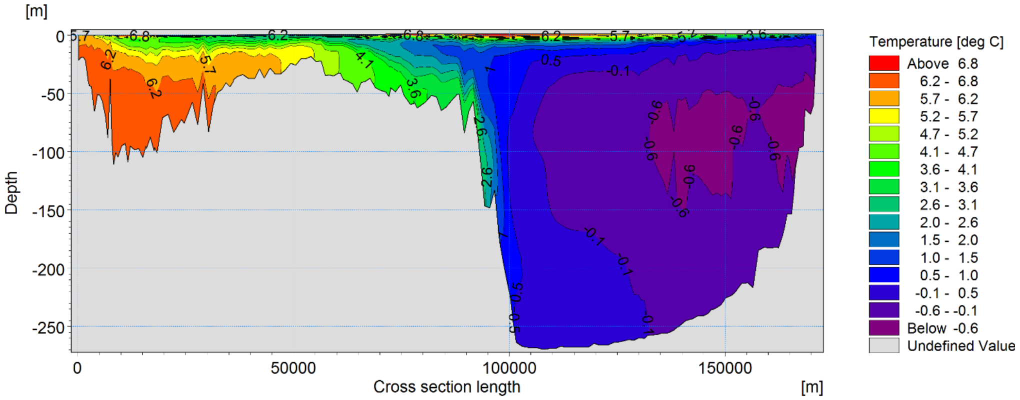

Figure 6. Vertical cross section of the temperature along the fjord on 01 August 2005. The simulation is performed with 40 vertical sigma layers. The mouth of the fjord is located on the left side of the figure, at cross section length 0 m. The start and end of the cross section along the fjord are indicated in Figure 3 with points IP1 and IP2, respectively. Moreover, the vertical transect follows the centreline of the fjord.

The comparison between the simulated vertical density, temperature and salinity profiles from the calibrated model and the measurements at the three calibration points is presented in Figure 7. In general, there is good agreement between the simulation and measurements, which gives us confidence that the main physics are well captured during summer. A very good comparison is obtained at point 2 and point 3. At point 1, however, deviations are observed in both temperature and salinity. The simulated temperature is approximately 1-2 °C warmer than that of the measurements. Moreover, the salinity in the depth range of 10-45 m is too saline. The reason for the deviation in temperature at point 1 is most likely because of the applied boundary condition at the mouth of the fjord. We checked the surface temperature of the applied boundary condition (taken from the global ocean physics reanalysis product) against the measurements made with the Solinst Levelogger Gold recording devices during the June-October 2011 period. The surface temperature taken from the global ocean physics reanalysis product is generally 0.5-2.5 °C degrees warmer than the measurements. This finding confirms our suspicion that the observed deviations in the temperature at point 1 are due to errors in the applied boundary condition.

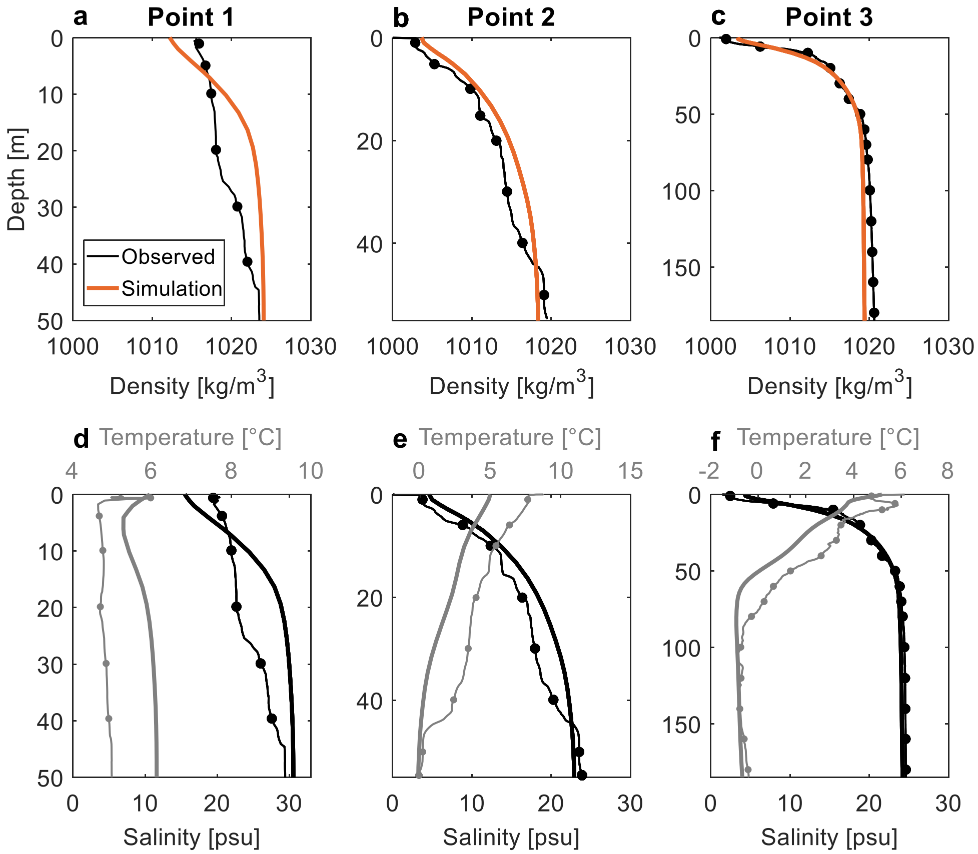

Figure 7. (a-c) Observed (black line with dots) and simulated (solid orange line) vertical profiles of the density at three locations in the fjord, as indicated in Figure 3. (d-e) are the observed (line with dots) and simulated (solid line) vertical profiles of the temperature (gray) and salinity (black) at points 1, 2 and 3 for subfigures (d), (e) and (f), respectively. The profiles were obtained on 3 August 2005.

4.3 Meltwater forcing sensitivity

As described in Section 2.2, varying Watson River catchment area values were reported in the literature, ranging from 3639 km^2 to approximately 12000 km^2. Using a larger catchment area of the Watson River would artificially reduce the discharges of the Umivit and Sarfartoq Rivers because these values are scaled with the catchment areas. To test the accuracy of the imposed runoff forcing, additional simulations were performed using Watson River catchment areas of 6000 km^2, 9000 km^2 and 12000 km^2. The results of these simulations are presented in Figure 8 for salinity. The temperature is not shown because the deviation between the different simulations was negligible. From Figure 8, it follows that using a larger catchment area of the Watson River (and therefore a smaller discharge of the Umivit River and Sarfartoq River) results in salinity that is too high, especially at Point 2, which is close to the Sarfartoq River. The best accordance with the measurements is obtained with the formerly used Watson catchment area of 3639 km^2, giving us confidence in the applied runoff forcing.

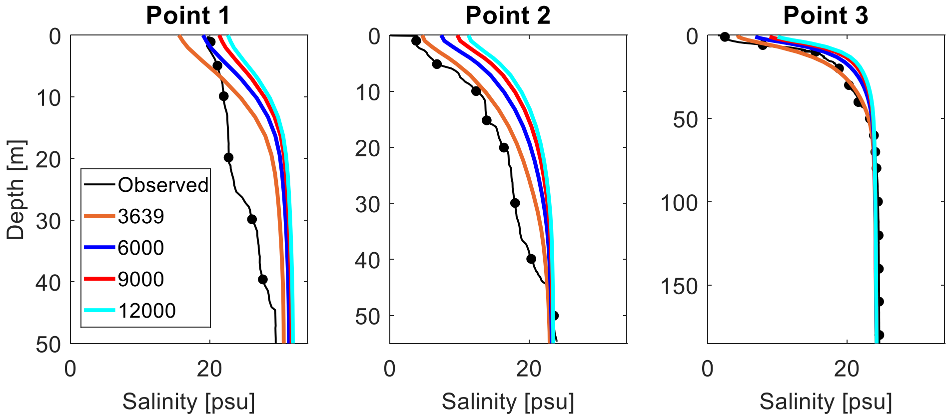

Figure 8. Sensitivity runs of varying meltwater runoff scenarios at points 1, 2 and 3, as indicated in Figure 3. The values given in the legend refer to the catchment area of the Watson River. Note that the value of 3639 km^2 is the value used in Figure 7. The profiles were obtained on 3 August 2005.

5 Results and discussion

5.1 Circulation pattern and currents

The circulation pattern in the fjord is primarily in the along-fjord direction, with currents in the across-fjord direction being very small. No rotational effects are observed in the fjord, which is supported by computing the internal Rossby radius (e.g., Cottier et al., 2010), which has a value of between 6-12 km at this latitude. The Rossby number is larger than the width of the fjord (approximately 5 km at its widest point), and therefore, rotational dynamics only provide a minor contribution to the flow. Given that the across-fjord variations are minor, the general circulation in the fjord is studied by plotting the time-averaged current speed along the length of the fjord in Figure 9a for August 2005. The currents in the deep inner part are slow, with typical time-averaged values of approximately 0.05 m/s. In the narrow and shallow middle part of the fjord, averaged values up to 1.3 m/s are observed. Moreover, extremely high instantaneous current velocities up to 3.5 m/s were found close to the Sarfartoq River (not shown here), where the width and depth of the fjord are small. The values for the month of August are slightly higher than those in the winter months because in summertime, meltwater inflow from the rivers causes some additional barotropic currents. To show this difference, we plotted the temporal variability in the currents at a location close to the mouth of the fjord in Figure 9b and in the inner, deep part of the fjord in Figure 9c. At both locations, two different regimes are visible. From approximately May until December, there is a net outflow in the upper layer, which is the light freshwater flowing out. During winter, the volume of freshwater is negligible, and no clear vertical gradient is observed. Furthermore, Figure 9a shows a correlation with the observed sea ice cover in the fjord. Generally, the sea ice cover extends to the middle of the fjord around the mouth of the Sarfartoq River (Figure 1), where the currents are very strong. Therefore, we believe that these strong currents prevent the sea ice from forming.

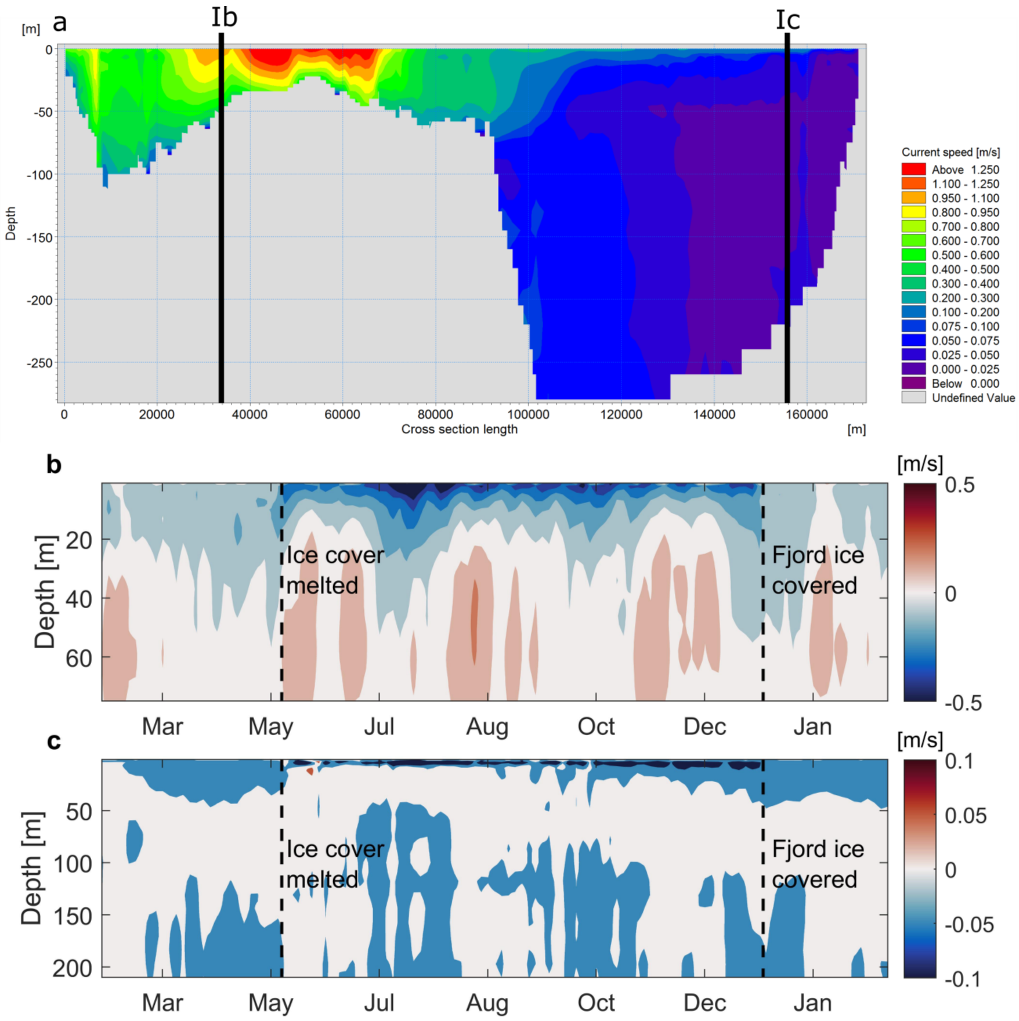

Figure 9 (a) Vertical cross section along the fjord showing the time-averaged, absolute current speed for August 2005. The start and end of the cross section along the fjord are indicated in Figure 3 with points IP1 and IP2, respectively. Moreover, the vertical transect follows the centreline of the fjord. Lines Ib and Ic indicate the locations of the vertical profiles showing the temporal variability in the currents directed into the fjord from March 2005 until March 2006 in subfigures (b) and (c), respectively. Note the differences in the definitions of the current speeds in (a) and (b, c); in (a), the shown values are the absolute values, while in (b and c), a positive value indicates a flow directed into the fjord.

5.2 Seasonal dynamics of water masses

A description of the water masses in the fjord Kangerlussuaq was given by Nielsen et al. (2010), which was based on two surveys of the vertical profiles of salinity and temperature (February 2006 and August 2005) that are used as initial conditions and for the calibration of the model in this paper. By using our numerical model, we provide a more comprehensive image of the seasonal dynamics of the water masses because we can study the development over time. The simulated seasonal variation in the vertical salinity and temperature profiles obtained at point 3 (see Figure 3) is presented in Figure 10. Cross sections of the salinity, temperature and density along the fjord during summer (01 August 2005) and winter (01 April 2005) are shown in Figure 11 and Figure 12, respectively.

The fjord is strongly stratified during summer in the inner deep part of the fjord. A clear layered structure of the water column is present with the salinity and temperature varying from approximately 5 psu and 7 °C at the surface down to 24.5 psu and -0.5 °C at the bottom, respectively (Figure 11). Wind mixing is only minor because there are gradual changes in salinity and temperature in the depth range of 40-70 m. Therefore, the deep-lying water mass appears to be shielded from atmospheric conditions (Nielsen et al., 2010). This shielding can also be concluded from the fact that the properties of the deep-lying water masses hardly change during summer. In the shallow outer part of the fjord, the tidal currents are very strong (Figure 9). The tidal mixing tends to breakdown stratification, resulting in smaller vertical gradients than in the deep part.

Three different water masses are present in summertime. At the mouth of the fjord, the water of the West Greenland current is found to have a salinity of approximately 33 psu and a temperature of 5 °C. In the inner deep part of the fjord, a runoff water-influenced top layer reaching down to approximately 70 m is found lying on top of a deep, relatively cold and saline water mass. The lower part of the runoff-influenced water layer (depth range of 20-70 m) is less dense than the deep-lying water mass but significantly denser than the water found at the surface. The origin of this intermediate water mass becomes clear by looking at Figure 10 during the period between May and August 2005. This mass is formed in spring and early summer, when the meltwater runoff is still relatively small. This intermediate water has a salinity of between 15 psu and 23.5 psu and a temperature from 0 °C to 4 °C.

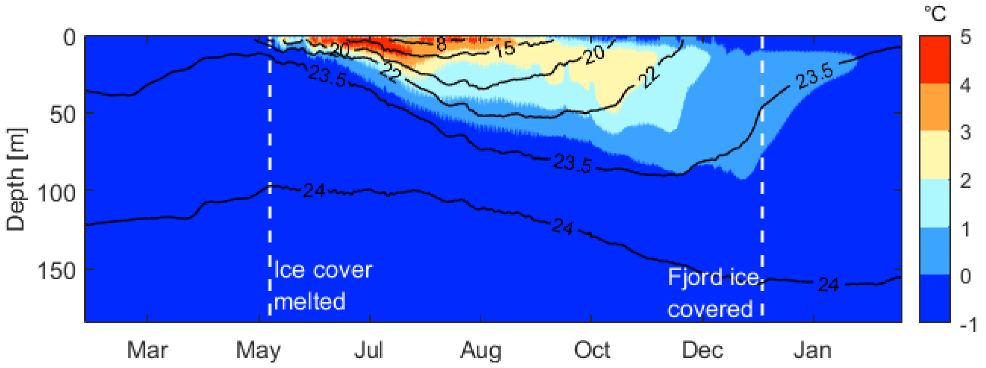

Figure 10. Simulated vertical temperature (colours) and salinity profiles (contour lines) at point 3 (Figure 3) for the one-year simulation (from March 2005 until March 2006).

The temperature, salinity and density show much smaller vertical gradients in wintertime (Figure 12), with salinity values ranging from 23 psu to 24 psu and temperatures from -0.1 °C to 0.5 °C. According to the observations made in February, the temperature should be close to the freezing point throughout the fjord, indicating that sea ice formation and cooling are the dominant physical processes in the winter (Nielsen et al., 2010). The MIKE 3 model is currently unable to include these processes because it does not include a sea ice module. A sea ice cover can be defined, but it is given as external data. When this cover is defined, the atmospheric conditions have no effect on the fjord's surface (sea ice acts as a barrier), and the boundary condition of the salinity and temperature at the surface is defined as a Neuman boundary condition that reads as follows:

$$\frac{\partial X}{\partial z} = 0 \qquad (2)$$

with X representing either the temperature or salinity, and z is the vertical coordinate. Therefore, the sea ice does not cool the water layers underneath. In addition, freshwater input due to sea ice melt and the process of brine release are not included in the model. These factors are the main drawback of setting up an MIKE 3 model to study Arctic fjords (Jakacki et al., 2017).

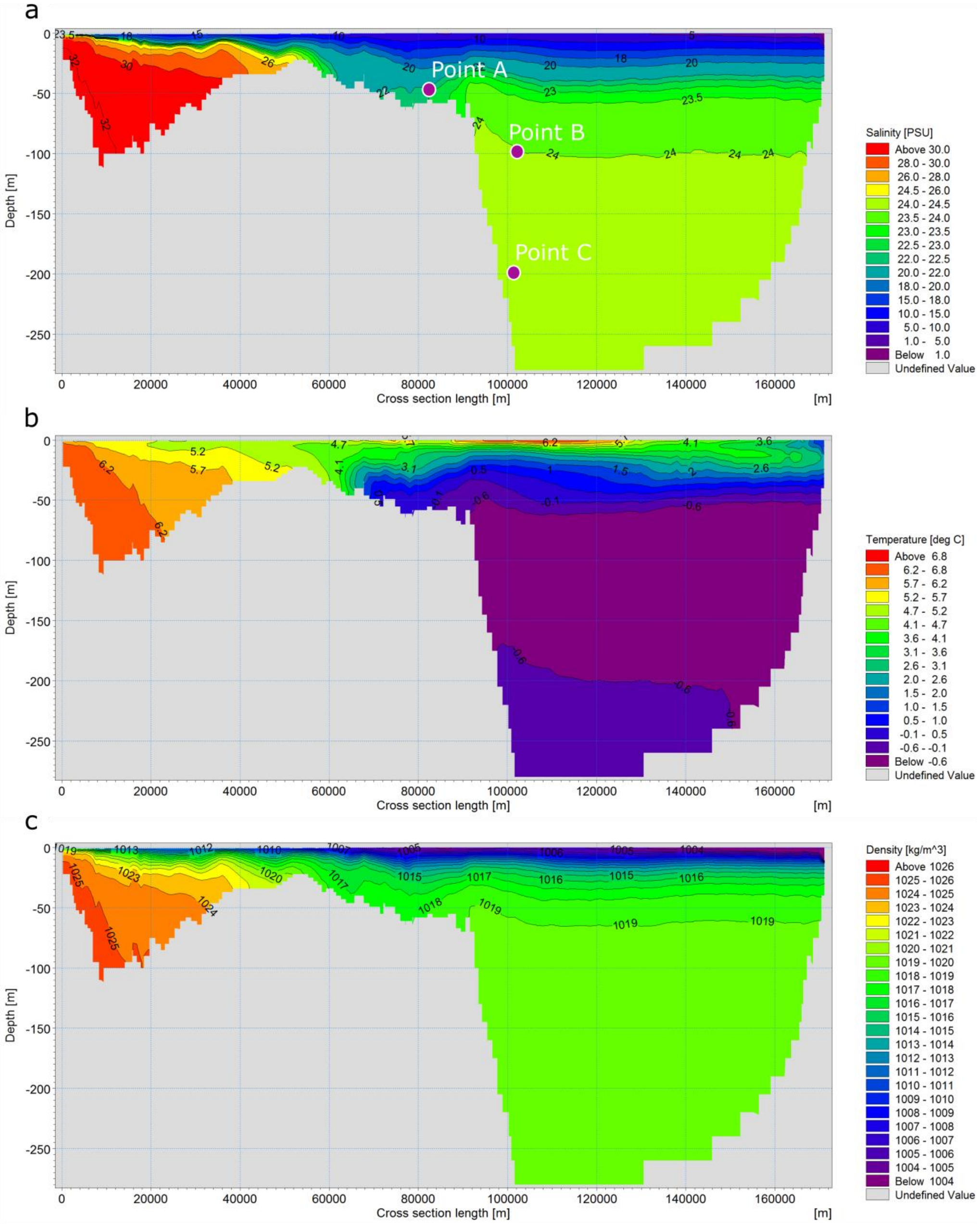

Figure 11. Vertical cross section along the fjord from the simulations of (a) salinity, (b) temperature and (c) density on 01 August 2005. The mouth of the fjord is located on the left side of the figure at cross section length 0 m. The start and end of the cross section along the fjord are indicated in Figure 3 with points IP1 and IP2, respectively. Moreover, the vertical transect follows the centreline of the fjord. Points A, B and C are the locations where the density is extracted in Figure 13.

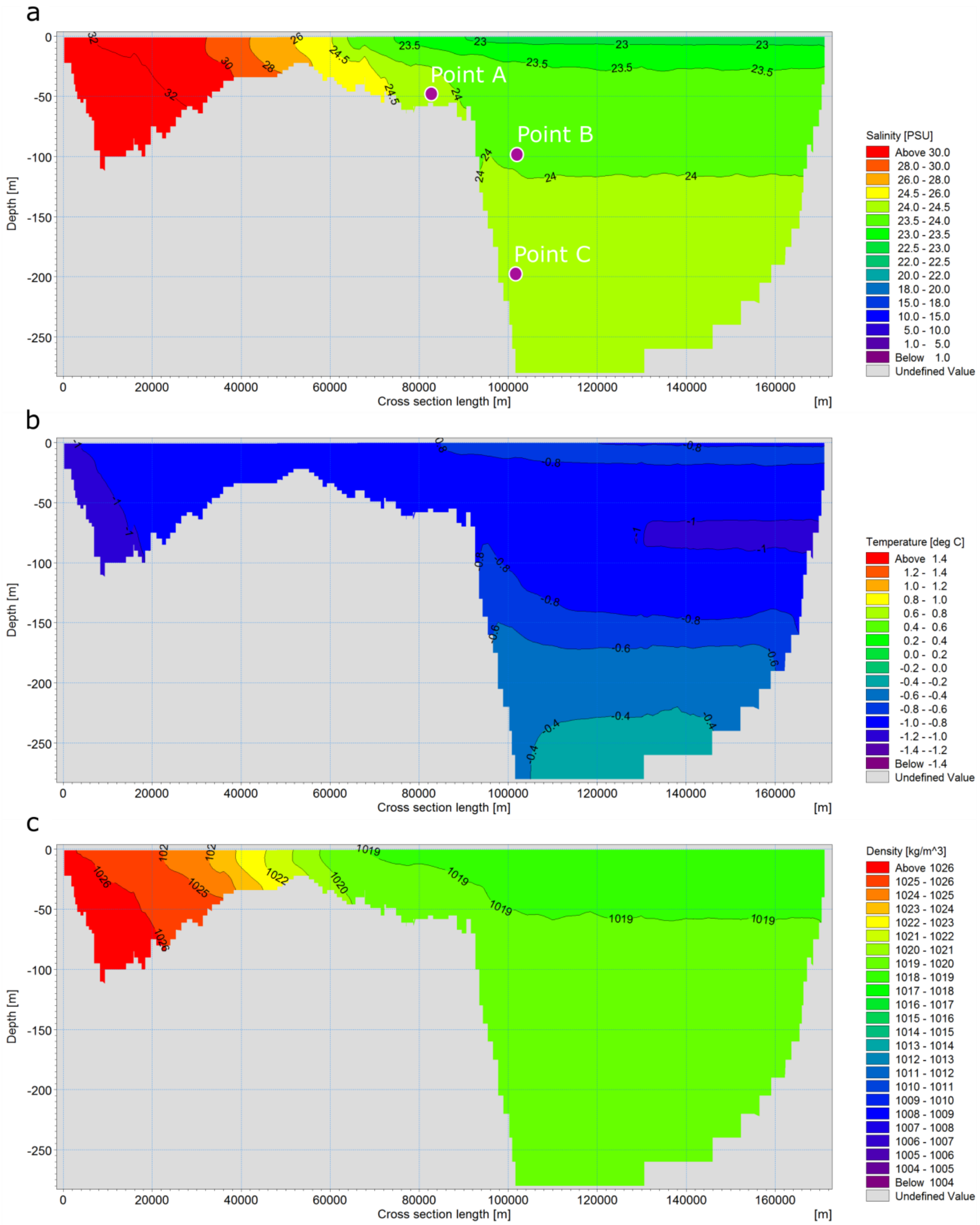

Figure 12. Vertical cross section along the fjord from the simulations of (a) salinity, (b) temperature and (c) density on 01 April 2005. The mouth of the fjord is located on the left side of the figure at cross section length 0 m. The start and end of the cross section along the fjord are indicated in Figure 3 with points IP1 and IP2, respectively. Moreover, the vertical transect follows the centreline of the fjord. Points A, B and C are the locations of the density extracted in Figure 13.

It was suggested by Nielsen et al. (2010) that the deep-lying water mass is barely subject to any renewal in summer, which is confirmed by our model results. In Figure 13, the seasonal density variation is plotted for one point in the middle, the shallow part of the fjord at a depth of 50 m (point A in Figure 11a) and two points in the inner deep part of the fjord at depths of 100 m and 200 m (points B and C in Figure 11a, respectively). All points are close to the steep slope in the bathymetry near the Sarfartoq River. There is barely any change in density at points B and C during the year, while the density at point A shows a variation between summertime and wintertime. This variation is because the incoming water mass of the West Greenland Current at the mouth of the fjord is significantly modified (i.e., mixed with the outflowing freshwater) before reaching the deep inner part of the fjord. The result is a smaller density at point A than at point B from approximately June to December, which suggests that there is hardly any mixing between these layers during summertime, and the deep part appears to be largely dynamically decoupled from the open ocean.

To investigate this further, we performed a tracer investigation using the transport module in MIKE 3 (DHI, 2016c). Conservative passive tracers with a concentration of 1 were continuously included, with one tracer at the seaside open boundary and one tracer at the three meltwater river sources. The along-fjord vertical distribution of the tracer's concentration is given in Figure 14. It follows that the deep-lying water mass is hardly influenced by the water mass of the West Greenland Current (Figure 14a) or meltwater runoff (Figure 14b) during the summertime, with tracer concentrations of approximately 0 in the deep part. The deep-lying water mass is (slowly) renewed by the West Greenland Current water mass (Figure 14c) and meltwater runoff (Figure 14d) during winter. Moreover, the meltwater runoff tracer that is present in wintertime (Figure 14d) originated during summertime.

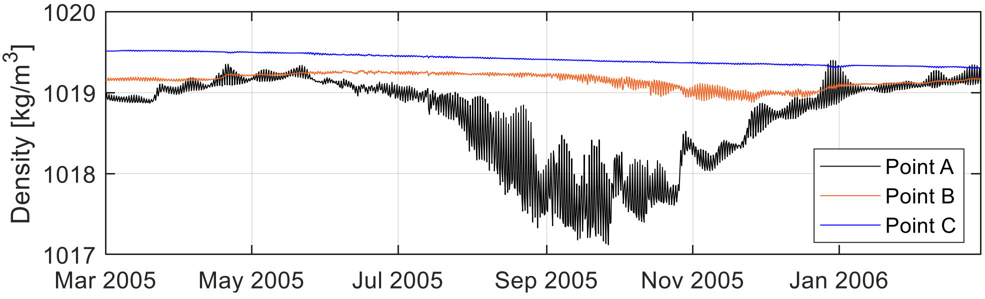

Figure 13. Seasonal density variations at three points (see Figure 11). Point A is located in the shallow inner part of the fjord at a depth of 50 m, and point B and point C are located in the inner, deep part of the fjord at depths of 100 m and 200 m, respectively.

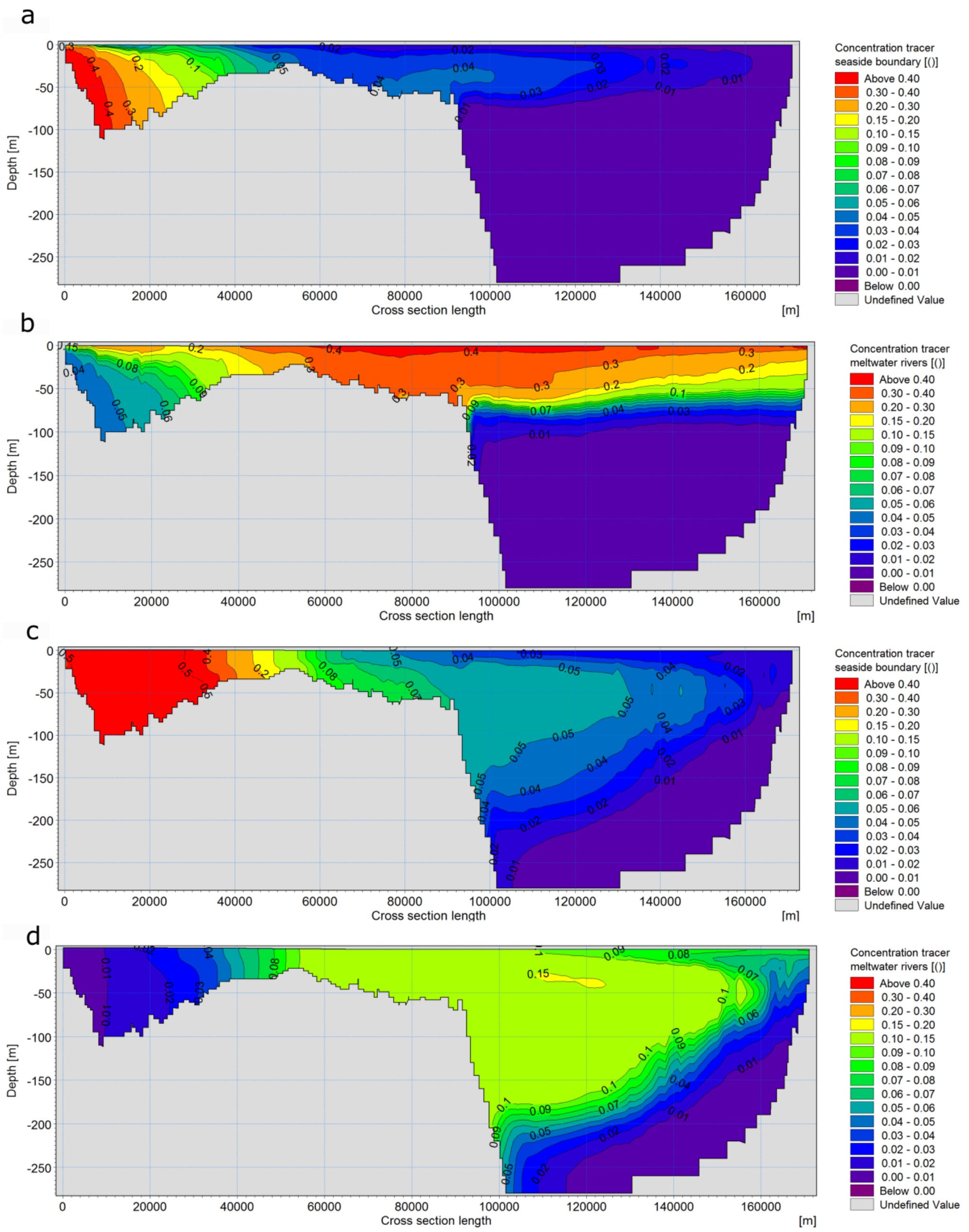

Figure 14. Vertical cross section of the tracer concentration released at the seaside boundary (a) and (c) and of the tracer concentration released at the meltwater river sources (b) and (d) along the fjord. Subfigures (a) and (b) were obtained on 01 October 2005, (c) and (d) are from 01 March 2006.

5.3 Meltwater runoff sensitivity analysis

We studied the fjord's response to different meltwater runoff scenarios by running three additional simulations for the March-December period. The amount of meltwater is either halved, doubled or multiplied by a factor of four compared to the reference case shown in Figure 4, and these cases are referred to as the '50% case', the '200% case' and the '400% case', respectively. In terms of the total annual discharge, the 'base case' has a value of 15.66 km^3 (all three meltwater rivers combined). For the 50% case, the total annual discharge is 7.83 km^3, the 200% case has a value of 31.32 km^3, and the value for the 400% case is 62.63 km^3. For comparison, the maximum observed total annual discharge of the Watson River corresponds to an approximate multiplication of the reference case by a factor of three (van As et al., 2018); therefore, only the 400% case lies outside the range of observations.

The vertical profiles of the temperature and salinity at one location in the fjord are presented in Figure 15. The surface temperature only shows a small deviation among the four scenarios (< 0.3 °C). In contrast, the different runoff scenarios have a substantial impact on the surface salinity, where it increases by 1.8 psu for the 50% case and reduces by 2.3 psu and 5.5 psu for the 200% and 400% cases, respectively. Similar values are found throughout the inner, deep part of the fjord (not shown here). Furthermore, the deep-lying water mass (below 100 m) only becomes fresher in the 400% case, while it is hardly influenced in the 50% and 200% cases.

It is very likely that the meltwater runoff into the fjord Kangerlussuaq will increase in the future due to climate change, which may have a severe impact on ecosystems. Lund-Hansen et al. (2018) found that meltwater runoff is the main driver of the variabilities in optical conditions, inorganic nutrients and primary production during summertime. The increase in meltwater runoff will have two effects on the fjord because the meltwater supplies nutrients and particle matter into the fjord. The increase in nutrient supply will increase productivity, while an increase in particle matter will increase light attenuation, thereby reducing productivity (Murray et al., 2015). To investigate the net effect of the increase in meltwater runoff on the productivity in the fjord, multiple modules in MIKE 3 including sediment transport and ecological modelling can be used. These are endeavours planned for future work.

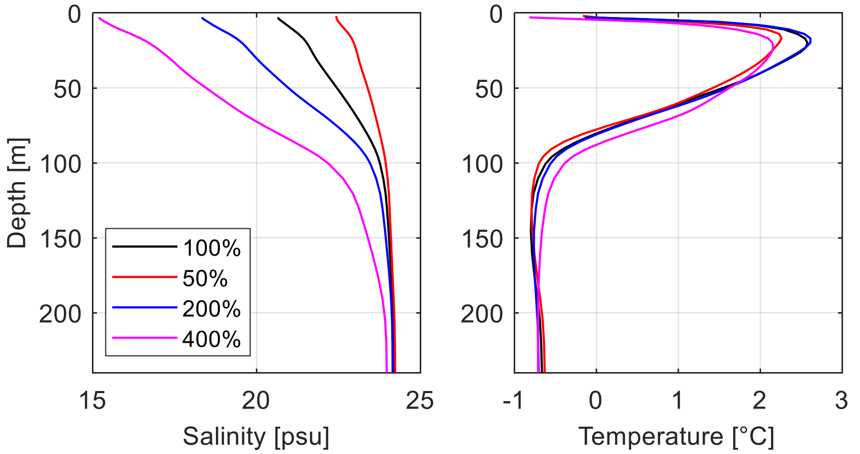

Figure 15. Vertical profiles of the temperature and salinity at point 3, as given in Figure 3, for the four meltwater runoff scenarios.

7 Conclusions

The commercially available MIKE 3 hydrodynamic model was set up for the fjord Kangerlussuaq to understand its seasonal variability and to study the response to changing freshwater runoff. The model was calibrated against in situ water level data and transects of temperature, salinity and density. Full validation could not be performed due to a lack of sufficient in situ data. The main findings are described as follows:

- The general circulation pattern in the fjord is along the fjord direction, and there is minimal across fjord variations because the fjord is too narrow to be influenced by the Earth's rotational dynamics.
- Two general current regimes are present. The first regime is in the summertime, where there is a net outflow of freshwater in the upper layer. The other regime is present during winter, when the freshwater content is negligible and small vertical gradients in the currents are observed.
- The tides are semidiurnal with a mean spring tidal range of 3.5 m.
- The deep inner part of the fjord is characterized by weak currents and is sea ice covered during wintertime. Very strong tidal currents are present in the shallow, outer part of the fjord, which is most likely the cause of the absence of sea ice during wintertime.
- The inner part of the fjord is strongly stratified during summer. In the outer part of the fjord, strong tidal mixing tends to breakdown stratification, and smaller vertical gradients are observed.
- The deep-lying water mass is hardly subject to any renewal and is almost dynamically decoupled from the open ocean during summertime. The latter is because the water of the West Greenland current flowing into the fjord is heavily modified before reaching the inner part of the fjord, resulting in a density smaller than that of the deep-water mass.

- A sensitivity study of meltwater runoff revealed that the surface salinity decreases by approximately 2.3 psu and 5.5 psu when the total discharge flowing into the fjord from August-December is doubled or multiplied by a factor of 4, respectively. Moreover, the most severe changes are observed in the upper 100 m in the inner, deep part of the fjord.

The main drawback of using the MIKE 3 model to study Arctic fjords is the lack of a sea ice module. Therefore, processes such as cooling, brine release and freshwater release during sea ice melt cannot be included in the model. For the fjord Kangerlussuaq, this means that the important physics during wintertime are not captured. For future studies, it is highly recommended to add a sea ice module to the model, thereby making the model suitable for studying sea ice-covered fjord systems during wintertime. Furthermore, it appears that the model overestimates vertical mixing when the default parameter values are used, and it is highly recommended to investigate this further.

Acknowledgements

We would like to thank and acknowledge DHI for providing access to MIKE 3 and for their assistance implementing the model. We like to thank Morten Rugbjerg from DHI for his assistance and feedback regarding the model setup. Further, we would like to acknowledge DMI for kindly providing the Envisat data. The Sentinel-2 image used in Figure 1 is available from the ESA and can be downloaded freely from the Sentinel data hub (https://scihub.copernicus.eu/). Finally, for the MODIS images used to study the sea ice cover, we acknowledge the use of imagery from the NASA Worldview application (https://worldview.earthdata.nasa.gov), which is part of the NASA Earth Observing System Data and Information System (EOSDIS).

References

Arendt, K.E., Nielsen, T.G., Rysgaard, S., Tönnesson, K., 2010. Differences in plankton community structure along the Godthåbsfjord, from the Greenland Ice Sheet to offshore waters. Mar. Ecol. Prog. Ser. 401, 49–62. https://doi.org/10.3354/meps08368

Bendtsen, J., Mortensen, J., Rysgaard, S., 2014. Seasonal surface layer dynamics and sensitivity to runoff in a high Arctic fjord (Young Sound/Tyrolerfjord, 74N). J. Geophys. Res. Ocean. 119, 2439–2461. https://doi.org/10.1002/2013JC009622.Received

Born, E.W., Böcher, J., 2001. The Ecology of Greenland. Atuagkat.

Box, J.E., Bromwich, D.H., Veenhuis, B.A., Bai, L.S., Stroeve, J.C., Rogers, J.C., Steffen, K., Haran, T., Wang, S.H., 2006. Greenland ice sheet surface mass balance variability (1988-2004) from calibrated polar MM5 output. J. Clim. 19, 2783–2800. https://doi.org/10.1175/JCLI3738.1

Cappelen, J., 2016. DMI Report 16-08 Weather observations from Greenland - Observation data with description 1–31.

Carrivick, J.L., Yde, J.C., Knudsen, N.T., Kronborg, C., 2018. Ice-dammed lake and ice-margin evolution during the Holocene in the Kangerlussuaq area of west Greenland. Arctic, Antarct. Alp. Res. 50. https://doi.org/10.1080/15230430.2017.1420854

Cheng, Y., Andersen, O.B., 2010. Improvement in global ocean tide model in shallow water regions., in: Altimetry for Oceans & Hydrology OST-ST Meeting. Lisbon.

CMEMS, 2019. Global Ocean Physical Reanalysis product. Product Identifier: GLOBAL_REANALYSIS_PHY_001_030. E.U. Copernicus Marine Service Information.

Cottier, F.R., Nilsen, F., Skogseth, R., Tverberg, V., Skarthhamar, J., Svendsen, H., 2010. Arctic fjords: a review of the oceanographic environment and dominant physical processes. Geol. Soc. London, Spec. Publ. 344, 35–50. https://doi.org/10.1144/SP344.4

Courtier, A., 1939. Classification of tides in four types. Int. Hydrogr. Rev.

DHI, 2017. MIKE 3 Flow Model - Scientific Documentation. DHI, Hørsholm, Denmark.

DHI, 2016a. MIKE zero - Mesh Generator - Step-by-step training guide. DHI, Hørsholm, Denmark.

DHI, 2016b. MIKE 21 & MIKE 3 Flow Model FM - Hydrodynamic and Transport Module - Scientific Documentation. DHI, Hørsholm, Denmark.

DHI, 2016c. MIKE 3 FLow Model FM - Transport Module - User guide. DHI, Hørsholm, Denmark.

Dziallas, C., Grossart, H.P., Tang, K.W., Nielsen, T.G., 2013. Distinct communities of free-living and copepod-associated microorganisms along a salinity gradient in Godthåbsfjord, West Greenland. Arctic, Antarct. Alp. Res. 45, 471–480. https://doi.org/10.1657/1938-4246.45.4.471

Hanna, E., Huybrechts, P., Steffen, K., Cappelen, J., Huff, R., Shuman, C., Irvine-Fynn, T., Wise, S., Griffiths, M., 2008. Increased runoff from melt from the Greenland Ice Sheet: A response to global warming. J. Clim. 21, 331–341. https://doi.org/10.1175/2007JCLI1964.1

Hasholt, B., Bech Mikkelsen, A., Holtegaard Nielsen, M., Andreas Dahl Larsen, M., 2013. Observations of Runoff and Sediment and Dissolved Loads from the Greenland Ice Sheet at Kangerlussuaq, West Greenland, 2007 to 2010. Zeitschrift für Geomorphol. Suppl. Issues 57, 3–27. https://doi.org/10.1127/0372-8854/2012/S-00121

Hawes, I., Lund-Hansen, L.C., Sorrell, B.K., Nielsen, M.H., Borzák, R., Buss, I., 2012. Photobiology of sea ice algae during initial spring growth in Kangerlussuaq, West Greenland: Insights from imaging variable chlorophyll fluorescence of ice cores. Photosynth. Res. 112, 103–115. https://doi.org/10.1007/s11120-012-9736-7

Holland, D.M., Thomas, R.H., De Young, B., Ribergaard, M.H., Lyberth, B., 2008. Acceleration of Jakobshavn Isbr triggered by warm subsurface ocean waters. Nat. Geosci. 1, 659–664. https://doi.org/10.1038/ngeo316

Hudson, B., Overeem, I., McGrath, D., Syvitski, J.P.M., Mikkelsen, A., Hasholt, B., 2014. MODIS observed increase in duration and spatial extent of sediment plumes in Greenland fjords. Cryosphere 8, 1161–1176. https://doi.org/10.5194/tc-8-1161-2014

Jakacki, J., Przyborska, A., Kosecki, S., Sundfjord, A., Albretsen, J., 2017. Modelling of the Svalbard fjord Hornsund. Oceanologia 59, 473–495. https://doi.org/10.1016/j.oceano.2017.04.004

Kattsov, V.M., Källén, E., Cattle, H., Christensen, J., Drange, H., Hanssen-bauer, I., Jóhannesen, T., Karol, I., Räisänen, J., Svensson, G., Chen, D., Polyakov, I., Rinke, A., 2005. Future Climate Change : Modeling and Scenarios for the Arctic, in: ARCTIC: ARCTIC CLIMATE IMPACT ASSESSMENT (ACIA). Cambridge University Press, Cambridge, pp. 99–150.

Kjeldsen, K.K., Mortensen, J., Bendtsen, J., Petersen, D., Lennert, K., Rysgaard, S., 2014. Ice-dammed lake drainage cools and raises surface salinities in a tidewater outlet glacier fjord, west Greenland 1310–1321. https://doi.org/10.1002/2013JF003034.Received

Lindbäck, K., Pettersson, R., Hubbard, A.L., Doyle, S.H., Van As, D., Mikkelsen, A.B., Fitzpatrick, A.A., 2015. Subglacial water drainage, storage, and piracy beneath the Greenland ice sheet. Geophys. Res. Lett. 42, 7606–7614. https://doi.org/10.1002/2015GL065393

Lund-Hansen, L.C., Andersen, T.J., Nielsen, M.H., Pejrup, M., 2010. Suspended Matter, Chl-a, CDOM, Grain Sizes, and Optical Properties in the Arctic Fjord-Type Estuary, Kangerlussuaq, West Greenland During Summer. Estuaries and Coasts 33, 1442–1451. https://doi.org/10.1007/s12237-010-9300-7

Lund-Hansen, L.C., Hawes, I., Holtegaard Nielsen, M., Dahllöf, I., Sorrell, B.K., 2018. Summer meltwater and spring sea ice primary production, light climate and nutrients in an Arctic estuary, Kangerlussuaq, west Greenland. Arctic, Antarct. Alp. Res. 50. https://doi.org/10.1080/15230430.2017.1414468

Mernild, S.H., Liston, G.E., Steffen, K., Van Den Broeke, M., Hasholt, B., 2010. Runoff and mass-balance simulations from the Greenland Ice Sheet at Kangerlussuaq (Søndre Strømfjord) in a 30-year perspective, 1979-2008. Cryosphere 4, 231–242. https://doi.org/10.5194/tc-4-231-2010

Mikkelsen, A.B., Hasholt, B., Knudsen, N.T., Nielsen, M.H., 2013. Jökulhlaups and sediment transport in Watson River, Kangerlussuaq, West Greenland. Hydrol. Res. 44, 58. https://doi.org/10.2166/nh.2012.165

Mortensen, J., Bendtsen, J., Motyka, R.J., Lennert, K., Truffer, M., Fahnestock, M., Rysgaard, S., 2013. On the seasonal freshwater stratification in the proximity of fast-flowing tidewater outlet glaciers in a sub-Arctic sill fjord. J. Geophys. Res. Ocean. 118, 1382–1395. https://doi.org/10.1002/jgrc.20134

Mortensen, J., Lennert, K., Bendtsen, J., Rysgaard, S., 2011. Heat sources for glacial melt in a sub-Arctic fjord (Godthåbsfjord) in contact with the Greenland Ice Sheet. J. Geophys. Res. Ocean. 116. https://doi.org/10.1029/2010JC006528

Murray, C., Markager, S., Stedmon, C.A., Juul-Pedersen, T., Sejr, M.K., Bruhn, A., 2015. The influence of glacial melt water on bio-optical properties in two contrasting Greenlandic fjords. Estuar. Coast. Shelf Sci. 163, 72–83. https://doi.org/10.1016/j.ecss.2015.05.041

Murray, T., Scharrer, K., James, T.D., Dye, S.R., Hanna, E., Booth, A.D., Selmes, N., Luckman, A., Hughes, A.L.C., Cook, S., Huybrechts, P., 2010. Ocean regulation hypothesis for glacier dynamics in southeast Greenland and implications for ice sheet mass changes. J. Geophys. Res. Earth Surf. 115, 1–15. https://doi.org/10.1029/2009JF001522

Myers, P.G., Kulan, N., Ribergaard, M.H., 2007. Irminger water variability in the West Greenland Current. Geophys. Res. Lett. 34, 2–7. https://doi.org/10.1029/2007GL030419

Nielsen, M.H., Erbs-Hansen, D.R., Knudsen, K.L., 2010. Water masses in Kangerlussuaq, a large fjord in West Greenland: the processes of formation and the associated foraminiferal fauna. Polar Res. 29, 159–175. https://doi.org/10.1111/j.1751-8369.2010.00147.x

Piwosz, K., Walkusz, W., Hapter, R., Wieczorek, P., Hop, H., Wiktor, J., 2009. Comparison of productivity and phytoplankton in a warm (Kongsfjorden) and a cold (Hornsund) Spitsbergen fjord in mid-summer 2002. Polar Biol. 32, 549–559. https://doi.org/10.1007/s00300-008-0549-2

Retamal, L., Bonilla, S., Vincent, W.F., 2008. Optical gradients and phytoplankton production in the Mackenzie River and the coastal Beaufort Sea. Polar Biol. 31, 363–379. https://doi.org/10.1007/s00300-007-0365-0

Rignot, E., Fenty, I., Menemenlis, D., Xu, Y., 2012. Spreading of warm ocean waters around Greenland as a possible cause for glacier acceleration. Ann. Glaciol. 53, 257–266. https://doi.org/10.3189/2012AoG60A136

Rignot, E., Koppes, M., Velicogna, I., 2010. Rapid submarine melting of the calving faces of West Greenland glaciers. Nat. Geosci. 3, 187–191. https://doi.org/10.1038/ngeo765

Rodi, W., 1984. Turbulence models and their application in hydraulics. International Association for Hydraulic Research, Delft.

Russell, A.J., Carrivick, J.L., Ingeman-Nielsen, T., Yde, J.C., Williams, M., 2011. A new cycle of jökulhlaups at Russell Glacier, Kangerlussuaq, West Greenland. J. Glaciol. 57, 238–246. https://doi.org/10.3189/002214311796405997

Shepherd, A., Ivins, E.R., Geruo, A., Barletta, V.R., Bentley, M.J., Bettadpur, S., Briggs, K.H., Bromwich, D.H., Forsberg, R., Galin, N., Horwath, M., Jacobs, S., Joughin, I., King, M.A., Lenaerts, J.T.M., Li, J., Ligtenberg, S.R.M., Luckman, A., Luthcke, S.B., McMillan, M., Meister, R., Milne, G., Mouginot, J., Muir, A., Nicolas, J.P., Paden, J., Payne, A.J., Pritchard, H., Rignot, E., Rott, H., Sørensen, L.S., Scambos, T.A., Scheuchl, B., Schrama, E.J.O., Smith, B., Sundal, A. V., Van Angelen, J.H., Van De Berg, W.J., Van Den Broeke, M.R., Vaughan, D.G., Velicogna, I., Wahr, J., Whitehouse, P.L., Wingham, D.J., Yi, D., Young, D., Zwally, H.J., 2012.

A reconciled estimate of ice-sheet mass balance. Science (80-.). 338, 1183–1189. https://doi.org/10.1126/science.1228102

Shore Protection Manual, 1984. Shore Protection Manual. US Army Corps of Engineergs, Washington DC.

Smagorinsky, J., 1963. General Circulation Experiments With the Primitive Equations. Mon. Weather Rev. 91, 99–164. https://doi.org/10.1175/1520-0493(1963)091<0099:gcewtp>2.3.co;2

Storms, J.E.A., de Winter, I.L., Overeem, I., Drijkoningen, G.G., Lykke-Andersen, H., 2012. The Holocene sedimentary history of the Kangerlussuaq Fjord-valley fill, West Greenland. Quat. Sci. Rev. 35, 29–50. https://doi.org/10.1016/j.quascirev.2011.12.014

Straneo, F., Cenedese, C., 2015. The Dynamics of Greenland's Glacial Fjords and Their Role in Climate. Ann. Rev. Mar. Sci. 7, 89–112. https://doi.org/10.1146/annurev-marine-010213-135133

Straneo, F., Curry, R.G., Sutherland, D.A., Hamilton, G.S., Cenedese, C., Våge, K., Stearns, L.A., 2011. Impact of fjord dynamics and glacial runoff on the circulation near Helheim Glacier. Nat. Geosci. 4, 322–327. https://doi.org/10.1038/ngeo1109

Straneo, F., Heimbach, P., Sergienko, O., Hamilton, G., Catania, G., Griffies, S., Hallberg, R., Jenkins, A., Joughin, I., Motyka, R., Pfeffer, W.T., Price, S.F., Rignot, E., Scambos, T., Truffer, M., Vieli, A., 2013. Challenges to Understand the Dynamic Response of Greenland's Marine Terminating Glaciers to Oceanic and Atmospheric Forcing. Bull. Am. Meteorol. Soc. 130117123745009. https://doi.org/10.1175/bams-d-12-00100

Sutherland, D.A., Pickart, R.S., 2008. The East Greenland Coastal Current: Structure, variability, and forcing. Prog. Oceanogr. 78, 58–77. https://doi.org/10.1016/j.pocean.2007.09.006

Sutherland, D.A., Straneo, F., Pickart, R.S., 2014. Characteristics and dynamics of two major Greenland glacial fjords. J. Geophys. Res. Ocean. 119, 3767–3791. https://doi.org/10.1002/2013JC009786

UNESCO, 1987. International oceanographic tables. Unesco Tech. Pap. Mar. Sci. 3, 195.

van As, D., Hasholt, B., Ahlstrøm, A.P., Box, J.E., Cappelen, J., Colgan, W., Fausto, R.S., Mernild, S.H., Mikkelsen, A.B., Noël, B.P.Y., Petersen, D., van den Broeke, M.R., 2018. Reconstructing Greenland Ice Sheet meltwater discharge through the Watson River (1949–2017). Arctic, Antarct. Alp. Res. 50. https://doi.org/10.1080/15230430.2018.1433799

Van As, D., Hubbard, A.L., Hasholt, B., Mikkelsen, A.B., Van Den Broeke, M.R., Fausto, R.S., 2012. Large surface meltwater discharge from the Kangerlussuaq sector of the Greenland ice sheet during the record-warm year 2010 explained by detailed energy balance observations. Cryosphere 6, 199–209. https://doi.org/10.5194/tc-6-199-2012

Appendix G Enhanced iceberg drift modelling in the Barents Sea with estimates of the release rates and size characteristics at the major glacial sources using Sentinel-1 and Sentinel-2

This paper is published in the Cold Regions Science and Technology journal.

Monteban, D., Lubbad, R., Samardzija, I., Løset, S., 2020a. Enhanced iceberg drift modelling in the Barents Sea with estimates of the release rates and size characteristics at the major glacial sources using Sentinel-1 and Sentinel-2. Cold Reg. Sci. Technol. 175, 103084. https://doi.org/10.1016/j.coldregions.2020.103084

Cold Regions Science and Technology 175 (2020) 103084

Contents lists available at ScienceDirect

Cold Regions Science and Technology

journal homepage: www.elsevier.com/locate/coldregions

Enhanced iceberg drift modelling in the Barents Sea with estimates of the release rates and size characteristics at the major glacial sources using Sentinel-1 and Sentinel-2

Dennis Monteban[a,b,*], Raed Lubbad[b], Ilija Samardzija[b], Sveinung Løset[b]

[a] *DTU space, Technical University of Denmark, Lyngby, Denmark*
[b] *Norwegian University of Science and Technology, Trondheim, Norway*

ARTICLE INFO

Keywords:
Iceberg drift model
Barents Sea
Iceberg production
Iceberg size characteristics
Sentinel satellites

ABSTRACT

Glaciers with termini at sea level may calve glacial ice features that can pose threats to offshore installations in the Barents Sea, especially in the central and northern part of this sea. It is therefore of great importance to estimate the annual iceberg encounter frequencies to select robust concepts for offshore field development, to design offshore structures and possibly to plan ice management operations. These encounter frequencies are often estimated using numerical models. Regardless of the model, considerable uncertainties often exist in the input data of icebergs at the sources, i.e., the annual number of icebergs released at the source and their size characteristics. The aim of this work is to reduce these uncertainties by utilizing state-of-the-art satellite remote sensing data and a complementary numerical model of iceberg drift and deterioration. Iceberg length and width distributions derived using Sentinel-2 optical imagery are presented at the major iceberg sources in the Barents Sea, which are Franz Josef Land, the eastern side of Svalbard and Novaya Zemlya. Over 22,000 icebergs were manually identified, with the largest observed iceberg being approximately 1 km long, originating from Franz Josef Land. Furthermore, a methodology is proposed to estimate the annual number of icebergs released into the Barents Sea by comparing the model results against Copernicus iceberg density data derived from the satellite synthetic aperture radar system onboard Sentinel-1. The importance of satellite remote sensing data cannot be understated because it is undoubtedly the best way to calibrate and validate the results of numerical iceberg drift models. Finally, with the calibrated model and the derived iceberg size, a map of the Barents Sea with updated annual iceberg encounter frequencies is presented.

1. Introduction

The Arctic has experienced greater warming than the lower latitudes, which is partly due to polar amplification (Screen and Simmonds 2010). In the Barents Sea, this warming has caused severe sea ice loss (Onarheim and Årthun 2017), increased water temperatures (Levitus et al. 2009), an impact on local ecosystems (Ellingsen et al. 2008) and Atlantification, i.e., the increased influence of relatively warm Atlantic water compared to colder Arctic water (Barton et al. 2018). A consequence is also a shorter ice season, implying an increased interest in shipping and natural resource exploitation in these waters (Henderson and Loe 2014; Moe 2010). This increased economic interest has caused offshore activities to move northwards, where floating glacial ice features may present serious hazards for navigation and offshore installations. The presence of icebergs in the vicinity of offshore structures greatly influences design concepts, and it is therefore of utmost importance to determine the probability of iceberg intrusion into an offshore field. Furthermore, forecasting iceberg drift is vital for ice management and rescue operations (e.g., Eik 2008).

Numerical models are currently an important tool that can be used to simulate iceberg drift and are consequently used to calculate the probability of iceberg presence at locations of interest. Various iceberg drift models have been presented in the literature, and these models have been applied to different regions, such as for the east coast of Canada (Kubat et al. 2005), the Weddell Sea (Lichey et al. 2001) and the Barents Sea (Keghouche et al. 2010; Marchenko et al. 2019). The accuracy of these models depends on the ability of the model to represent the physical processes occurring during iceberg drift and deterioration, the quality of the metocean input data (i.e., wind, currents, waves, and sea ice conditions), and how these models are seeded at the iceberg sources (i.e., the number of icebergs released per year and their size distributions).

---

[*] Corresponding author at: DTU space, Technical University of Denmark, Lyngby, Denmark.
E-mail address: dmont@space.dtu.dk (D. Monteban).

https://doi.org/10.1016/j.coldregions.2020.103084
Received 19 November 2019; Received in revised form 18 March 2020; Accepted 27 April 2020

The major sources of icebergs in the Barents Sea are Franz Josef Land, the Arctic archipelagos of eastern Svalbard, and Novaya Zemlya. The most dominant source is Franz Josef Land, which consists of nearly 2600 km of tidewater ice cliffs (Løset 1993). The adjacent waters are relatively deep, allowing large icebergs to escape from the glacier terminus. The Svalbard archipelago is a secondary source with approximately 1030 km of tidewater ice cliffs (Dowdeswell 1989). Icebergs are typically generated non-uniformly in surges over a year, with the most frequent time of iceberg release being late summer and autumn (Løset 1993). Icebergs producing glaciers are dynamic in nature where the ice flows seawards. Glacier flow continues until the yield strength of the glacial ice is reached (Pollard et al. 2015). When the strain rate is too high, fracture processes begin that initialize the formation of icebergs (Hindmarsh 2012). The amount of iceberg calving fluxes is controlled by the rate of glacier flow, the mass balance of the glacier, crevassing within the glacier and by whether the terminus is grounded or afloat (Løset et al. 2006). To date, there is no estimate of the number of icebergs released from each iceberg source in the Barents Sea, which is, as shown here, a major uncertainty when calculating the probability of iceberg occurrence.

The first well-documented iceberg study in the Barents Sea was the multi-sensor ice data acquisition programme ICEBASE (Sea Ice Investigations in the Barents Sea), which was funded by BP Norway, Esso Norway and Mobil Exploration Norway. The campaign was executed during mid-winter and fall 1987, and the main purpose was to obtain comprehensive information about sea ice and icebergs in the Barents Sea (Løset and Carstens 1996). The specific elements of the acquisition programme were precision stereo aerial photography, helicopter-borne impulse radar, satellite imagery, airborne synthetic aperture radar and three ground truthing field campaigns. ICEBASE became a model for its successor, the *Ice Data Acquisition Programme* (IDAP). IDAP was conducted by the OKN ("Operator Committee North of 62°N") over a five-year period from 1988 to 1992 (Spring 1994; Spring et al. 1993).

IDAP data provide average iceberg size characteristics of 91 $m \times 64$ $m \times 15$ m for the length, width and sail height, respectively. The iceberg length and width distributions from IDAP are typically used as input data for iceberg drift models in the Barents Sea (Hansen et al. 2019; Keghouche et al. 2010). However, the locations of the icebergs observed during the IDAP campaign were generally not close to any of the iceberg-producing glaciers. Moreover, it is quite questionable that the distribution derived from the IDAP data is valid at all the different iceberg sources in the Barents Sea.

In this paper, we use the iceberg drift model developed by Eik (2009) and Keghouche et al. (2010) with some modifications, and satellite remote sensing data to study the characteristics of icebergs at the major sources in the Barents Sea, which includes two aspects: 1) the initial iceberg length and width distributions and 2) the number of icebergs released per year that drift freely into the Barents Sea. The paper is structured as follows: Section 2 provides a brief description of the iceberg drift and deterioration model, including the main equations, the numerical implementation, the computational domain and the metocean input data. In addition, a sensitivity analysis is presented for the two input parameters of the iceberg seeding, and we demonstrate that the output of the model is highly sensitive towards these parameters. In Section 3, we use Sentinel-2 optical imagery to study the initial iceberg length and width distributions at each of the major iceberg sources separately. The Copernicus iceberg density product that is primarily based on Sentinel-1 data is used to estimate the number of icebergs that are released per year, which is described in Section 4. Moreover, the estimated number of icebergs is used to compute the annual encounter frequency and the annual number of icebergs in the Barents Sea. Finally, a discussion is presented in Section 5 prior to the main conclusions in Section 6.

2. Iceberg drift and deterioration model

The iceberg model consists of drift equations, deterioration equations and some stability criteria allowing icebergs to rollover. For readability, only a brief description of the model is given here. The full set of equations and values for all the required parameters are provided in Appendix A.

2.1. Main equations and input data

The basic equation that describes the iceberg drift motion is typically written in the form (e.g., Kubat et al. 2005)

$$m(1 + C_m)\frac{d\boldsymbol{V}_i}{dt} = \boldsymbol{F}_a + \boldsymbol{F}_w + \boldsymbol{F}_c + \boldsymbol{F}_{si} + \boldsymbol{F}_{wd} + \boldsymbol{F}_p \tag{1}$$

where m is the iceberg mass, C_m is the added mass coefficient, $\boldsymbol{V}_i$ is the iceberg velocity, t is the time, $\boldsymbol{F}_a$ and $\boldsymbol{F}_w$ are the air (wind) and the water (current) form drag, respectively, $\boldsymbol{F}_c$ is the Coriolis force, $\boldsymbol{F}_{si}$ is forcing from the sea ice adjacent to the iceberg, $\boldsymbol{F}_{wd}$ is the force due to the wave radiation stress and $\boldsymbol{F}_p$ is pressure gradient force. The model used in this study, is as any model, somewhat idealized with the following assumptions:

- The force due to wave radiation stress, $\boldsymbol{F}_{wd}$, is only implicitly included. Initially, we implemented and tested the explicit formulation of the wave radiation stress as presented by Eik (2009). This resulted in some erroneous trajectories that may be attributed to uncertainties in the wave forcing term. Similar findings are also reported by Hansen et al. (2019). Therefore, we chose to follow the approach of Keghouche et al. (2009) and model the force from wind waves implicitly through optimization of the wind drag coefficient. The effects of swell waves on the drift are neglected.
- The added mass coefficient is assumed to be 0. This again follows the approach of Keghouche et al. (2009). In their study, both the wind and current drag coefficient were calibrated against iceberg drift tracks in the Barents Sea. These optimized values were found with no added mass included and hence, no added mass was used here.
- The water drag is computed based on the current velocity in the surface layer, neglecting the vertical profile of the currents. This was done for simplicity as done in many other studies (Bigg et al. 1997; Eik 2009; Wagner et al. 2017a) and because the vertical resolution of the input data of the currents does not include an accurate vertical current profile. In like manner, the wind drag is approximated based on the surface wind.
- It was assumed that the pressure gradient force, $\boldsymbol{F}_p$, can be approximated by the geostrophic currents, i.e., the surface slope, following multiple previous studies (Gladstone et al. 2001; Stern et al. 2016; Wagner et al. 2017a). This term was combined with the Coriolis force term following Stern et al. (2016), see Eq. (A7) in Appendix A.

The iceberg drift track, $\boldsymbol{x}_i(t)$, is computed using the MATLAB (The MathWorks, Inc., Natick, MA, USA) built-in function ODE15S solver with a specified time step of 2 h. The expressions for the different forcing terms are primarily taken from Eik (2009) and Keghouche et al. (2010) and are described in Appendix A.

The iceberg decay representation considers only the three most dominant mechanisms (following the approach of Keghouche et al. 2010 and Wagner et al. 2017a), which are: wave erosion (M_e), basal turbulent melt (M_b) and thermal sidewall erosion from buoyant convection (M_v). The formulations for these terms are taken from Wagner et al. (2017a) and Gladstone et al. (2001). The iceberg length (L_i), width (W_i) and height (sail + draft) (H_i) deteriorate according to:

Table 1
Specifications of the used metocean and bathymetry data used in the iceberg model.

Parameter	Spatial resolution	Temporal resolution	Model/product name	Reference
Bathymetry	1 × 1 min	–	IBCAO	Jakobsson et al. (2012)
Wind	0.25° × 0.25°	2 h	ERA5	Copernicus Climate Change Service (C3S) (2017)
Waves	0.25° × 0.25°	2 h	ERA5	Copernicus Climate Change Service (C3S) (2017)
Currents	25 × 25 km	Daily	TOPAZ	Bertino et al. (2008)
Temperature	25 × 25 km	Daily	TOPAZ	Bertino et al. (2008)
Sea ice concentration	25 × 25 km	Daily	TOPAZ	Bertino et al. (2008)
Sea ice thickness	25 × 25 km	Daily	TOPAZ	Bertino et al. (2008)
Sea ice drift	25 × 25 km	Daily	TOPAZ	Bertino et al. (2008)

$$\frac{d(L_i)}{dt} = \frac{d(W_i)}{dt} = -(M_e + M_v) \tag{2}$$

$$\frac{d(H_i)}{dt} = -M_b \tag{3}$$

Furthermore, a stability criterion is implemented that assures that the iceberg capsizes when its width-to-height ratio, $\varepsilon \equiv W_i/H_i$, falls below a critical value (Wagner et al. 2017b). This criterion is defined as follows:

$$\varepsilon_c = \sqrt{6\frac{\rho_i}{\rho_w}\left(1 - \frac{\rho_i}{\rho_w}\right)} \tag{4}$$

where ρ_i is the density of the glacial ice and ρ_w is the density of the sea water.

A summary of the metocean and bathymetry data used in the iceberg model is presented in Table 1. The bathymetry of the Barents Sea is taken from the International Chart of the Arctic Ocean. The wind and wave data are taken from the *European Centre for Medium-range Weather Forecast* (ECMWF) reanalysis (ERA5) model. The sea ice data, current data and temperature data are obtained from the *Arctic Ocean Reanalysis System* (TOPAZ) product from the E.U. Copernicus Marine Service Information. For each time step, the metocean input data are read from the node closest to the iceberg's location. Moreover, for the data with a temporal resolution of 1 day, the values are kept constant during the 12 time steps per day (2-h time step).

2.2. *Iceberg sources*

The region covered by the iceberg drift model, together with the bathymetry of the Barents Sea and the major ocean currents, is shown in Fig. 1. In addition, this figure shows the five main iceberg sources for the Barents Sea (Keghouche et al. 2010). The icebergs are released uniformly from 1 July to 30 November because during this period, icebergs are most frequently released (Kubyshkin et al. 2006) and the maximum iceberg extension occurs during this time (Abramov 1992). Polygons are defined at the 5 major sources, and the icebergs are generated at random locations within this polygon. Furthermore, at these locations, the model requires two different inputs: 1) the number of icebergs released per year and 2) the initial size distributions. However, large uncertainties are associated with these two inputs.

2.3. *Iceberg seeding – sensitivity analysis*

We perform a sensitivity analysis here towards the numbers of icebergs released at the source and the iceberg size characteristics to show the impact of the large uncertainties in the model input data at the iceberg sources on the model outputs, i.e., the annual probability of iceberg occurrence in the Barents Sea. All the simulations extend over a 10-year period (2000–2009), and we generate icebergs only at one source, i.e., the west side of Franz Josef Land. We choose this particular source because icebergs originating from Franz Josef Land have the largest spread over the domain of the Barents Sea (Keghouche et al. 2010). The iceberg length (L_i) is generated randomly using a Weibull distribution with a location parameter of 30.1, a scale parameter of 64.97, and a shape parameter of 1.15, which was derived from the IDAP measurements. The iceberg width (W_i) and total height (sail + draft) (H_i) are computed from the empirical relationships given in Eqs. (5) and (6), respectively (Dezecot and Eik 2015).

$$W_i = 0.7\, L_i\ exp(-0.00062\, L_i) \tag{5}$$

$$H_i = 0.3\, L_i\ exp(-0.00062\, L_i) \tag{6}$$

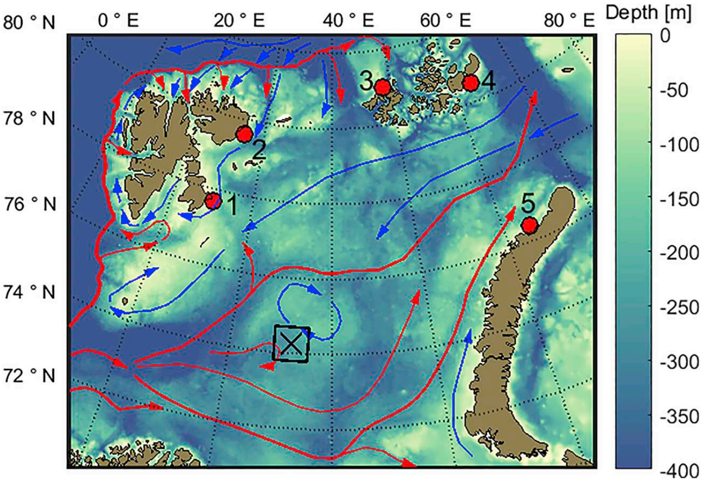

Fig. 1. Map showing the computational domain of the iceberg drift and deterioration model. The bathymetry is given in a colour scale (Jakobsson et al. 2012), and the arrows show the Barents Sea ocean currents (Eriksen et al. 2018; Vihtakari et al. 2019). The blue arrows indicate Arctic water influx and currents, and the red arrows show the Atlantic water influx and currents. The 5 main sources of icebergs are displayed and denote: 1) Edgeøya, 2) Austfonna, 3) Franz Josef Land West, 4) Franz Josef Land East and 5) Novaya Zemlya. The black cross indicates the location of the sensitivity study (Section 2.3), where the expected annual number of icebergs is extracted for a box of 100 × 100 km. (For interpretation of the references to colour in this figure legend, the reader is referred to the web version of this article.)

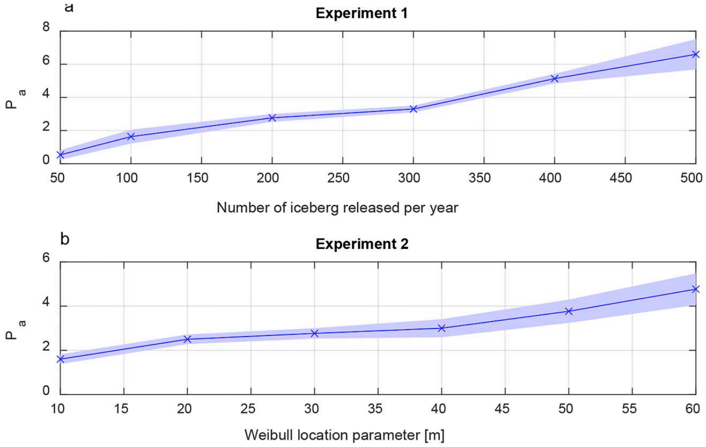

Fig. 2. Computed annual number of icebergs (P_a) entering field A (the 100 × 100 km box, shown in Fig. 1) as a function of a) the number of icebergs released annually from the source and b) the initial iceberg length at the source. The shaded area indicates the standard deviation.

An iceberg is removed from the simulations when its total height is less than 1 m or when it leaves the computational domain (extent shown in Fig. 1). For numerical experiment #1, we vary the number of icebergs released from 50 to 500 icebergs per year. For numerical experiment #2, the number of icebergs released at the source is fixed to 200 icebergs per year, and we vary the icebergs' length by varying the Weibull location parameter within the range of 10–60 m. The input of the iceberg length in experiment #1 is randomized, as well as the release of the icebergs in time and space (for both experiments). This causes the model to be not completely deterministic, and repeating a simulation will not result in the exact same numbers. Therefore, all the simulations were repeated 3 times for both experiments, which allows the computation of the statistics (means and standard deviations).

The results are presented in Fig. 2 as the annual number of icebergs (P_a) entering field A (the black box of 100 × 100 km shown in Fig. 1). The annual number of icebergs entering field A increases approximately linearly with the number of icebergs released from the source per year and with an increasing Weibull location parameter, i.e., with larger icebergs. This finding clearly demonstrates that it is vital to have reliable data on the seeding of the model at the iceberg sources.

3. Iceberg size characteristics from Sentinel-2 imagery

The numerical experiments above highlight the large sensitivity towards the size characteristics of the released icebergs at the source. Heretofore, no iceberg size characteristics have been available of newly calved icebergs for each of the individual sources. For this reason, we utilized *Sentinel-2* (S2) optical imagery to study the release of icebergs at the different sources. Despite the low scene availability due to the polar night and heavy cloud cover (e.g., Dietz et al. 2012), optical satellite imagery was chosen because of its high spatial resolution compared to, for instance, *synthetic aperture radar* (SAR). Level-1C data were used that can freely be downloaded from the Sentinel data hub of the *European Space Agency* (ESA). The S2 satellite carries a *multispectral instrument* (MSI) that samples 13 different bands. For this study, the bands in the visible range (B2, B3 and B4) that have a spatial resolution of 10 m were used. Furthermore, S2 has a swath width of 290 km and a revisit time of 2–3 days at mid-latitudes (with the twin satellites in orbit).

3.1. Description of the iceberg identification method

We decided to manually process the S2 data. Manual work has some disadvantages, such as a high time expenditure causing it to be unsuitable for large-scale applications, and the subjectivity of the observer (Baumhoer et al. 2018). Nevertheless, manual processing is very accurate and precise, and for the purpose of this study, it was found feasible as the focus was on a limited number of glaciers.

S2 data were collected for the five iceberg sources of the Barents Sea. For the two major sources located at Svalbard (Edgeøya and Austfonna), images of the area just in front of the main glacier were collected. For the other three iceberg sources, Franz Josef Land East, Franz Josef Land West and Novaya Zemlya, two locations were identified for each source as they consist of multiple calving glaciers. In Fig. 3, the eight selected locations are shown together with some S2 images of typical glaciers for each source. The data were collected for the 4-year period where S2 imagery is available (2016–2019) and the criteria for selecting the images were as follows:

- Images should be within the period 1 July until 1 November.
- The cloud cover should be less than 15%.
- Events involving pulses of icebergs being released were sought.
- Subsequent images should be at least 2 weeks apart to avoid duplicates as much as possible. In general, subsequent images were approximately 1 month apart.
- Images that include a considerable amount of sea ice were not used to avoid the misidentification of ice floes as icebergs.

The software programme used to analyse the S2 data was QGIS (QGIS Development Team 2019). Icebergs that were larger than 30 m, i.e., 3 pixels, were manually detected and polygons were drawn around the identified icebergs. The length and width of the polygons were computed with the built-in function ‘oriented minimum box’, which uses the rotating callipers algorithm (Toussaint 1983). The length of the iceberg was defined as the longest length of the fitted minimum surrounding box, and the shortest length was considered the iceberg width.

3.2. Results

The number of images processed and the number of identified icebergs for each iceberg source are provided in Table 2. In addition, the mean and maximum iceberg lengths and widths are given. In total, 71 images were processed, and 22,318 icebergs were identified. The largest observed iceberg was approximately 1 km long and originated from the west side of Franz Josef Land.

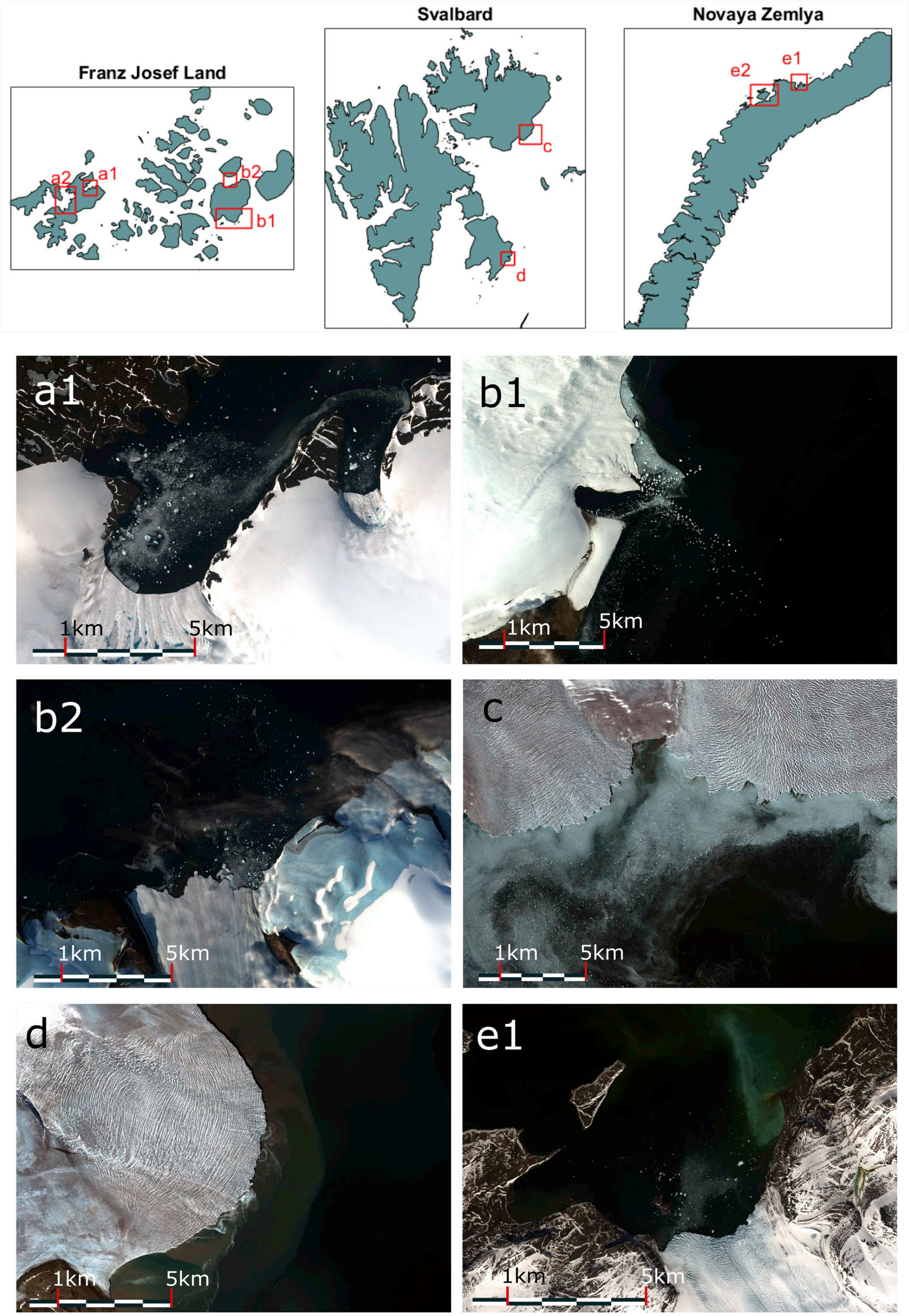

Fig. 3. S2 imagery of some selected glaciers at the iceberg sources. The images were acquired on the following dates: (a1) 04 August2019, (b1) 02 August 2018, (b2) 12 September 2016, (d) 21 August 2016 and (e1) 07 July 2017.

Table 2
Number of images processed and the number of identified icebergs, including the mean and maximum iceberg lengths and widths, for the five major iceberg sources. The 8 different locations are indicated in Fig. 3.

Geographical area	Location	Number of images	Number of icebergs	Iceberg length [m] (mean, max)	Iceberg width [m] (mean, max)
Franz Josef Land East	a1	8	1529	(61, 560)	(46, 215)
	a2	6	1639		
Franz Josef Land West	b1	9	4121	(62, 1016)	(45, 293)
	b2	8	2131		
Austfonna	c	8	7900	(52, 240)	(38, 147)
Edgeøya	d	13	785	(40, 121)	(30, 73)
Novaya Zemlya	e1	10	1576	(50, 254)	(37, 148)
	e2	9	2637		
Total		71	22,318	(55, 1016)	(41, 293)

The iceberg length and iceberg width data at each source were fitted to a 3-parameter *generalized extreme value* (GEV) distribution defined by:

$$f(x\mid k,\mu,\sigma)=\frac{1}{\sigma}\exp\left(-\left(1+k\frac{x-\mu}{\sigma}\right)^{-\frac{1}{k}}\right)\left(1+k\frac{x-\mu}{\sigma}\right)^{-1-\frac{1}{k}} \tag{7}$$

where x is the statistical value, μ is the location parameter, σ is the scale parameter and k ($\neq 0$) is the shape parameter (e.g., Kotz and Nadarajah 2000). Notably, in the case of $k > 0$, the distribution is also known as the Fréchet distribution. The location, scale and shape parameters of the GEV were found using maximum likelihood estimation, and the values are given in Table 3. Fig. 4 shows the results for the Franz Josef Land East source. A good fit is observed for both the iceberg length and the iceberg width. The tail of the iceberg length (Fig. 4b) is captured well, while the tail of the iceberg width (Fig. 4d) shows a small deviation from the fit. Satisfactory fits with the GEV distribution are also observed at the other sources (not shown here).

To demonstrate the differences between the iceberg sources, the exceedance plot of the iceberg length for each source is presented in Fig. 5. It is evident that the most severe icebergs originate from Franz Josef Land and, in particular, from the west side. The smallest icebergs originate from Edgeøya. For comparison, the iceberg length with a recurrence interval of 100 is 85 m for Edgeøya, 108 m for Austfonna, 128 m for Novaya Zemlya, 188 m for Franz Josef Land East and 240 m for Franz Josef Land West.

In Fig. 6, the iceberg lengths against the iceberg widths is plotted for the icebergs of all the sources combined. The highest density of points is found in the length interval of 30–50 m. Approximately 54% of all the identified icebergs are within this range. In addition, the empirical relationship between the lengths and the widths derived from IDAP given in Eq. (5) is also provided. It was found that this relationship fit our data very well. We applied a fitted line as well, which resulted in an almost identical empirical line, and hence, Eq. (5) was not altered. What is notable from Fig. 6 is that the icebergs that have a length larger than 300 m all have a smaller width than the empirical formula predicts. Due to wave actions, we believe that these large elongated icebergs will most likely break up when they reach more open water. Therefore, it was not deemed necessary to adjust the fitted line to better capture these very large icebergs.

Table 3
Estimated values for the fitted GEV distribution for the iceberg lengths and iceberg widths.

Geographical area	Iceberg length [m]			Iceberg width [m]		
	Location	Scale	Shape	Location	Scale	Shape
Franz Josef Land West	44.96	14.15	0.40	34.50	10.88	0.27
Franz Josef Land East	46.48	15.64	0.25	36.11	11.40	0.20
Austfonna	44.50	10.67	0.12	32.93	7.88	0.04
Edgeøya	34.60	5.86	0.22	27.30	4.86	0.02
Novaya Zemlya	39.86	12.08	0.18	31.12	8.41	0.12

Furthermore, the geometrical form of the icebergs can be defined by a shape factor (S_{peri}) as used by Løset and Carstens (1996):

$$S_{peri}=\frac{4\pi A}{p^2} \tag{8}$$

where A is the cross-sectional area of the iceberg at the water-line plane and p is the iceberg perimeter. This factor is 0.785 for squares and decreases for elongated shapes. The average value of the geometrical shape factor computed as a function of an iceberg cut-off length for the icebergs of all the sources combined is shown in Fig. 7. The shape factor is approximately 0.78 when all the icebergs are considered (i.e., a cut-off length of 30 m) and decreases for larger icebergs. The shape factor decreases when only larger icebergs are considered, which shows that the large icebergs are more elongated than the small icebergs. For comparison, Løset and Carstens (1996) found a shape factor of nearly 0.78 as well, which is based on aerial stereo photo analysis of the multi-sensor ice data acquisition programme ICEBASE.

3.3. *Comparison with IDAP*

Fig. 8 presents the distribution of the iceberg lengths for all the identified icebergs at all the sources combined. In addition, the Weibull distribution fitted to the IDAP data is shown. We find many more icebergs in the length range of 30–70 m than when using only IDAP measurements. However, care must be taken when comparing the observations. During the identification of icebergs from S2 optical imagery, a cut-off length of 30 m was applied. Growlers and bergy bits were ignored during the IDAP campaign, and therefore, the minimum identified icebergs length are, to a certain extent, similar. In this study over 22,000 icebergs were identified, while during IDAP, only 330 icebergs were observed. Furthermore, we identified icebergs in close vicinity to the sources at Franz Josef Land, Svalbard and Novaya Zemlya, whereas the IDAP campaign covered areas only in the vicinity east of Svalbard (mainly the Spitsbergen Bank and the waters towards the Olga Strait). In addition, because stereo photos during IDAP were acquired from a plane, it is likely that IDAP is slightly biased towards larger icebergs. Finally, the iceberg length in IDAP is defined as the maximum length of the iceberg. In this study, the iceberg length was found from fitting a minimum box around the defined polygons. Generally, the obtained length by fitting a minimum surrounding box is very close to the maximum length of an iceberg, so this approach does not result in significant differences.

4. Number of icebergs released into the Barents Sea per year

Many icebergs were identified from S2 optical imagery in Section 3, but it is not straightforward to utilize these data when trying to extract information on how many icebergs are released from each iceberg source. The main reason for this is that only a few usable images are available per year. Another way to estimate the number of icebergs released per year is from the calving flux *(q)*, which quantifies the discharge volume per year. Together with the mean volume of calved icebergs, and by assuming a percentage of the total calved volume that turns into icebergs that drift freely into the Barents Sea *(P_{er})*, the number of icebergs that drift freely from the source into the Barents Sea ($N_{Barents}$) is estimated as

$$N_{Barents}=P_{er}\,\frac{q}{(L_{mean}\,W_{mean}\,H_{mean})} \tag{9}$$

where L_{mean}, W_{mean}, and H_{mean} are the mean iceberg length, width and total height (draft + sail), respectively. The iceberg calving fluxes at the major sources in the Barents Sea are presented in Table 4, which are

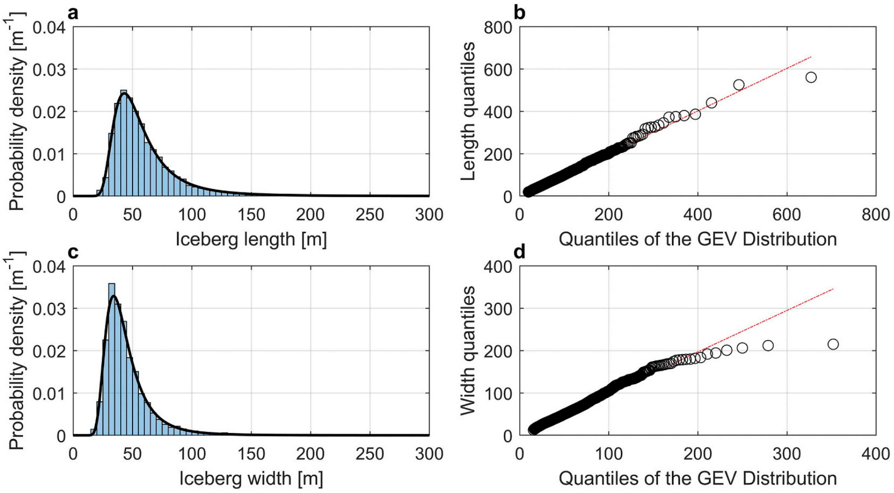

Fig. 4. Distribution of the iceberg length (a) and iceberg width (c) for Franz Josef Land East, together with the fitted GEV distribution indicated by the thick black line. (b) and (d) give the corresponding Q–Q plots that compare the GEV distribution with the iceberg lengths and iceberg widths, respectively.

based on precipitation studies and satellite remote sensing observations. From these fluxes, together with the iceberg size distributions from the IDAP campaign, Keghouche et al. (2010) estimated the annual number of generated icebergs from all sources to be approximately 19,000–20,000. Their approximation assumes that the entire calving flux results in icebergs. However, a large portion of the glacial ice flux from the glacier will just produce growlers and bergy bits, which will melt before reaching the central and southern Barents Sea. In addition, it is unclear how many icebergs are grounded and melted close to the glacier. Keghouche et al. (2010) used a percentage of 1% and consequently simulated only 200 icebergs per year to limit the amount of computations. Hansen et al. (2019) found a percentage P_{er} of 3%, which used the iceberg size characteristics from IDAP and was based on calibrating their iceberg drift model against the Abramov atlas (Abramov and Tunik 1996). However, as Hansen et al. (2019) described, the atlas has multiple sources of uncertainty. The key problem is that the statistics cannot be taken as fully representative because many icebergs were most likely not detected, and it is unclear how this phenomenon was accounted for. In this study, we overcome the shortcomings of Hansen et al. (2019) in our estimation of the percentage P_{er} by comparing the output of our iceberg drift model against direct observations made by satellite remote sensing, which we believe is much more accurate than the Abramov atlas.

4.1. *Copernicus iceberg density product*

The output of the iceberg drift model was compared against the E.U. *Copernicus Marine Environment Monitoring Service* (CMEMS) Arctic Ocean – SAR sea iceberg concentration product (CMEMS 2019). This data product contains the iceberg number density in grid cells of 10 × 10 km, which are inferred from SAR, and a *constant false alarm rate* (CFAR) concept is used to identify iceberg pixels. The observations from 2016 are solely based on Sentinel-1 *extra wide* (EW) swath data, which have a spatial resolution of 40 m. Unfortunately, only a part of the Barents Sea is covered by this data product, and therefore we can compare the model with the remote sensing data only at a few locations.

A major difficulty with this data product is duplicate icebergs. When subsequent images are separated by only a day, there is a large chance that icebergs are counted more than once. Therefore, it was decided to include data that are acquired some days apart. In Fig. 9, the number of icebergs in the Barents Sea is shown by using data that are 6 days apart for the months of July until December. The time interval of 6 days was found by plotting the number of identified icebergs for a few grid cells and the corresponding second derivative, both as a function of the time interval between the data (Fig. 10). The number of identified icebergs (Fig. 10a) decreases first exponentially, while at some point, the function becomes approximately linear. Because the second derivative of a

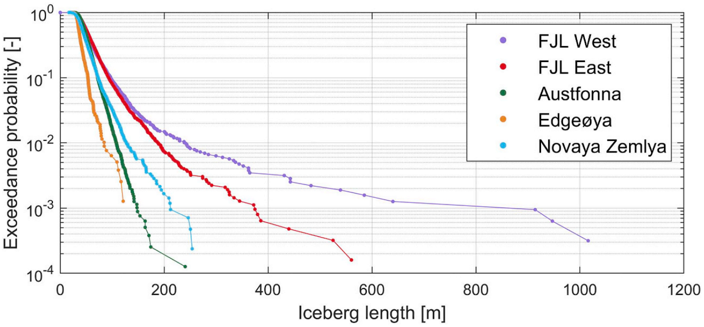

Fig. 5. Probability of exceedance of the iceberg length for the five major iceberg sources. The abbreviation FJL refers to Franz Josef Land.

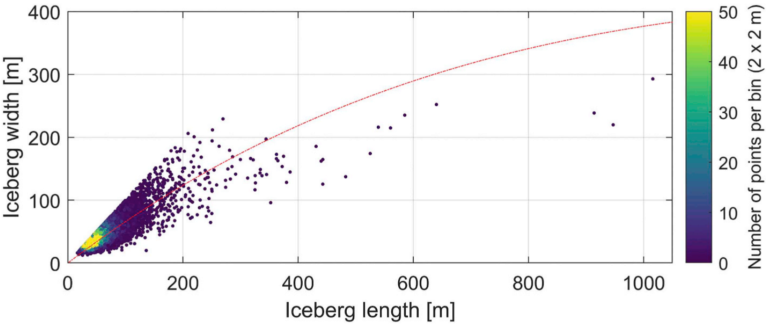

Fig. 6. Iceberg length vs iceberg width of the icebergs from all the sources combined (22,318 icebergs in total). The colour code indicates the density of the data points within a bin of 2 × 2 m. The red line is the empirical relation between the iceberg length and iceberg width as defined in Eq. (5). (For interpretation of the references to colour in this figure legend, the reader is referred to the web version of this article.)

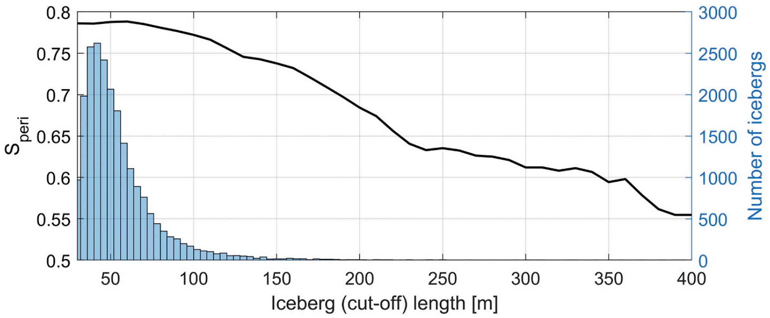

Fig. 7. Average geometrical shape factor, S_{peri}, computed for icebergs larger than the cut-off length plotted against the left y-axis. In addition, the histogram of the iceberg length for the icebergs of all the sources combined is plotted against the right y-axis.

linear line is zero, we find this point where the second derivative becomes smaller than a set tolerance value of 3 (see Fig. 10b). By assuming that icebergs are equally distributed over time, a linear relation between the number of identified icebergs and the time interval is expected. Therefore, when the time interval is doubled, only half the number of days is included, which means that half the number of icebergs is identified when assuming that each day has the same number of icebergs. Therefore, the point where the function becomes linear in Fig. 10 (time interval of 6 days) is considered long enough to minimize duplicate icebergs and, on the other hand, short enough to minimize omitting icebergs.

In addition, the data plotted in Fig. 9 are given only for selected grid cells because grid cells that are close to land and include shallow areas will contain many grounded icebergs. These grounded icebergs will be counted more than once, leading to unreliable numbers. Therefore, these grid cells were omitted during the comparison of the model output with the remote sensing data.

Table 4
Major iceberg calving locations and rates in the Barents Sea, taken from Keghouche et al. (2010) and references therein.

Geographical area	Calving location	Discharge rate (km^3 yr^{-1})
Franz Josef Land (eastern side)	80.5°N, 62.8°E	2.64
Franz Josef Land (western side)	81.0°N, 48.7°E	1.76
Austfonna	79.6°N, 27.0°E	2.7
Edgeøya	77.7°N, 25.0°E	0.6
Novaya Zemlya	76.4°N, 63.0°E	1.0

Another way of estimating the time interval is by computing the residence time of icebergs. To do so, we used the iceberg drift model, described in Appendix B. This is very similar to the drift model described in Appendix A, but it uses sea current data of higher temporal resolution

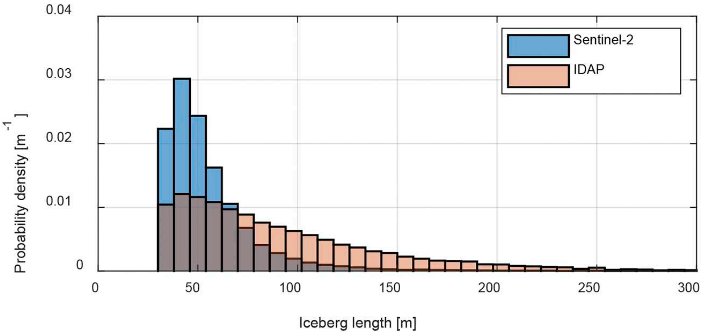

Fig. 8. Distribution of the iceberg lengths for all the icebergs observed in this study and from the Weibull distribution fitted to the IDAP measurements.

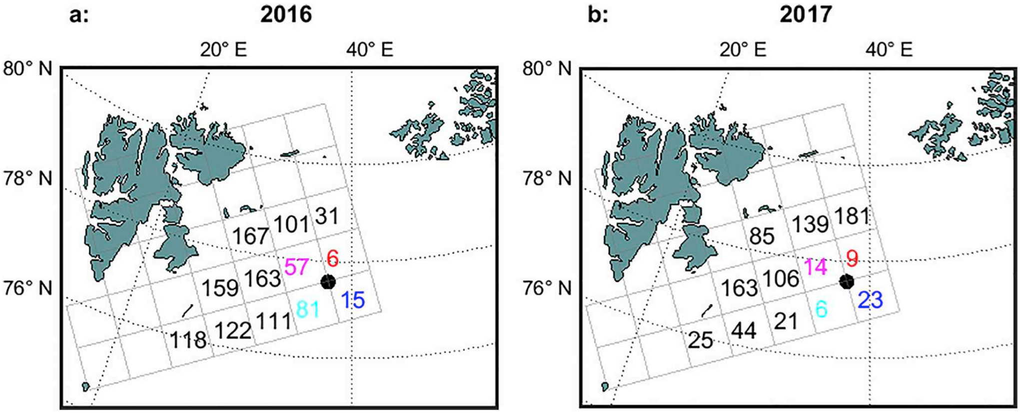

Fig. 9. Iceberg number density for grid cells of 100 × 100 km for the years 2016 and 2017 during the period 01 July until 30 November. The coloured numbers indicate the locations of the coloured lines in Fig. 10. The time interval between the data used was 6 days. The black dot indicates the centre of the box where the residence time shown in Fig. 11 is computed.

(including tidal currents). The higher temporal resolution current data are less accurate than the original current data used (Table 1) and were therefore not used for the other computations in this study.

The residence time was computed for a box of 100 × 100 km, centred around the location (77.5°N, 35°E), which is located in the middle of the 4 grid cells with coloured numbers (Fig. 9). In total, 1000 icebergs with an initial length of 100 m were generated in the centre of the box, and icebergs are removed from the simulation when they leave the 100 × 100 km box. The histogram of the residence time is given in Fig. 11. A mean residence time of 113.2 h was found, with a standard deviation of 83.5 h. This residence time is similar to the previously found time interval of 6 days, giving confidence in the validity of our specified time interval.

4.2. Comparison model results with the Copernicus iceberg density product

To estimate the percentage variable P_{er} in Eq. (9), the mean iceberg length and width found from S2 in Section 4 (Table 2) were used. The mean iceberg height (draft + sail) is computed from Eq. (6). The calving rates for all the iceberg sources are provided in Table 4. The percentage variable was estimated assuming it is constant for all the sources. Although it most likely differs from source to source, it was not possible to validate each source individually because the Copernicus data product does not cover the entire Barents Sea.

Model runs were performed for a range of percentages, and the results were compared with the values given in the cells shown in Fig. 9. A direct comparison between the numbers in the grid cells is extremely difficult, as there are variations from simulation to simulation due to the randomized input. Therefore, the focus was mainly on the contour lines of the number of icebergs per year predicted by the model. A reasonable comparison between the model output and the remote sensing product was obtained for a percentage of 1%, see Fig. 12. Most attention was given to the 50- and 200-iceberg contour lines because they showed less natural variation when the simulations were repeated. For the case (P_{er} = 1%) given in Fig. 12, the contour line of 200 icebergs is approximately above the grid cells with values between 100 and 180 icebergs, and the 50-iceberg contour line is almost beneath these grid cells. The percentage of 1% corresponds to 2603 icebergs released per year that drift freely into the Barents Sea. For each iceberg source individually, the number of icebergs released can be computed from the ratio of the discharge rate (Table 4) and results in: 351, 542, 909, 428 and 373 for Franz Josef Land West, Franz Josef Land East, Austfonna, Edgeøya and Novaya Zemlya, respectively.

4.3. Annual probability and annual number of icebergs in the Barents Sea

Finally, a simulation was performed to compute the annual probability and the annual number of icebergs in the Barents Sea. The simulation spans a duration of 27 years (1991–2017). The computational domain includes the entire Barents Sea (Fig. 1), and the 5 major iceberg sources are included. The initial length of the icebergs is taken from the fitted GEV distributions derived in Section 3.2 (Table 3), and the corresponding iceberg widths and total heights (sail + draft) are computed from Eq. (5) and Eq. (6), respectively. The annual number of icebergs released is computed from Eq. (9) by using the estimated percentage value (P_{er}) of 1% for the calving flux from Table 4 and the mean initial iceberg sizes (Table 2). The annual probability map of the Barents Sea is provided in Fig. 13, and the annual number of icebergs is given in Fig. 14.

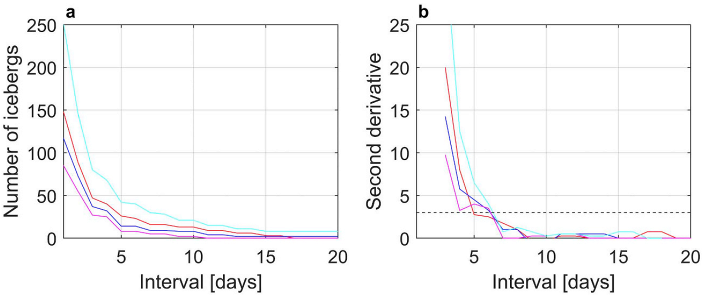

Fig. 10. The number of icebergs identified and the corresponding second derivative as a function of the time interval between subsequent data for the year 2017. The colour of the lines indicates the position of the grid cell, which can be seen in Fig. 9. The black dashed line indicates the used tolerance value of 3 for the second derivative.

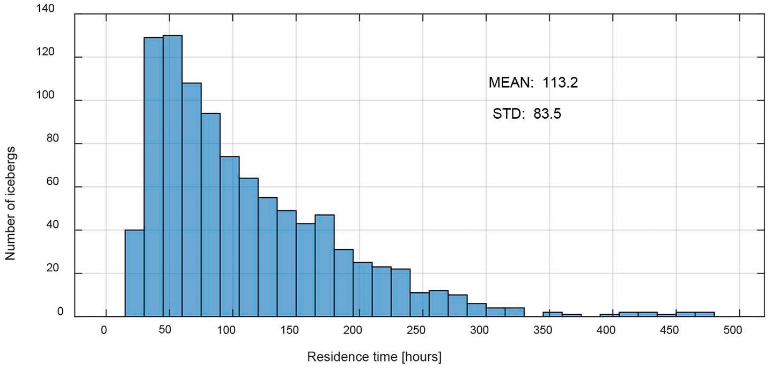

Fig. 11. Iceberg residence time for a 100 × 100 km box, centred around (77.6°N, 37.7°E). This location is indicated in Fig. 9.

5. Discussion

Although increasingly more and better-quality satellite remote sensing data are becoming available, they are not yet sophisticated enough to be used in fully operational applications. Therefore, we must still rely on numerical modelling, which is a valuable source of generating iceberg statistics. To gain confidence in the output of these models, they need to be calibrated and validated, and satellite remote sensing is undoubtedly the best and most suitable data to do so.

S2 optical imagery was used to study the size characteristics of icebergs close to the major sources in the Barents Sea. The images were manually processed to derive iceberg size statistics. Manual processing was found feasible for this study, as only a limited number of glaciers were considered. However, because the work is very time consuming, it would be of great value to have an automated algorithm to detect icebergs. This will increase the number of processed S2 images considerably and will, for instance, enable the study of seasonal dependency of iceberg sizes being calved. However, building such an algorithm is rather complicated, as there are multiple challenges present (e.g., false identification of icebergs and degraded image quality due to cloud cover) and was beyond the scope of this work.

To estimate the number of icebergs released per year that are able to drift freely into the Barents Sea, the Copernicus iceberg density data product for 2016 and 2017 was utilized. The major uncertainty and challenge with this dataset is to determine the time interval between subsequent data. This interval needs to be large enough to avoid double counting and short enough to avoid missing icebergs. We used two different approaches to estimate the time interval that gave similar results, giving us confidence in the used value of 6 days. The model results had the best comparison with the satellite data product when using a percentage of 1% of the total iceberg calving flux. The percentage value was assumed to be constant for all the sources. It is most likely that this percentage differs from source to source, but due to a lack of validation data (only a part of the Barents Sea is covered), we were not able to give an estimate at each source individually.

Furthermore, the effects of climate change will increase the uncertainties associated with the iceberg seeding of the model. A primary factor that controls the temporal release of icebergs during a year is the presence of landfast sea ice at the terminus of tidewater glaciers (Carr et al. 2013; Dalton et al. 2017; Herdes et al. 2012). Various studies have shown that the sea ice extent (Comiso et al. 2017) and the sea ice thickness (Renner et al. 2014) have been declining in the Arctic. Sea ice acts as a barrier between the open ocean and glaciers, and the loss of sea ice, as well as the thinning of sea ice, weakens this buttressing force, which leads to increased glacial ice discharge (Liu et al. 2015; Robel 2017). Furthermore, the expected future increase in the ocean surface temperature will increase submarine melting, which can amplify calving by undercutting and destabilizing the glacier front (Luckman et al.

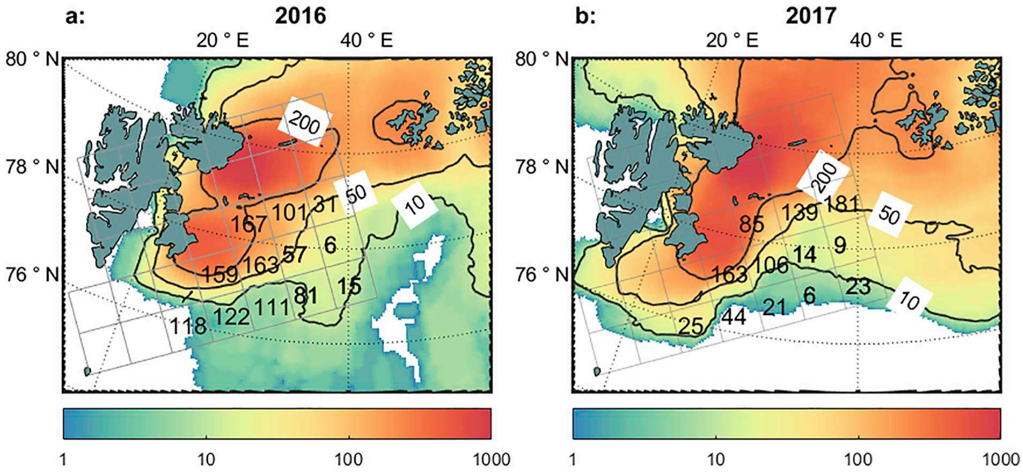

Fig. 12. The coloured area shows the number of icebergs computed from the numerical iceberg drift model for 2016 (a) and 2017 (b). The overlaid grid shows the number of icebergs found from the Copernicus iceberg density product.

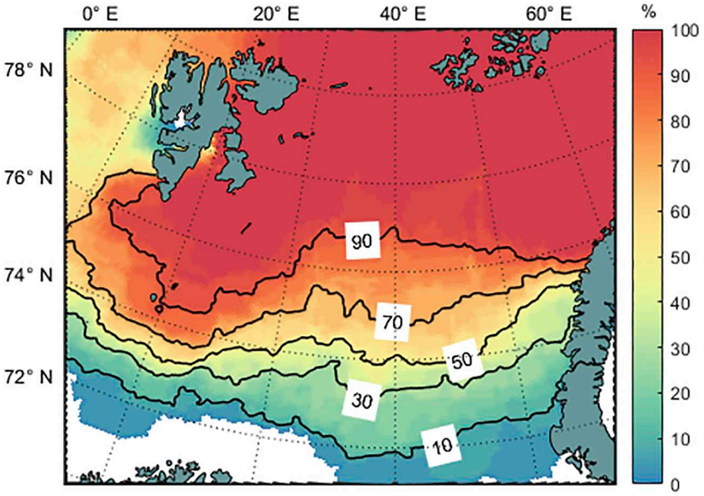

Fig. 13. Annual probability of iceberg occurrence in the Barents Sea. The map is computed for icebergs entering a box of 100 × 100 km.

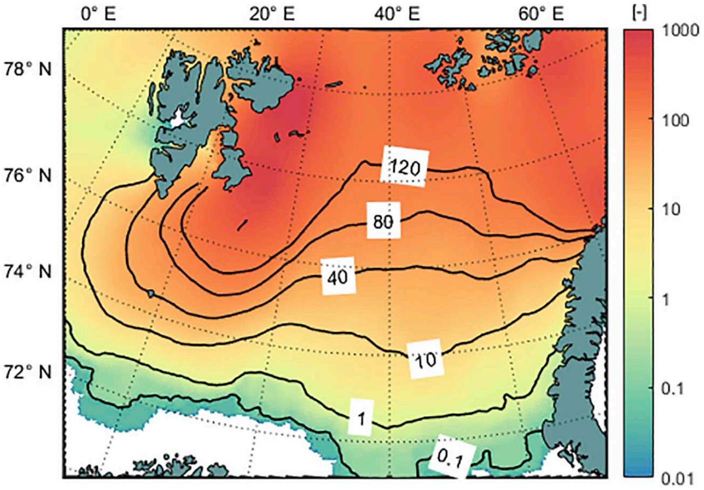

Fig. 14. Annual number of icebergs in the Barents Sea. The map is computed for icebergs entering a box of 100 × 100 km.

2015; O'Leary and Christoffersen 2013). This phenomenon may suggest an increase in iceberg discharge into the Barents Sea. However, not all the key processes of calving and submarine melting are fully understood, and it is therefore extremely difficult to predict tidewater glacier responses to climate forcing with confidence (Benn et al. 2017). The numerical iceberg drift model used in this study will be a very suitable tool to study how the predicted changes due to climate change affect the iceberg encounter probabilities in the Barents Sea.

In this study, we focused on the uncertainty in iceberg seeding at the major glacial sources. However, the model output is also dependent on the quality of the metocean input data and on how accurately the different forcing formulations represent the physical actions from the environment on the icebergs. As in any model, the idealized model used is based on assumptions made for other iceberg drift models for the Barents Sea (Eik 2009; Keghouche et al. 2010). The consequences of these approximations were not investigated in this study because they were already evaluated in the aforementioned studies. We believe that satellite remote sensing shows great potential to study and quantify the accuracy of the different forcing formulations, as increasingly more validation data are becoming available. Quantifying the importance of the different forcing terms using satellite remote sensing data and improving the numerical model are endeavours planned for future work.

6. Conclusions

In this paper, a numerical iceberg drift and deterioration model was used to quantify the sensitivity of two parameters of iceberg seeding at the major iceberg sources of the Barents Sea: 1) the annual number of icebergs released that drift freely into the Barents Sea and 2) their initial size distributions. The sensitivity experiments showed the following:

- The expected number of icebergs that enter a box of 100 × 100 km (centred around 74.25°N, 36°E) per year increases approximately linearly with increasing iceberg sizes and with an increasing annual number of icebergs released from the sources.

Sentinel-2 satellite optical imagery was used to manually identify icebergs close to the major sources in the Barents Sea, namely, Franz Josef Land, eastern Svalbard and Novaya Zemlya for the years 2016–2019. The main findings are as follows:

- The most severe icebergs originate from Franz Josef Land West, while the smallest icebergs come from the Svalbard source Edgeøya.
- Over 22,000 icebergs were identified, with the largest iceberg being approximately 1 km long and originating from Franz Josef Land West.
- We provide values of the fitted GEV distribution for the iceberg length and iceberg width at each iceberg source separately.
- The average geometrical shape factor of all the identified icebergs is 0.78, and this factor decreases for larger icebergs, meaning that large icebergs are more elongated.
- An empirical relationship between iceberg lengths and iceberg widths is given.

Furthermore, the Copernicus iceberg density product was utilized to estimate the annual number of icebergs released from the major sources and the following was found:

- The model results are largely comparable to the iceberg density product when using a release rate of 1% of the total glacial calving flux.

Finally, a simulation extending a 27-year period was performed using the newly obtained iceberg size characteristics and annual number of released icebergs to compute the annual probability of iceberg occurrence and the expected number of icebergs per year for the entire Barents Sea.

Declaration of Competing Interests

The author declare that they have no known competing financial interests or personal relationships that could have appeared to influence the work reported in this paper.

Acknowledgements

We thank the students Tom ten Voorde and Nauman Raza for their help in digitizing the icebergs from optical imagery. This project is partly based on Sentinel-2 optical imagery, which was kindly made available by the ESA and can be freely downloaded from the ESA's Sentinel data hub. The Copernicus iceberg density product is available at http://marine.copernicus.eu/services-portfolio/access-to-products/?option=com_csw&view=details&product_id=SEAICE_ARC_SEAICE_L4_NRT_OBSERVATIONS_011_007. The bathymetry data are taken from the International Bathymetric Chart of the Arctic Ocean and are available at https://www.ngdc.noaa.gov/mgg/bathymetry/arctic/arctic.html. The meteorological input data are taken from the European Centre for Medium-range Weather Forecast ERA5 model (https://cds.climate.copernicus.eu/cdsapp#!/dataset/reanalysis-era5-single-levels?tab=overview.) and the Copernicus TOPAZ product (http://marine.copernicus.eu/services-portfolio/access-to-products/?option=com_csw&view=details&product_id=ARCTIC_REANALYSIS_PHYS_002_003). Finally, we acknowledge the support from the SAMCoT CRI through the Research Council of Norway and all the SAMCoT partners.

Appendix A. Iceberg drift and deterioration equations and parameters

A.1. Equations of iceberg drift

All the equations used in the iceberg drift model together with the required input parameters are summarized here. The drift equations are taken from the paper by Eik (2009) and the references therein, unless stated otherwise. The values of the parameters in the equations are provided in Table A1. The used basic equation reads:

$$m(1 + C_m)\frac{d\boldsymbol{V}_i}{dt} = \boldsymbol{F}_c + \boldsymbol{F}_p + \boldsymbol{F}_a + \boldsymbol{F}_w + \boldsymbol{F}_{si} + \boldsymbol{F}_{wd} \tag{A1}$$

The Coriolis force ($\boldsymbol{F}_{cor}$) is given in Eq. (A2), with the Coriolis parameter ($\boldsymbol{f}$) shown in Eq. (A3).

$$\boldsymbol{F}_{cor} = -m\,\boldsymbol{f}\times\boldsymbol{V}_i \tag{A2}$$

$$\boldsymbol{f} = 1.45\bullet 10^{-4}\ \sin(\varphi)\,\mathbf{k} \tag{A3}$$

The pressure gradient, $\boldsymbol{F}_p$, was approximated by the geostrophic currents. Following Stern et al. (2016), the 'Coriolis related-force', $\boldsymbol{F}_{cor\_geo}$, which defines the Coriolis force minus the geostrophic balance part, reads:

$$\boldsymbol{F}_{cor\_geo} = -m\,\boldsymbol{f}\times(\boldsymbol{V}_i - \boldsymbol{V}_g) \tag{A4}$$

where $\boldsymbol{V}_g$ is the geostrophic current based on Slagstad et al. (1990). The wave radiation stress force, $\boldsymbol{F}_{wd}$, is implicitly taken into account in the calibrated wind drag coefficient and together with Eq. (A4), Eq. (A1) can be written as:

$$m(1 + C_m)\frac{d\boldsymbol{V}_i}{dt} = -m\,\boldsymbol{f}\times(\boldsymbol{V}_i - \boldsymbol{V}_g) + \boldsymbol{F}_a + \boldsymbol{F}_w + \boldsymbol{F}_{si} \tag{A5}$$

The expression for the drag forces due to the currents ($\boldsymbol{F}_w$) and the wind ($\boldsymbol{F}_a$) is defined as:

$$\boldsymbol{F}_{a,w} = \frac{1}{2}\rho_{a,w}\,C_{a,w}\,A_{a,w}\,|\boldsymbol{V}_{a,w} - \boldsymbol{V}_i|(\boldsymbol{V}_{a,w} - \boldsymbol{V}_i) \tag{A6}$$

where $A_{a,\,w}$ is the cross-sectional area on which the wind/current velocity acts. We adopt the approach from (Wagner et al. 2017a) and define these areas as follows:

$$A_w = \frac{\rho_i}{\rho_w}\frac{2}{\pi}(L_i + W_i)\,H_i \tag{A7}$$

$$A_a = \frac{\rho_w - \rho_i}{\rho_i}A_w \tag{A8}$$

The expression for the sea ice forces ($\boldsymbol{F}_{si}$) is:

$$\boldsymbol{F}_{si} = 0: C_i \leq 0.15$$

$$\boldsymbol{F}_{si} = \frac{1}{2}\rho_{si}\, C_{si}\, A_{si}\, |\boldsymbol{V}_{si} - \boldsymbol{V}_i|\, (\boldsymbol{V}_{si} - \boldsymbol{V}_i): 0.15 < C_i < 0.9 \tag{A9}$$

$$\boldsymbol{F}_{si} = -(\boldsymbol{F}_a + \boldsymbol{F}_w + \boldsymbol{F}_{\boldsymbol{cor\_geo}}): C_i \geq 0.9\&\mathrm{h} > \mathrm{h}\, min$$

where C_i is the ice concentration, A_{si} is the cross-sectional area on which the sea ice acts and h_{min} is the minimum sea ice thickness. The formulations of the latter two parameters are defined in Eq. (A10) and Eq. (A11), respectively.

$$A_{si} = \frac{2}{\pi}\,(L_i + W_i)\, h \tag{A10}$$

$$h_{min} = \frac{P}{P^*\, \exp(-20\,(1 - C_i))} \tag{A11}$$

A.2. Deterioration equations

The deterioration of the icebergs is driven by wave erosion M_e, bottom melt M_b and buoyant convection at the sidewalls M_v. The formulation of the wave erosion term is taken from (Gladstone et al. 2001) and reads (m/s):

$$M_e = \frac{1}{86400}\left(\left[\frac{1}{6}(\widetilde{T}_o + 2)\right] S_s \left[\frac{1}{2}(1 + \cos(C_i^3 \pi))\right]\right) \tag{A12}$$

where $\widetilde{T}_o$ is the sea surface temperature and S_s is the sea state defined as:

$$S_s = \frac{3}{2}\, |\boldsymbol{V}_a - \boldsymbol{V}_w|^{1/2} + \frac{1}{10}\, |\boldsymbol{V}_a - \boldsymbol{V}_w| \tag{A13}$$

The formulations of the bottom melt and buoyant convection at the sidewalls are taken from the paper by Wagner et al. (2017a) and references therein, and they read (m/s):

$$M_b = a_1\, |\boldsymbol{V}_i - \boldsymbol{V}_w|^{0.8} \frac{\widetilde{T}_o - \widetilde{T}}{L_i^{0.2}} \tag{A14}$$

$$M_v = b_1 \widetilde{T}_o + b_2 \widetilde{T}_o^{\,2} \tag{A15}$$

where $a_1 = 8.7 \times 10^{-6}\, m^{-0.4} s^{-0.2}$, $b_1 = 8.8 \times 10^{-8}\, ms^{-1}\, {}^{\circ}C^{-1}$ and $b_2 = 1.5 \times 10^{-8}\, ms^{-1}\, {}^{\circ}C^{-2}$.

Table A1
Description and values of the parameters used in the iceberg model.

Parameter	Description	Value	Reference
ρ_w	Water density	1027 [kg/m^3]	
ρ_i	Glacial ice density	850 [kg/m^3]	
ρ_a	Air density	1.225 [kg/m^3]	
ρ_{si}	Sea ice density	900 [kg/m^3]	
C_w	Water drag coefficient	0.25 [−]	Keghouche et al. (2009)
C_a	Air drag coefficient	0.7 [−]	
C_{si}	Sea ice drag coefficient	1.0 [−]	Eik (2009)
P	Sea ice strength	660.9 [N/m]	Eik (2009)
P^*	Sea ice coefficient	20,000 [N/m^2]	
$\widetilde{T}$	The effective iceberg temperature	−4 °C	Wagner et al. (2017a)

Appendix B. Local model for computation residence time

For the computation of the residence time in Section 4.1, some small adjustments to the model were made. This adjusted model is referred to as the 'local model' and is used only for the computation of the residence time. All the other computations throughout this manuscript use the equations provided in Appendix A. The difference between the local model and the model presented in Appendix A is that higher temporal resolution currents are generated, where the water velocity, V_{water}, is defined as:

$$\boldsymbol{V}_{\boldsymbol{water}} = \boldsymbol{V}_t + \boldsymbol{V}_g \tag{B1}$$

with V_t the tidal current and V_g the geostrophic current. The geostrophic data are based on those from Slagstad et al. (1990), and the tidal current is generated from the 4 major tidal constituents (M2, S2, N2 and K1) using the method of Gjevik et al. (1994). Finally, the wind-induced surface current is defined in the local model as:

$$\boldsymbol{V}_{\boldsymbol{wind}} = \frac{2}{100}\, \boldsymbol{ws} \tag{B2}$$

where $\boldsymbol{ws}$ is the wind speed.

References

Abramov, V.A., 1992. Russian iceberg observations in the Barents Sea, 1933–1990. Polar Res. 11, 93–97. https://doi.org/10.1111/j.1751-8369.1992.tb00415.x.

Abramov, V., Tunik, A., 1996. Atlas of Arctic Icebergs: The Greenland, Barents, East-Siberian and Chukchi Seas in the Arctic Basin. Backbone Publ. Co.

Barton, B.I., Lenn, Y.D., Lique, C., 2018. Observed atlantification of the Barents Sea causes the Polar Front to limit the expansion of winter sea ice. J. Phys. Oceanogr. 48, 1849–1866. https://doi.org/10.1175/JPO-D-18-0003.1.

Baumhoer, C.A., Dietz, A.J., Dech, S., Kuenzer, C., 2018. Remote sensing of antarctic glacier and ice-shelf front dynamics-a review. Remote Sens. 10, 1–28. https://doi.org/10.3390/rs10091445.

Benn, D.I., Cowton, T., Todd, J., Luckman, A., 2017. Glacier calving in Greenland. Curr. Clim. Chang. Reports 3, 282–290. https://doi.org/10.1007/s40641-017-0070-1.

Bertino, L., Lisæter, K.A., Scient, S., 2008. The TOPAZ monitoring and prediction system for the Atlantic and Arctic Oceans. J. Oper. Oceanogr. 1, 15–18. https://doi.org/10.1080/1755876X.2008.11020098.

Bigg, G.R., Wadley, M.R., Stevens, D.P., Johnson, J.A., 1997. Modelling the dynamics and thermodynamics of icebergs. Cold Reg. Sci. Technol. 26, 113–135. https://doi.org/10.1016/S0165-232X(97)00012-8.

Carr, J.R., Vieli, A., Stokes, C., 2013. Influence of sea ice decline, atmospheric warming, and glacier width on marine-terminating outlet glacier behavior in northwest Greenland at seasonal to interannual timescales. J. Geophys. Res. Earth Surf. 118, 1210–1226. https://doi.org/10.1002/jgrf.20088.

CMEMS, 2019. Arctic Ocean - SAR sea iceberg concentration product. Product Identifier: SEAICE_ARC_SEAICE_L4_NRT_OBSERVATIONS_011_007. E.U. Copernicus Marine Service Information.

Comiso, J.C., Meier, W.N., Gersten, R., 2017. Variability and trends in the Arctic Sea ice cover: results from different techniques. J. Geophys. Res. Ocean. 122, 6883–6900. https://doi.org/10.1002/2017JC012768.

Copernicus Climate Change Service (C3S), 2017. ERA5: Fifth generation of ECMWF atmospheric reanalyses of the global climate. Copernicus Climate Change Service Climate Data Store (CDS) 01-03-2019. https://cds.climate.copernicus.eu/cdsapp#!/home.

Dalton, A., Knudby, A., Tivy, A., 2017. Iceberg Production and Characteristics at the Termini of Tidewater Glaciers around the Prince of Wales Icefield, Ellesmere Island. Arctic, Antarct. Alp. Res. 51, 412–427. https://doi.org/10.1080/15230430.2019.1634442.

Dezecot, C., Eik, K., 2015. Barents East blocks Metocean Design Basis, Statoil Report. Document no.: ME2015-005.

Dietz, A.J., Kuenzer, C., Gessner, U., Dech, S., 2012. Remote sensing of snow - a review of available methods. Int. J. Remote Sens. 33, 4094–4134. https://doi.org/10.1080/01431161.2011.640964.

Dowdeswell, J.A., 1989. On the nature of Svalbard icebergs. J. Glaciol. 35, 224–234.

Eik, K., 2008. Review of experiences within ice and iceberg management. J. Navig. 61, 557–572. https://doi.org/10.1017/S0373463308004839.

Eik, K., 2009. Iceberg drift modelling and validation of applied metocean hindcast data. Cold Reg. Sci. Technol. 57, 67–90. https://doi.org/10.1016/j.coldregions.2009.02.009.

Ellingsen, I.H., Dalpadado, P., Slagstad, D., Loeng, H., 2008. Impact of climatic change on the biological production in the Barents Sea. Clim. Chang. 87, 155–175. https://doi.org/10.1007/s10584-007-9369-6.

Eriksen, E., Gjøsæter, H., Prozorkevich, D., Shamray, E., Dolgov, A., Skern-Mauritzen, M., Stiansen, J.E., Kovalev, Y., Sunnanå, K., 2018. From single species surveys towards monitoring of the Barents Sea ecosystem. Prog. Oceanogr. 166, 4–14. https://doi.org/10.1016/j.pocean.2017.09.007.

Gjevik, B, Nost, E, Straume, T, 1994. Model simulations of the tides in the Barents Sea. Journal of geophysical research 99 (2), 3337–3350.

Gladstone, R.M., Bigg, G.R., Nicholls, K.W., 2001. Iceberg trajectory modeling and meltwater injection in the Southern Ocean. J. Geophys. Res. Ocean. 106, 19903–19915. https://doi.org/10.1029/2000jc000347.

Hansen, E., Borge, J., Arntsen, M., Olsson, A., Thomson, M., 2019. Estimating icebergs hazards in the Barents Sea using a numerical iceberg drift and deterioration model. In: Proceedings of the 25th International Conference on Port and Ocean Engineering under Arctic Conditions, Delft.

Henderson, J., Loe, J., 2014. The Prospects and Challenges for Arctic Oil Development. The Oxford Institute for Energy Studies, Oxford. https://doi.org/10.26889/9781784670153.

Herdes, E., Copland, L., Danielson, B., Sharp, M., 2012. Relationships between iceberg plumes and sea-ice conditions on Northeast Devon ice cap, Nunavut, Canada. Ann. Glaciol. 53, 1–9. https://doi.org/10.3189/2012AoG60A163.

Hindmarsh, R.C.A., 2012. An observationally validated theory of viscous flow dynamics at the ice-shelf calving front. J. Glaciol. 58, 375–387. https://doi.org/10.3189/2012JoG11J206.

Jakobsson, M., Mayer, L., Coakley, B., Dowdeswell, J.A., Forbes, S., Fridman, B., Hodnesdal, H., Noormets, R., Pedersen, R., Rebesco, M., Schenke, H.W., Zarayskaya, Y., Accettella, D., Armstrong, A., Anderson, R.M., Bienhoff, P., Camerlenghi, A., Church, I., Edwards, M., Gardner, J.V., Hall, J.K., Hell, B., Hestvik, O., Kristoffersen, Y., Marcussen, C., Mohammad, R., Mosher, D., Nghiem, S.V., Pedrosa, M.T., Travaglini, P.G., Weatherall, P., 2012. The International Bathymetric Chart of the Arctic Ocean (IBCAO) version 3.0. Geophys. Res. Lett. 39, 1–6. https://doi.org/10.1029/2012GL052219.

Keghouche, I., Bertino, L., Lisæter, K.A., 2009. Parameterization of an iceberg drift model in the barents sea. J. Atmos. Ocean. Technol. 26, 2216–2227. https://doi.org/10.1175/2009JTECHO678.1.

Keghouche, I., Counillon, F., Bertino, L., 2010. Modeling dynamics and thermodynamics of icebergs in the Barents Sea from 1987 to 2005. J. Geophys. Res. Ocean. 115, 1–14. https://doi.org/10.1029/2010JC006165.

Kotz, S., Nadarajah, S., 2000. Extreme Value Distributions: Theory and Applications. Imperial College Press, London.

Kubat, I., Sayed, M., Savage, S.B., Carrieres, T., 2005. An operational model of iceberg drift. Proc. Int. Offshore Polar Eng. Conf. 2005, 752–758.

Kubyshkin, N.V., Buzin, I.V., Glazovsky, A.F., Skutin, A.A., 2006. Determination of the area of generation of big icebergs in the barents sea - Temperature distribution analysis. Proc. Int. Offshore Polar Eng. Conf. 634–638.

Levitus, S., Matishov, G., Seidov, D., Smolyar, I., 2009. Barents Sea multidecadal variability. Geophys. Res. Lett. 36, 1–5. https://doi.org/10.1029/2009GL039847.

Lichey, C., Hellmer, H., Hartmut, H., 2001. Modeling giant-iceberg drift under the influence of sea ice in the Weddell Sea, Antarctica. J. Glaciol. 47, 452–460. https://doi.org/10.3189/172756501781832133.

Liu, Y., Moore, J.C., Cheng, X., Gladstone, R.M., Bassis, J.N., Liu, H., Wen, J., Hui, F., 2015. Ocean-driven thinning enhances iceberg calving and retreat of Antarctic ice shelves. Proc. Natl. Acad. Sci. U. S. A. 112, 3263–3268. https://doi.org/10.1073/pnas.1415137112.

Løset, S., 1993. Thermal energy conservation in icebergs and tracking by temperature. J. Geophys. Res. 98, 1–10.

Løset, S., Carstens, T., 1996. Sea ice and iceberg observations in the western Barents Sea in 1987. Cold Reg. Sci. Technol. 24, 323–340. https://doi.org/10.1016/0165-232X(95)00029-B.

Løset, S., Shkhinek, K.N., Gudmestad, O.T., Høyland, K.V., 2006. Actions from Ice on Arctic Offshore and Coastal Structures.

Luckman, A., Benn, D.I., Cottier, F., Bevan, S., Nilsen, F., Inall, M., 2015. Calving rates at tidewater glaciers vary strongly with ocean temperature. Nat. Commun. 6, 1–7. https://doi.org/10.1038/ncomms9566.

Marchenko, A., Diansky, N., Fomin, V., 2019. Modeling of iceberg drift in the marginal ice zone of the Barents Sea. Appl. Ocean Res. 88, 210–222. https://doi.org/10.1016/j.apor.2019.03.008.

Moe, A., 2010. Russian and Norwegian petroleum strategies in the Barents Sea. Arct. Rev. Law Polit. 1, 225–248.

O'Leary, M., Christoffersen, P., 2013. Calving on tidewater glaciers amplified by submarine frontal melting. Cryosphere 7, 119–128. https://doi.org/10.5194/tc-7-119-2013.

Onarheim, I.H., Årthun, M., 2017. Toward an ice-free Barents Sea. Geophys. Res. Lett. 44, 8387–8395. https://doi.org/10.1002/2017GL074304.

Pollard, D., DeConto, R.M., Alley, R.B., 2015. Potential Antarctic Ice Sheet retreat driven by hydrofracturing and ice cliff failure. Earth Planet. Sci. Lett. 412, 112–121. https://doi.org/10.1016/j.epsl.2014.12.035.

QGIS Development Team, 2019. QGIS Geographic Information System. Open Source Geospatial Foundation Project. http://qgis.osgeo.org.

Renner, A.H.H., Gerland, S., Haas, C., Spreen, G., Beckers, J.F., Hansen, E., Nicolaus, M., Goodwin, H., 2014. Evidence of Arctic sea ice thinning from direct observations. Geophys. Res. Lett. 41, 5029–5036. https://doi.org/10.1002/2014GL060369.

Robel, A.A., 2017. Thinning sea ice weakens buttressing force of iceberg mélange and promotes calving. Nat. Commun. 8. https://doi.org/10.1038/ncomms14596.

Screen, J.A., Simmonds, I., 2010. The central role of diminishing sea ice in recent Arctic temperature amplification. Nature 464, 1334–1337. https://doi.org/10.1038/nature09051.

Slagstad, D, Støle-Hansen, K, Loeng, H, 1990. Density driven currents in the Barents Sea calculated by a numerical model, Modeling, Identification and Control. Modeling, Identification and Control (MIC) 11 (4), 181–190. https://doi.org/10.4173/mic.1990.4.1.

Spring, W., 1994. Ice Data Acquisition Program (IDAP) Summary Report. Dallas E&P Engineering, Dallas.

Spring, W., Vinje, T., Jensen, H., 1993. Iceberg and sea ice data obtained in the annual expeditions of the Barents Sea Ica Data Acquisition Program (IDAP). In: Proceedings of the 12th International Conference on Port and Ocean Engineering under Arctic Conditions, Hamburg.

Stern, A.A., Adcroft, A., Sergienko, O., 2016. The effects of Antarctic iceberg calving-size distribution in a global climate model. J. Geophys. Res. Ocean. 121, 5773–5788. https://doi.org/10.1002/2016JC011835.

Toussaint, G.T., 1983. Solving geometric problems with the "rotating calipers". In: Proc. IEEE MELECON'83.

Vihtakari, M., Sundfjord, A., de Steur, L., 2019. Barents Sea ocean-current arrows modified from Eriksen et al. (2018). Norwegian Polar Institute and Institute of Marine Research Available at. https://github.com/MikkoVihtakari/Barents-Sea-currents.

Wagner, T.J.W., Dell, R.W., Eisenman, I., 2017a. An analytical model of iceberg drift. J. Phys. Oceanogr. 47, 1605–1616. https://doi.org/10.1175/JPO-D-16-0262.1.

Wagner, T.J.W., Stern, A.A., Dell, R.W., Eisenman, I., 2017b. On the representation of capsizing in iceberg models. Ocean Model 117, 88–96. https://doi.org/10.1016/j.ocemod.2017.07.003.